DESIGN OF RUBBLE-MOUND STRUCTURE AS SCOUR PROTECTION FOR VERTICAL SEAWALLS: LAYER THICKNESS, MEDIAN ROCK MASS AND ENERGY DISTRIBUTION THROUGH THE LAYERS

BY

ANCHEN STREUDERST

Thesis presented in fulfilment of the requirements for

the degree of Master of Engineering in the

Faculty of Civil Engineering at Stellenbosch University.

Supervisor: Prof JS Schoonees

March 2021

DECLARATION

By submitting this thesis electronically, I declare that the entirety of the work contained therein is my own, original work, that I am the sole author thereof (save to the extent explicitly otherwise stated), that reproduction and publication thereof by Stellenbosch University will not infringe any third party rights and that I have not previously in its entirety or in part submitted it for obtaining any qualification.

_____

Anchen Streuderst

_____

Student number

_____

Date

ENGLISH ABSTRACT

This study contributes to the optimal design of a rubble-mound structure used as toe protection for a vertical seawall. A concrete seawall is placed on top of a screed layer. In front of the seawall, the rubble-mound berm consisting of a core, filter layer and armour layer functions as a protection for the seawall and its foundation. Scouring of the screed layer is among the leading causes of seawall failure. To determine design guidelines to minimise the scouring of the screed layer, forty-two physical model tests were conducted at Stellenbosch University Hydraulics Laboratory. The (horizontal) erosion of the screed layer and scoured screed area for each experiment was observed, measured and analysed. The scoured area was computed using a new method developed by the author using the *Image Processing Toolbox* in MATLAB.

Wave celerity increases as the wave period increases, leading to a rise in the rate of wave energy transmission through the structure. Subsequently, more scour of the screed develops as more wave energy reaches the screed layer. The scour areas for peak wave periods ranging between 6s and 12s were narrowly grouped, whereas the scoured areas for the 16s and 18s wave periods were significantly scattered and higher. In one of the most extreme cases tested, an 18s wave period caused 83% of the screed layer to be washed out.

The rubble-mound structures with the highest crest provided the best protection. At an 18s peak wave period, the largest structure experienced a 20% scoured area, whereas the lowest structure experienced 80% scour of the screed layer. Increasing the filter layer (underlayer) beneath the armour layer proved to be effective and economical. By adding two layers of rock to the filter layer (underlayer), a 19% increase in the total crest height led to a 50% decrease in the scoured screed area. A thicker layer generates an irregular surface resulting in better interlocking and increased porosity which improves wave energy dissipation and armour layer stability. Additionally, a larger median rock mass in the underlayers enhanced the energy dissipation and structural stability. The filter criterion stating that the underlayer's rock mass should be a tenth of the upper layer proved to be the most effective in the majority of experiments.

As a first approximation, to determine the energy distribution, the dynamic pressure head was measured at different elevations in the rubble-mound and converted into velocity. Even though the small-scale model produced high variability in the measurements, the general trend indicated that the outer layers contain the highest energy region, with limited energy penetrating the core (34% on average). The armour layer had the highest measured energy when the median rock mass of the filter layer was small since the flow was concentrated in the armour layer. When the median rock mass of the filter layer was larger, the water was dissipated into the filter layer and became less violent in the armour layer, resulting in the highest energy region being in the filter layer. Equations were developed using dimensional analysis to predict the energy in the rubble-mound structure layers based on identified factors affecting the flow through porous media. The results indicate that a well-designed rubble-mound berm can effectively dissipate the approaching wave

energy and accordingly limit the energy penetrating the core and so reduce scouring of the screed layer below the seawall.

AFRIKAANS OPSOMMING

Die studie dra by tot die optimale ontwerp van ‘n ruklipstruktuur wat gebruik word as toonbeskerming vir ‘n vertikale seemuur. Die betonseemuur word geplaas bo-op ‘n vlaklaag. Seewaarts van die muur bestaan die ruklipstruktuur uit ‘n kern, filterlaag en bolaag. Uitskuring van die vlaklaag is een van die hoofoorsake van seemuurswigting. Twee-en-veertig fisiese model toetse is gedoen in Stellenbosch Universiteit se Hidroulika Laboratorium om te bepaal hoe om die uitskuring te verminder van die vlaklaag. Die horisontale uitskuring van die vlaklaag en die uitskuringsoppervlak vir die eksperimente is waargeneem, gemeet en geanaliseer. Die uitskuring oppervlak is bereken deur ‘n nuwe metode wat deur die skrywer ontwikkel is. Die metode maak gebruik van MATLAB se *Image Processing Toolbox*.

Die golfsnelheid neem toe soos die golfperiode toeneem, dit lei tot ‘n toename in die oordragstempo van die golfenergie. Gevolglik ontwikkel ‘n groter uitskuringsoppervlak want meer energie bereik die vlaklaag. Die uitskuringsoppervlakte van die piekgolfperiodes tussen 6s en 12s is baie naby aan mekaar gegroepeer, maar die uitskuring van die 16s en 18s is aansienlik hoër. In een van die uiterste gevalle het ‘n 18s-golfperiode veroorsaak dat 83% van die vlaklaag uitgeskuur het.

Die hoogste ruklipstrukture het die beste beskerming vir die vlaklaag gebied. By ‘n 18s piekgolfperiode het die grootste struktuur 20% uitskuring van die vlaklaag ervaar, waar die kleinste struktuur 80% uitskuring gehad het. Dit is bevind dat deur die filterlaag dikker te maak, in plaas van die bolaag, meer effektief en ekonomies is. Deur twee lae klip by die filterlaag te sit (19% toename in die totale hoogte), lei tot ‘n 50% afname in die uitskuringsoppervlak van die vlaklaag. ‘n Dikker laag genereer ‘n onreëlmatige oppervlak wat lei tot beter ineensluiting en ‘n toename in porositeit wat die golfenergieverspilling en strukturele stabiliteit verbeter. Addisioneel, dra ‘n groter gemiddelde klipmassa in die onderlae ook by tot golfenergieverspilling en bolaagstabiliteit. Die filterkriteria wat bepaal dat die onderlae ‘n tiende van die massa moet wees van die bolaag was die effektiefste in die meerderheid van eksperimente.

As ‘n eerste benadering is die dinamiese druk op verskillende hoogtes in die ruklipstruktuur gemeet en omgeskakel na snelheid om die energieverspreiding te bereken. Al het die klein-skaalmodel hoë wisseling in die druklesings veroorsaak, het die algemene tendens nogtans getoon dat die bolae die hoogste energie bevat, en beperkte energie die kern bereik (gemiddeld 34%). Die bolaag het die hoogste energie wanneer die filterlaag se gemiddelde klip massa kleiner is want die vloei word dan gekonsentreer in die bolaag. Wanneer die gemiddelde klipmassa van die filterlaag groter is, kan die water na die filterlaag beweeg en word minder aktief in die bolaag. Dit veroorsaak dat die hoogste energie in die filterlaag is. Vergelykings is geskep deur die proses van dimensionele analise om die energie in die ruklipstruktuur lae te bereken gebaseer op geïdentifiseerde faktore wat die vloei deur poreuse media beïnvloed. Die resultate toon dat ‘n goeie ontwerpte ruklipstruktuur die energie wat die kern bereik beperk, en so ook die uitskuring van die vlaklaag onder die seemuur verminder.

ACKNOWLEDGEMENTS

I am grateful for the following people:

- My supervisor, Prof JS Schoonees for sharing his expertise in the coastal engineering field and for guiding me through my thesis.
- The laboratory personnel; Johann Nieuwoudt, Iliyaaz Williams and Jody February, who provided practical solutions and was always willing to assist me. They created a fun working environment with their cheerfulness and stories.
- Carl Wehlitz from the CSIR, who helped me obtain the necessary material for the screed layer and who was always willing to share his insight and knowledge.
- My flatmate, Nicole Taylor, who came up with the idea to measure the scour area using MATLAB and who helped me write the necessary code, and for a fun two years of living and studying together.
- My father, Johan Streuderst, for his advice, support and giving me the opportunity to study what I am passionate about.
- My mother, Heilani Streuderst, for her continuous prayers and keeping me motivated and encouraged.
- My fiancé, Pero Buys, for his insights and advice as a Civil Engineer. For his continued love and hard work that inspired me to finish my thesis and give my best.

DEDICATIONS

This thesis is dedicated to my Lord and Saviour, Jesus Christ.

"Have you not known? Have you not heard? The Lord is the everlasting God, the Creator of the ends of the earth. He does not grow faint or weary; his understanding is unsearchable." Isaiah 40:28

TABLE OF CONTENTS

LIST OF FIGURES

LIST OF TABLES

ABBREVIATIONS

2D	Two-dimensional
A_{For}	Forchheimer laminar term constant
ARC	Active Reflection Compensation
B_c	Crest Width (m)
B_{For}	Forchheimer turbulent and/or oscillatory term constant
COV	Coefficient of variation
D_{n50}	Nominal rock diameter (m)
ds	Z-coordinate of the structure surface (m)
d_0	Water depth at the flat slope (m)
d_1	Water depth at the start of the 1:20 slope (m)
d_2	Water depth at toe of rubble-mound structure (m)
d_3	Water depth above rubble-mound structure (m)
$D_{15\ (cover)}$	Diameter that exceeds the coarsest 85% of the layer above the underlayer (m)
$D_{85\ (under)}$	Diameter that exceeds the coarsest 15% of the underlayer (m)
E_d	Dissipated wave energy
E_{da}	Dissipated wave energy in the armour layer
E_{dc}	Dissipated wave energy in the core
E_{df}	Dissipated wave energy in the filter layer
E_i	Incident wave energy
ELL	Extreme Lower Limit
E_r	Reflected wave energy
E_t	Transmitted wave energy
EUL	Extreme Upper Limit
f	Wave frequency (Hz)
F	Fetch length (m)
g	Standard gravity (9.81m/s^2)
h	Water depth (m)
H	Incident wave height (m)
h_c	Breakwater structure height/crest height (m)
H_i	Significant/incident wave Height (m)
H_m	Maximum wave height (m)
H_{max}	Transmitter maximum pressure head limit (m)
H_{min}	Transmitter minimum pressure head limit (m)
H_{m0}	Zero-moment wave height (m)
$(H_{m0})_0$	zeroth-moment deep water wave height (m)

H_{out}	Measured dynamic pressure head (m)
H_s	Significant wave height (m)
h_t	Depth of toe below water (m)
h_w	Water level at the seawall (m)
i	Hydraulic gradient
I_{max}	Transmitter maximum current output (A)
I_{min}	Transmitter minimum current output (A)
IQR	Interquartile range
JONSWAP	Joint North Sea Wave Project
k	Incident regular wave number
k	Permeability coefficient
K	Scale factor for wave transmission
KC	Keulegan-Carpenter number
K_d	Dissipation coefficient
K_{da}	Armour layer dissipation coefficient
K_{dc}	Core dissipation coefficient
K_{df}	Filter layer dissipation coefficient
KE	Kinetic energy (J)
k_p	Wave number associated with the spectral peak liner wave theory
K_r	Reflection coefficient
k_t	Layer thickness coefficient
K_t	Transmission coefficient
L	Incident regular wavelength (m)
L_m	Offshore wavelength (m)
L_0	Deep-water wavelength (m)
L_{10}	Shallow water wavelength (m)
ΔL	Average width of the core material (m)
m	Gradient of the slope
M_y	Mass corresponding to passing value y
M_{50}	50% value on mass distribution curve
n	Number of layers in the rubble-mound structure
n_A	Number of rocks in the armour layer
n_f	Number of rocks in the filter layer
NLL	Nominal Lower Limit
n_{RRM}	Uniformity index (steepness of grading curve)
NUL	Nominal Upper Limit
n_v	Volumetric porosity
N_x	Scaling ratio

p	Pressure (kg/ms^2)
PIV	Particle Image Velocimetry
PM	Pierson-Moskowitz spectrum
Q	Ratio of broken waves to the total number of waves
q_1	First quartile of data
q_2	Second quartile of data
q_3	Third quartile of data
R	Resistance of the transmitter (Ω)
R_c	Crest freeboard
RRD	Rosin-Rammled Diameter
RRM	Rosin-Rammler Mass
s_{op}	Wave steepness
S_m	Maximum vertical scour depth in the seabed (m)
T	Oscillation period (s)
TBC	To be confirmed
T_p	Peak wave period (s)
u	Horizontal velocity component (m/s)
$\hat{U}$	Amplitude of the oscillating velocity (m/s)
$(u_{rms})_m$	Horizontal bottom velocity root-mean-square
u_v	Seepage velocity (m/s)
U_{10}	Wind speed 10m above sea surface (m/s)
V_{atm}	Atmospheric hydrostatic pressure voltage reading (V)
w	Vertical velocity component (m/s)
W	Internal energy dissipation in rubble-mound structure (kg/s^3)
x	Measured voltage reading (V)
X_m	Value of variable X in the model
X_p	Value of variable X in the prototype
X_{12}	Distance between probe 1 and probe 2 in the wave flume (m)
X_{23}	Distance between probe 2 and probe 3 in the wave flume (m)
X_{13}	Distance between probe 1 and probe 3 in the wave flume (m)
y	Fraction passing value
ξ	Surf similarity parameter
$\propto$	Beach slope
$\propto$	Calibration constant (taken as 1)
$\propto_{For}$	Forchheimer laminar coefficient
β_{For}	Forchheimer turbulent coefficient
Δ	Relative density (kg/m^3)
ρ	Density of water (kg/m^3)

γ	Peak enhancement factor = 3.3
γ_b	Average breaker index (taken as 0.7)
υ_w	Kinematic viscosity of water = 1.787 x 10^{-6} m^2/s
η	Wave elevation (m)
θ	Shields parameter

1 INTRODUCTION

1.1 BACKGROUND

Coastal erosion is a threat worldwide due to coastal zones being among the most vulnerable environments in terms of climate change. Coastal zones are known as “vulnerability hot spots” with regards to climate change. The impact of climate change on our coasts is evident through sea-level rise, variations in wave height and wave direction, intense rainfall, storm surges and flooding (Betzold and Mohamed, 2017).

As a reaction to climate change, coastal defences are positioned to act as protection against coastal hazards. One such coastal defence structure is a seawall. Seawalls are a dominant form of coastal protection but are often poorly designed and constructed due to a lack of capacity (funds, design expertise) as well as a lack of research. Consequently, an increase rather than a decrease in erosion results. Or at best, the erosion will be relocated to a different location (Betzold and Mohamed, 2017). Figure 1-1 shows an example of a vertical seawall in Southern California.

Figure 1-1: Vertical seawall in Southern California (Coastal Care, 2019)

Seawalls do not offer a sure means of defence and protection. Precautions should be in place against scouring of material underneath a seawall due to the seawall’s vulnerability to wave attack (Chadwick, Morfett & Borthwick, 2013). Scour, in coastal engineering, is the removal of granular bed material in the vicinity of coastal structures through the presence of hydrodynamic forces (USACE, 2002).

Scouring is one of the leading causes of failure at seawalls. Studies conducted in the United Kingdom show that 34% of seawall failures are directly related to erosion of the foundation or beach material, and that scour is responsible for 14% of all failures (CIRIA, 2007). Vertical seawalls reflect almost all the incident wave energy, while potentially causing erosive action at the toe of the wall. If adequate toe protection is absent, the seawall could become undermined, leading to total failure (Chadwick, Morfett & Borthwick, 2013). Figure 1-2 illustrates the eroded profile in front of a vertical seawall after a storm event.

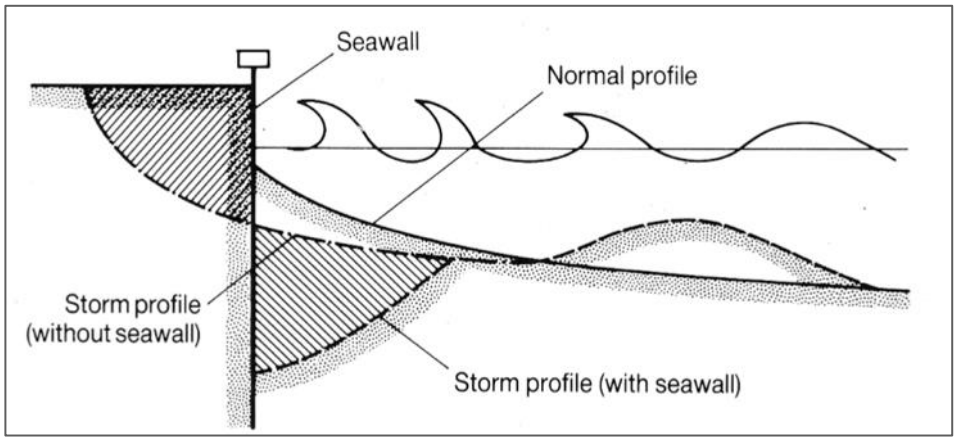

Figure 1-2: Scour in front of a seawall due to a storm event (CIRIA, 2007)

The study aims to contribute to the design guidelines of a vertical seawall placed on a screed layer with a rubble-mound structure as toe protection. The rubble-mound structure consists of an armour layer, filter layer (underlayer) and core (see Figure 1-3). The screed layer is critical for level placement and stability of the seawall. This thesis builds on the recommendations made by Malan (2016) and Van Wageningen (2018) who conducted laboratory tests to determine the optimal screed layer thickness and berm width of a rubble-mound structure to minimise scouring of the screed layer. Due to scour leading to many structure failures, prevention for local scour should be a principle design objective.

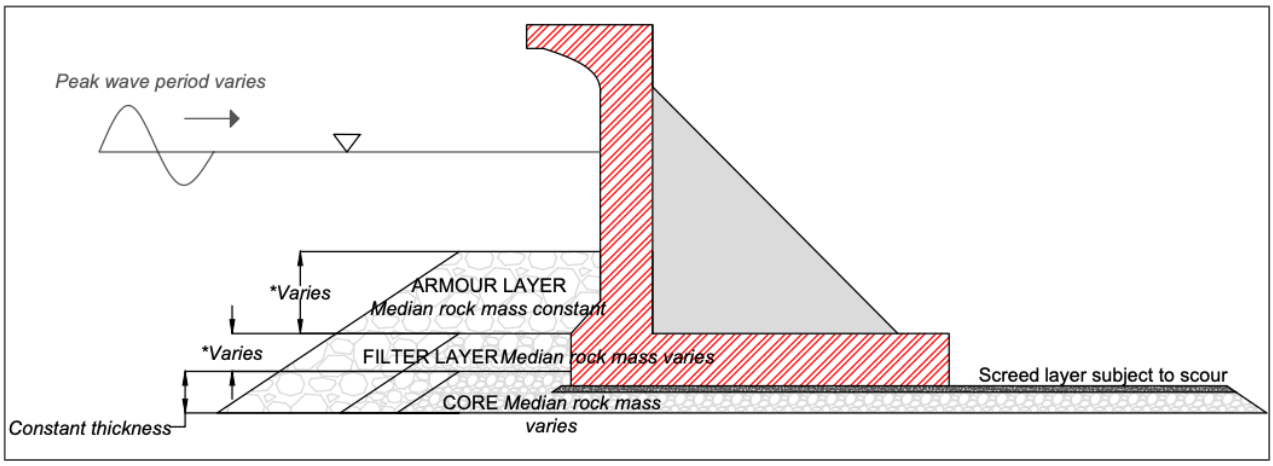

Figure 1-3: Structure cross-section indicating parameters examined to meet the stated objectives

1.2 OBJECTIVES

The overall objective of this thesis is to improve the design approach relating to the prevention of the scour of the screed layer beneath coastal seawalls. This leads to the following more specific objectives with reference to the situation as given in Figure 1-3:

- Determine the effect of a wide range of peak wave periods on the scour of the screed layer (including storm wave periods).
- Determine the influence of the rubble-mound structure layer thickness on the scour of the screed layer.
- Determine the influence of the median rock mass in the layers of the rubble-mound structure on the scour of the screed layer.
- Determine, as a first approximation and from basic principles, the flow velocity and energy distribution in the rubble-mound structure and its effect on screed layer scour development.
- Predict, by dimensional analysis, the kinetic energy in the layers of the rubble-mound structure and the penetration of wave energy to the screed layer.

1.3 SCOPE

The scope of this thesis includes studying literature to gain knowledge regarding the design of vertical seawalls and rubble-mound structures. The literature study covers existing research about scouring underneath vertical seawalls and a brief investigation into the aspects of physical laboratory experiments. Physical modelling was included to investigate the scour of the screed layer; specifically the effect of peak wave periods and the following variables: median rock mass of the filter layer and core of the rubble-mound structure and the armour layer and filter layer (underlayer) thickness. It should be noted that the stability of the armour layer is not part of the scope.

1.3.1 Outline of Methodology

The impact of the median rock mass is determined by changing the median rock mass between underlying layers while keeping the layer thickness constant. Two different filter rules are applied to determine the effect of rock mass on scouring. The two filter rules are: $\frac{M_{50\,lower}}{M_{50\,upper}} = \frac{1}{10}$ and $\frac{M_{50\,lower}}{M_{50\,upper}} = \frac{1}{15}$. The effect of the layer thickness on scouring is tested by configuring six different structures with different layer thicknesses, while the median rock mass remains constant.

The range of peak wave periods tested covers typical nearshore South African conditions: 6s, 8s, 10s, 12s, 14s, 16s and 18s. The latter two periods are associated with storm conditions (data obtained from the CSIR Wavenet) (CSIR, 2020). The wave height (H_s) is also that of a characteristic South African condition: 1.3m.

Measurements of the dynamic pressure head in the various layers of the rubble-mound structure are taken during the forty-two physical model tests. The pressure measurements are used to calculate the flow velocity through the rubble-mound structure as well as the kinetic energy and energy dissipation in the respective layers. Dimensional analysis is applied to predict the kinetic energy in the layers of the rubble-mound structure based on the significant parameters affecting the energy distribution. The effect of the energy that penetrates the core has on scour development is also analysed. The aim is, however, not to present a theoretical and in-depth analysis of the flow and energy through porous media. But instead, gain insight into the energy distribution in the rubble-mound structure, and lay the foundation of future research. The results presented in the study are based on simple assumptions and should only be accepted as a first approximation to the flow through porous media.

1.4 The Layout of the Thesis

The format of this thesis, expanding upon the content of each chapter is as follows:

- *Chapter 1 – Introduction*

The background and motivation behind the study is provided as well as the objectives it aims to achieve, the scope and an outline of the methodology.

- *Chapter 2 – Literature Study*

Provides an overview of existing literature in the field. It includes a review of literature about basic coastal parameters, coastal defence structures, scour in the marine environment, wave energy dissipation, physical models and laboratory techniques. Specific literature on seawall and screed scour is included.

- *Chapter 3 – Methodology*

The experimental test plan for the laboratory work is provided as well as the method to analyse the results.

- *Chapter 4 – Visual Inspection*

Describes the visual observations made concerning wave breaking, overtopping, water levels, structural deformation and flow inside the rubble mound (porous media) during the execution of the experiments.

- *Chapter 5 – Scour Experimental Results and Analysis*

Processing of the raw data and statistical analysis of the results are presented.

- *Chapter 6 – Flow Velocity and Energy Distribution in Layers*

Calculations of the flow velocity and energy distribution through the layers of the rubble-mound and the effects of energy penetration on scour development in the screed material are reported.

- *Chapter 7 – Conclusions and Recommendations*

The conclusions about the study are provided and recommendations are proposed for future research.

2 LITERATURE STUDY

2.1 COASTAL PARAMETERS

2.1.1 WAVE STEEPNESS AND WAVE ENERGY

The surf similarity parameter – also known as the Iribarren number – is used to describe breaking wave action on a slope (such as a beach). The Iribarren number is expressed by Equation 2-1 (Van der Meer, 1992).

$$\xi = \frac{\tan\propto}{\sqrt{s_{op}}} \qquad 2\text{-}1$$

Where

s_{op} = Wave steepness = $\frac{2\pi H}{gT^2}$

$\propto$ = Beach slope

The surf similarity parameter describes the type of wave breaking on a gently sloping structure or the beach. The three types of wave breaking illustrated in Figure 2-1 are: spilling breaker, plunging breaker and a surging breaker (Van der Meer, 1992).

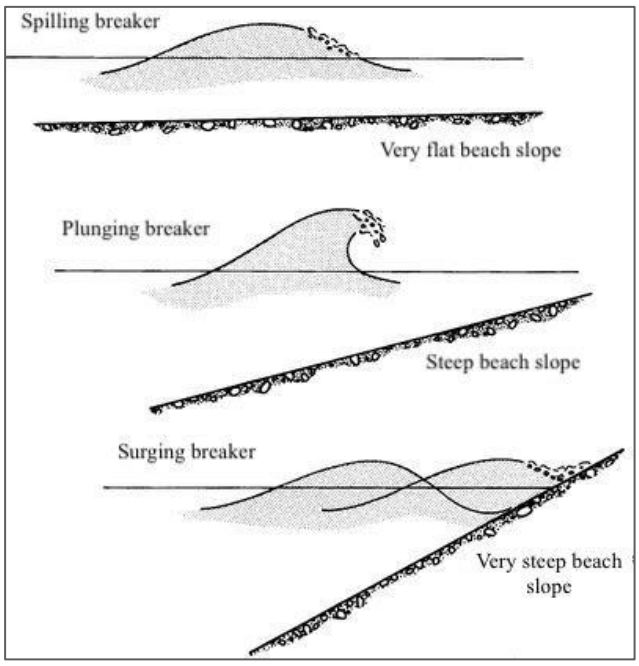

Figure 2-1: Main types of breaking waves (Chadwick, Morfett & Borthwick, 2013)

The linear wave theory applies to oscillating waves. The water particles of the wave move forward and backwards with each consecutive wave with a distinct crest and trough (USACE, 2002). The energy contained

within a wave consists of the kinetic, potential and surface tension energy. Surface tension is neglected for ocean waves, and the potential and kinetic energy are equal when using the linear wave theory. Equation 2-2 is used to calculate the energy per unit area in the ocean (Chadwick, Morfett & Borthwick, 2013).

$$E = \frac{\rho g H^2}{8} \qquad 2\text{-}2$$

The wave power (transmission of wave energy) can be expressed by:

$$P = EC_G \qquad 2\text{-}3$$

Where

C_G = Group wave celerity (m/s)

2.1.2 HYDRAULIC RESPONSES

The most critical hydraulic interactions relevant in the design of a coastal defence structure include wave run-up, wave run-down, wave transmission, reflection and overtopping (CIRIA, 2007).

2.1.2.1 Wave Run-Up and Wave Run-Down

Wave run-up and run-down describe the extreme levels reached due to breaking wave action. Wave run-up and run-down is defined vertically relative to the still water level. The wave run-up is the highest level that the incident wave will reach on the beach or structure (USACE, 1984). The run-up level determines the level of the structure crest. The run-down level determines the lower extent of the armour layer (CIRIA, 2007).

2.1.2.2 Wave Overtopping

When the wave-run up levels are extreme, wave overtopping may occur (water discharges over the crest of the structure). Wave overtopping occurs for a few waves during the design lifetime. It is usually accepted if the rate of overtopping remains low, with minimum damage to the structure or protected area (CIRIA, 2007).

2.1.2.3 Wave Reflection

Wave reflection often causes a confused sea state in front of the structure due to the interaction of the reflected waves with the incident waves. Wave reflections lead to an increase in the peak orbital velocities, which

increases the movement of bed material (CIRIA, 2007).

2.1.2.4 Wave Transmission

Wave transmission is relevant to a structure with porous material. It is the process where longer wave periods lead to the transmission of wave energy through the structure (CIRIA, 2007). When a wave approaches a structure (H_i), such as the breakwater shown in Figure 2-2, a part of the incident energy is reflected, giving a wave height H_r seaward of the structure. The remaining energy will either be transmitted via overtopping or transmitted through the breakwater, causing a wave height H_t on the leeward side of the structure (if the structure is open on the leeward side). The incident energy that is not reflected or transmitted is dissipated in the structure (preserving the balance of energy) (Van der Meer and Daemen, 1994).

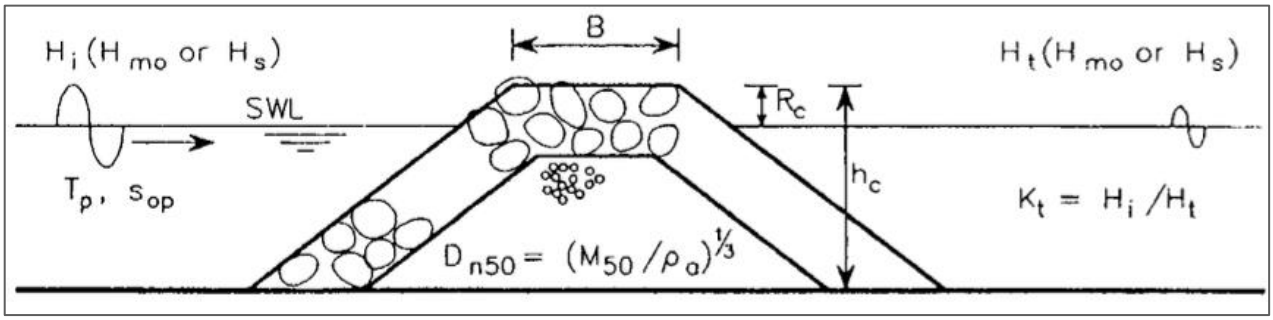

Figure 2-2: Breakwater and the relevant parameters involved in wave transmission (Van der Meer et al., 2004)

The wave transmission coefficient (K_t) is the ratio between the incident and transmitted wave height (Equation 2-4). The incident wave height is the height of the wave as measured at the toe of the structure, and the transmitted wave height is the height of the wave as measured behind the structure. Referring to Figure 2-2, the governing parameters that determine the transmitted wave height are the significant wave height (H_i), peak wave period (T_p), water depth at the structure (h) and the structure height (h_c). The governing parameters regarding the breakwater are crest height (h_c), crest width (B_c) (shown as (B) in Figure 2-2), slope angle ($\cot\propto$) and the material properties (D_{n50}, permeability and porosity) (Van der Meer *et al.*, 2004).

$$K_t = {}^{H_i}/_{H_t} \qquad 2\text{-}4$$

There are two main formulae for determining K_t, developed initially by Daemen and Van der Meer (1994) and d'Angremond, Kees & Van der Meer (1996). In a recent study by (Van der Meer *et al.*, 2004), the existing formulae were improved by using two different relations. The first relationship is for the scenario where $B_c/H_i < 10$. In this case, Equation 2-5 is used to determine K_t.

$$K_t = (0.031\frac{H_i}{D_{n50}} - 0.024)\frac{R_c}{D_{n_{50}}} + -5.42\, s_{op} + 0.0323\frac{H_i}{D_{n_{50}}} - 0.071\,(\frac{B}{D_{n_{50}}})^{1.84} + 0.51 \qquad 2\text{-}5$$

$$0.075 < K_t < 0.75$$

The second relationship is where $B_c/H_i > 10$. In this case, Equation 2-6 is used to determine K_t.

$$K_t = -0.35\frac{R_c}{H_i} + 0.51\left(\frac{B}{H_i}\right)^{-0.65} \text{x } [1 - \exp(-0.41\xi_{op})] \quad \text{2-6}$$

$$0.05 < K_t < -0.006\frac{B}{H_i} + 0.93$$

2.2 Coastal Protection Structures

2.2.1 General Classification

Coastal areas and their inhabitants are protected through the placement of specific measures and structures. There are two approaches to coastal defence schemes: “soft engineering” and “hard engineering”. Hard engineering measures are rigid or semi-rigid structures that are constructed to prevent deformation from wave and current action. Soft engineering measures are building with natural processes in mind and mainly relying on biological (e.g. mangroves) or geophysical coastal processes (sediment transport) to prevent erosion (IADC, 2017).

The stability of a coastal structure can be classified by Equation 2-7, known as the stability number. Small values of this equation result in structures like caissons and seawalls. The diameter used for seawalls and caissons is the height or width of the structure. The H/ΔD-value should be smaller than one for these structures since no or only minor damage is allowed for a fixed structure. Seawalls and caissons are also known as statically stable structures (Van der Meer, 1992).

$$N_s = \frac{H}{\Delta D_{n50}} \quad \text{2-7}$$

Another type of structure is a dynamically stable structure where profile development is relevant. This includes the displacement of sand or gravel under wave action and is roughly classified to have a H/ΔD-value greater than six (Van der Meer, 1992).

2.2.2 CONSTRUCTION MATERIALS

2.2.2.1 Classification of Soil

The Unified Soil Classification System (USCS) classifies soil according to grain size. Table 2-1 provides a summary of the general types of soils (USACE, 2002).

Table 2-1: Types of soil (Coastal Engineering Manual, 2002)

Soil	Particle Size	Description
Boulders and cobbles	$d_{boulders} > 300mm$ $75mm < d_{cobbles} < 300mm$	• Rounded or angular • Bulky • Stable components for stabilizing slopes and fill material
Gravels and sand	$4.76mm < d_{gravels} < 75mm$ $0.074mm < d_{sand} < 4.76mm$	• Rounded or angular • Natural or by crushing larger stones
Silts and clays	$d_{cobbles} < 0.074mm$	• Silts are unstable, difficult to compact and easily eroded • Clays exhibit plastic behaviour and cohesive strength

2.2.2.2 Sand

When it is technically feasible, earth and sand should be used as a filler, since coastal projects tend to be quite large and require a large volume of construction materials. For seawalls, sand is used as backfill or foundation material. When using the sand as a backfill material, it is essential to compact the soil to provide supportive soil pressure to resist hydrostatic pressures and wave loads (USACE, 2002).

2.2.2.3 Rock

The critical parameter with regards to defining the rock used in a coastal defence structure is the nominal diameter in Equation 2-8. M_{50} is the 50% exceedance value on the mass distribution curve (Van der Meer, 1992).

$$D_{n50} = \left(\frac{M_{50}}{\rho_r}\right)^{\frac{1}{3}} \quad 2\text{-}8$$

The D_{85}/D_{15}-ratio and the M_{85}/M_{15}-ratio indicate the grading of the rock. The D_{85} and D_{15} denote that 85% and 15% of the grain diameters in the sample were below these values respectively. Similarly, M_{85} and M_{15} concern the respective grain masses in the sample. The grading widths are defined in Table 2-2 (Van der Meer, 1992).

Table 2-2: Grading widths (Van der Meer, 1992)

Narrow Grading	Wide Grading	Very Wide Grading
$D_{85}/D_{15} < 1.5$	$1.5 < D_{85}/D_{15} < 2.5$	$D_{85}/D_{15} > 2.5$
$1.7 < M_{85}/M_{15} < 2.7$	$2.7 < M_{85}/M_{15} < 16$	$16 < M_{85}/M_{15} < 125$

2.2.3 SEAWALL

Seawalls are a hard protection adaptation strategy (Williams et al., 2016). The primary function of a seawall is to prevent flooding from large and powerful waves caused by storm events as well as to protect and stabilise the shore from erosion that is caused by wave action (Ayers, 1950). One example of an existing seawall that protects against storm events is the concrete seawall constructed in Galveston, Texas. The seawall was built in 1902 as a reaction to the hurricane in 1900 where 6000 people lost their lives. This seawall has saved many lives and a large amount of money (due to reduced property damage) in the years since it has been constructed (USACE, 2002).

By protecting the infrastructure on the landward side of the seawall, erosion of the seabed at the seaward side of the structure will enhance. It will eventually result in a steeper seabed profile and cause more massive waves at the structure (assuming there is no recovery of the seabed profile in the milder season). The erosion at the toe of the structure can cause instability of the seawall. Toe instability can be overcome by scour protection. Scour protection has the primary purpose of trying to prevent instability of seawalls by placing foundations on the seabed. This foundation typically consists of a rock bed on stone or geotextile filer. Impermeable vertical walls are much more likely to experience near-structure scour than sloping rubble-mound structures (USACE, 2002).

2.2.3.1 Types of Seawalls

Seawalls can be vertical faced or sloped, held in place by gravity (e.g. a concrete gravity wall or rubble mound) or by concrete piling. The surfaces can consist of concrete slabs, rubble-mound stone or concrete armour units. Vertical seawalls are known as non-energy absorbing walls. Sloping seawalls, on the other hand, would absorb some of the wave energy (USACE, 2002).

Figure 2-3 to Figure 2-5 illustrate three different types of seawalls. The type of seawall to be constructed will depend on the topography of the site, wave characteristics, tidal range and the foundation conditions (Ayers, 1950).

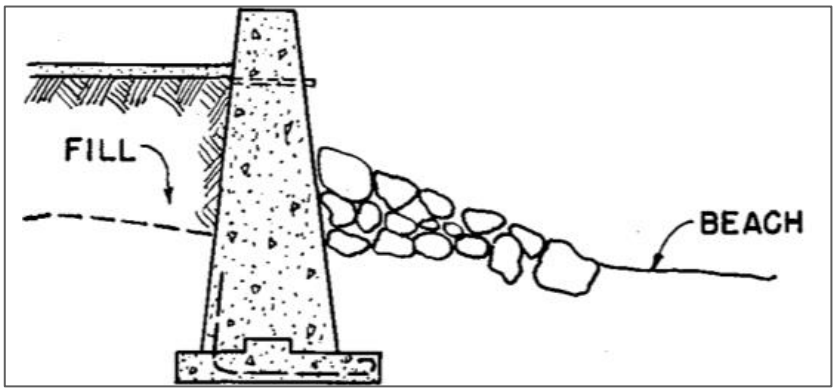

Figure 2-3: Vertical face gravity seawall (Ayers, 1950)

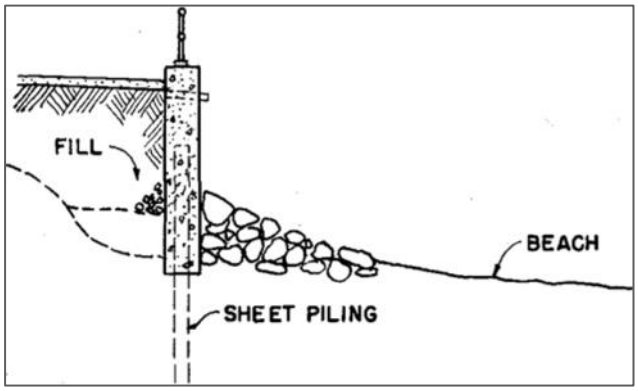

Figure 2-4: Vertical face concrete piling seawall (Ayers, 1950)

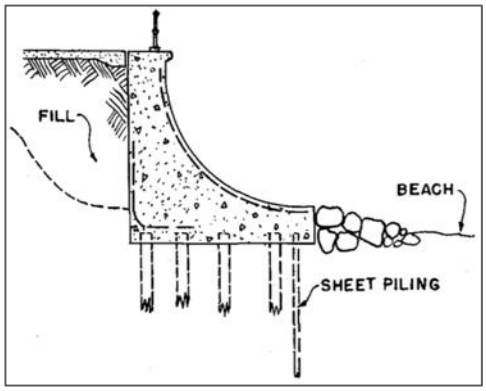

Figure 2-5: Curved face seawall (Ayers, 1950)

2.2.3.2 Modes of Failure

The standard failure modes for gravity seawalls are discussed below (USACE, 2002).

- *Seaward Sliding of Gravity Wall*

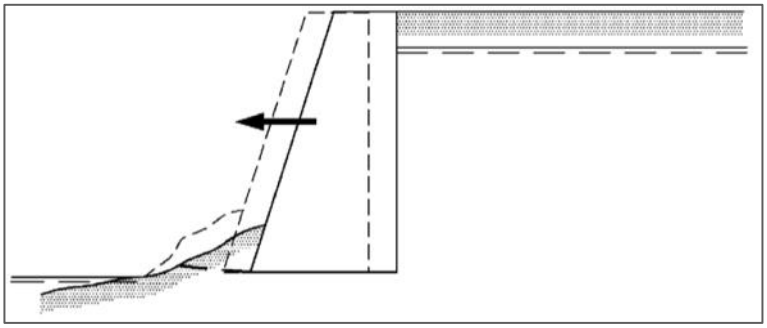

Figure 2-6: Seaward sliding of the gravity wall (USACE, 2002)

The pressure from the rear side exceeds the sum of the frictional resistance at the base. Pressure from the back is caused by groundwater and active soil pressure.

- *Seaward Overturning of Gravity Wall*

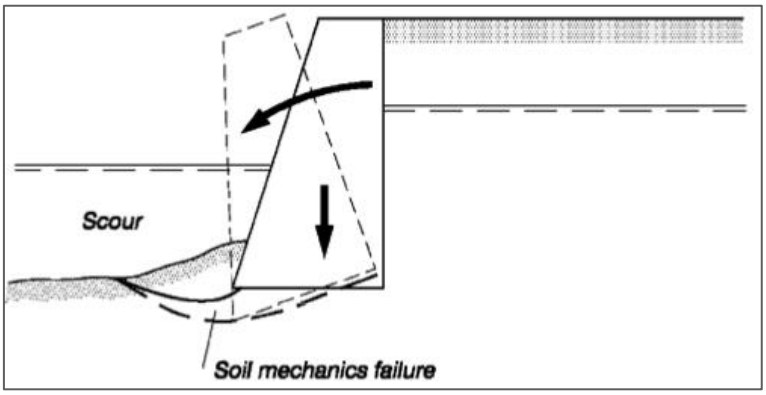

Figure 2-7: Seaward overturning of the gravity wall (USACE, 2002)

The scouring at the front of the seawall reduces the bearing capacity and the passive resistance of the foundation soil. The combination of the backfill pressure, the weight of the wall and groundwater will lead to bearing capacity failure and thus an overturning wall.

- *Rotational*

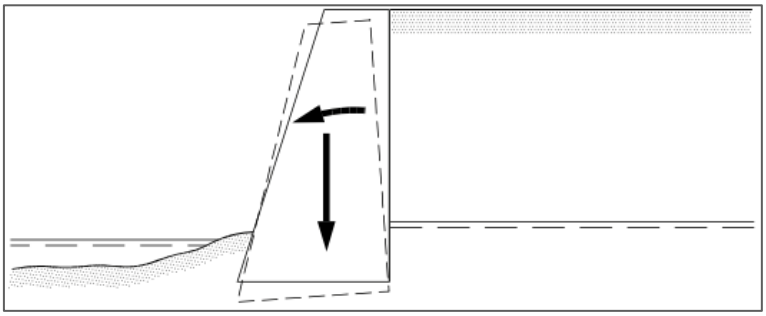

Figure 2-8: Rotational failure of the seawall (USACE, 2002)

Rotation of the seawall.

- *Rotational Slip Failure*

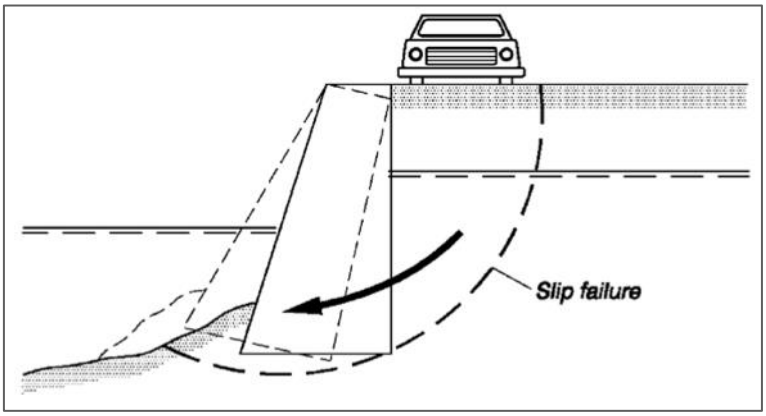

Figure 2-9: Rotational Slip Failure (USACE, 2002)

The soil strength is exceeded by the surface loads, groundwater and the driving moment from the weight of the soil.

- *Landward Overturning of Gravity Wall*

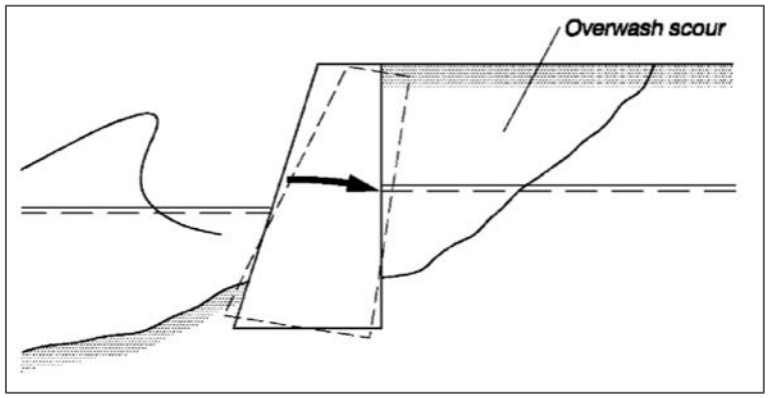

The scour is caused by heavy overtopping, which leads to passive resistance from the backfill. Wave loads can also drive this type of failure on the front, which will lead the wall towards a landward tilt.

Figure 2-10: The land overturning of the gravity wall (USACE, 2002).

- *Displacement of Individual Components*

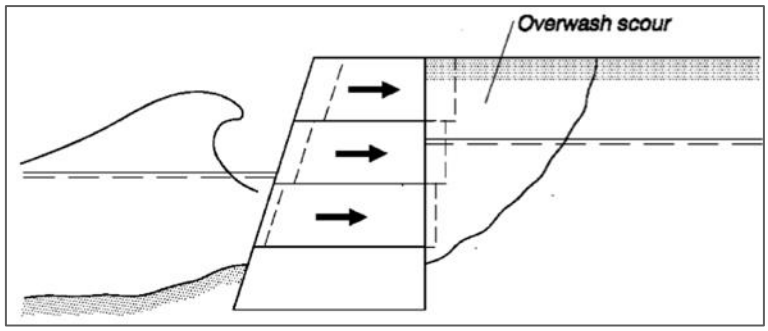

The scour is caused by heavy overtopping, which leads to passive resistance from the backfill. Wave loads on the front of the structure can push the wall elements out of position, causing structural failure.

Figure 2-11: Displacement of individual gravity wall components (USACE, 2002)

- *Settlement of Soil*

The last scenario of failure is when the soil settles due to soil mechanics failure when the load is exceeded by the bearing capacity or by the consolidation of the foundation soil.

2.2.4 Rubble-Mound Structure

The rubble-mound structure (or partial rubble-mound) can function as a type of scour protection that is placed in front of a vertical coastal defence structure to prevent undermining at the toe of the structure. Scour protection is provided to ensure the integrity of the seawall in extreme cases where the beach material may be removed. The rubble-mound structure follows the alignment of the seawall that it has to protect (CIRIA, 2007). Only from the 1930s onwards were empirical formulae developed for the design of rubble structures. Until then, the designs were based primarily on the site conditions and general knowledge (USACE, 1984).

2.2.4.1 Structure Components

The structure consists of various layers of stones that are randomly shaped and placed. The layers include the following: bedding layer, the core of quarry stone, multiple layers of larger rock and a cover-layer (USACE, 2002). Figure 2-12 shows the various layers for a three-layered structure.

The average layer rock size of each layer is given in Figure 2-12 in terms of the primary armour unit mass (M) (USACE, 2002). Short descriptions of each layer are provided. The thickness of each layer is calculated using Equation 2-9 (Van der Meer, 1998).

$$t = n\, k_t D_{n50} \qquad 2\text{-}9$$

Where
n = Number of rocks in the respective layer
k_t = Layer thickness coefficient (USACE, 1984)

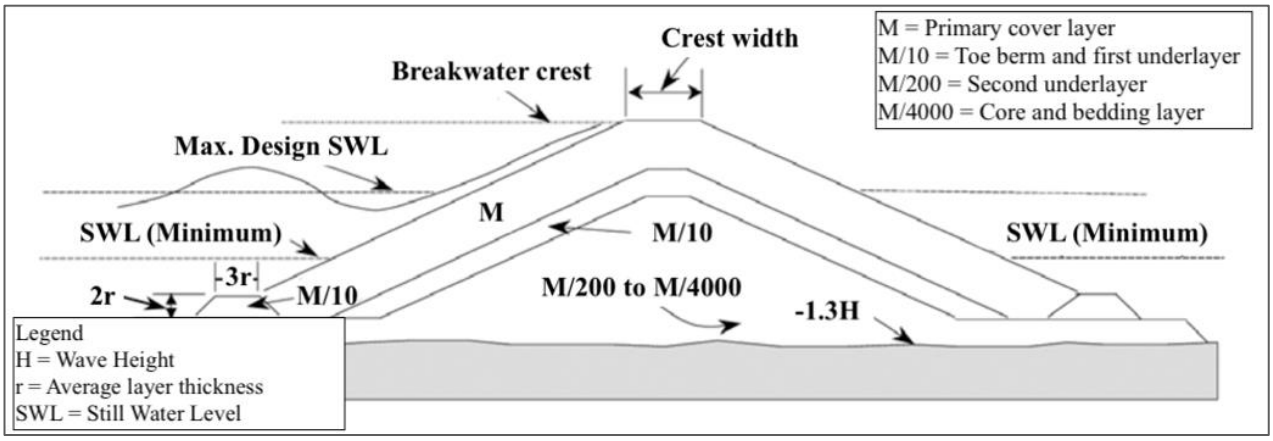

Figure 2-12: Rubble-mound cross-section (USACE, 2002)

- *Primary Armour Layer (Cover Layer)*

The cover layer can either be stone from a quarry or concrete units. These stones are selected based on weight and density. The units in the cover layer can be placed at random or in an orderly manner to obtain interlocking between the individual units (USACE, 1984).

- *Granular Filter Layer (Underlayer)*

Using granular filter layers can be challenging during construction due to the requirement that uniform thickness should be obtained. The challenge arises when construction must take place underwater. The structure should be designed to allow water to be transported through the structure, and at the same time

prevent the transport of finer material. Thus, the primary purpose is to avoid finer material washout through the filter layer voids. Other functions of the filter layer (underlayer) include (USACE, 2002):

- Dissipating the energy caused by turbulent flow.
- Distributing the weight of the structure to ensure uniform settlement.
- Regulating an uneven formation layer (CIRIA, 2007).
- Reducing the hydrodynamic loads on the outer stone layers (Van Gent and Wolters, 2015).
- Provide drainage to the structure (Van Gent and Wolters, 2015).

The under layer should have a minimum thickness of two quarry stones. If both the cover layer and the underlayer are quarry stone, the rocks in the underlayer should be one-tenth of the mass of the overlaying armour units (M/10). The second underlayer should be one-twentieth the mass of the first underlayer (M/200) and with a thickness of at least two quarry stones (USACE, 1984).

The stone size distribution in this layer is quite broad. The smallest stones should be too large to pass through the voids in the overlying layer. Using larger stones in the underlayer will make the layer less smooth and consequently increase the interlocking. The structure will be more porous, which leads to increased stability. Segregation of the stones is not permitted (USACE, 2002).

- *Bedding Layer, Filter Blanket and Screed Layer*

Cohesionless soil, like sand, requires a filter blanket to prevent the removal of sand through the voids of the rubble, which will lead to a settlement. The wave action against rubble structures creates turbulence in the structure as well as in the underlying soil. Wave action causes the soil to be drawn into the structure, causing the rubble structure to sink into the ground. Seawalls, including those protected by rubble structures, need to be able to withstand the groundwater pressure that will lead to washing out of the soil through the structure (USACE, 1984).

If the large quarry stone is placed directly on the soil in an area where there are waves and currents (i.e. the surf zone), the rubble structure will settle into the underlying soil which will require additional rubble to compensate. Even though this has the advantage of a stable foundation, it is better to overcome this by using a bedding layer or filter blanket (USACE, 1984).

A bedding layer may be required even if a filter layer is not required. It dissipates the forces from the horizontal waves, tides and longshore currents (USACE, 1984). It consists of smaller stone sizes with a very narrow grading size distribution. The stones should be placed and handled in such a way that minimises segregation of the material size distribution (USACE, 2002).

The thickness of the bedding layer will depend on the depth of water in which the structure is placed, but it should have a thickness of at least 0.3 m. A bedding layer (and filter blanket) can be used under the following conditions (USACE, 1984):

1. The water depth is less than three times the maximum wave height.
2. The anticipated velocities are strong enough to move the foundation material.
3. The foundation is not as hard and durable as bedrock.

The screed layer consists out of fine rock and is laid on the seabed before the concrete seawall elements or larger stones are lowered into position. Its primary function is to assure the level placement of the structure by allowing the (normally pre-cast) structural elements to sink into the layer under their self-weight (Malan, 2016). The screed layer also provides additional contact area between the rock foundation and concrete elements. The screed layer will also improve the stability of the structure since more contact area means there will be more friction (Van Wageningen, 2018).

There are not many design guidelines available for the screed layer. The thickness of the layer is based on engineering judgement. The optimal solution lies somewhere between a thin enough layer to minimise the scour susceptibility and a thick enough layer to even out irregularities. Information about the scouring process of granular material from the screed layer of a rubble-mound structure is very scarce. The majority of research on scour focuses on the scouring of sand from seaward of the structure rather than the scouring of the screed layer underneath the structure. Recent exceptions are studies by Malan (2016) and Van Wageningen (2018).

- *Toe Protection and Berm*

The purpose of toe protection is to prevent scour and to support the main armour layer (USACE, 2002). Figure 2-13 illustrates this concept.

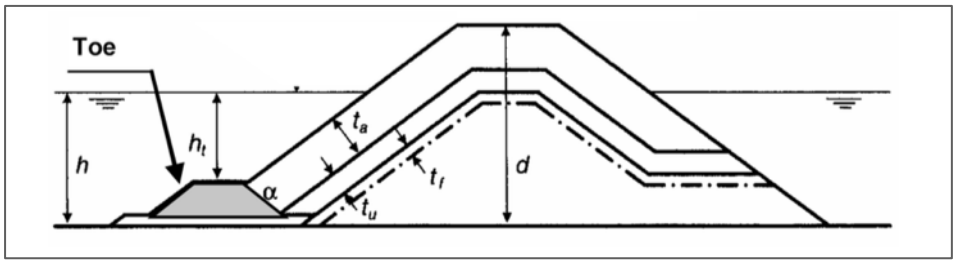

Figure 2-13: Toe protection to prevent scour of the rubble-mound breakwater (CIRIA, 2007)

Toe protection is implemented to prevent scour from undermining the toe of the mound, causing the armour layer to slide down the slope (Figure 2-14) (USACE, 2002). The ability of the foundation to resist the highest

waves is one of the most critical factors that influences the structural integrity of the structure (USACE, 1984).

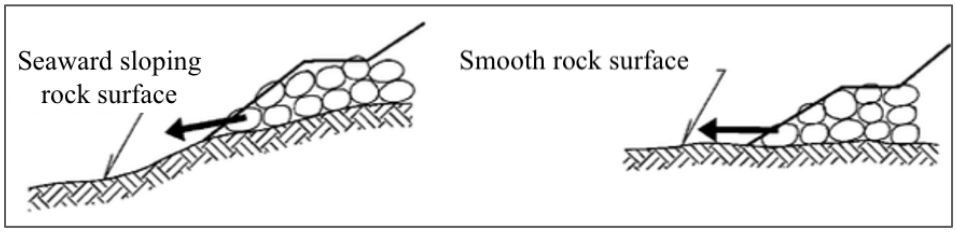

*Figure 2-14: Instability of toe protection leading to armour layer sliding downslope (*Coastal Engineering Manual, *2002)*

If the toe protection and the armour layer have the same size armour stone, the toe will most probably be stable. But in most cases, the size of the armour stone in the toe is reduced (CIRIA, 2007). If the toe becomes unstable, it will accelerate the instability of the primary armour layer. The stability of the toe berm is affected by the following factors: water depth at the toe berm, incident wave height, width of the berm and the block density. Well-graded stones are used at the toe of sloping and vertical-front structures to prevent undermining by scouring (USACE, 2002).

As can be seen in Figure 2-13, h_t is the depth of the upper surface of the toe below the water, and h is the overall water depth. If the value of the ratio h_t/h is between 0.3 and 0.5, it indicates that the toe is relatively high above the seabed. In this case, the toe should be considered as a bermed structure (Van der Meer, 1992). A berm is a stepped structure in front of a seawall or breakwater with the primary function to support the armour layer. The berm width is between 5 and 10 times the stone dimension of the berm (Gravesen, 2008).

2.2.4.2 Filter Rules

To prevent the smaller rocks in the underlayer(s) or core from being washed out through the over-layer by the wave action, specific criteria for filter rules are applied in the design (USACE, 1984). The original design criteria for granular filters are based on the geometry of voids between the packed spheres (USACE, 2002). The requirements are as follows:

- *Criterion 1: Retention ratio*

$D_{85\,(under)}$ is the diameter that exceeds the coarsest 15% of the underlayer. $D_{15\,(cover)}$ is the diameter that exceeds the coarsest 85% of the layer above the under layer. This criterion is put in place to prevent the loss of the core material washing through to the filter layer (USACE, 2002).

$$D_{15\,(cover)} \leq (4\ to\ 5)\ D_{85\,(under)} \qquad 2\text{-}10$$

- *Criterion 2: Permeability ratio*

The hydraulic gradient across the layer is reduced by ensuring adequate permeability of the filter layer (USACE, 2002).

$$\frac{D_{15\,(\text{filter})}}{D_{15\,(\text{foundation})}} > (4 \text{ to } 5) \qquad 2\text{-}11$$

- *Criterion 3: Internal stability ratio*

The internal stability criteria should be applied to prevent the loss of finer particles caused by a wide gradation of material (USACE, 2002).

$$\frac{D_{60\,(\text{filter})}}{D_{10\,(\text{foundation})}} < 10 \qquad 2\text{-}12$$

- *Criterion 4: Median mass ratio*

The USACE (1984) recommends that the ratio for the underlayer stone mass to the armour layer stone mass should lie between the two fractions as indicated by Equation 2-13.

$$\frac{M_{50u}}{M_{50a}} = \frac{1}{15} \text{ to } \frac{1}{10} \qquad 2\text{-}13$$

2.3 Motion of Water through a Porous Medium

The Navier-Stokes equations describe the wave motion in the ocean. Due to the complexity of these equations, approximations are made to derive equations which are easier to solve. Non-breaking wave equations are derived based on the assumption that the flow of non-breaking waves is inviscid and irrotational. In the region from non-breaking to breaking waves to broken waves, the full Navier-Stokes equation is applied. After the wave breaks, the approximate equations can be used once again. The flow models are less accurate for breaking waves because of the importance of viscous effects (Van Gent, 1995)

The same Navier-Stokes equations can be applied to the wave motion inside a porous structure. They must be adapted to implement porosity and friction terms. The Navier-Stokes equation with these additional terms is described by the Forchheimer equation (Van Gent, 1995). The Forchheimer equation and relevant parameters are discussed in the sub-sections to follow.

2.3.1 FORCHHEIMER EQUATION

The flow through a rubble-mound structure in the prototype is dominated by turbulent and inertial resistance. For a small-scale model of rockfill, laminar resistance is considered. Laminar flow is expressed with Darcy's law. The seepage flow velocity is directly related to the hydraulic gradient and permeability coefficient (Equation 2-14) (Van Gent, 1995).

$$u_v = ki \tag{2-14}$$

Where

u_v = Seepage velocity (m/s)

k = Permeability coefficient

i = Hydraulic gradient

Darcy's law cannot be used to describe the flow through a rubble-mound structure. The permeability coefficient, seepage velocity and hydraulic gradient should be replaced by a nonlinear relationship: the Forchheimer equation. The Forchheimer equation (Equation 2-15) is derived theoretically from the Navier-Stokes equation, as mentioned above. The Navier-Stokes equation cannot be applied in numerical models until it is somehow averaged, and a more useful equation is derived. The averaged equation describes the average flow of the porous medium and not the flow around the stones in the pores individually (Van Gent, 1992).

$$i = A_{For} u_v + B_{For} u_v |u_v| \tag{2-15}$$

The pressure gradient (i) is defined in Equation 2-19. The A_{For} and B_{For} are defined by Equation 2-16 and Equation 2-17, respectively. Equation 2-18 is used when a coastal structure is exposed to strongly oscillatory flow and is a function of the Keulegan-Carpenter number (KC). The Keulegan-Carpenter number is used to describe drag forces vs inertia forces (Van Gent, 1992).

$$A_{For} = \propto_{For} \frac{(1-n_v)^2}{{n_v}^3} \frac{\upsilon_w}{g{D_{n50}}^2} \tag{2-16}$$

$$B_{For} = \beta_{For} \frac{1-n_v}{{n_v}^3} \frac{1}{gD_{n50}} \tag{2-17}$$

$$B_{For} = \beta_{For} \left(1 + \frac{7.5}{Kc}\right) \frac{1-n_v}{{n_v}^3} \frac{1}{gD_{n50}} \tag{2-18}$$

Where

$\propto_{For} = 1684 + 3.12 \times 10^{-3} \left(\frac{g}{\upsilon^2}\right)^{\frac{2}{3}} {d_{15}}^2$

$\beta_{For} = 1.72 + 1.57 \exp\left[-5.10 \times 10^{-3} \left(\frac{g}{\nu^2}\right)^{\frac{1}{3}} d_{15}\right]$

υ_w = Kinematic viscosity of water = 1.787×10^{-6} m^2/s

n_v = Volumetric porosity

Kc = Keulegan-Carpenter number = $\frac{\hat{U}T}{n_v D_{n50}}$

$\hat{U}$ = Amplitude of the oscillating velocity (m/s)

T = Oscillation period (s)

The rockfill resists the flow of the water moving through the structure. The pressure gradient acts as a force to give the water acceleration through the porous medium. The pressure gradient can be written as (Van Gent, 1992):

$$i = -\frac{1}{\rho g}\frac{\partial p}{\partial x} \qquad 2\text{-}19$$

Where

p = Pressure kg/ms^2

ρ = Density of water (kg/m^3)

2.3.2 PERMEABILITY

Permeability is a property that a material holds which allows fluids to diffuse through it, without the fluid being physically or chemically altered. It is mainly a function of gradation and particle size. However, the internal water flow is dependent on many other variables such as the porosity and roughness of the stones. Permeability usually increases with an increase in grain size. This trend can be seen in Figure 2-15 (CIRIA, 2007).

Van der Meer (1998) conducted a study with regards to the wave attack on rocky slopes. He derived a rough coefficient to estimate the notional permeability (*P*) for different layer compositions (this coefficient cannot be used as an extension of Darcy's law). Examples of different values of the permeability factor are shown in Figure 2-16. The lower limit of *P* is an armour layer with an impermeable core, and the upper limit is a homogenous structure consisting only out of armour stones.

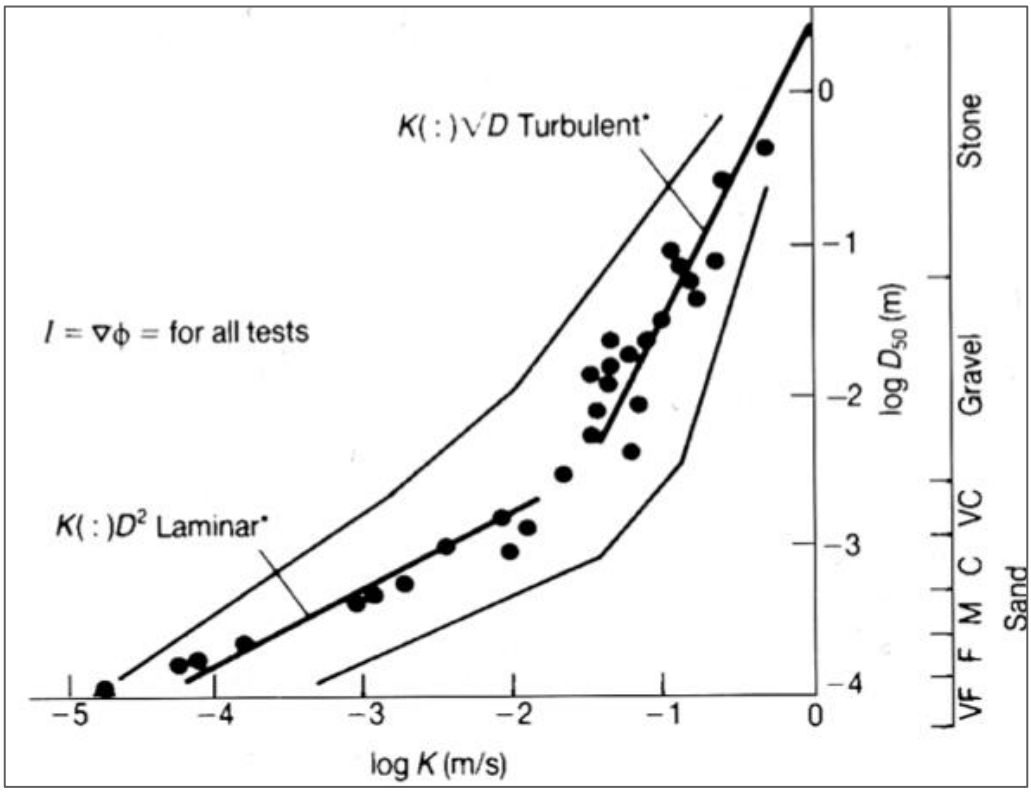

Figure 2-15: Relationship between permeability and stone size (CIRIA, 2007)

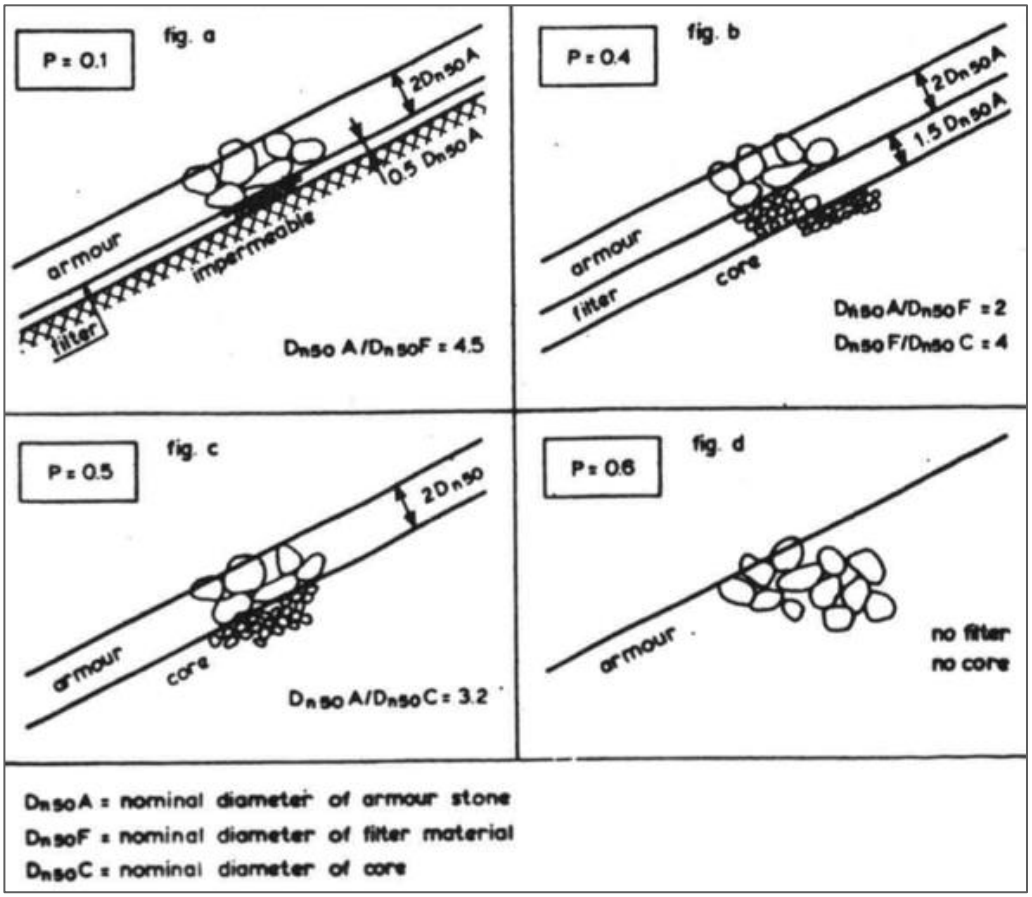

Figure 2-16: Coefficients of permeability determined for various layer compositions (Van der Meer, 1992)

The notional permeability coefficients from Figure 2-16 were derived by investigating three structures with different permeabilities: a revetment with an impermeable core, one with a permeable core and one homogeneous structure. The impermeable core can be regarded as the lower boundary for permeability. A homogenous core with a diameter of 0.25m is assumed to be the upper boundary in terms of permeability. A homogenous structure is when the stones of the core and armour layer have the same diameter. An almost impermeable core will have a core stone diameter of 0.0125m or less. The graphs below illustrate the volume of water (Q) that dissipated into the core.

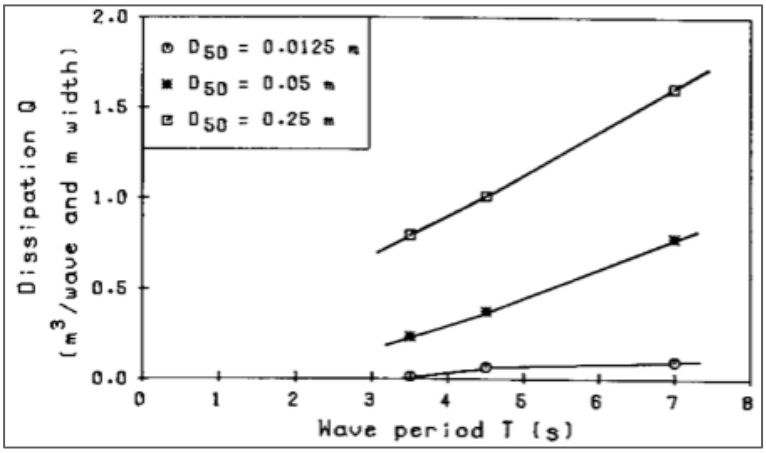

Figure 2-17: Water dissipation into a rubble-mound structure as a function of wave period (Van der Meer, 1998)

As can be seen in the Figure 2-17, a higher permeability (larger stone diameter), leads to higher dissipation of water in the core. Figure 2-18 shows that a larger wave period will also result in more water dissipation within the core.

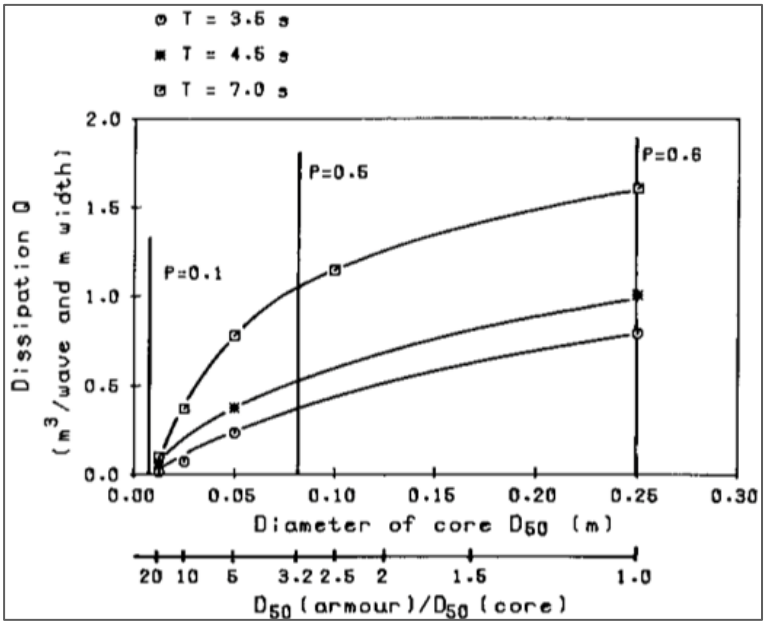

Figure 2-18: Water dissipation into a rubble-mound structure as a function of core diameter (Van der Meer, 1998)

2.4 ENERGY IN A RUBBLE-MOUND STRUCTURE

2.4.1 ENERGY DISSIPATION ON A RUBBLE-MOUND STRUCTURE

2.4.1.1 Energy Dissipation due to Breaking Waves

In a study conducted by Schoonees (2001), it was determined that the Battjes and Janssen (1978) model is the most accurate method to determine the energy dissipation due to wave breaking on a beach slope. The analogy of energy loss in a hydraulic jump was used. The derived equation is given in Equation 2-20.

$$D_b = 0.25 \propto Q\rho g \frac{{H_m}^2}{T_p} \qquad 2\text{-}20$$

Where

$\propto$ = Calibration constant (taken as 1)

H_m = Maximum wave height (m) = $0.88 \frac{L}{2\pi} \tanh(\frac{2\pi h}{L} . \frac{\gamma_b}{0.88})$

Q = Ratio of broken waves to the total number of waves

γ_b = Average breaker index (taken as 0.7)

The ratio of broken waves to the total number of waves is determined by assuming a Rayleigh distribution for the wave height given in Equation 2-21.

$$\frac{1-Q}{-\ln Q} = (\frac{H_{rms}}{H_m})^2 \qquad 2\text{-}21$$

Where

$H_{rms} = \frac{H_s}{\sqrt{2}}$ = root mean square wave height

From Equation 2-21, one can obtain Equation 2-22. This equation is solved iteratively to acquire the value of Q.

$$1 - Q + \left(\frac{H_{rms}}{H_m}\right)^2 \ln Q = 0 \qquad 2\text{-}22$$

2.4.1.2 Distribution of Energy Dissipation

The incident energy (E_i) of a wave that approaches a rubble-mound breakwater will either be dissipated (E_d), reflected (E_r) or transmitted (E_t) through the structure. Each of the energy components are expressed by the square of the corresponding wave height i.e. $E_i = f(H_i^2)$ (Oumeraci and Partenscky, 1990):

$$E_i = E_d + E_r + E_t \quad 2\text{-}23$$

The wave reflection coefficient (K_r), dissipation coefficient (K_d) and the transmission coefficient (K_t) are correlated by the relationship given in Equation 2-24 (Muttray *et al.*, 1992).

$$K_r^2 + K_d^2 + K_t^2 = 1 \quad 2\text{-}24$$

With

$$K_r = \sqrt{\frac{E_r}{E_i}}$$

$$K_d = \sqrt{\frac{E_d}{E_i}}$$

$$K_t = \sqrt{\frac{E_t}{E_i}}$$

When considering a bermed structure with several layers, the dissipated energy is distributed among the various layers, this is illustrated in the study by Oumeraci and Partenscky (1990) who conducted tests on a tetrapod armoured breakwater (E_{da}) with a filter layer (E_{df}), and core (E_{dc}):

$$E_d = E_{da} + E_{df} + E_{dc} \quad 2\text{-}25$$

Equation 2-26 is derived from Equation 2-24 for the local dissipation coefficients. The quantities involved in Equation 2-24 and Equation 2-26 are dependent on the water depth and incident wave parameters, especially the relative water depth (d/L) and the wave steepness. These two parameters have a large effect on the two equations since they strongly affect the kinematics and shape of the waves (Muttray *et al.*, 1992).

$$K_{da}^2 + K_{df}^2 + K_{dc}^2 = 1 \quad 2\text{-}26$$

With

$$K_{da} = \sqrt{\frac{E_{da}}{E_d}}$$

$$K_{df} = \sqrt{\frac{E_{df}}{E_d}}$$

$$K_{dc} = \sqrt{\frac{E_{dc}}{E_d}}$$

The highest amount of energy dissipation takes place in the armour and filter layer. The wave dissipation is mainly dependent on the surf similarity parameter (ξ). This dependency results from the shape of the breakers on the outer slope. The spilling breakers and plunging breakers are associated with the greatest impact velocities and air entrainment, thus giving the largest damping values. Collapsing breakers and surging breakers will yield the lowest damping values. The pronouncement can be made that greater energy dissipation on the outer slope is related to a smaller surf similarity (Oumeraci and Partenscky, 1990).

Figure 2-19 is an illustration of the wave motion from the sea-structure interface to the breakwater core as a function of the surf similarity parameter. Using Figure 2-19 and Figure 2-20 in cooperation, an evaluation can be made of the different energy components involved in Equation 2-23 and Equation 2-25 (Oumeraci and Partenscky, 1990).

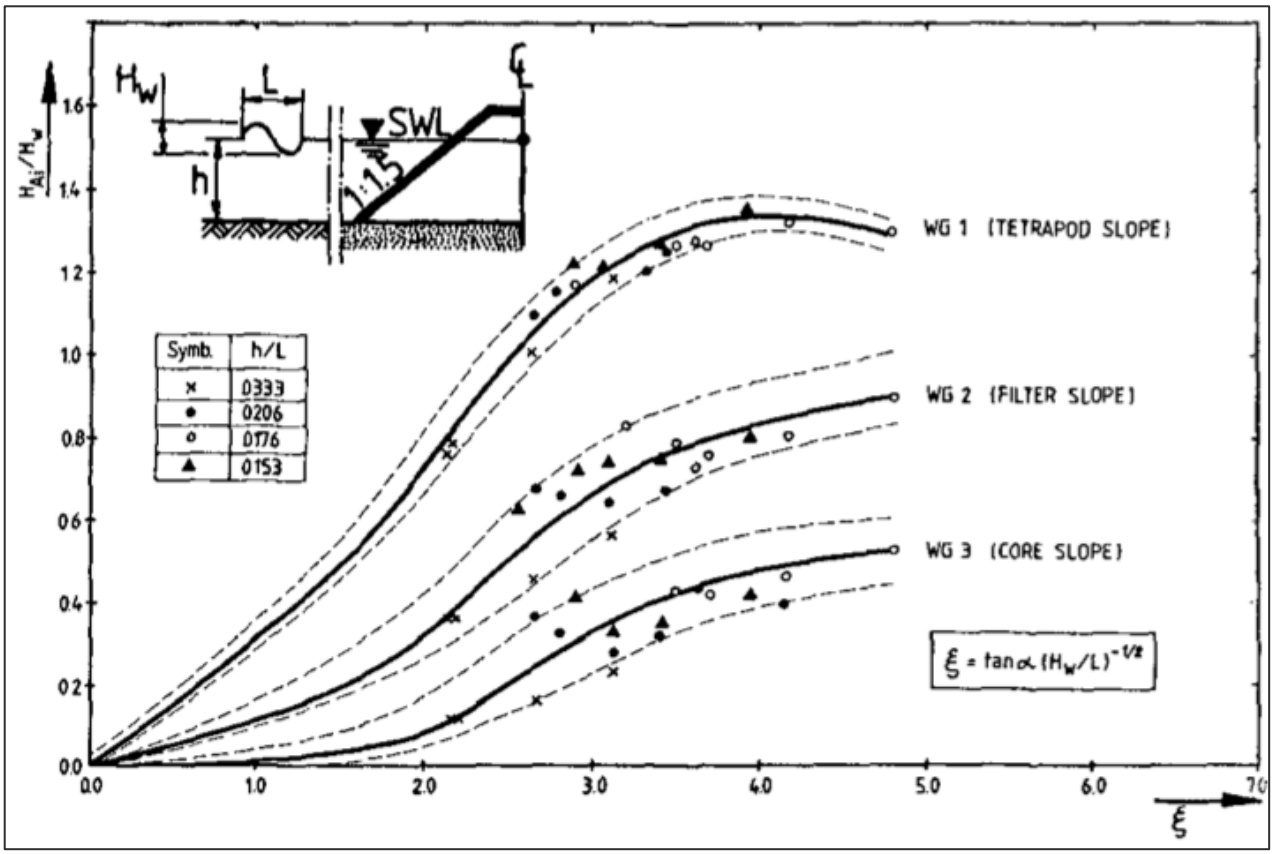

Figure 2-19: Wave damping at the armour layer and under layer vs surf similarity parameter (Oumeraci and Partenscky, 1990)

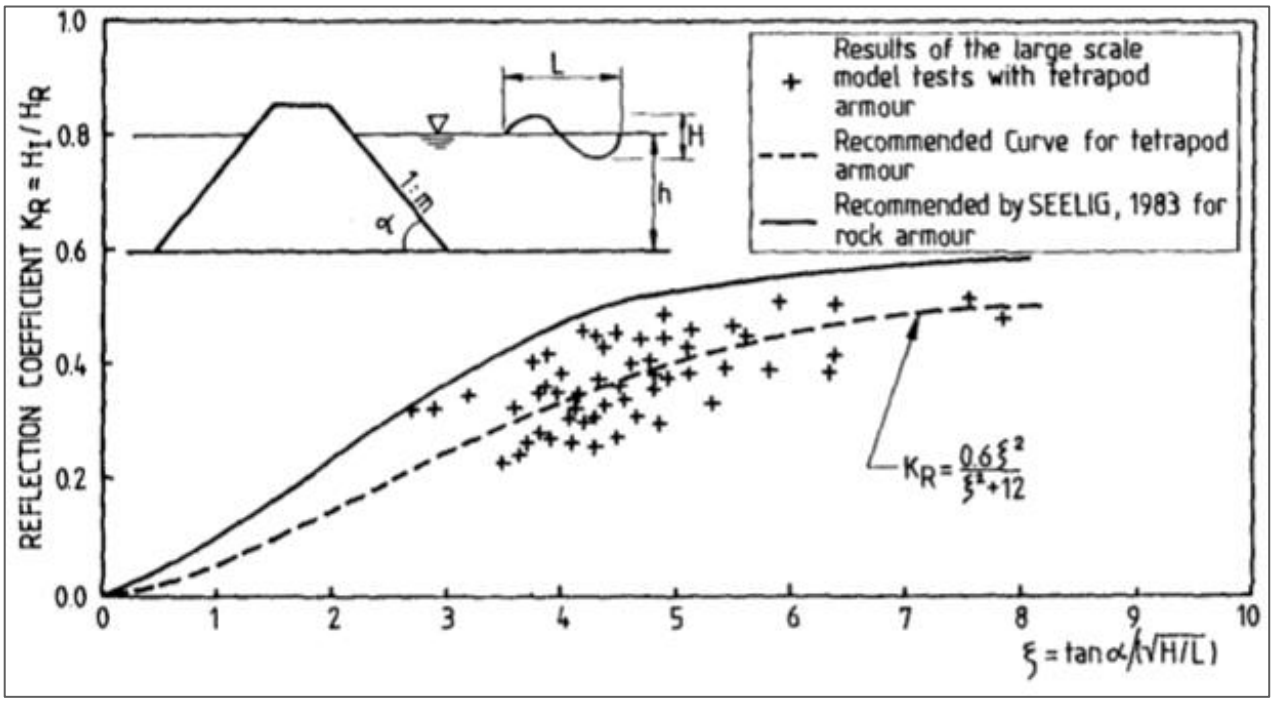

Figure 2-20: Reflection coefficient vs surf similarity parameter (Oumeraci and Partenscky, 1990)

The experimental study by Muttray *et al*. (1992) investigated the energy dissipation within the various layers of an Accropode armoured breakwater. It confirmed the results of Oumeraci and Partensky (1990) that the most significant energy dissipation occurs at the outer layers. Figure 2-21 to Figure 2-24 illustrate the various energy components at different wave periods for irregular waves.

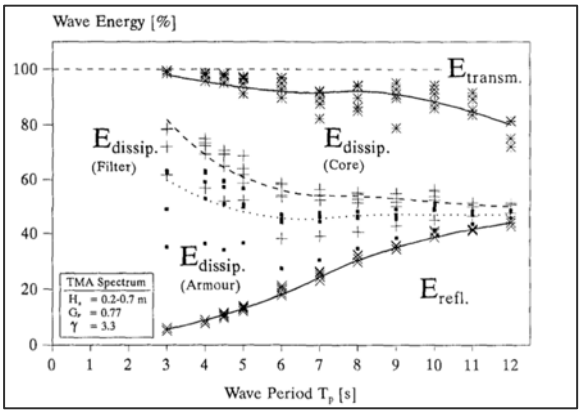

Figure 2-21: Wave energy against the wave period (Muttray et al., *1992)*

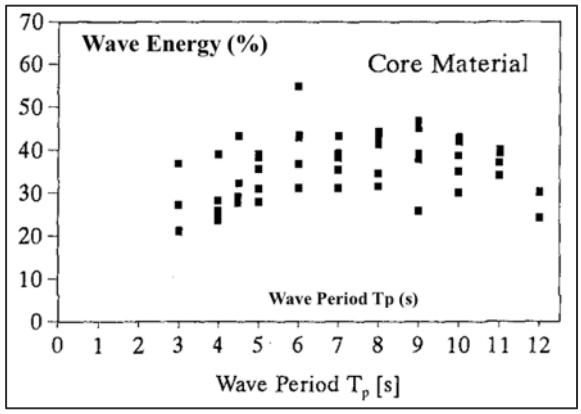

Figure 2-22: Energy dissipation in the core (Muttray et al., *1992)*

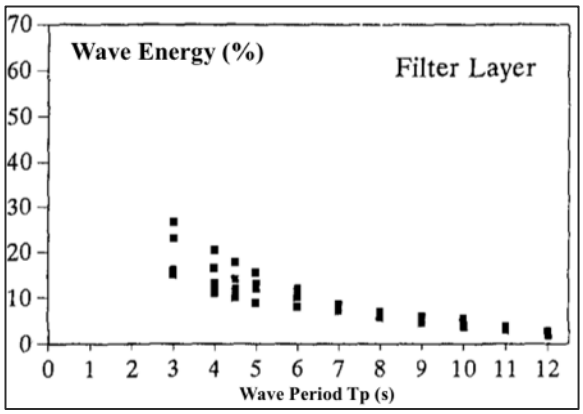

Figure 2-23: Energy dissipation in the filter layer (Muttray et al., *1992)*

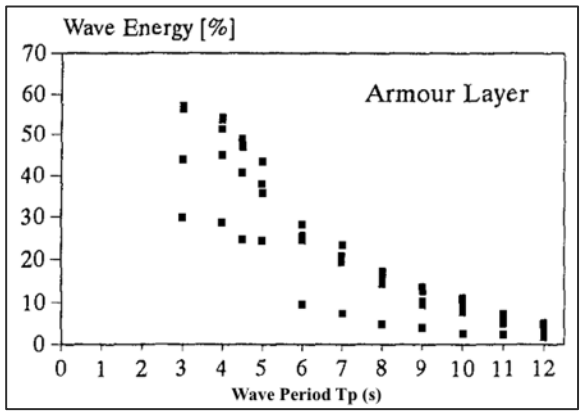

Figure 2-24: Energy dissipation in the armour layer (Muttray et al., *1992)*

2.4.2 KINETIC ENERGY IN A RUBBLE-MOUND STRUCTURE

Two-dimensional experiments tests were conducted by Ruy *et al.* (2016) with the primary goal to determine the effect of porosity on energy dissipation within a submerged breakwater. Two conditions were tested: a permeable and an impermeable breakwater.

Energy dissipation is usually estimated by using the wave elevation data. In this study, however, the researchers used the PIV (particle image velocimetry) technique to obtain the velocity fields under the wave-free surface. By using the PIV technique, the flow characteristics and the kinetic energy distribution could be measured to understand the interaction of the waves with the breakwater.

The wave flow fields indicated that the kinetic energy dissipation is dependent on the porosity of the structure. There was a decrease in the kinetic energy when the tests were conducted on the permeable condition; the impermeable condition had an increase in the mean kinetic energy on the top of the structure. It was observed that the dissipated energy on top of the structure increased with an increase in wave periods. The kinetic energy was calculated by using the Equation 2-27.

$$KE = \frac{1}{T}\int_{t=0}^{t=T}\int_{z=ds}^{z=\eta}\frac{(u^2+w^2)}{2}\,dz\,dt \qquad 2\text{-}27$$

Where

KE = Mean kinetic energy (J)

T = Wave period (s)

η = Wave elevation (m)

ds = Z-coordinate of the structure surface (m)

u = Horizontal velocity component (m/s)

w = Vertical velocity component (m/s)

If the increase in wave height is large enough, there will be an increase in the potential energy and a decrease in kinetic energy. As a wave approaches a shallow water region, there will be a decrease in the wave speed, and if the energy flux remains constant, the potential energy will increase (Ryu *et al.*, 2016).

2.5 Scour in the Marine Environment

2.5.1 Defining Scour in the Marine Environment

Coastlines are being eroded by wind, waves, rainfall and currents. Erosion is further exacerbated by the rise of the sea level, which allows waves to travel further landward and cause damage to the encountered seabed, beaches and structures. Damage is also caused by higher energy waves resulting from a deeper nearshore as a result of sea level rise (Sutherland, 2003).

The erosion process caused by the presence of a structure is known as scour. A broad definition of scour is that it is the erosive force caused by water moving across an erodible surface. In a coastal engineering context, scour can be defined as the removal of granular bed material in the vicinity of coastal structures through the presence of hydrodynamic forces. When the hydrodynamic shear stresses on the bottom are high enough to start sediment transport, the physical process of scour will occur (USACE, 2002).

When a coastal structure is placed in the coastal zone, the structure will influence the flow pattern which will lead to phenomena such as the generation of turbulence, the occurrence of wave breaking, wave reflection, diffraction etc. These phenomena will ultimately lead to an increase in the local sediment transport capacity and thus scour. Scour threatens the stability of all coastal structures (Sumer & Fredsoe, 2002).

Scour can lead to partial damage or complete failure. The scouring process will undermine the toe of the structure; the structure will not be able to support itself, loose stability and then ultimately collapse. When a structure is damaged by scour, there are numerous negative consequences such as (USACE, 2002):

1. A decrease in the functionality of the structure
2. Additional costs to repair or replace the structure
3. The infrastructure the coastal defence structure was supposed to protect will be lost or inundated
4. A loss of confidence in the capability of the structure to perform

The basic options for reducing scour near marine structures include: reducing wave reflections by increasing the structure permeability and decreasing the structure slope steepness, placing a scour-control blanket over the problem area and isolating the site, improving the hydraulic performance of the protective berm and improving the quality of the foundation bed material via reinforcement (Hoffmans & Verheij, 1994)

2.5.2 Equilibrium Scour Depth

Scour holes would eventually over a specific period reach a stable configuration (except when global instability overtakes the scour hole resulting in structural failure). A stable configuration occurs when the same hydrodynamic conditions are present and the seabed remains unchanged throughout a certain period (USACE, 2002).

The maximum scour depth is obtained by determining the equilibrium stage of the scour. It is crucial to define the maximum potential scour depth, especially in the design of the structure foundation and scour protection. To reach the equilibrium scour depth, a certain amount of time (or a specified number of waves) should elapse (Sumer & Fredsoe, 2002). In the two-dimensional laboratory tests conducted by Van Wageningen, (2018) it was found that (horizontal) scour of the screed layer below the tested seawall in that case reached an equilibrium after 2000 waves.

2.5.3 Clear-water Scour vs Live-bed Scour

Clear-water scour typically occurs in steady, uniform flow conditions. It is the scour process when there is no sediment motion further away from the structure due to the bottom shear stresses being high only in a localised portion of the bed. The sediment outside the local region will be unaffected and motionless (Sumer & Fredsoe, 2002).

Live-bed scour is the process where sediment motion will prevail over the entire bed (Sumer & Fredsoe, 2002). It is caused by the bottom shear stresses exceeding the level for incipient movement over the whole seabed (USACE, 2002). As can be seen in Figure 2-25, clear-water scour will reach a maximum point after live-bed scour reaches equilibrium with regards to time.

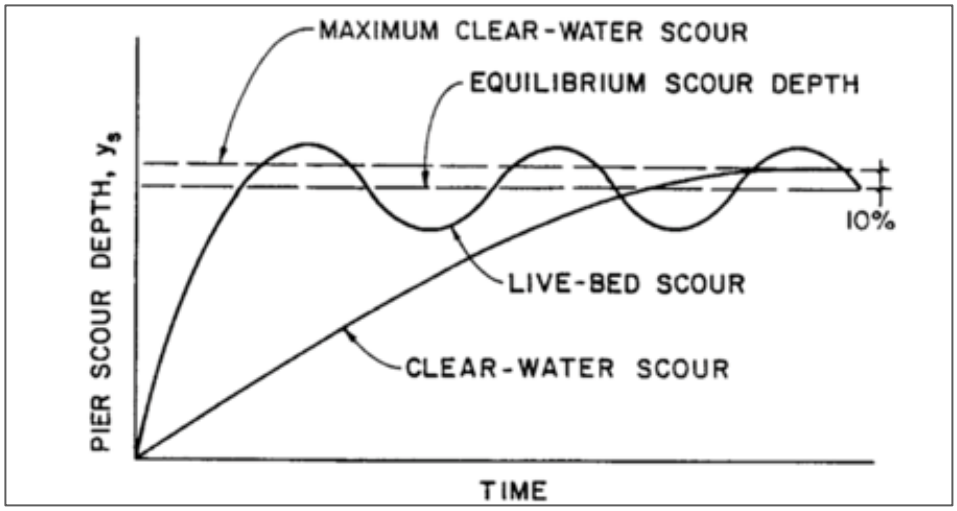

Figure 2-25: Scour depth vs time for clear-water scour and live-bed scour (Arneson et al., 2012)

2.5.4 Local Scour vs Global Scour

Local scour takes place around individual structural elements whereas global scour is the result from the combined action of the flow effects and will take place around a structure in its entirety (Sumer & Fredsoe, 2002).

2.6 Scour Underneath Vertical Seawalls

A concern for Coastal Engineers is the scouring at the base underneath a vertical seawall that provides support to the seawall. Scour underneath a vertical seawall has been the subject of many research studies mainly looking at vertical scour of the seabed in front of the wall that then extends to undermine the toe and foundation of the structure. There are nevertheless limited studies that focus specifically on the scouring process of granular material, such as that of a screed layer underneath a vertical seawall. However, recent screed erosion studies by Malan (2016) and Van Wageningen (2018) are reviewed later, in Section 3.7.

2.6.1 General Influences on Scour

Toe scour at seawalls is a dynamic process. It is mainly dependent on the water level and incident wave conditions. The main aspects that influence the degree of scour are discussed below.

- *Wave Height and Period*

The wave height and period define the offshore wavelength. Through past studies, the notion has been made that low wave steepness (low H_s/L_m-ratio) will cause more significant toe scour than steeper waves (Sutherland, 2003).

- *Water Depth*

The water depth relative to the wave height at the toe of the structure governs the orbital wave velocities. In the studies conducted by Powell and Lowe (1994) and Whitehouse and Powell (1998) it is concluded that scour is the most severe when the initial water depth at the toe is twice the offshore wave height.

- *Storm Duration*

Scouring is not a quick process, but the duration of the wave and water level plays an important role. Scouring will increase when the sediment is exposed for a longer duration to harsh oceanic conditions (Powell and Lowe, 1994).

- *Wave Approach Angle*

The scour depth will be greater when waves hit the wall against an oblique angle than when they crash into the wall perpendicularly. The interference of the incident waves with the reflected waves produces an interloping pattern of short crested waves, creating immense wave heights and increasing the scour potential (Sutherland, 2003).

- *Sediment Supply*

The larger the amount of sediment that is supplied to beaches, the faster scour holes will be filled again after a storm event, reducing the damage (Sutherland, 2003).

- *Grain Size*

Very few studies have been conducted around the effect of the grain size on scour. In a study by (McDougal, Kraus and Ajiwibowo, 1996), it is concluded that the scour depth will increase with a decrease in grain size.

2.6.2 Effect of Wave Type on Scour

There are three main types of nearshore waves: non-breaking, breaking and broken waves. The forces exerted by non-breaking waves are mainly hydrostatic. Broken and breaking waves exercise an additional force on the structure due to turbulent water and the pressure from entrapped air pockets. A structure on which waves will break should be designed for greater forces. Dynamic forces are more significant than hydrostatic forces (USACE, 1984).

2.6.2.1 Nonbreaking Waves

Shore structures such as vertical walls are usually placed at depths where the waves will break against them. In some regions where the fetch is limited, and the depth of the structure is greater than 1.5 times the maximum expected wave height, nonbreaking waves occur (USACE, 1984).

When the waves reach the seawall, the waves will be reflected by some extent. Nonbreaking waves have the most significant degree of reflection. Nearly all the energy from the incident non-breaking waves approaching the vertical faced seawall will be reflected (assuming the structure is non-porous). The reflection coefficient will be very high and consequently lead to a large scour area (Sumer & Fredsoe, 2002). A standing wave pattern is produced from the reflection, which leads to a confused energy-enhanced sea state in front of the wall and ultimately to an increase in seabed scour (Powell, 1987).

2.6.2.2 Breaking Waves

The scour due to breaking waves is determined by the following four factors: breaker type, the presence of a seawall, sediment properties and the wave boundary layer over the seabed (Sumer & Fredsoe, 2002). Figure 2-26 illustrates the variables defining these four parameters.

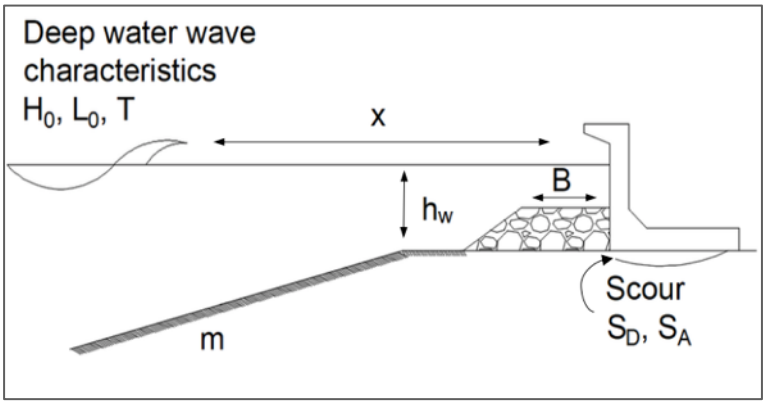

Figure 2-26: Definition sketch of parameters affecting scour (Van Wageningen, 2018)

- *Breaker Types*

There are three types of broken waves or breakers (as mentioned in Section 2.1.1). The breakers will differ in their energy dissipation as well as in the loads they exert on the wall (Powell, 1987). The factors that will influence the characteristics of the breaker type are the deepwater wave height (H_0), deepwater wavelength (L_0) and the gradient of the slope (m) (Sumer & Fredsoe, 2002). Dimensionless products are created from the factors:

$$\frac{H_o}{L_o}, \text{m}$$

- *The presence of the seawall*

Beaches that are left undisturbed are in a constant, quasi-cyclic state of flux under the wave action. With the presence of a seawall, and assuming the wave action reaches the seawall, there will be an accelerating reduction in beach levels due to the seawall interrupting the flow of water. The water table goes up and thus an increase in the backwash volume. The material is transported offshore, and the foreshore levels are lowered (Powell, 1987). The parameters that will influence the scour at a vertical seawall are the water level at the wall (h_w) and the distance from the breaking point to the wall (x). The dimensionless products during the scour process are given below (Powell, 1987):

$$\frac{h_w}{H_0}, \frac{x}{L_o}, \frac{T_w\sqrt{gH_0}}{h_w}$$

- *The sediment properties*

Sediment will be transported in suspension or as bed-load. The suspended sediment is easier transported by the current. Currents are an efficient transport mechanism, and waves are an efficient suspension mechanism. Thus, the combination of waves and currents will result in the highest transport rates. The parameters that will influence the scour regarding the sediment properties are the shields parameter (θ) and the fall-velocity (w) to friction-velocity (U_{fm}) ratio (Powell, 1987).

$$\theta, \frac{w}{U_{fm}}$$

- *The wave boundary layer over the seabed*

The flow in the boundary layer is influenced by the bed category of the boundary-layer flow. The dimensionless products are given as (Powell, 1987):

$$\frac{H_0}{d}, \textit{ Reynolds number}$$

Where d is the water depth and the Reynolds number defined by Equation 2-42.

2.6.3 Existing Research on Scour at Vertical Seawalls

This section gives the available design formulations for the prediction of breaking and non-breaking waves on scour development. A brief overview of a few formulations that contributed to the research field will be discussed. The set-up of laboratory models in existing research, as presented in this section, differs from the model as tested in this thesis as their focus was on vertical scour of the seabed in front of a seawall. However, as mentioned, recent screed scour studies by Malan (2016) and Van Wageningen (2018) which examine horizontal scour of the screed layer beneath a seawall are reviewed later, in Section 3.7.

2.6.3.1 Research on Non-Breaking Waves

- *Xie Experimental Study conducted in 1981 and 1985 (Normal Incidence Waves)*

The equation produced in this study is based on 12 movable-bed model tests. The maximum scour of the seabed is estimated in front of an impermeable vertical seawall with normally, regular non-breaking waves (Sumer & Fredsoe, 2002).

$$\frac{S_m}{H} = \frac{0,4}{[sinh\ (kh)]^{0,135}} \quad 2\text{-}28$$

With

S_m = Maximum scour depth (m)

H = Incident wave height (m)

h = Water depth (m)

k = $\frac{2\pi}{L}$ = Incident regular wave number

L = Incident regular wavelength (m)

- *Hughes and Fowler Study Conducted in 1991 (Normal Incidence Waves)*

An empirical equation for normally incident, non-breaking waves (Hughes & Fowler, 1991):

$$\frac{S_m}{(u_{rms})_m T_p} = \frac{0,05}{[sinh\ (k_p h)]^{0,35}} \quad 2\text{-}29$$

Where

T_p = Peak wave period (s)

k_p = Wave number that is associated with the spectral peak linear wave theory

$(u_{rms})_m$ = Horizontal bottom velocity root-mean-square

$(u_{rms})_m$ can be calculated by an equation developed by (Hughes, 1993):

$$\frac{(u_{rms})_m}{g k_p T_p H_{mo}} = \frac{\sqrt{2}}{4\,\pi\, cosh(k_p h)} \left[0.54 cosh\left(\frac{1,5 - k_p h}{2,8}\right)\right] \quad 2\text{-}30$$

Where

H_{mo} = Zero-moment wave height (m)

g = Standard gravity (9.81 m/s^2)

- *Silvester Study Conducted in 1991 (Oblique Incidence Waves)*

Silvester (1991) concluded that obliquely incident waves would cause more scour than their equivalent normal incident waves. Oblique waves approaching a vertical wall will be reflected with nearly 100% efficiency.

- *O'Donoghue Study Conducted in 2001 (Normal Incidence Waves)*

O'Donohgue (2001) focused on developing a method to determine the N-type sediment bed response. N-type sediment is the transport of relatively coarse sediment towards an area where the velocities are at their highest and which results in accretion. The study revealed that scour is non-linearly dependent on the wave period.

2.6.3.2 Research on Breaking Waves

- *Chesnut and Schiller Study Conducted in 1971 (Normal Incidence Waves)*

Maximum scour occurs when the distance from the seawall to the point of wave breaking is between 0.5-0.67 of the distance from the point of the breaking wave to the pre-seawall position of the mean water line (Sumer & Fredsoe, 2002).

- *Song and Schiller Study Conducted in 1973 (Normal Incidence Waves)*

The effect the location of the seawall has on wave reflection was investigated. The results indicate that for small values of the standing wave steepness (smaller than 0.02), scour depth becomes independent of the location of the seawall on the beach (Sumer & Fredsoe, 2002).

- *Shore Protection Manual Study Conducted in 1984 (Normal Incidence Waves)*

A design relationship of $S \leq H_0$ was developed. This design relationship is a general guide that indicates the maximum scour depth is roughly equal to the unbroken wave height at the toe of the structure (USACE, 1984).

- *Powell Study Conducted in 1987 (Normal Incidence Waves)*

The maximum scour will occur when the water has a depth that is roughly equal to 1.5 times the offshore regular wave height (Powell, 1987).

- *Fowler Study Conducted in 1992 (Normal Incidence Waves)*

(Fowler, 1992) conducted laboratory experiments to evaluate the existing methods for estimating wave-induced scour depth at a vertical seawall. Figure 2-27 illustrates the results obtained. The scatter of the data is quite large. However, the data demonstrates that there is an increase in scour depth with an increasing dimensionless product ($\frac{h_w}{L_o}$). The wide scatter is most likely due to the scour depth being dependent on other parameters as well.

The small scour depth for the negative values of $\frac{h_w}{L_o}$ in Figure 2-27 is to be expected. When the seawall is far away onshore, there may be cases where no scour will occur. As the wall is moved closer to the sea ($\frac{h_w}{L_o}$ increasing), the waves will break closer to the structure, and so the scour will increase. The proposed equation obtained from the laboratory experiments is given in Equation 2-31. This equation is only applicable between the range *-0.011* < $\frac{h_w}{L_0}$ < *0.045 and 0.015* < $\frac{H_0}{L_0}$ < *0.04*.

$$\frac{S_m}{(H_{m0})_0} = (22.72\frac{h}{L_0} + 0.25)^{\frac{1}{2}} \qquad 2\text{-}31$$

Where

S_m = Maximum scour depth (m)

$(H_{m0})_0$ = Zeroth-moment deep water wave height (m)

h = Water depth (m)

L_0 = Deep-water wavelength = $\frac{g}{2\pi}$ T_p^2

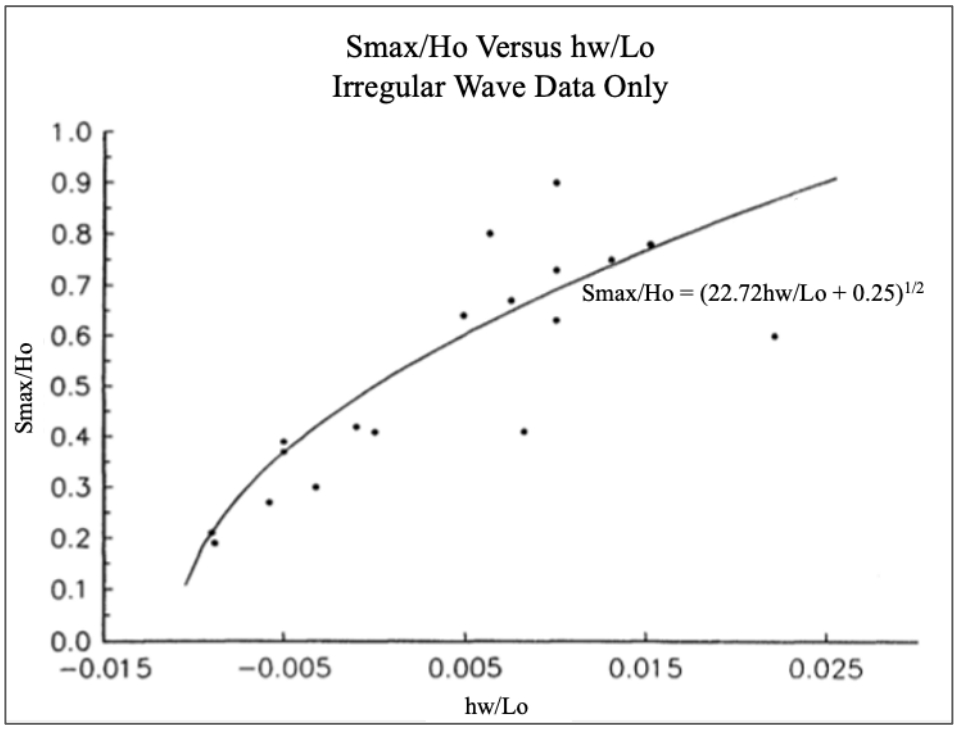

Figure 2-27: Maximum scour depth vs relative depth at seawall using irregular wave data and a beach slope of 1:15 (Fowler, 1992)

- *Van Rijn Study Conducted in 1993 (Normal Incidence Waves)*

Table 2-3 displays the design relationships that were obtained in Van Rijn's study. The maximum scour depth (in this case S_{max}) was obtained using a known water depth (Sumer & Fredsoe, 2002).

Table 2-3: Maximum scour due to water depth design relationships (Van Rijn, 1993)

S_{max}/h_{toe}	For Depths (m)
1.5 – 1	< 2
1 – 0.7	2 – 4
0.7 – 0.5	4 – 10
0.5 – 0.3	10 – 20

- *Powell and Lowe Experimental Study Conducted in 1994 (Normal Incidence Waves)*

The experimental study proved the importance of wave steepness on the scour depth as well as illustrating that an accretion and erosion region will form. The erosion region can reach values of up to $S/H_s = 1{,}5$ where S is the vertical scour depth (Powell and Lowe, 1994).

- *McDougal, Kraus and Ajiwibowo Study in 1996 (Normal Incidence Waves)*

The beach profile was determined by predicting the wave transformation and the cross-shore sediment transport algorithm. The empirical formulae developed in this numerical study is given in Equation 2-32 (McDougal, Kraus & Ajiwibowo, 1996).

$$\frac{S}{H_o} = 0.41m^{0.85}\left(\frac{L_0}{H_0}\right)^{\frac{1}{5}}\left(\frac{h_w}{H_0}\right)^{\frac{1}{4}}\left(\frac{H_0}{d}\right)^{\frac{1}{3}} \qquad 2\text{-}32$$

- *Coastal Engineering Manual Study in 2002 (Normal Incidence Waves)*

A rule-of-thumb method was developed that states the maximum scour will occur when the vertical wall is located around the plunge point of the breaking wave. Thus, by reducing the wall reflection, the amount of scour will also be reduced. The design relationship is given in Equation 2-33.

$$S_m = H_{max} \text{ or } S_m \approx h \qquad 2\text{-}33$$

2.7 PHYSICAL MODELLING AND LABORATORY TECHNIQUES

2.7.1 PHYSICAL MODELLING FUNDAMENTAL CONCEPTS

A physical model is a system that is fashioned at a reduced size to present the dominant forces that act on the physical system. The model must act similarly to the prototype that it is intended to present; this introduces the concept of similitude or scale laws. Similitude is achieved when the significant factors that cause reactions are in proportion between the model and prototype (Hughes, 1993).

In coastal engineering, there are generally two types of physical models: fixed-bed models and movable-bed models. In this study, a fixed-bed model will be conducted. The objective of this type of model is to study hydrodynamic phenomena. Fixed-bed models consist of definite boundaries which cannot be changed by the hydrodynamic processes. The borders would instead modify the hydrodynamic processes (Hughes, 1993).

The scale factors used for short waves (wave periods between 1 and 20 seconds) are generally recommended to be between 1:10 and 1:50. The largest scale may not be economically feasible and the smaller scales may be influenced by scale effects. The selection of the best scale will depend mainly on past engineering experience (Hughes, 1993). This section will investigate the main topics to be considered and applied in the modelling of a vertical seawall and rubble-mound structure including the screed layer beneath the seawall.

2.7.2 SCALE FACTOR

A scale or physical model is a representation of a physical phenomenon on a scale smaller than that of reality; therefore, the need for a scale factor arises (CIRIA, 2007). A scaling ratio denotes model and prototype correspondence. It is the relationship of the value of specific parameter in the prototype to the value of the same parameter in the model. The ratio is given in Equation 2-34. The value of N_x is usually in the range of 2 and 60. The subscripts *p* and *m* refer to prototype and model, respectively (Hughes, 1993).

$$N_x = \frac{X_p}{X_m} = \frac{\text{Value of X in Prototype}}{\text{Value of X in Model}} \qquad 2\text{-}34$$

In physical modelling, specific scale requirements which involve the density of a material may require using other materials than that used in the prototype to represent the sand, armour stone etc. These materials include concrete, iron, polystyrene etc. (CIRIA, 2007).

2.7.3 HYDRAULIC CRITERIA

In coastal engineering problems, the forces that are associated with surface tension and elastic compression are small and can be neglected. The Froude and Reynolds number should be used as an essential criterion. The similarity of these numbers in the model and in the prototype will provide the correct hydrodynamic similitude for a coastal model (Hughes, 1993). The Froude and Reynold similitudes are derived from their respective equations and can be seen in Appendix A.

2.7.3.1 Froude Criterion

The Froude number is dimensionless (Equation 2-35). The number expresses the inertia and gravity forces in hydrodynamic processes (Hughes, 1993).

$$\sqrt{\frac{\text{inertial force}}{\text{gravity force}}} = \sqrt{\frac{\rho L^2 V^2}{\rho L^3 g}} = \frac{V}{\sqrt{gL}} \qquad 2\text{-}35$$

The Froude number should be the same in both the model and the prototype:

$$\left(\frac{V}{\sqrt{gL}}\right)_p = \left(\frac{V}{\sqrt{gL}}\right)_m \qquad 2\text{-}36$$

When expressing Equation 2-36 in terms of scale ratio and rearranging the terms, Equation 2-37 is generated. Equation 2-37 is known as the Froude model criterion and should be applied when flows are modelled and where the inertial forces are balanced by gravitational forces (Hughes, 1993).

$$\frac{N_v}{\sqrt{N_g N_L}} = 1 \text{ or } N_{Fr} = 1 \qquad 2\text{-}37$$

Velocity is expressed as unit length per unit time; accordingly, the scale ratio of velocity is given as N_L/N_t. By substituting this into Equation 2-37, the Froude time scale is obtained as presented in Equation 2-38 (Hughes, 1993).

$$N_t = \sqrt{\frac{N_L}{N_g}} \qquad 2\text{-}38$$

The gravitational scale in the model and prototype is the same, thus $N_g = 1$. The Froude time scale can be simplified to Equation 2-39 (Hughes, 1993). This equation is used when comparing the prototype and model wave periods.

$$N_t = \sqrt{N_L} \quad 2\text{-}39$$

The time scale for the fluid parameters for specific weight is given by Equation 2-40 (Hughes, 1993).

$$N_\gamma = N_\rho N_g \quad 2\text{-}40$$

When Equation 2-40 is substituted into the Froude time scale, Equation 2-41 is obtained. This equation can be used to express the scale ratios of dynamic scale parameters in terms of prototype and model fluid properties, especially in situations where the fluid properties differ (saltwater versus freshwater) (Hughes, 1993).

$$N_t = \sqrt{\frac{N_\rho N_L}{N_\gamma}} \quad 2\text{-}41$$

2.7.3.2 Reynold Criterion

The Reynolds number is used in fluid mechanics to describe the type of flow that passes a body as either turbulent or laminar flow. It gives the ratio of the inertial force to the viscous force of a particle. If the Reynolds number is similar in both the model and prototype, there will be a dynamic similarity to the inertia and viscous forces (Hudson *et al.*, 1979). The Reynolds number is given in Equation 2-42 (Hughes, 1993).

$$\frac{\text{inertial force}}{\text{viscous force}} = \frac{\rho L^2 V^2}{\mu V L} = \frac{\rho L V}{\mu} \quad 2\text{-}42$$

The same concept applies as in the case of the Froude criterion; similitude is achieved when the Reynolds number of the model equals the Reynolds number of the prototype (Hughes, 1993).

$$\left(\frac{\rho L V}{\mu}\right)_p = \left(\frac{\rho L V}{\mu}\right)_m \quad 2\text{-}43$$

When expressing Equation 2-43 in terms of scale ratio and rearranging the terms, the Reynolds model criterion in Equation 2-44 is generated (Hughes, 1993).

$$\frac{N_v N_L N_p}{N_\mu} = 1 \text{ or } N_{Re} = 1 \quad 2\text{-}44$$

The Reynolds time scale is given in Equation 2-45. It is obtained by substituting $N_v = N_L/N_t$ into the Reynolds criterion (Hughes, 1993).

$$N_t = \frac{(N_L)^2 N_p}{N_\mu} \qquad 2\text{-}45$$

2.7.4 Scale and Laboratory Effects

Scale and laboratory effects can have a significant impact on the results of the model. It is essential to be aware of the potential effects they can have on the model outcomes (Hughes, 1993).

2.7.4.1 Scale Effects

Scale effects are forces that are negligible in the prototype but can have a significant impact on the hydraulic processes of a small-scale model. Examples of scale effects are surface tension, viscosity and surface roughness. Scale effects also become a problem when the scale ratio of a physical parameter is not maintained over the entire domain of the model. The best solution to avoid scale effects is to build the model as large as possible (Hughes, 1993).

A method has been produced by (Costa, 1984) to reduce the scale effects relating to elasticity, viscosity, surface tension etc. He conducted a technique to modify the Froude time scale. This technique would provide better prototype-to-model correspondence, but the method is not very practical. Designers concluded that it is better to rather live with these scale effects. It is better to be more practical by quantifying the scale effects and examining them in a critical manner (Hughes, 1993).

The most critical scale effects applicable in this thesis are wave reflection, wave transmission, surface tension, viscosity, friction, wave breaking and material particle size. There are, however, many other scale effects that have an impact on the physical modelling process, only the most prominent ones are discussed.

- *Wave Reflection*

The relative increase in friction at the model scale can cause the reflected waves in the model to be smaller than the reflected waves in the prototype. If the waves that are reflected must remain “true” due to it being of importance to the physical process, this can be achieved by using a larger scale, and the stones in the model sized according to the geometric scale.

- *Wave Transmission*

As mentioned, the model will experience an increase in frictional losses. Frictional losses will ultimately lead to less wave transmission in the model. The size of the modelling stones can be increased through geometric scaling to counter this scale effect (Hudson *et al.*, 1979). The scale factor, K, can be calculated through

methods developed by Le Méhauté (1965) and Keulegan (1973). Hudson (1979) proposes that the scale factor should be calculated using both methods. The average of these two methods will generate the scaling factor to be used. The scale factor is given by Equation 2-46.

$$\frac{L_p}{L_m} = K\,\frac{D_p}{D_m} \text{ or } N_L = K\,N_D \qquad 2\text{-}46$$

Where

L = Geometrically undistorted model characteristic length (m)

D = Stone size linear dimension (m)

Le Méhauté (1965) assumed that the scale effects in the armour layer are negligible and that the core material of the model has the same gradation as the prototype. This method reduces the scale effects that will arise from the flow through the core of the scaled rubble-mound structure. The method includes the use of a nomogram, given in Figure 2-28.

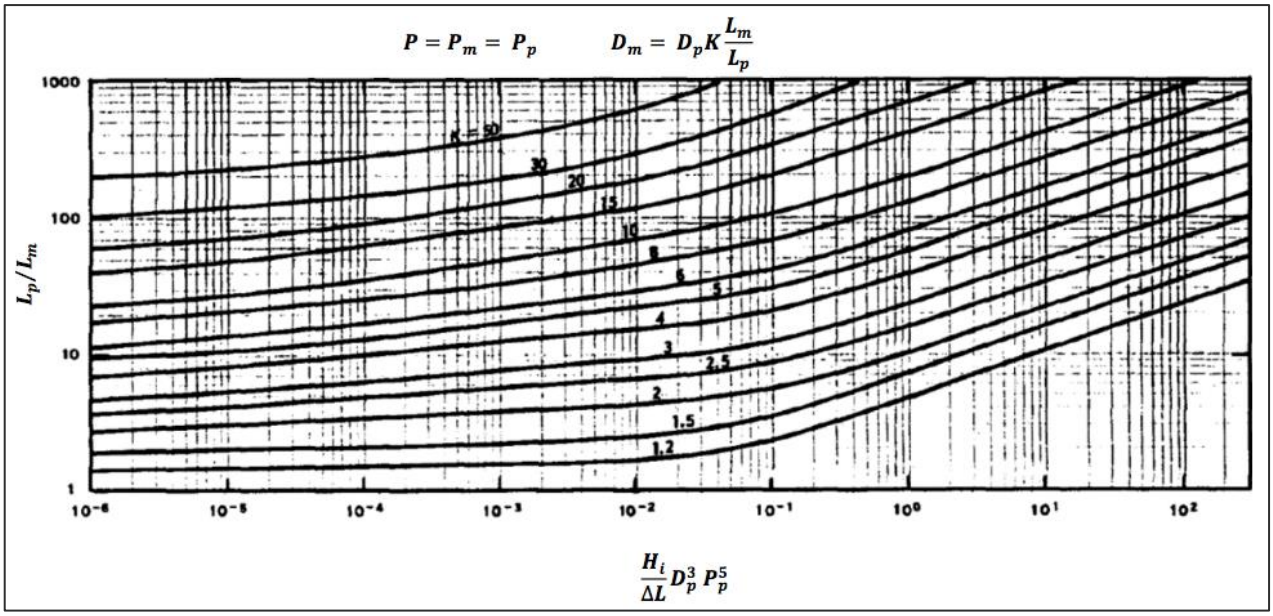

Figure 2-28: Le Méhauté's nomogram for sizing model rubble-mound structures to prevent the scaling effect of wave transmission (Le Méhauté, 1965)

The solid lines in Figure 2-28 are the constant values of the scale factor (K). The y-axis is the geometric length scale, and the x-axis is the dimensional factor which combines several given parameters. In this nomogram, H_i is the incident wave height, ΔL is the average width of the core material, D_p is the quarry stone diameter of the core material of the prototype (D_p should be taken as smaller than 10% of the gradation curve and should be measured in centimetres) and P is the porosity of the core material (Hughes, 1993).

Keulegan (1973) developed two equations to determine the scale factor. The first relationship developed represents the wave transmission in the prototype when the Reynolds number is larger than 2000. In this equation, it is assumed that the energy losses are from turbulent dissipation. The first relationship is given as:

$$(\frac{H_i}{H_t})_p = 1 + \gamma_p (\frac{H_i}{2h})_p (\frac{\Delta L}{L})_p \quad 2\text{-}47$$

$$\gamma_p = \frac{P_p{}^{-4}}{10.6} (\frac{L}{D})_p (gh \frac{T^2}{L^2})_p{}^{4/3} \quad 2\text{-}48$$

The second relationship developed was for wave transmission when the Reynolds number is between 20 and 2000. In this equation, viscous dissipation will occur within the structure. The second relationship is given as:

$$(\frac{H_i}{H_t})_m{}^{2/3} = 1 + \gamma_m (\frac{H_i}{2h})_m{}^{2/3} (\frac{\Delta L}{L})_m \quad 2\text{-}49$$

$$\gamma_m = \frac{P_m{}^{-4}}{1.52} (\frac{\nu T}{DL})_m{}^{1/3} (\frac{L}{D})_m (gh\frac{T^2}{L^2})_m{}^{4/3} \quad 2\text{-}50$$

The Reynolds number for the two relationships developed by Keulegan (1973), should be calculated with Equation 2-51. The velocity used in the calculation of the Reynolds number is given in Equation 2-52.

$$R_n = \frac{PH_iLD}{2\nu hT} \quad 2\text{-}51$$

$$V_{seepage} = \frac{PH_iL}{2hT} \quad 2\text{-}52$$

The prototype equations (Equation 2-47 and Equation 2-48) developed by Keulegan (1973) should be used in correspondence with prototype parameters to determine the prototype-scale wave transmission since wave transmission similarity requires the following:

$$(\frac{H_i}{H_t})_p = (\frac{H_i}{H_t})_m \quad 2\text{-}53$$

The same wave transmission ratio can then be used in the model equations (Equation 2-49 and Equation 2-50) in correspondence with model parameters to determine the value of D_m. D_p and D_m can then be substituted into Equation 2-48 to obtain the scale factor.

- *Surface Tension*

The scale effect associated with surface tension becomes a problem when the water is shallow or when the waves are short. The rule-of-thumb is that surface tension should be addressed when the water depth is less than 2cm or when the wave period is less than 0.35s in the model (Le Méhauté, 1965). If the model has short wave periods or shallow water depths, wave motion damping will occur. It will also have an impact on the wave celerity since wave celerity is a function of surface tension. Accordingly, wave celerity will impact wave refraction (Hughes, 1993).

- *Viscosity and Friction*

When short-wave models are scaled according to the Froude criteria, viscous and frictional effects are not simulated correctly due to the Reynolds number still being different between the model and prototype. This scale effect can usually be taken as insignificant because of viscosity and friction becoming negligible for short-wave models modelled over a short distance (Le Méhauté, 1965).

- *Wave Breaking*

In the model, the size of the entrained air bubbles is more extensive than in prototype due to surface tension. Air entrainment is also more extensive in the model than in the prototype. Le Méhauté (1965) concluded that wave breaking would remain in similitude during the process of energy dissipation even when all the finer details of the flow process differ.

- *Material Particle Size*

The scale effects associated with small granular material, as found in the screed layer, is significant to consider in the model. When the screed layer material is scaled to model dimensions, the material must preserve its prototype behaviour. The model particles should be prevented from being as small as that of clay. Clay is a cohesive soil and will have different internal forces and pore water interaction than that of sand and gravel. In comparison, sand and gravel have similar characteristics (CIRIA, 2007).

2.7.4.2 Laboratory Effects

In a short-wave model, the laboratory effects that can be expected are related to the following (Hughes, 1993):

1. The physical constraints of the boundaries on the flow
2. The waves and current generation can cause nonlinear effects
3. The simplification of prototype forcing conditions

A potential problem in a two-dimensional wave flume is cross-waves; they are caused when a mechanical wave board generate energetic wave conditions. The two-dimensional wave tank will restrict the hydrodynamics. Another boundary-effect to be taken into consideration is the waves that get reflected by the wave board. In nature, the waves will move toward a structure on the beach (like a vertical seawall) and get reflected seaward. In the model, waves will travel toward the seawall and get reflected back into the flume. Instead of the waves dispersing in the ocean, they are reflected at the opposite side of the flume by the wave board and travel back to the structure. This laboratory effect can be handled in the following ways (Hughes, 1993):

1. Gentle slopes and rubberised “horsehair” mats can minimise the reflection of the waves to less than 5% of the incident wave height
2. The experiments can be conducted in a series of wave bursts. Each wave burst should end before the reflected waves can reach the testing section of the wave tank
3. Unwanted reflected wave energy can be detected and absorbed through active wave absorption (this technique is applied in this two-dimensional model used in this thesis, with the Dynamic Wave Absorption System of the HR Wallingford Wavemaker)

2.7.5 Coastal Defence Structure Modelling

The two-dimensional physical model applicable in this study consists of a vertical seawall and a rubble-mound structure. A two-dimensional wave flume test is a rapid and relatively inexpensive method to conduct tests of normal wave attack on coastal structures. This section will briefly investigate some of the significant aspects of two-dimensional coastal defence structure modelling applicable in this thesis.

2.7.5.1 Physical Model of a Rubble-Mound Structure

When conducting a model of a rubble-mound structure, or any coastal structure, the first step is to re-create the bathymetry. In the case of a two-dimensional model, the slope should be constructed in the flume. The preparation of the model material should be prepared next. The core material usually consists of crushed limestone or basalt. A sieve or powered shaker with screens with the correct mesh size should be used to obtain the appropriate size distribution. The underlayer can be hand-picked or separated according to the size distribution using the powered sieve shaker. The armour layer is fabricated from limestone, basalt or granite. The material selection is dependent on the scaling criterion for the specific armour weight. The sharp edges of the armour stone may require some rounding; this can be achieved by using a shipping hammer (Hughes, 1993).

During the construction of the model, it is essential to replicate the random placement of the armour units like it would be in the prototype. The units should not "key in". By limiting the number of stones to pick from when placing the units will help suppress the tendency to select the units that fit the best (Hughes, 1993).

Once the model has been constructed, it is necessary to "shakedown" the structure, allowing the armour units to nest in. The "shakedown" is executed by exposing the model to lower energy waves before any of the real tests are performed. Wave heights that are typically 50% of the design wave height can be used (Hughes, 1993).

There are no mathematical equations that explain the detailed behaviour of rubble-mound structures during wave attack. Dimensional analysis or inspection should be applied to determine similitude relationships (Hughes, 1993). Dimensionless products that include all the parameters for a rubble-mound structure are conducted by (Hudson *et al*., 1979). These products are given as:

$$F\left(\frac{l_a}{h}, \frac{H}{L}, \frac{h}{L}, \propto, \beta, \Delta, \theta, \frac{V_w}{\sqrt{g l_a}}, \frac{V_w l_a}{\mu/\rho_w}, \frac{\xi_a}{l_a}, \frac{\rho_w}{(\rho_a - \rho_w)}, D\right) = 0$$

To achieve similitude, the dependent variable in the physical model should be the same as the dependent variable in the prototype. This requires the following equations to be true (Hughes, 1993):

$$\left(\frac{l_a}{h}\right)_p = \left(\frac{l_a}{h}\right)_m \quad \text{2-54}$$

$$\left(\frac{H}{L}\right)_p = \left(\frac{H}{L}\right)_m \quad \text{2-55}$$

$$\left(\frac{h}{L}\right)_p = \left(\frac{h}{L}\right)_m \quad \text{2-56}$$

$$(\propto)_p = (\propto)_m \quad \text{2-57}$$

$$(\beta)_p = (\beta)_m \quad \text{2-58}$$

$$(\Delta)_p = (\Delta)_m \quad \text{2-59}$$

$$(\theta)_p = (\theta)_m \quad \text{2-60}$$

$$\left(\frac{V_w}{\sqrt{g l_a}}\right)_p = \left(\frac{V_w}{\sqrt{g l_a}}\right)_m \quad \text{2-61}$$

$$\left(\frac{V_w l_a}{\mu/\rho_w}\right)_p = \left(\frac{V_w l_a}{\mu/\rho_w}\right)_m \quad 2\text{-}62$$

$$\left(\frac{\xi_a}{l_a}\right)_p = \left(\frac{\xi_a}{l_a}\right)_m \quad 2\text{-}63$$

$$\left(\frac{\rho_w}{(\rho_a - \rho_w)}\right)_p = \left(\frac{\rho_w}{(\rho_a - \rho_w)}\right)_m \quad 2\text{-}64$$

$$\left(\frac{\rho_a}{\rho_w}\right)_p = \left(\frac{\rho_a}{\rho_w}\right)_m \quad 2\text{-}65$$

The following criterion must be met with regards to rubble-mound structures to achieve the requirements above:

1. The structure should be geometrically undistorted in length scale. A reasonable approximation of the shape and size distribution is necessary for the primary and under layer armour units.
2. The flow hydrodynamics must conform to the Froude criteria. The inertial forces relative to gravity forces must scale fittingly.
3. The primary armour layer and underlaying layers requires turbulent flow conditions. This criterion can be satisfied by building a large enough model.
4. The surface roughness of the model and prototype must be the same. In the model, the roughness can be decreased by making the surfaces of the units as smooth as possible. If there is an abundance of friction in the model between the armour units, the results will show higher stability, which can cause an unsafe design.
5. The relative mass density relationship between the model and the prototype must be equal.

2.7.5.2 Physical Model of a Vertical Seawall

In the case of breaking as well as non-breaking waves, the model should be scaled according to Froude scaling. The scale effects for non-breaking waves are relatively small. Vertical walls are, however, often placed on a shoreline where waves break directly on the wall. Waves breaking directly on the wall will cause scale effects that are hard to define. The construction material of the wall should be rigid. Wood, steel or plastic are usually popular selections. The model should be ballasted sufficiently (Hughes, 1993).

2.7.5.3 Wave Loads on the Structure

The waves will cause the main loads on the system. A wave generation technique should be adopted to implement the required wave load on the structure. Spectral distribution of the irregular waves must be

applied. The three widespread wave energy spectrums are the TMA spectrum, the Pierson-Moskowitz (PM) spectrum and the JOint North Sea WAve Project (JONSWAP) spectrum (CIRIA, 2007).

The PM spectrum has been in use since 1964 and is limited to describing sea states that are not fetch or duration limited. More recent studies are based on observations made in the North Sea, which resulted in the JONSWAP spectrum (Chadwick, Morfett & Borthwick, 2013). The JONSWAP spectrum is more complicated than the PM spectrum due to it being a function of the fetch and wind speed. The JONSWAP spectrum also introduces a new parameter called the peak enhancement factor (γ). The spectrum is given by Equation 2-66.

$$S(f) = \frac{K_j g^2}{(2\pi)^4 f^5} \exp[-\frac{5}{4}(\frac{f_p}{f})^4]\gamma^a \qquad 2\text{-}66$$

Where

a = exp $[-\frac{(f-f_p)^2}{2W^2 {f_p}^2}]$

$K_j = \frac{0.076}{{X_{10}}^{0.22}}$

$X_{10} = \frac{gF}{{U_{10}}^2}$

U_{10} = Wind speed 10m above sea surface (m/s)

F = Fetch length (m)

$f_p = \frac{3.5g}{U_{10}\ {X^{0.35}}_{10}}$

γ = Peak enhancement factor = 3.3

W = 0.07 for $f \leq f_p$ or W = 0.09 for $f > f_p$

f = Wave frequency (Hz)

The wave height and wave period for the JONSWAP spectrum can be estimated with the two equations below.

$$H_s = 0.00051\ U_{10}\ F^{0.5} \qquad 2\text{-}67$$

$$T_s = 0.059\ (U_{10}\ F)^{0.33} \qquad 2\text{-}68$$

The wavemaker should absorb the waves that are reflected by the seawall. Otherwise, these waves will reflect from the wavemaker back to the seawall. If the waves are not adequately absorbed, it will lead to an increase in wave energy. Active Reflection Compensation (ARC) is accomplished when a wave generator can detect the water level in front of it and correct the position of the water level to the required level, and so absorb the wave energy. At the structure toe, a wave gauge should be used to attain the incident wave characteristics.

They can be obtained by measuring the surface elevations and removing the reflected waves from the structure (CIRIA, 2007).

It should be decided if first-order or second-order wave generation techniques should be used. First-order methods generate sinusoidal waves (regular waves), but waves are not sinusoidal in prototype or wave flumes. Second-order methods generate non-sinusoidal waves (irregular waves) (CIRIA, 2007).

2.7.5.4 Probe Positioning

It is vital to obtain the desired wave heights in the wave flume. The incident and reflected wave heights should be measured to ensure that the wave-maker is calibrated; this will produce accurate results. The incident and reflected wave heights can be measured with wave probes that use capacitance variance.

A method developed by (Mansard and Funke, 1980) is a 3-point model that uses a least square analysis for decomposing the measured spectra into the incident and reflected spectra. Figure 2-29 below defines the Least Squares Method.

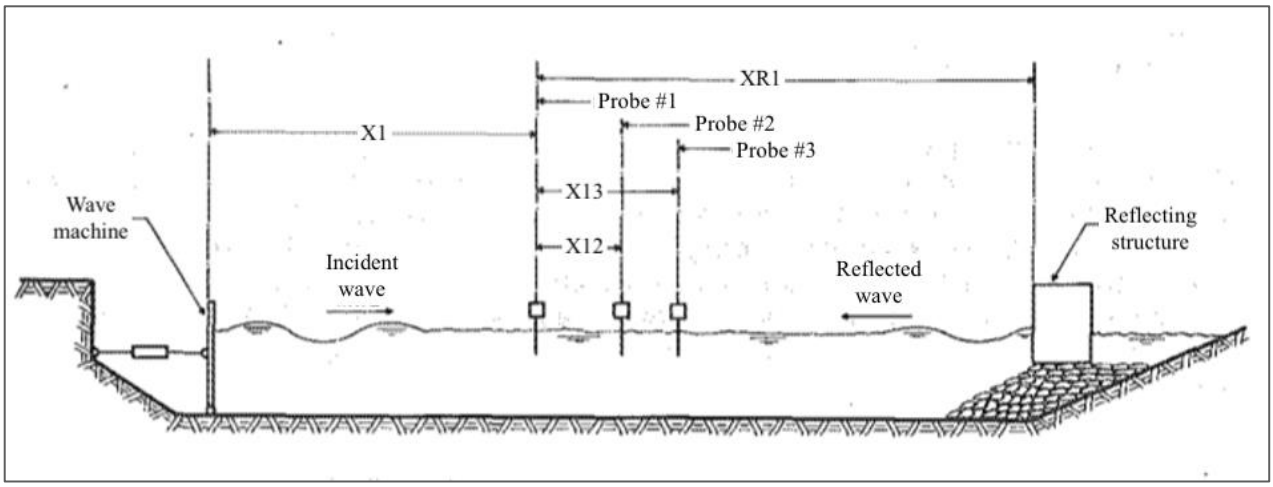

Figure 2-29: Set-up for wave reflection measurement in the least-squares analysis (Mansard and Funke, 1980)

The spacings of the probes are as defined in Equations 2-69 and Equation 2-70. The probe should be positioned at least one wavelength away from a reflective structure; this can either be the wavemaker or the structure under inspection. The probes should also be placed on a relatively flat surface.

$$X_{12} = \frac{L_p}{10} \qquad 2\text{-}69$$

$$\frac{L_p}{6} < X_{13} < \frac{L_p}{3} \text{ with } X_{13} \neq \frac{L_p}{5} \text{ and } X_{13} \neq \frac{3L_p}{10} \qquad 2\text{-}70$$

Where

X_{12} = Distance between Probe 1 and Probe 2

X_{13} = Distance between Probe 1 and Probe 3

X_1 = Distance between Probe 1 and wavemaker

X_{R1} = Distance between reflecting structure and Probe 1

The probes record the varying voltage readings as the water level around the probe change. The voltage variations are converted into time-series data. This time-series data is representative of the surface elevations from which the wave parameters are calculated.

2.7.5.5 Measuring Structural Damage

There are two approaches to measuring the damage to coastal structures. The first one is to measure or count the number of displaced units and the second method entails the process of using the profile of the cross-section. The cross-section is measured before and after each test. The amount of damage will be the difference between the two measurements. The damage to a structure can also be described by using the damage level parameter. The parameter is obtained using Equation 2-71 (CIRIA, 2007).

$$S_d = \frac{A_e}{D_{n50^2}} \qquad 2\text{-}71$$

Where

A_e = Eroded cross-section are (m^2)

The damage level parameter is a dimensionless parameter that describes the erosion area related to the stone size. The method developed in this thesis (as described in Section 3.6.2) as well as those used by Malan (2016) and Van Wageningen (2018) physically measure the damage (as the horizontal scour distance, measured from the seaward face of the seawall or area of eroded screed below the seawall) and produce quantifiable results based on case-specific conditions.

An intrusive measuring method was used by Malan (2016) to measure the scour damage underneath a vertical seawall. Wooden dowels were used to measure the development of scour in laboratory tests by probing underneath the seawall. The length the dowel penetrated was measured, and this is the scour depth. This method is, however, not recommended since it disturbs the original scour pattern when the dowels are pressed in underneath the seawall.

A non-intrusive method was used by Van Wageningen (2018). An image of the scour damage underneath the seawall was created using ultrasound sonar equipment. Sonar technology from the medical field was used due to a lack of availability of sonar equipment to measure physical laboratory experiments in coastal experiments.

2.8 Literature Study Summary

This section presents a summary of each of the significant aspects covered in the Literature Study.

- *Coastal parameters*

A well-known parameter used in coastal engineering is the surf similarity parameter. This parameter is used to describe the wave action on a slope and distinguishes between the three breaker types: spilling, plunging and surging. The four hydraulic responses that have an impact on coastal defence structures are: wave run-up and wave run-down, wave overtopping, wave reflection and wave transmission. Wave transmission is discussed in slightly more depth due to the theory presented by (Van der Meer *et al.*, 2004) directly being used in this current study. The transmitted wave height is mainly dependent on the incident wave characteristics, water depth at the structure toe, crest height, width of the structure, slope angle and the material properties. In this thesis the transmitted wave height is not relevant due to the impermeable seawall, the focus is on the transmission mechanism in the rubble mound itself which can bring wave energy to the screed layer.

- *Coastal protection structures*

A seawall is defined as a “hard engineering” scheme since it is a rigid structure with the primary purpose to prevent infrastructure damage landwards of the structure due to wave action, flooding and currents. Through protecting the landward side, erosion often develops seaward of the seawall leading to structural failure. Adequate toe protection, like a rubble-mound structure, is one method to slow down the process of erosion. The rubble-mound structure consists of various layers adhering to numerous filter rules. These filter rules are implemented to prevent finer material being washed through the rubble-mound structure while still making allowance for the transport of water.

- *The motion of water and energy dissipation in a rubble-mound structure*

The Forchheimer equation, derived from the Darcy equation can be used to describe the flow through a porous medium. The Forchheimer equation is a function of laminar, turbulent and oscillatory flow. The porosity (and permeability) of a structure has an enormous influence on the energy dissipation. As the water flows through the porous structure, the layers of the rubble-mound structure dissipate energy. The energy dissipation due to

wave breaking is the dominant form of energy dissipation and is derived from the analogy of energy loss in a hydraulic jump by (Battjes and Janssen, 1978). The energy of the incident wave that is not dissipated by the structure will either be reflected or transmitted.

- *Scour in the marine environment and underneath vertical seawalls*

Scour can be defined as the removal of granular bed material in the vicinity of coastal structures through the presence of hydrodynamic forces. Scour can lead to partial damage or complete failure of coastal defence structures. The main factors influencing scour underneath a seawall are wave height, wave period, water depth, storm duration, wave approach angle, grain size and sediment supply. Recent research on scour in the seabed at a seawall is reported in CEM (2002), where a rule-of-thumb method states that the maximum scour will occur when the vertical seawall is located around the plunge point of the breaking wave. Concerning scour of the screed beneath a seawall, research by Malan (2016) and Van Wageningen (2018) which is more relevant for this thesis will be addressed and described in Chapter 3.7.

- *Physical modelling and laboratory techniques*

A physical model must represent the phenomena that have an impact on the prototype behaviour. The Froude criterion is used to ensure similitude in the model. Scale and laboratory effects have an enormous influence on the model results. Scale effects such as wave reflection, wave transmission, surface tension, viscosity, friction, wave breaking, and small granular material should be critically analysed. Granular scour that develops underneath a vertical seawall has been measured in previous studies using two methods: probing dowels and medical sonar equipment.

3 METHODOLOGY

3.1 PROBLEM STATEMENT

3.1.1 GENERAL PROBLEM STATEMENT

The design of the structure being investigated in this thesis is a typical design for a vertical seawall protected by a rubble-mound structure, inspired by a structure in the Middle East. The two preceding studies conducted at Stellenbosch University researched minimising the scour of the screed layer under a vertical seawall. Guidelines are provided in these studies for the design and construction of granular scour protection (Malan 2016; Van Wageningen 2018).

The stone mass (of the filter layer and core) and the layer thickness (of the armour layer and filter layer) to prevent screed scour were the focus of this study. Low-quality of design and construction of the rubble-mound foundation is one of the main reasons for the development of scour in the screed layer.

The design of the cross-section was kept the same as in the study by Van Wageningen (2018). The structure layout, indicating the different layers, is given in Figure 3-1. The rock sizes used were based on two filter rules widely used in practice, as recommended in the Shore Protection Manual (USACE, 1984). The findings of this thesis will contribute to the design and construction process of a rubble-mound structure in front of a vertical seawall by quantifying the consequences (on screed erosion) of using the wrong stone size or layer thickness. If this study concludes that the extent of such an error has an excessively large negative impact, design and construction practices and guidelines for this type of structure will need to be revised. The cost of structure failure outweighs the price of a proper structure with the right dimensions and materials.

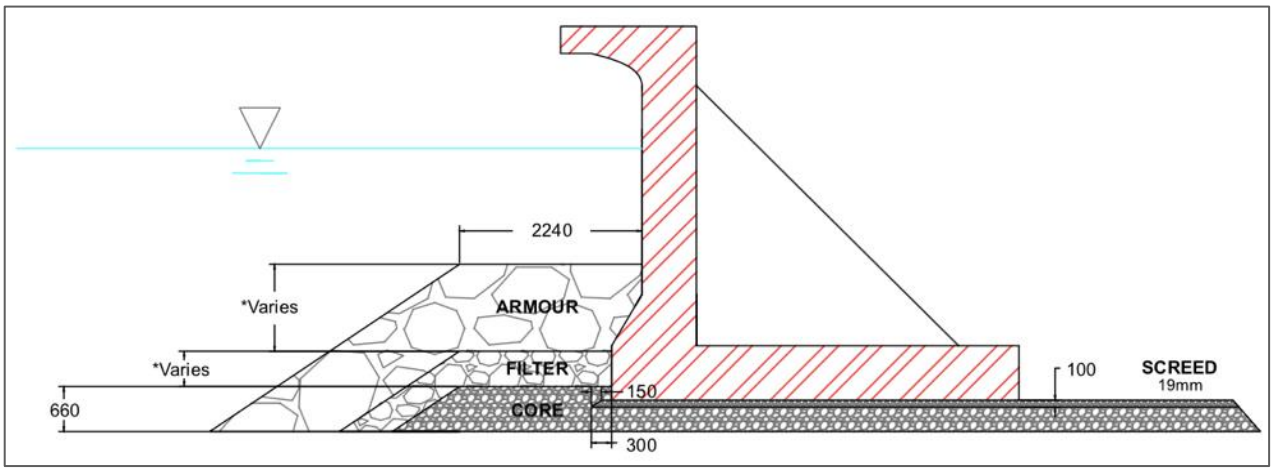

Figure 3-1: Cross-section of vertical seawall with rubble-mound in prototype

3.1.2 MODELLING METHODOLOGY

To investigate the problems outlined, six different structures will be tested in this study using seven different peak wave periods per structure. The six structures are chosen based on previous research suggesting that by improving the design of the respective variables in the structures, it can contribute to minimising scour development. The difference between the various structures is given in Table 3-1. The rubble-mound structure thickness in Table 3-1 refers to the height from the seabed to the top of the primary armour layer.

Table 3-1: Characteristics of the six modelled structures

Structure	Rock size filter rule	Rubble-mound structure thickness (prototype) (mm)	Number of rocks per layer
Structure A1	$\frac{M_{50\ lower}}{M_{50\ upper}} = 1/10$	2546	Armour = 2 layers of rock Filter = 2 layers of rock
Structure A2	$\frac{M_{50\ lower}}{M_{50\ upper}} = 1/10$	3489	Armour = 3 layers of rock Filter = 3 layers of rock
Structure A3	$\frac{M_{50\ lower}}{M_{50\ upper}} = 1/10$	3144	Armour = 2 layers of rock Filter = 4 layers of rock
Structure B1	$\frac{M_{50\ lower}}{M_{50\ upper}} = 1/15$	2470	Armour = 2 layers of rock Filter = 2 layers of rock
Structure B2	$\frac{M_{50\ lower}}{M_{50\ upper}} = 1/15$	3375	Armour = 3 layers of rock Filter = 3 layers of rock
Structure B3	$\frac{M_{50\ lower}}{M_{50\ upper}} = 1/15$	3114	Armour = 3 layers of rock Filter = 2 layers of rock

Numerous studies have been conducted with regards to the calculation of the energy dissipation on the outer side of a structure; this external energy dissipation will be briefly investigated through computations using the method of Battjes and Janssen (1978). There are, however, limited studies on the internal energy dissipation within such a porous structure, and none of these studies addresses the distribution of energy dissipation through the various layers of a rubble-mound structure. This study provides a first approximation of the flow velocity, kinetic energy and energy dissipation within the different layers of the structure. The kinetic energy in each layer of the rubble-mound structure will be predicted using the process of dimensional analysis. Lastly, the effect the kinetic energy in the core has on the scour development underneath the seawall will be presented.

3.1.3 CONSTANT AND VARIABLE PARAMETERS

Table 3-2 summarises the constant and variable parameters applied in the two-dimensional laboratory model.

Table 3-2: Constant and variable parameters

Constant Parameters	Variable Parameters
Bathymetry	Wave period
Position of seawall structure	Median rock size of the rubble-mound structure
Design of seawall structure	Layer thickness in rubble-mound structure
Berm width	
Width of screed toe	
Screed layer thickness	
Construction methods	

3.1.4 Model Scale

The scale used for the physical model was 1:20. The model scale is chosen due to the capacity of the modelling flume and capabilities of the wave-maker. The Froude similarity law is used to scale the model instead of the Reynolds criteria due to gravity forces predominating in free-surface flows. Table 3-3 indicates the main scale factors applicable in this thesis according to the Froude similarity law. All scale effects applicable in the model will be taken into account and analysed thoroughly.

Table 3-3: Froude similarity law scaled factors (Hughes, 1993)

Characteristic	Dimension	Applicable Parameter	Froude Scale	Froud Scale 1:20
Length	[L]	Water depth, wave height, structure dimensions	N_L	20
Area	$[L^2]$	Scour area	N_L^2	400
Volume	$[L^3]$	Rock and sediment volume	N_L^3	8 000
Time	[T]	Wave period	$\sqrt{N_L}$	4.47
Velocity	$[LT^{-1}]$	Flow velocity through rock voids	$\sqrt{N_L}$	4.47
Mass	[M]	Rock and sediment mass	N_L^3	8 000
Energy	$[ML^2T^{-2}]$	Energy distribution	N_L^4	160 000
Pressure	$[ML^{-1}T^{-2}]$	Dynamic and kinetics pressure in layers	N_L	20

3.1.5 Hypothesis

There are three variable parameters in this thesis (Table 3-2). The influence of each of these parameters on scour and energy distribution can be determined independently. The increase in wave period is expected to result in a decrease in the scour area. Even though the water particles in longer waves have higher orbital velocities, it is anticipated that the reflection and interaction of the shorter period waves are more crucial than the high orbital velocities. A confused sea state is produced in front of the structure when the incident and

reflected waves interact. A shorter wave period will cause more interactions. A vertical seawall has a very high reflection coefficient, leading to an increase in the peak orbital velocities, which increases the probability of movement of the bed material. The increase in scour of the screed layer with a decrease in the wave period trend was already proven by Van Wageningen (2018). It is expected that the larger peak wave periods tested additionally in this model, would adhere to the same non-linear relationship.

When using rock sizes according to the filter rule, $\frac{M_{50\,lower}}{M_{50\,upper}} = \frac{1}{15}$, it is expected to result in less scour of the screed layer than the filter rule which states; $\frac{M_{50\,lower}}{M_{50\,upper}} = \frac{1}{10}$. In the first-mentioned criterion, the rock sizes will become smaller in the underlying layers, which will make the structure less permeable, allowing less water to filter through the layers towards the core. A lower porosity will also lead to an increase in the stability of the armour layer. The core will also be more compact, resulting in less filtration of the screed layer through it.

For the filter rule $\frac{M_{50\,lower}}{M_{50\,upper}} = \frac{1}{15}$ it is hypothesised that the energy in the armour layer will be higher than for the filter rule $\frac{M_{50\,lower}}{M_{50\,upper}} = \frac{1}{10}$ due to increased compaction in the filter layer and core. Additionally, less energy will have to be dissipated in the core for structures adhering to the filter rule leading to a smaller median rock mass, due to the lower permeability restricting the energy from entering the core.

An increase in the layer thickness is expected to decrease the scour area. It is projected that with a thinner rubble-mound structure, the scour area will increase exponentially. A thicker rubble-mound structure will provide excessive protection due to an increase in interlocking. It will not allow the wave energy to penetrate as far into the screed layer since more of the wave energy can be dissipated at the outer layers.

The outer layer of the rubble-mound structure is located where most of the wave action takes place, and thus the highest energy region. The further you move away from this region, the less kinetic energy there will be. As mentioned above, less wave energy will penetrate through to the core with a thick berm than with a thin berm. Hence, a thicker rubble-mound structure will allow less kinetic energy in the core and screed areas.

3.2 Hydraulic Research Facility and Equipment

The laboratory experiments were conducted at Stellenbosch University Hydraulic Laboratory. The equipment available for two-dimensional modelling is discussed below.

- *Wave Flume*

The two-dimensional glass wave flume used is 40m long, 1m wide and has a maximum operational water depth of 0.8m (Figure 3-2).

- *Wave Maker*

The waves in the flume are generated by a single paddle wave maker from HR Wallingford (Figure 3-3). The wave maker can produce both regular and irregular wave spectrums. The wave maker has a built-in integrated Dynamic Wave Absorption System. This system helps absorb and compensate for reflecting waves from vertical structures such as seawalls. The wave maker can operate in a maximum water depth of 800mm and generate a wave height up to 350mm. The JONSWAP spectrum was used in the modelling as this spectrum is characteristic around the South African coastline (HR Wallingford, 2010).

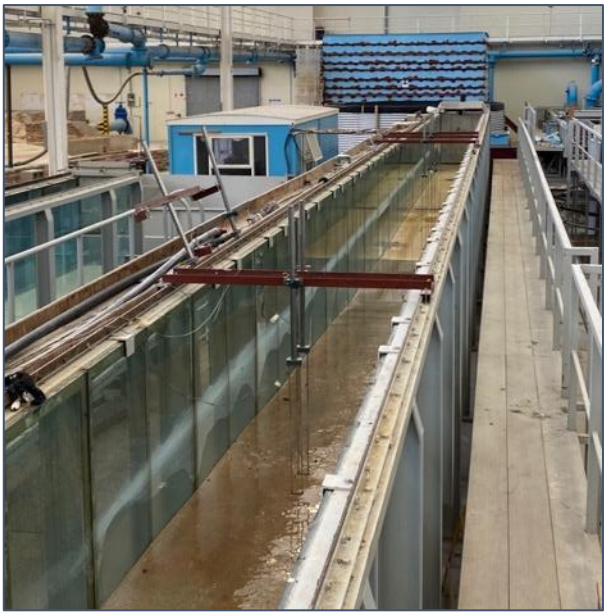

Figure 3-2: Wave flume

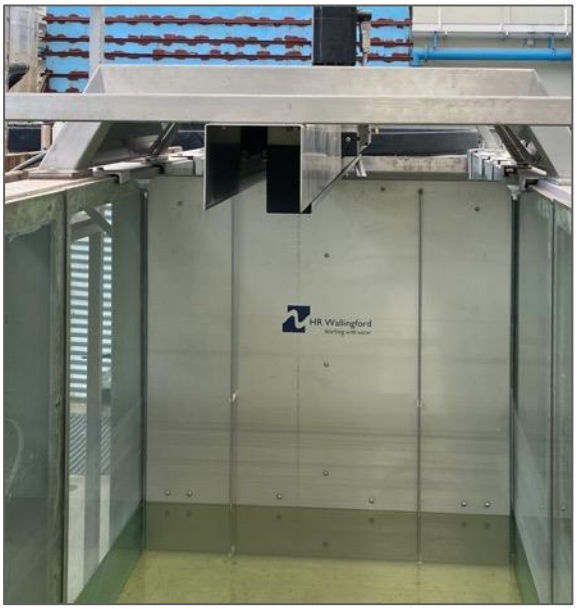

Figure 3-3: HR Wallingford Wave Generator paddle

- *Probes*

Resistive wave probes are used with HRDAQ software. Six probes were used in total, three probes were placed in deepwater, and three probes were placed in shallow water. The deepwater probes were placed 11m from the wave-maker. The shallow water probes were placed 21.75m from the wave-maker on the flat slope where the seawall will be positioned during testing. The two sets of probes must be placed at least one wavelength from any reflective structure as well as on a flat slope to obtain the most accurate results.

The equations in Section 2.7.5 were used to determine the spacings for the probe positioning in the wave flume. The probe spacings, as well as the calculation method, can be seen in Appendix C. The spacings

differed for each test due to the change in wavelength for every test. The shift in wavelength was necessitated by the difference in the wave period and water level combination which was applied. The change in water level was required due to the varying thickness of the berm and the requirement to keep the top of the berm at a constant depth below the water level. The layout of the probes for a test on Structure A1 with a wave period of 12s is given in Figure 3-4.

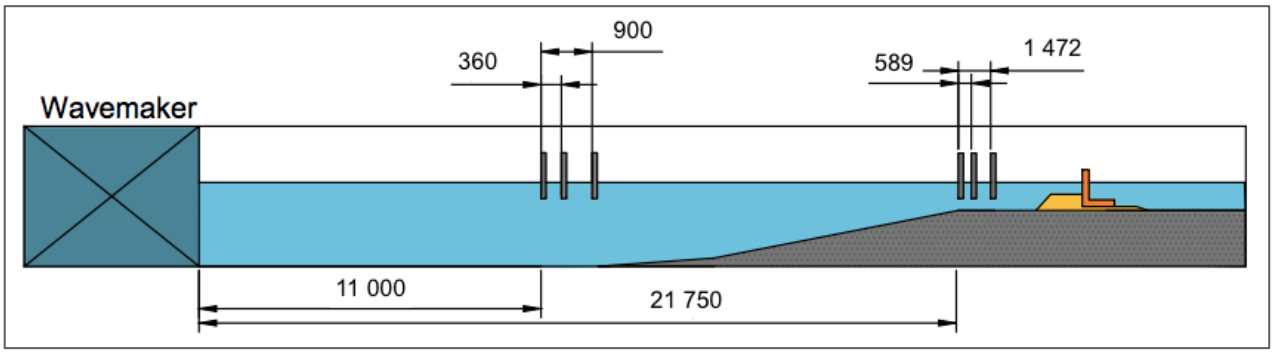

Figure 3-4: Probe spacings in mm for Structure 1(for a wave period of 12s)

The wave probes were calibrated before each test to ensure accuracy of readings. The probes were calibrated through adjusting the probes in the flume to three different known heights and recording these with the HRDAQ software for direct comparison.

- *PicoLog 1000 Series PC Data Logger*

Four pressure transmitters connected to the data logger box were used to measure the pressure in the layers of the rubble-mound structure. The layout of the pressure transmitters elevated vertically through the rubble-mound structure layers is given in Figure 3-13. The multi-channel voltage data logger box has a sampling rate of 1 millisecond and a voltage range between 0 and 2.5V (Pico Technology, 2009).

3.3 Structure Design and Construction

3.3.1 Vertical Seawall Design

The seawall model was constructed using Perspex. As mentioned, the design of the cross-section was kept the same as in the study by Van Wageningen (2018). The prototype in the Middle East was designed to be 5.5m high and 6m wide. The modelled structure dimensions, scaled according to Froude scaling to the selected scale of 1 in 20, are illustrated in Figure 3-5. The length of the model section (across the flume) was 990mm. The sides were sealed with *SOUDAL Fix All* to ensure the seawall sat securely in the 1000mm wide flume. Bricks were packed on the back of the seawall to be used as counterweight.

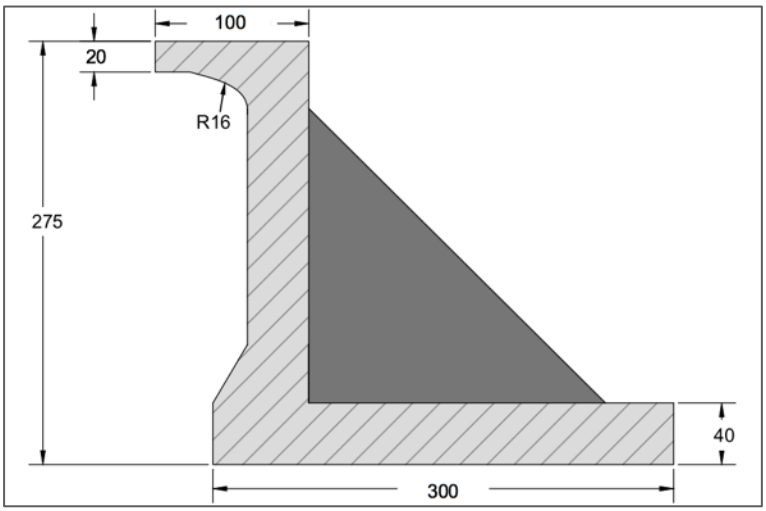

Figure 3-5: Dimensions of vertical seawall model

3.3.2 RUBBLE-MOUND STRUCTURE DESIGN

The rubble-mound structure consisted of three layers – armour layer, filter layer (underlayer) and core – composed of different rock sizes. The grading curves are given in Appendix G. In this report, the filter layer had the same purpose and design as an underlayer as defined and discussed in the Literature Study.

It was decided to scale down the screed layer according to Lé Mehauté and Keulegan's methods as recommended by Hudson *et al*. (1979). As mentioned in the literature, this method considers frictional losses and viscous effects and is more accurate on smaller scale models than the Froude similarity law. If scaled according to the Froude similarity law, the erosion could be considerably overexaggerated in the model.

The calculated diameter of the screed layer was 2.5mm and can be classified as coarse sand. Filter sand between the range of 0.9-3.4mm was used in the model (calculations in Appendix E). It is the same filter sand used in the study by Van Wageningen (2018). The rock sizes used in the two filter rules applied in the two-dimensional model can be seen in Table 3-4 and Table 3-5. The density of the scaled-down material remained the same as the prototype density.

Table 3-4: Rock diameter and mass for Filter Rule 1

Structure A1, A2, A3	Prototype		Model	
Layer	Median mass	Median diameter	Median mass	Median diameter
Armour layer	465kg	560mm	58kg	28mm
Filter layer	47kg	260mm	5,8kg	13mm
Core	4,7kg	121mm	0,6kg	6mm
Screed	NA	19mm	NA	2,5mm

Table 3-5: Rock diameter and mass for Filter Rule 2

Structure B1, B2, B3	Prototype		Model	
Layer	Median mass	Median diameter	Median mass	Median diameter
Armour layer	465kg	560mm	58kg	28mm
Filter layer	31kg	227mm	3,9kg	11mm
Core	2,1kg	92mm	0,3kg	5mm
Screed	NA	19mm	NA	2,5mm

The six structures are given in Figure 3-6 to Figure 3-11.

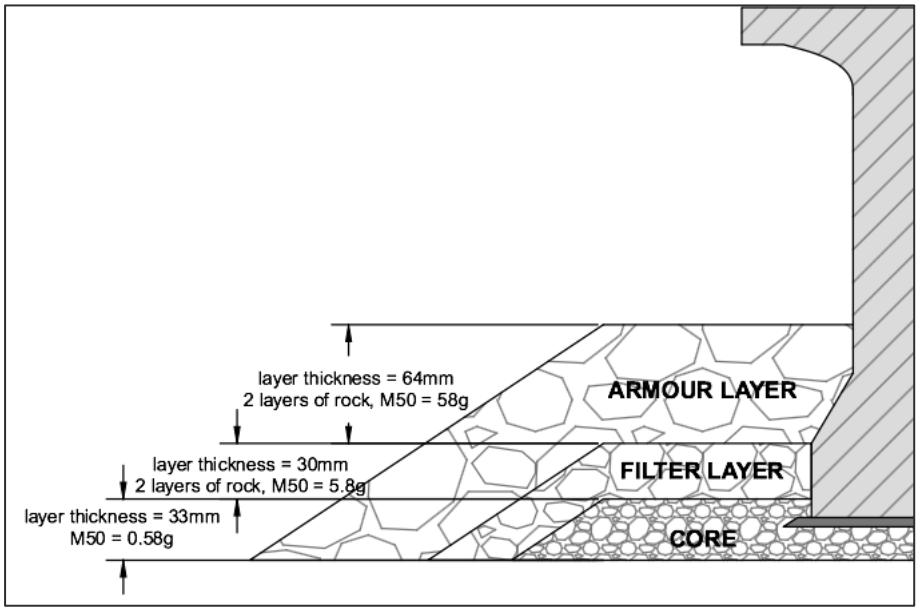

Figure 3-6: Structure A1 rubble-mound characteristics

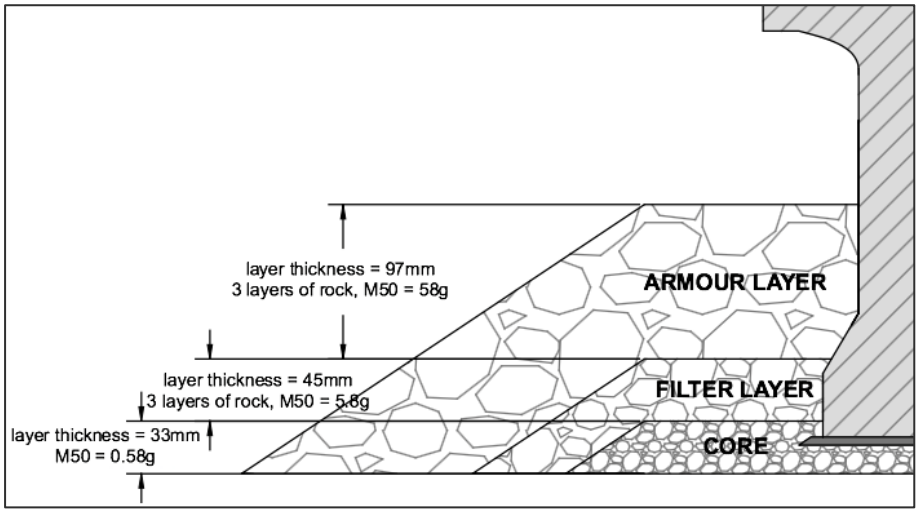

Figure 3-7:Structure A2 rubble-mound characteristics

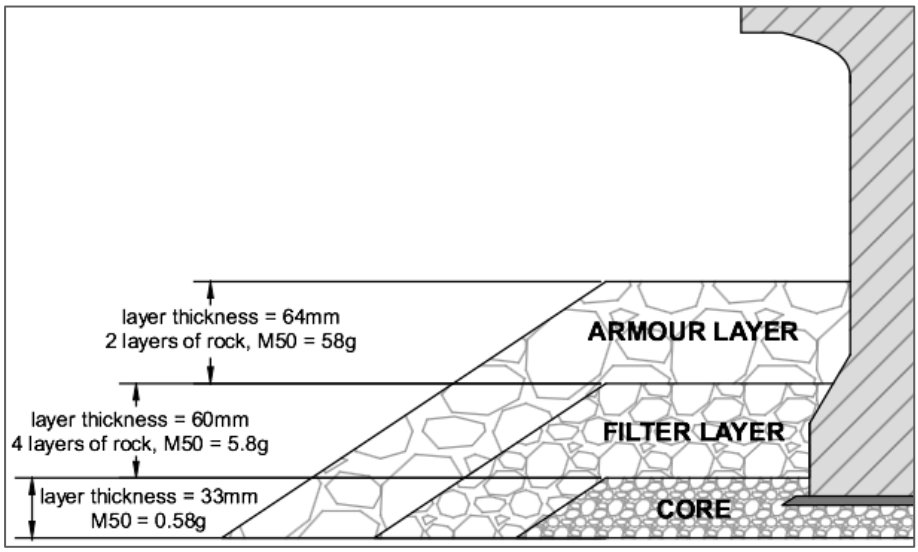

Figure 3-8: Structure A3 rubble-mound characteristics

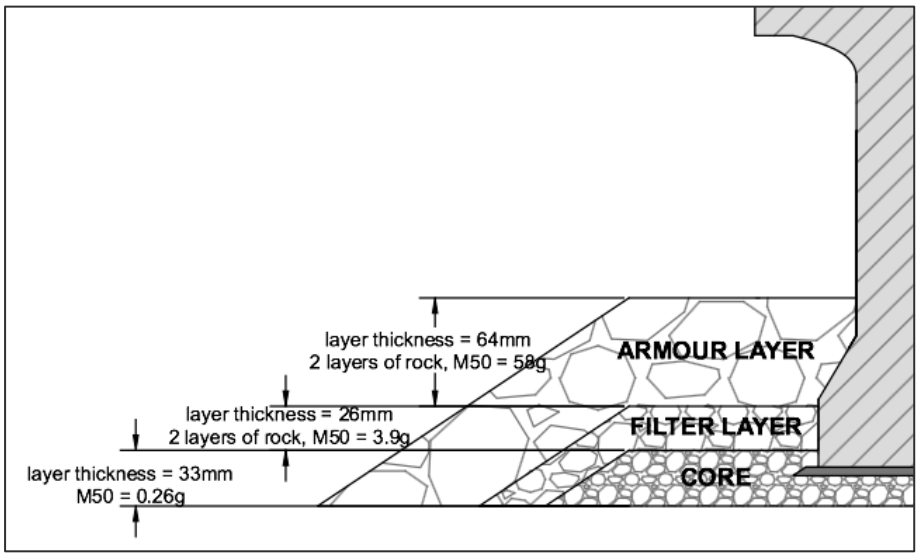

Figure 3-9: Structure B1 rubble-mound characteristics

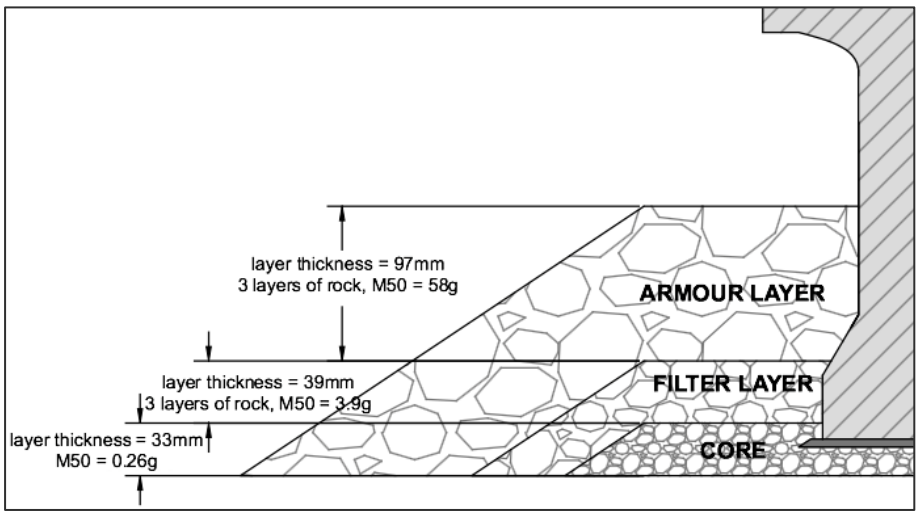

Figure 3-10: Structure B2 rubble-mound characteristics

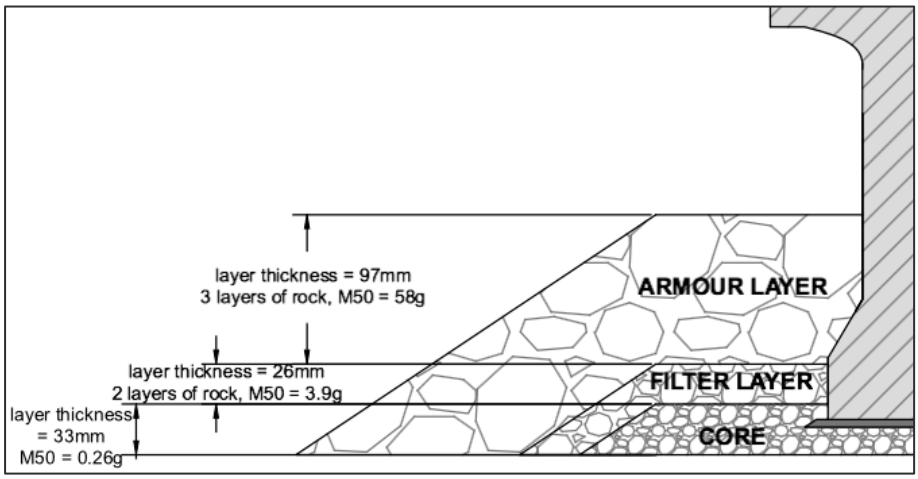

Figure 3-11: Structure B3 rubble-mound characteristics

3.4 Wave Characteristics and Bathymetry

3.4.1 Wave Period, Wave Height and Water Level

The tested wave period range included standard peak wave periods along the South African coastline, as well as extreme cases. The peak wave periods tested in the two-dimensional model were 6s, 8s, 10s, 12s, 14s, 16s and 18s. The significant wave height was kept constant at H_{m0} = 1.3m.

The water depth on the top of the rubble-mound structure (i.e. above the crest of the armour layer) was kept constant at 1m (0.05m in the model). The water depth directly seawards of the structure therefore changed as the thickness of the rubble-mound structure changed. It was assumed that the waves started breaking at the start of the rubble-mound structure slope. Waves break at approximately $d = 1.28\,x\,H = 1.664m$ (in prototype). The calculated water levels for testing are given in Appendix B.

3.4.2 Bathymetry

A slope of 1:50 was selected for the deep water, and a slope of 1:20 was chosen for the shallow water slope approaching the seawall structure. The slope furthest from the test section was constructed to ensure a smooth transition from the flat area to the steeper slope leading up to the structure. The slopes were chosen after investigating typical slopes along the South African coastline (Schoonees, 2014).

The length of the shallow water slope approaching the seawall should have a minimum distance equal to the longest wavelength to be tested to ensure the wave develop entirely. The longest prototype wavelength was calculated as 118m. Calculations for the wavelength are in Appendix B. Using Froude scaling; the minimum required shallow water slope length was 5.9m for the model. Hence, the length of the 1:20 slope was taken

as 6m. The length of the deepwater ramp was taken as 2.75m in the model. The layout of the bathymetry for the model is presented in the Figure 3-12.

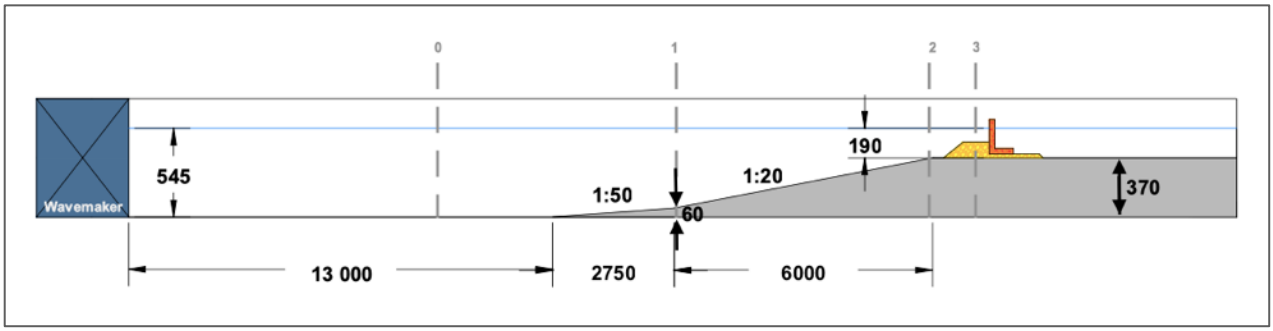

Figure 3-12: Bathymetry and water levels for Structure 1 in the model (mm)

3.5 Energy Distribution

3.5.1 General Approach

The interaction of the incident waves and a porous structure is a complex problem. The energy associated with a wave approaching a structure is divided among the reflection energy, transmission energy, internal energy dissipation and the external energy dissipation:

$$Total\ Energy = Reflection\ Energy + Transmission\ Energy + Internal\ Energy\ Dissipation + External\ Energy\ Dissipation$$

This study considered the energy dissipation (both external and internal). The external energy dissipation is the energy that is dissipated on the outer side of the structure. It was assumed that the external energy dissipation was only due to wave breaking and the bottom friction was taken as negligible due to it being small compared to the energy dissipation due to wave breaking. The method of (Battjes and Janssen, 1978) was used to determine the external energy dissipation due to wave breaking.

The flow through the porous structure causes internal energy dissipation. The internal energy dissipation can further be divided among the energy dissipation of the various layers:

$$\begin{aligned} Internal\ Energy\ Dissipation &= Energy\ Dissipation\ in\ the\ Armour\ Layer\ (ED_{Armour}) \\ &+ Energy\ Dissipation\ in\ the\ Filter\ Layer\ (ED_{Filter}) \\ &+ Energy\ Dissipation\ in\ the\ Core\ (ED_{Core}) \\ &+ Energy\ Dissipation\ in\ the\ Screed\ Layer\ (ED_{Screed}) \end{aligned}$$

The flow velocity for each layer was calculated to obtain the internal energy dissipation in the layers. The flow velocity was also used to calculate the kinetic energy in each layer. The kinetic energy in the core was identified to be of additional importance. The kinetic energy that reaches the core is potentially a good indication of the scour that will develop underneath the seawall. If the core cannot dissipate enough energy, it can lead to a remarkable amount of scouring of the screed layer and foundation.

3.5.2 Parameters Influencing Energy Distribution

3.5.2.1 Major Parameters Influencing Energy Distribution

Numerous parameters have an influence on the distribution and degree of energy within the layers of the rubble-mound structure. Only the major identified parameters were investigated in this study as a first approximation. The primary parameters are given in Table 3-6.

Table 3-6: Major parameters influencing energy dissipation in a rubble-mound structure

Parameter	Influencing factor	Variable or fixed
Material characteristics	Stone size and stone mass (affecting permeability)	Variable
Rubble-mound structure geometric design	Layer thickness and berm width	Layer thickness is a variable; berm width remains fixed
Incident wave characteristics	Surf similarity parameter (the parameter is influenced by wave period, wave height, water depth and slope)	Wave period and water depth is a variable; the other factors remain fixed

3.5.2.2 Minor Parameters Influencing Energy Distribution

Additional parameters whose influence were identified as less critical on the energy distribution in the rubble-mound structure include:

1. The slope angle of the core
2. Grading range
3. Particle shape (gross shape, roughness, surface texture, aspect ratio)
4. The orientation of the stones
5. Packing arrangement

3.5.3 Flow Velocity through Voids in Rock Layers

3.5.3.1 Procedure for Obtaining the Maximum Flow Velocity

The Water Laboratory does not have the necessary equipment to measure the flow velocity in the layers of the rubble-mound structure. Stellenbosch University does have a PIV system, but it was not available at the time of the conducted tests. Therefore, the flow velocity was determined from basic principles.

Pressure transmitters were used to measure the pressure at the top and bottom of each respective layer. The pressure recordings of the breaking waves were schematised to represent the most extreme velocities experienced between the rock voids. The outlay of the pressure transmitters in the seawall is illustrated in Figure 3-13. Table 3-7 indicates the colours representing the layers of each structure, as well as the respective pressure transmitters used to calculate the hydraulic gradient for each layer.

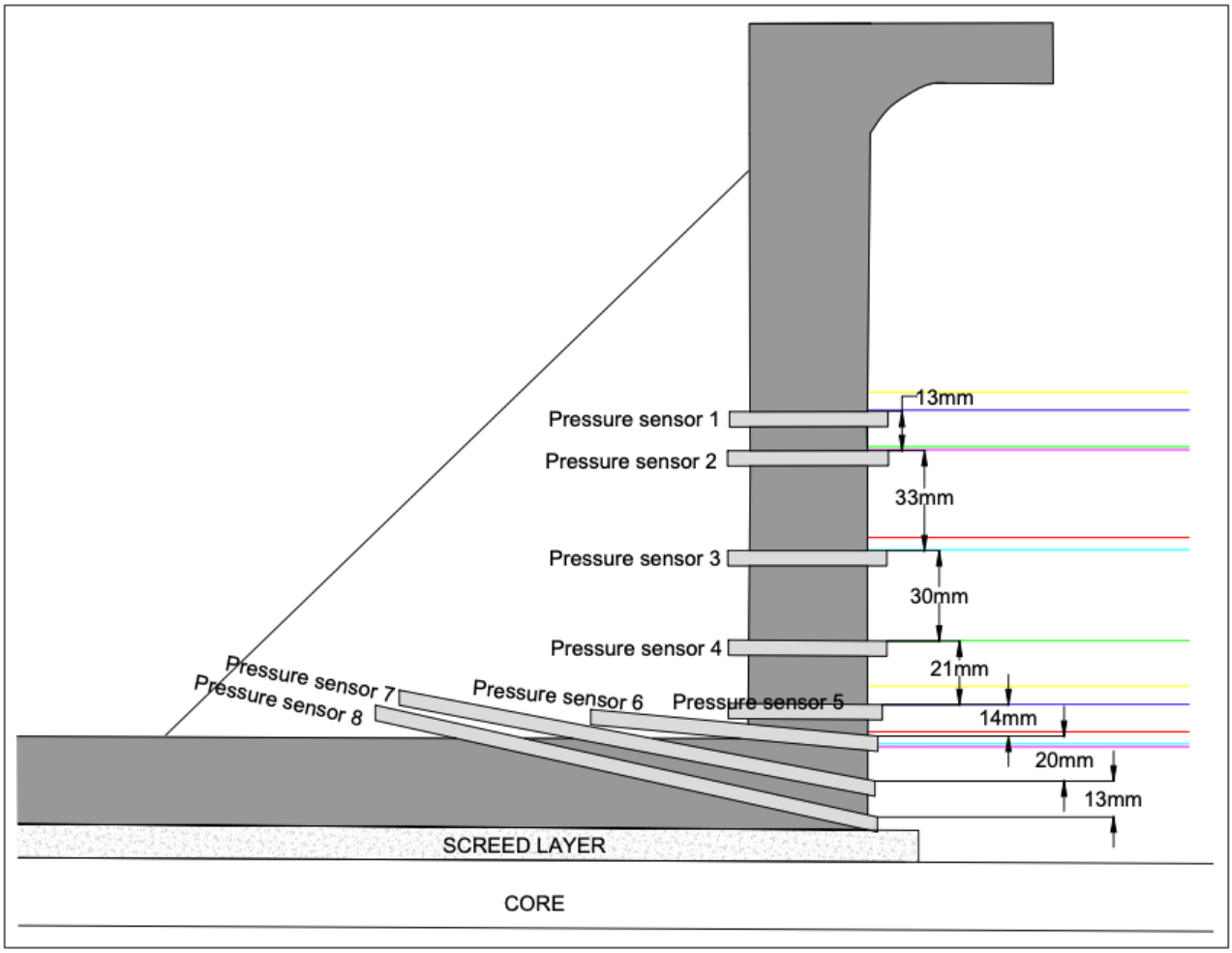

Figure 3-13: Layout of pressure sensors

Table 3-7: Pressure sensors used in each structure

Structure	Colour indicating rubble-mound structure layers in Figure 3-13	Pressure sensors
Structure A1	Red	8, 7, 6, 3
Structure A2	Yellow	8, 7, 5, 1
Structure A3	Green	8, 7, 4, 2
Structure B1	Light blue	8, 7, 6, 3
Structure B2	Dark blue	8, 7, 5, 1
Structure B3	Purple	8, 7, 6, 2

The pressure transmitters work in combination with a data logger box and convert the electric current readings to voltage. The specifications of the pressure transmitter and PicoLog data logger box are given in. Table 3-8.

Table 3-8: Pressure transmitter specifications

Pressure transmitter parameter	Minimum limit	Maximum limit
Pressure head (H)	-0.1m	+0.5m
Output current (I)	4mA	20mA
Resistance (R)	120Ω	120Ω

Using Ohm's law, the voltage was converted into the total pressure head. The total pressure head (H_{out}) is a combination of dynamic and kinetic pressure head.

$$H_{out} = \frac{H_{max} - H_{min}}{I_{max} - I_{min}} \frac{x}{R} - V_{atm} \qquad 3\text{-}1$$

Where

H_{out} = Measured dynamic pressure head (m)

H_{max} = Transmitter maximum pressure head limit (m)

H_{min} = Transmitter minimum pressure head limit (m)

x = Measured voltage reading (V)

I_{max} = Transmitter maximum current output (A)

I_{min} = Transmitter minimum current output (A)

R = Resistance of transmitter (Ω)

V_{atm} = Atmospheric hydrostatic pressure voltage reading (V)

The hydraulic gradient of each layer was calculated by dividing the difference between the dynamic pressure heads at the top and bottom of each layer by the layer thickness (Equation 2-19). The Forchheimer formula (Equation 2-15) was used to convert the hydraulic gradient into the flow velocity through the voids of the different layers in the rubble-mound structure. The two coefficients (A_{FOR} and B_{FOR}) in the Forchheimer equation are a function of the rock diameter, gravitational acceleration, kinematic viscosity and volumetric porosity. The volumetric porosity was calculated using Equation 3-2 (CIRIA, 2007).

$$n_v = \frac{e}{1+e} \qquad 3\text{-}2$$

Where

$e = \frac{1}{90}(e_o)\arctan(0.645 n_{RRD})$

$n_{RRD} = 3\, n_{RRM}$

e_o = 0.94 (coefficient of porosity for a rock with an elongated shape)

3.5.3.2 Maximum Flow Velocity

In the case of non-breaking waves, the pressure at the various locations in the seawall is nearly in phase with the wave elevation. In the case of breaking waves, there is a sudden surge in the pressure as the kinetic energy increases in the various layers. Tremendously high pressures are generated for a short duration. The high pressures are illustrated by Figure 3-13 for Test A2-10S. The spikes in the graph are for the instances when the wave breaks against the structure.

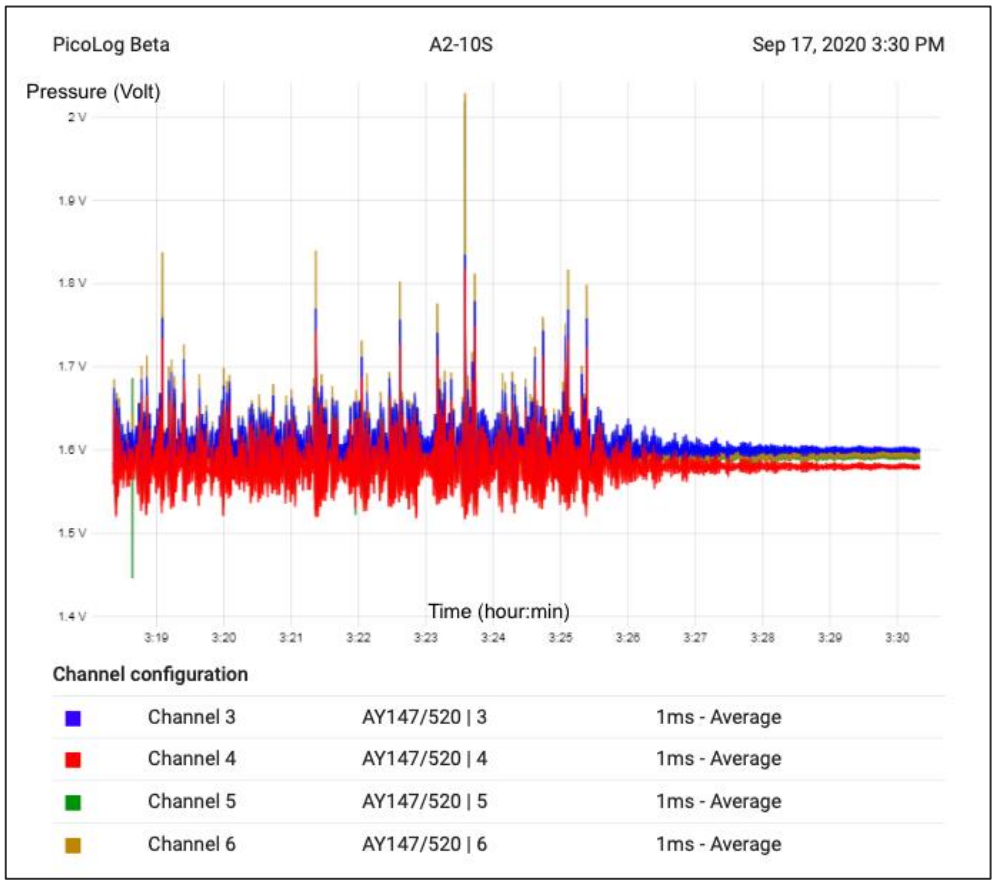

Figure 3-14: Pressure recording for Test A2-10S

The pressure recordings after 3:26 PM show a nearly straight line. The straight line is when there are no approaching waves, and the water level is almost still. These recordings only display the hydrostatic pressure due to the water depth. The pressure recordings shown before 3:26 pm are a function of the hydrostatic pressure component and the dynamic pressure component which are caused by the water particle acceleration.

The calculation of the velocity during the short period when the wave breaks was essential since more scour develop when the orbital velocity is at a maximum. Hence, it was the objective of this study to calculate the velocity when both the hydrostatic and dynamic pressure components were present and at a maximum.

3.5.4 KINETIC ENERGY DISTRIBUTION

The calculated flow was used to determine the kinetic energy in each layer using Equation 3-3 (Gregersen, 2020).

$$KE = \frac{\rho A u_v^2}{2} \qquad 3\text{-}3$$

Where

ρ = Density of water taken as 997kg/m^3

u_v = Velocity through voids in structure (m/s)

A = Unit area (m^2)

3.5.5 ENERGY DISSIPATION

3.5.5.1 External Energy Dissipation

The energy dissipation due to wave breaking was calculated using the Battjes and Janssen (1978) method. This method was developed for wave breaking on a beach profile. But as a first approximation, this method was applied in this study for wave breaking on a rubble-mound structure. When calculating the energy dissipation at the top of the rubble-mound structure, nearest to the seawall, the transmitted wave height was used. The incident wave approaching the rubble-mound structure will have a change in wave height as it makes its way into the structure.

The transmitted wave height was calculated for the forty-two experiments using the process as described by Van der Meer *et al*. (2004). The incident wave characteristics were identified; the incident wave height remained constant at H_i =1.3m, and the wave period ranged between 6s and 18s.

The $\frac{B_c}{H_i}$ *-ratio* was calculated to determine the formula to use for calculating the transmission coefficient. The rubble-mound structure width ($B_c = 4\ D_{n50}$) was a fixed variable in this two-dimensional model. The $\frac{B_c}{H_i}$ *-ratio* was calculated as smaller than 10. Thus, Equation 2-5 was used to calculate the transmission coefficient. The transmitted wave height was calculated using Equation 3-4.

$$H_t = H_i \text{ x } K_t \qquad 3\text{-}4$$

Once the transmitted wave height was obtained, the method of (Battjes and Janssen, 1978) was used to calculate the energy dissipation due to wave breaking. The first step was to determine the maximum wave height. The Raleigh distribution was then used to determine the ratio of broken waves to the total number of waves. Once all the parameters were calculated, the energy dissipation due to wave breaking was calculated for each test.

3.5.5.2 Internal Energy Dissipation

The energy dissipation within the layers of the rubble-mound structure was calculated using Equation 3-5. The energy dissipation is a function of the flow velocity obtained using the Forchheimer equation and the hydraulic gradient (I) (Jensen and Klinting, 1983).

$$W = \rho g I u_v \qquad 3\text{-}5$$

The flow inside the rubble-mound structure is unsteady, continuously changing direction and velocity. Even though the velocity inside the rubble-mound is constantly changing sinusoidally, it was not taken into account in the calculation of the internal energy dissipation. The reasoning was that this study merely represented a first approximation to the distribution of the internal energy dissipation.

3.5.6 Kinetic Energy in the Structure Prediction through Dimensional Analysis

Dimensional analysis was applied to determine the relationship of the kinetic energy in the structure to that of the main identified parameters (Table 3-6) affecting the energy distribution in the rubble-mound structure. The process combines the physical variables into dimensionless products. The aim was to reduce the number of variables that influence the kinetic energy to be considered in the two-dimensional model (Chadwick, Morfett & Borthwick, 2013)

The assumption is made that there is a dependent variable, independent variables and redundant variables. Based on the model and the relevant variables, the kinetic energy in the structure is a function of the wave period (T), median rock mass in the core ($m_{50,core}$), the layer thickness of the structure (t) and the water depth can be converted into the wavelength (L):

$$KE = f[T, m_{50,core}, t, L]$$

The procedure for obtaining a dimensionless product included writing the function in the form of a power product:

$$KE = K[T^a \,.{m_{50,core}}^b \,.\, t^c \,.\, L^d]$$

Each quantity was then reduced to its basic dimensions:

$$KE = ML^2T^{-2}$$

$$T = T$$
$$m_{50,core} = M$$
$$t = L$$
$$L = L$$

And then tabulated as a matrix:

$$\begin{array}{c} \\ M \\ L \\ T \end{array} \begin{array}{c} \begin{array}{ccccc} KE & T & m & t & L \end{array} \\ \begin{bmatrix} 1 & 0 & 1 & 0 & 0 \\ 2 & 0 & 0 & 1 & 1 \\ -2 & 1 & 0 & 0 & 0 \end{bmatrix} \end{array}$$

The velocity equation was rewritten in terms of the basic dimensions:

$$ML^2T^{-2} = K[T^a \,.M^b \,.L^c \,.L^d]$$

The function has the dimensions ML^2T^{-2} for dimensional similarity. Since a product relationship exists, the sum of the indices of each dimension on the right-hand side of the equation is equal to the index of the same dimension on the left-hand side of the equation. This resulted in the following equations:

$$Mass: 1 = b$$
$$Length: 2 = c + d$$
$$Time: -2 = a$$

There are three equations with four unknowns. Thus, a complete answer is unachievable. A partial solution is still produced by rewriting each of the three equations above in terms of *c*. Substituting the equations (all in terms of *c*) into the original equation leads to:

$$KE = K\left[T^{-2} \,.{m_{50,core}}^1 \,.\, t^c \,.\, L^{2-c}\right]$$
$$KE = K[\left(\frac{L}{T}\right)^2 \left(\frac{t}{L}\right)^c \, m_{50,core}]$$

There are two unknowns in the equation above: *K* and *c*. Since the equation is a product, it can be rewritten as:

$$\frac{KE}{m_{50,core}}(\frac{T}{L})^2 = K\left(\frac{t}{L}\right)^c$$

Two products have emerged from the process. Both dimensionless groups are independent on unit and scale; this entails the groups being equally applicable to the prototype as they are to the model. The two products are given as:

$$\Pi_1 = \frac{KE}{m_{50,core}} (\frac{T}{L})^2$$

$$\Pi_2 = \left(\frac{t}{L}\right)^c$$

The dependent variable is recognised as Π_1, and Π_2 is identified as the independent variable of the model. The measured values and known parameters of this two-dimensional model will be used to plot a graph, with the x-axis being the independent product and the y-axis the dependent product. The kinetic energy can be determined for structures adhering to the geometric design, material characteristics and wave characteristics as tested in this two-dimensional model. The independent product is calculated first. The corresponding dependent product can be read from the graph once the independent product is known. The known parameters are substituted into the dependent product, and the only remaining unknown variable – the kinetic energy – is obtained.

3.6 Scour Data Acquisition

Two methods were considered to determine the horizontal extent of scouring of the screed layer once the seawall concrete element had been lifted off the screed layer. The distance and areas are measured horizontally landward from the seaward edge of the original undisturbed screed layer (Figure 3-15). The first method uses a Handheld 3D Scanning Tablet. The second method makes use of the *Image Processing Toolbox* in MATLAB. Both these methods and their accuracies are discussed in the following sub-sections.

3.6.1 Handheld 3D Scanning Tablet

The 3D Handheld DPI-10 Scanning Tablet is powered by Dot3D Pro Software and is used by mobile specialists who want to capture 3D spatial data. Data can be captured and viewed on the tablet. Thus, the results of the experiments are immediately obtainable in the laboratory. Once it is determined that the quality of the captured data is satisfying, the data can further be processed in more detail on an additional software program.

A scoured screed layer was set-up with known scour depths to determine the accuracy. Scour depth measurements (measuring the horizontal distance landward from the seaward edge of the undisturbed screed layer) were taken every 5cm across the flume with the scanning tablet. This test was repeated three times.

The data was then imported into AutoCAD to determine the distances as measured with the scanning tablet. The test results are given in Appendix I. Table 3-9 shows the accuracy of the three tests over a range of distances.

Table 3-9: Accuracy results of Handheld 3D Scanning Tablet

Range of the scour depth measurements	Accuracy (%)
< 10mm	56
10mm to 15mm	77
15mm to 25mm	74
25mm to 35mm	90
35mm to 45mm	96

From the results of (Van Wageningen, 2018), the majority of scour depths were expected to be smaller than 25mm. The accuracy of the scour depth measurements shorter than 25mm is low with the 3D scanner and therefore ruled out as an option to use in this two-dimensional model to measure the screed scour.

3.6.2 MATLAB IMAGE PROCESSING

A new method was developed by the author to determine the scoured area (in the horizontal plane) of the screed layer, which has proven to be very accurate. The process consisted of taking a photo of the screed layer after the experiment and measuring the area identified as scour. The rubble-mound structure was deconstructed partially first; then, a gantry crane was used to lift the seawall from the remaining part of the core. A gantry crane was used to avoid human error and to ensure that the wall was lifted carefully without disturbing the screed layer. After the seawall was removed, a photo was taken of the scoured screed layer.

Figure 3-15 illustrates the top view of the screed layer before and after the experiment. In the upper drawing in Figure 3-15, the screed layer is undisturbed as the experiment has not commenced. The lower drawing indicates the scour pattern after 2000 waves. The area measured as scour (m^2) is illustrated by grey diagonal stripes. The scour depth (m) is evident in Figure 3-15 and denoted as SD. The same scour depth measured in Figure 3-15 is illustrated in Figure 3-16. Figure 3-16 shows the horizontal scour depth measurement relative to the cross-section of the vertical seawall.

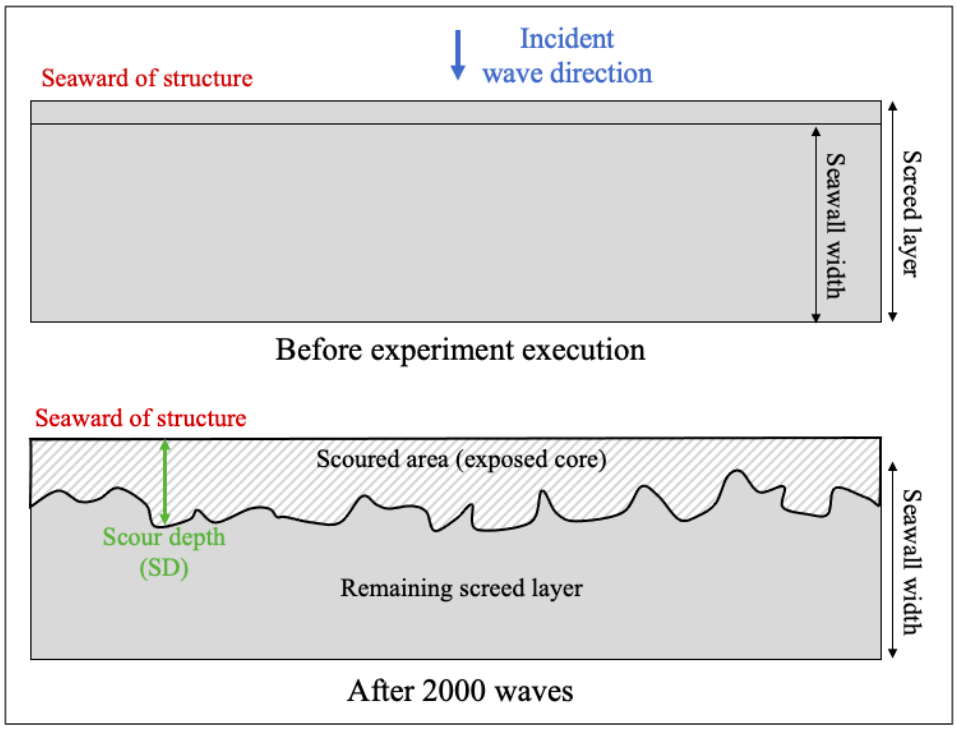

Figure 3-15: Top View sketch of the screed layer before and after the experiment

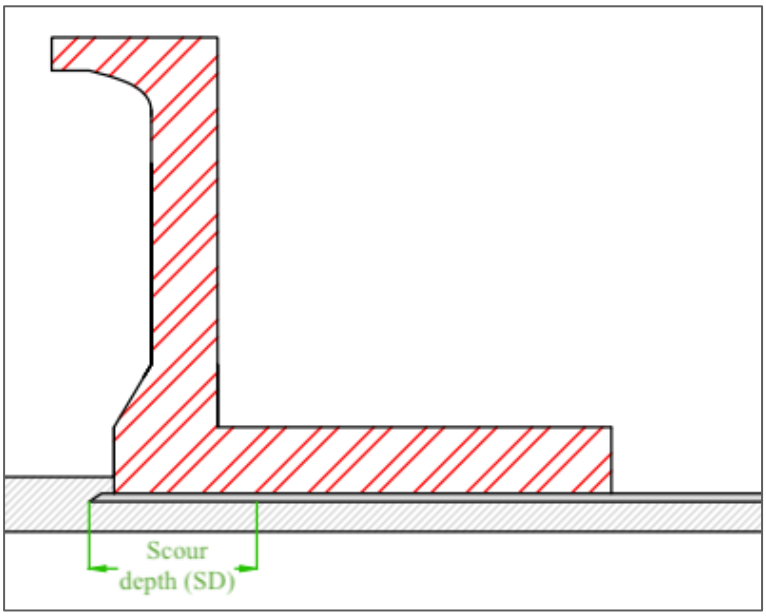

Figure 3-16: Cross-section of seawall indicating horizontal scour depth (SD)

MATLAB code was written to calculate the area of the scour that develops underneath the vertical seawall. The *Image Processing Toolbox* was implemented that enabled the program to construct a grayscale for the image under consideration. The foreground (the remaining filter sand of the screed layer) and background (the respective core material) were divided by a threshold value, chosen individually for each inserted figure. The threshold value represents the dividing line between the foreground and background.

An original image was imported into MATLAB and calibrated with a known dimension of the model. MATLAB produced a histogram indicating two peaks. The threshold value was taken as the value between the two peaks. In the case of the histogram in Figure 3-17, the threshold value was chosen as 87.

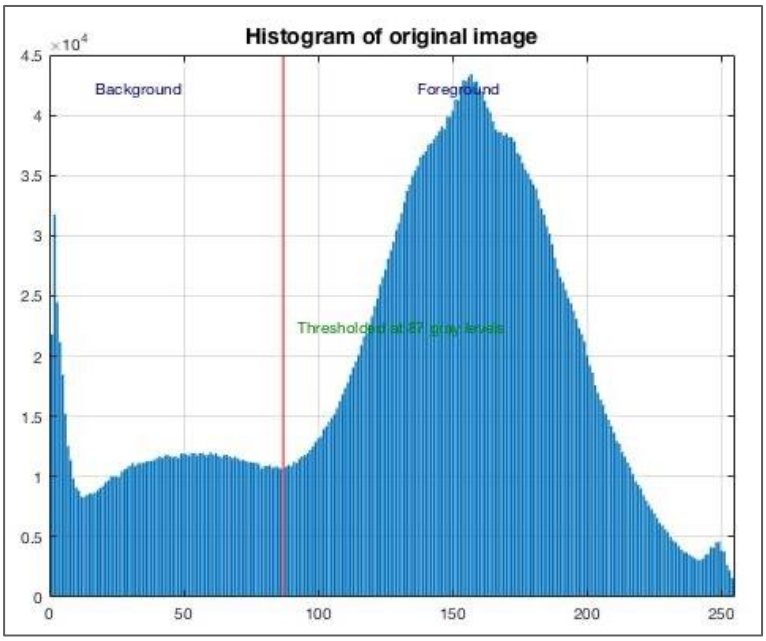

Figure 3-17: Histogram to determine the threshold value for MATLAB

Figure 3-18 shows the original image imported into MATLAB. From the original image, a binary image was created, dependent on the chosen threshold value. Figure 3-19 shows the fabricated binary image. This image contrasts the foreground and background. Figure 3-20 indicates every area MATLAB identified as scour and highlights individual scoured areas with green. Each separate area was calculated and summed to give the total scour for a specific test.

Figure 3-18: Original image of scour imported into MATLAB

Figure 3-19: Binary image produced by MATLAB

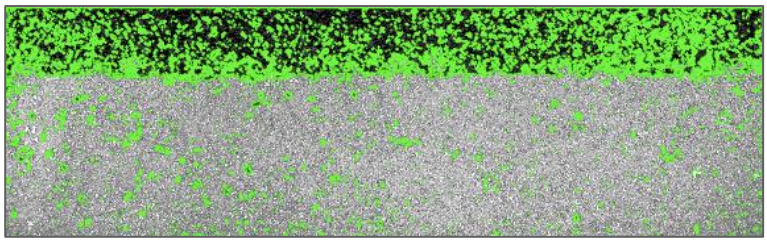

Figure 3-20: Areas identified as scour

The MATLAB program has proven to be outstandingly accurate. The image of a 0.3cm x 0.3cm black square was imported into the program and MATLAB gave the result as 0.09014cm^2; this is a 99.8% accuracy. The process to determine the accuracy by using the black square is given in Appendix J.

3.7 Model Comparison with Malan (2016) and Van Wageningen (2018)

Two separate studies performed by Malan (2016) and Van Wageningen (2018) at Stellenbosch University concerning granular scour development underneath a vertical seawall are briefly discussed in this section.

3.7.1 Discussion of the Studies

3.7.1.1 Malan Study Conducted in 2016

The study conducted in 2016 had the main objective to review existing design methods for scour protection at the foundation of a vertical seawall. Emphasis was placed on the design and construction of the screed layer directly underneath the seawall. The layout of the structure modelled is illustrated in Figure 3-21.

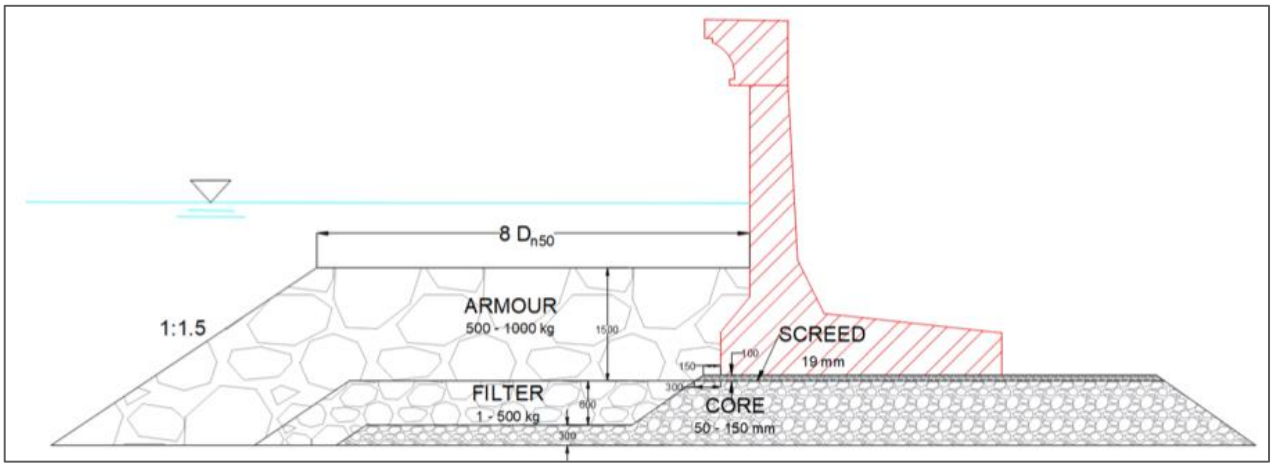

Figure 3-21: Modelled seawall by (Malan, 2016)

The conclusions drawn from the study were:

- A thick screed layer will experience more damage caused by scour. There is, however, a minimum and maximum requirement for the screed layer thickness. The minimum layer thickness requirement states that the layer should be at least 2 to 3 times the diameter of the largest stones used in the stone distribution. The maximum layer thickness requirement says that the layer thickness should be less than five times the diameter of the largest stones used in the stone distribution
- The width of the toe in front of the seawall should be as narrow as possible while still adhering to the required filter rules
- During construction, it should be refrained from compacting the screed layer
- No sediment should be added to the screed layer

3.7.1.2 Van Wageningen Study Conducted in 2018

The influence of the berm width, wave period and screed layer thickness were considered with the objective to gain knowledge of the scouring process. The layout of the modelled structure is illustrated in Figure 3-22.

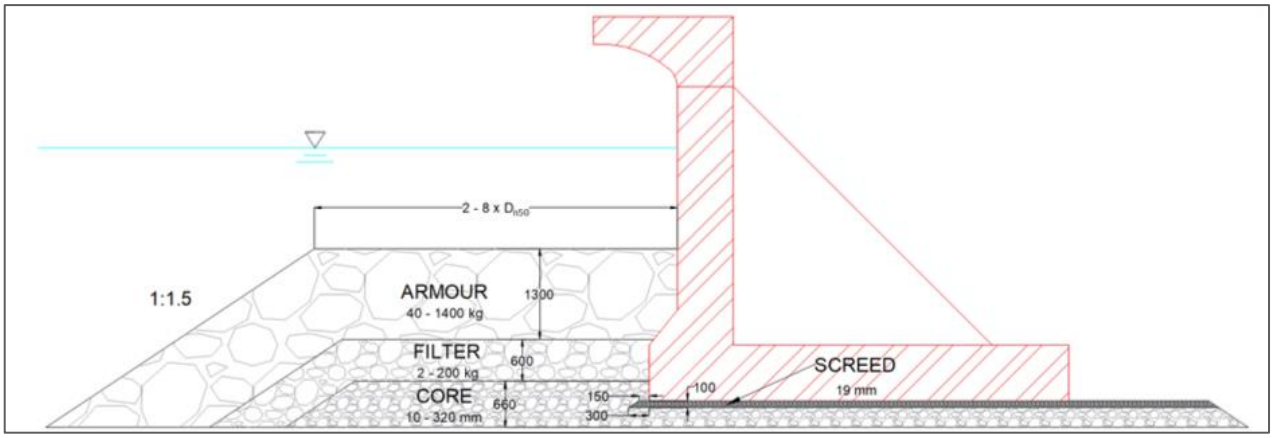

Figure 3-22: Modelled seawall by (Van Wageningen, 2018)

The conclusions drawn from the study were:

- Shorter wave periods cause a deeper scour depth than the longer wave periods
- The wider the berm of the rubble-mound structure, the smaller the scour depth would be due to wave attack. A $4D_{n50}$ berm width is recommended due to various criteria
- A thicker screed layer resulted in more scour. The screed layer thickness for the prototype is recommended to be 200mm. This thickness is adequate to level out any irregularities of the bedding and make allowance for construction tolerances

3.7.2 MAIN SET-UP DIFFERENCES

Table 3-10 is a summary of the main differences between the set-ups of the three conducted studies.

Table 3-10: Model set-up comparison between three studies

	(Malan, 2016)	(Van Wageningen, 2018)	Current Thesis
Wave Height	Range of wave heights: 1.364m – 2.031m	One wave height: 1.3m	One wave height: 1.3m
Peak Wave Period	One peak wave period, an average of 8s	Four peak different wave periods: 8s, 10s, 12s, 14s	Seven different peak wave periods: 6s, 8s, 10s, 12s, 14s, 16s, 18s
Bathymetry	Deepwater slope 1:55 Shallow water slope 1:20	Deepwater slope 1:50 Shallow water slope 1:18.6	Deepwater slope 1:50 Shallow water slope 1:20
Seawall Position	Seawall position remained fixed with regards to bathymetry	Seawall position remained set with regards to bathymetry	Seawall position remained fixed with regards to bathymetry
Berm Width	One berm width: ($8D_{n50}$)	Five berm widths: $2D_{n50}$, $3D_{n50}$, $4D_{n50}$, $6D_{n50}$, $8D_{n50}$	One berm width: $4D_{n50}$
Rock Grading	Coarse rock grading	Light rock grading	Light rock grading
Filter Rule	Filter rule: $\frac{M_{50\ lower}}{M_{50\ upper}} = \frac{1}{10}$	Filter rule: $\frac{M_{50\ lower}}{M_{50\ upper}} = \frac{1}{10}$	Filter rules: $\frac{M_{50\ lower}}{M_{50\ upper}} = \frac{1}{15}$, $\frac{M_{50\ lower}}{M_{50\ upper}} = \frac{1}{10}$
Layer Thickness	Two layers of rock per layer	Two layers of rock per layer	Layers of rock vary (between two to four rocks per layer)
Addition of Sediment to Screed Layer	Tested a sand mixture, clay mixture and no added sediment mixture	No added sediment	No added sediment
Screed Layer Thickness	One screed thickness: 100mm	Three screed thicknesses: 100mm, 200mm and 300mm	One screed thickness: 100mm
Screed Toe Layout	Screed layer exposed as well as core covering screed layer	Core covers screed layer	Core covers screed layer
Construction Methods	Different degrees of compaction of foundation	Constant degree of compaction	Constant degree of compaction
Scour Measurements	Dowel measurements	Dowel and sonar measurements	MATLAB image processing

3.8 TEST PLAN

Test Series A examined three structures with rock sizes applying the filter rule $\frac{M_{50\ lower}}{M_{50\ upper}} = \frac{1}{10}$, whereas Test Series B examined three structures with rock sizes using the filter rule $\frac{M_{50\ lower}}{M_{50\ upper}} = \frac{1}{15}$. Test Set C was for verification tests. Two thousand waves were generated per test; this is the number of waves it takes for the scour to reach equilibrium (Van Wageningen, 2018). The Test Plan is given in Table 3-11. The number of rocks in the armour layer is denoted by n_A, and the number of rocks in the filter layer by n_F.

Table 3-11: Test plan

Test nu.	Test Code	Duration (no. waves)	Input wave period (s)	Input wave height (m)	Filter rule between layers	Layer thickness (no. rocks per layer)	Total berm thickness (mm)
1	A1 – 6S	2000	6	1,3	Factor = 1/10	$n_A = 2$, $n_F = 2$	2546
2	A1 – 8S	2000	8	1,3	Factor = 1/10	$n_A = 2$, $n_F = 2$	2546
3	A1 – 10S	2000	10	1,3	Factor = 1/10	$n_A = 2$, $n_F = 2$	2546
4	A1 -12S	2000	12	1,3	Factor = 1/10	$n_A = 2$, $n_F = 2$	2546
5	A1 – 14S	2000	14	1,3	Factor = 1/10	$n_A = 2$, $n_F = 2$	2546
6	A1 – 16S	2000	16	1,3	Factor = 1/10	$n_A = 2$, $n_F = 2$	2546
7	A1 – 18S	2000	18	1,3	Factor = 1/10	$n_A = 2$, $n_F = 2$	2546
8	A2 – 6S	2000	6	1,3	Factor = 1/10	$n_A = 3$, $n_F = 3$	3489
9	A2 – 8S	2000	8	1,3	Factor = 1/10	$n_A = 3$, $n_F = 3$	3489
10	A2 – 10S	2000	10	1,3	Factor = 1/10	$n_A = 3$, $n_F = 3$	3489
11	A2 – 12S	2000	12	1,3	Factor = 1/10	$n_A = 3$, $n_F = 3$	3489
12	A2 – 14S	2000	14	1,3	Factor = 1/10	$n_A = 3$, $n_F = 3$	3489
13	A2 – 16S	2000	16	1,3	Factor = 1/10	$n_A = 3$, $n_F = 3$	3489
14	A2 – 18S	2000	18	1,3	Factor = 1/10	$n_A = 3$, $n_F = 3$	3489
15	A3 – 6S	2000	6	1,3	Factor = 1/10	$n_A = 2$, $n_F = 4$	3144
16	A3 – 8S	2000	8	1,3	Factor = 1/10	$n_A = 2$, $n_F = 4$	3144
17	A3 – 10S	2000	10	1,3	Factor = 1/10	$n_A = 2$, $n_F = 4$	3144
18	A3 – 12S	2000	12	1,3	Factor = 1/10	$n_A = 2$, $n_F = 4$	3144
19	A3 – 14S	2000	14	1,3	Factor = 1/10	$n_A = 2$, $n_F = 4$	3144
20	A3 – 16S	2000	16	1,3	Factor = 1/10	$n_A = 2$, $n_F = 4$	3144
21	A3 – 18S	2000	18	1,3	Factor = 1/10	$n_A = 2$, $n_F = 4$	3144
22	B1 – 6S	2000	6	1,3	Factor = 1/15	$n_A = 2$, $n_F = 2$	2470
23	B1 – 8S	2000	8	1,3	Factor = 1/15	$n_A = 2$, $n_F = 2$	2470
24	B1 – 10S	2000	10	1,3	Factor = 1/15	$n_A = 2$, $n_F = 2$	2470
25	B1 – 12S	2000	12	1,3	Factor = 1/15	$n_A = 2$, $n_F = 2$	2470
26	B1 – 14S	2000	14	1,3	Factor = 1/15	$n_A = 2$, $n_F = 2$	2470
27	B1 – 16S	2000	16	1,3	Factor = 1/15	$n_A = 2$, $n_F = 2$	2470
28	B1 – 18S	2000	18	1,3	Factor = 1/15	$n_A = 2$, $n_F = 2$	2470
29	B2 – 6S	2000	6	1,3	Factor = 1/15	$n_A = 3$, $n_F = 3$	3375
30	B2 – 8S	2000	8	1,3	Factor = 1/15	$n_A = 3$, $n_F = 3$	3375

Table 3-11: Test Plan continued

Test nu.	Test Code	Duration (no. waves)	Input wave period (s)	Input wave height (m)	Filter rule between layers	Layer thickness (no. rocks per layer)	Total berm thickness (mm)
31	B2 - 10S	2000	10	1,3	Factor = 1/15	$n_A = 3$, $n_F = 3$	3375
32	B2 - 12S	2000	12	1,3	Factor = 1/15	$n_A = 3$, $n_F = 3$	3375
33	B2 - 14S	2000	14	1,3	Factor = 1/15	$n_A = 3$, $n_F = 3$	3375
34	B2 - 16S	2000	16	1,3	Factor = 1/15	$n_A = 3$, $n_F = 3$	3375
35	B2 - 18S	2000	18	1,3	Factor = 1/15	$n_A = 3$, $n_F = 3$	3375
36	B3 - 6S	2000	6	1,3	Factor = 1/15	$n_A = 3$, $n_F = 2$	3114
37	B3 - 8S	2000	8	1,3	Factor = 1/15	$n_A = 3$, $n_F = 2$	3114
38	B3 - 10S	2000	10	1,3	Factor = 1/15	$n_A = 3$, $n_F = 2$	3114
39	B3 - 12S	2000	12	1,3	Factor = 1/15	$n_A = 3$, $n_F = 2$	3114
40	B3 - 14S	2000	14	1,3	Factor = 1/15	$n_A = 3$, $n_F = 2$	3114
41	B3 - 16S	2000	16	1,3	Factor = 1/15	$n_A = 3$, $n_F = 2$	3114
42	B3 -18S	2000	18	1,3	Factor = 1/15	$n_A = 3$, $n_F = 2$	3114
43	C1-TBC	2000	TBC (wave period with most scour)	1,3	Factor = 1/10	$n_A = 2$, $n_F = 2$	2546
44	C1-TBC	2000	TBC (wave period with most scour)	1,3	Factor = 1/15	$n_A = 2$, $n_F = 2$	2470
45	C2-10S-1	2000	10	1,3	Chosen rock size	$n_A = 2$, $n_F = 2$	TBC (Depends on chosen rock size)
46	C2-10S-2	2000	10	1,3	Chosen rock size	$n_A = 3$, $n_F = 3$	TBC (Depends on chosen rock size)
47	C2-10S-3	2000	10	1,3	Chosen rock size	TBC (Depends on chosen rock size)	TBC (Depends on chosen rock size)

Test Set C1 in Table 3-11 covered the verification tests for the two experiments with the largest scour areas. Test Set C2 covered the verification tests for each structure adhering to the recommended median mass filter rule.

4 VISUAL INSPECTION

4.1 WAVE BREAKING

The bathymetry was designed to cause spilling or plunging type waves in the absence of a structure. It was expected that once the structure was placed in position, the waves would not break on the rubble-mound structure, but breaking would only occur on the front face of the vertical seawall. As was observed by Van Wageningen (2018), it was also observed in the tests for this thesis, that the reflected and incident waves superimposed to create larger waves causing the waves not to break on the rubble-mound structure but on the seawall itself. It was this direct wave impact on the seawall during breaking against the structure which was responsible for scouring. The vertical face of the seawall directed the water downward in the form of a jet. The turbulent flow of water mobilized and transported the sediment.

4.2 OVERTOPPING

The overtopping discharge is a function of the variable parameters: wave period associated with the spectral peak in deep water, water depth in front of the structure and structure geometry. The conducted tests with larger wave periods experienced heavier overtopping than the tests with the smaller wave periods. Larger wave periods have larger wavelengths, resulting in more water being carried by the wave, causing more overtopping. The wave celerity also increases with a larger wave period, which consequently leads to an increase in the momentum of the wave. From Figure 4-1 taken during Test B2-16S, it is evident how the wave momentum had built up, resulting in water being reflected seawards as well as water overtopping.

Figure 4-1: Overtopping in Test B2-16S

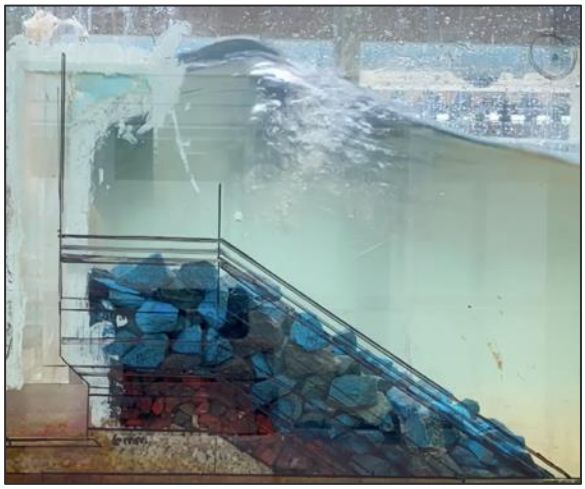

Figure 4-2: Collision between the incident and reflected wave in Test B2-6S

The smaller period waves had a more frequent reflection, where the incident and reflected waves collided, causing splashing at the collision. The splashing seldom overtopped the seawall but was instead reflected seaward. Splashing isn't observed as often at the longer wave periods due to the crash between reflected and incident waves not occurring as frequently. Figure 4-2 is from Test B2-6S. In this figure, the incident and reflected waves collided in front of the structure.

The second variable is the water depth in front of the structure. An increase in water depth seawards of the structure resulted in more overtopping of water over the seawall. The overtopping was due to the waves breaking closer to the crest of the seawall, resulting in less water being reflected by the seawall recurve. The effect of the third variable, i.e. structure geometry, could not be seen as clearly in the overtopping.

4.3 Water Level above Berm

The shorter wave periods caused waves to approach the structure more regularly and were reflected in shorter intervals than the larger wave periods. The short reflection intervals caused a rapid change in the wave direction and celerity due to the incident waves colliding with the reflected waves. This rapid change caused a faster and smaller drawback of the water level at the berm. Figure 4-3 and Figure 4-4 show the drawback of the wave to be smaller and the water level above the berm remaining higher in Test A1-6S.

The larger wave periods created more time for the wave to drawback, and thus the build-up of the water had more time to evolve, resulting in a shallower water level above the rubble-mound structure. Figure 4-5 shows the exposed berm of Test A1-14S due to a longer drawback resulting in a larger build-up causing more momentum. The wave breaking against the structure for that same test can be seen in Figure 4-6.

Figure 4-3: Wave drawback in Test A1-6S

Figure 4-4: Wave breaking against the seawall in Test A1-6S

Figure 4-5: Wave drawback in Test A1-14S

Figure 4-6: Wave breaking against the seawall in Test A1-14S

4.4 Rubble-Mound Structure Deformation

It was observed that for the smaller wave periods, the deformation of the rubble-mound structure was minimal. At the larger wave periods, the berm was distorted significantly resulting in hydraulic instability. The larger degree of deformation was due to the waves moving with more momentum and a larger celerity in the larger wave periods, consequently being more destructive.

The rubble-mound structures with a smaller layer thickness also experienced more deformation than the rubble-mound structures that had thicker layers and so were higher (with less freeboard). The deformation is due to the armour layer in the thicker rubble-mound structures providing more protection for the underlying layers than in the case of the smaller rubble-mound structures, resulting in more stable underlayers.

The most extreme cases of deformation were for the instances when the smaller rubble-mound structures experienced the larger wave period tests. In these tests, the scour was so large that the filter layer rocks were able to move to underneath the seawall replacing the rocks in the screed layer. The rocks in the core also repositioned themselves underneath the seawall. The armour layer crest flattened, and the upper rocks of the structure progressed towards the toe, resulting in the toe extending further away from the seawall.

Figure 4-7 shows the rubble-mound structure before the start of Test B3-18S, and Figure 4-8 shows the same rubble-mound structure after 2000 waves. In Figure 4-8, the filter layer rocks (the red rocks) can be seen underneath the seawall, and the armour layer rocks (the blue rocks) became flattened at the crest and extended the toe of the structure.

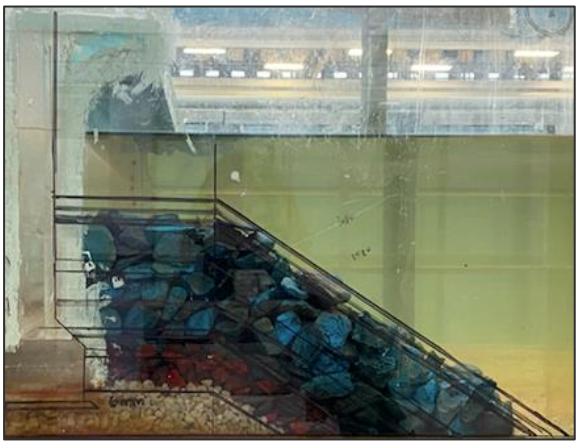

Figure 4-7: Test B3-18S before deformation of the rubble-mound structure

Figure 4-8: Test B3-18S after deformation of the rubble-mound structure

The failure mode associated with the deformation was identified as the rotation of individual units and the subsequent down-slope displacement of the units during wave breaking. The cycle of a unit is illustrated in Figure 4-9. Consequently, the units above the rotating unit slid down the slope to fill the opening.

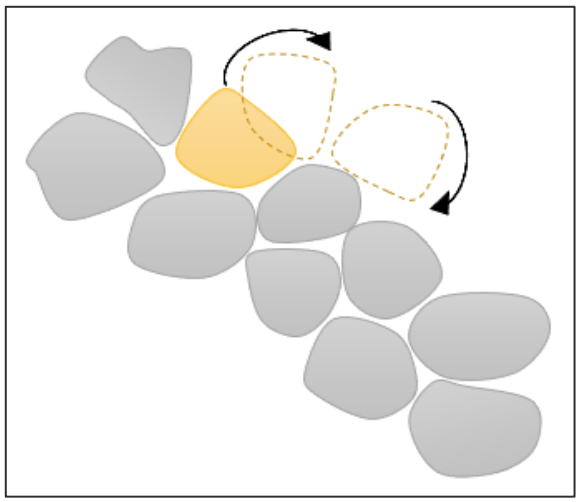

Figure 4-9: Downslope displacement of an individual unit

Figure 4-10 and Figure 4-11 are the before and after images for Test B3-6S. It is noted that there was no significant change in the structure after the 2000 waves for this short peak wave period.

Figure 4-10: Test B3-6S before deformation of the rubble-mound structure

Figure 4-11: Test B3-6S after deformation of the rubble-mound structure

4.5 Flow In and Around the Rubble-Mound Structure

A purple dye was placed in the core of the rubble-mound structure to determine the flow pattern. It was observed that with non-breaking waves, oscillatory flow in the structure was more dominant than when the waves were breaking against the seawall. When the waves were breaking against the seawall, the water moved upward through the structure in an irregular pattern. Table 4-1 shows a time sequence of the purple dye moving through the structure for a wave period of 12s.

Table 4-1: Time-sequence of purple dye moving through rubble-mound

t=0s

t=1s

t=2s

t=3s

t=4s

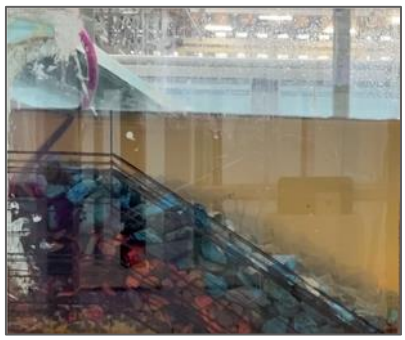

t=5s

Table 4-1: Time-sequence of purple dye moving through rubble-mound continued

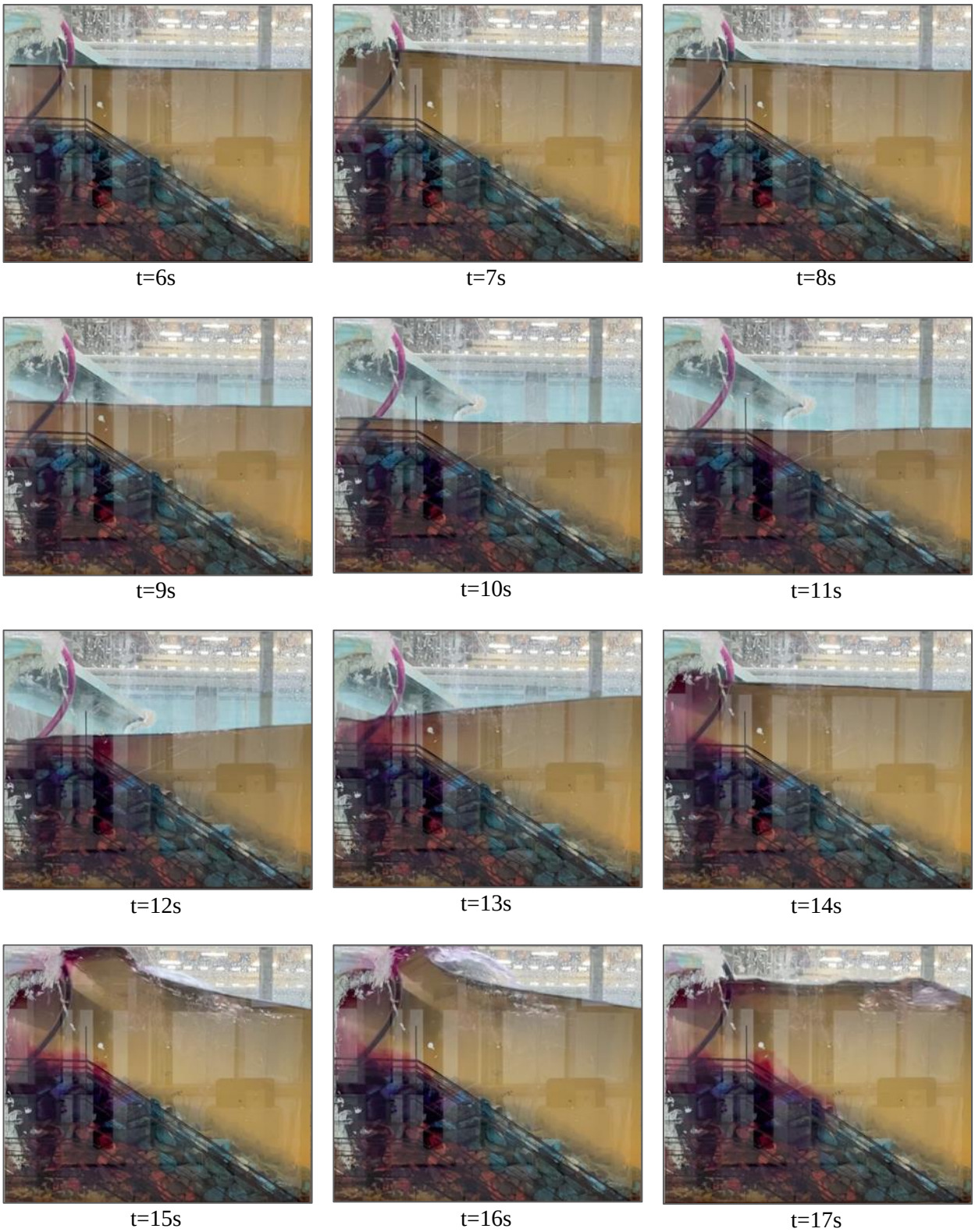

Table 4-1: Time-sequence of purple dye moving through rubble-mound continued


t=18s


t=19s


t=20s

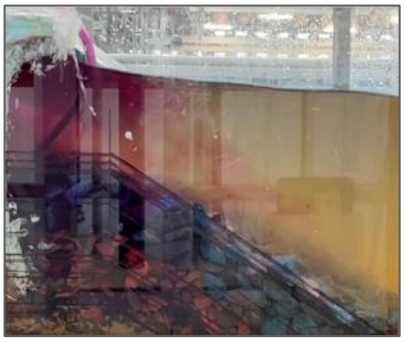
t=21s

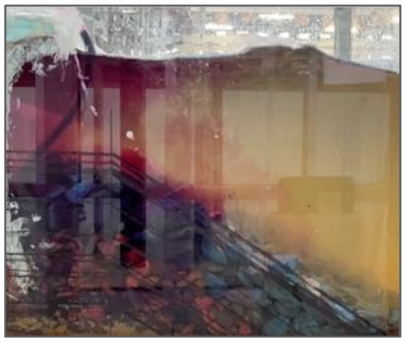
t=22s

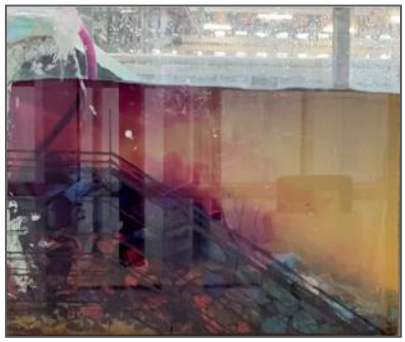
t=23s

From the time sequence above it was observed that the dye did not return to its original position as time passed as would be the case with the oscillatory flow, but rather moved through the structure to different locations (compare t=0s with t=23s). The movement of the dye in the vertical direction was more dominant than the action in the horizontal direction in the case of non-breaking waves. Once a wave broke against the structure, the dye was transported significantly in the horizontal direction by the reflected wave (see t=18s).

Before the approaching wave broke against the seawall, there was no dye above the rubble-mound structure (t=11s). When the water started pulling back, right before the wave breaking (t=12s), the dye pulled the structure along with the momentum of the water. The thrust of the reflected wave through the recurve, almost "pulled" the dye in the rubble-mound upward through the structure. As the wave was reflected by the recurve, the dye was reflected with it (t=15s). This process repeated itself until the dye was no longer in the rubble-mound but around the rubble-mound. And over a more extended period, the dye was no longer visible as it dissipated into the water in the wave flume.

The impermeable seawall limited the oscillatory flow in the structure. The solid structure blocked the dye from moving backwards and forwards in oscillatory motion. Instead, the dye was directed upward out of the structure as waves broke against the seawall and were reflected. The dye then oscillated in front and above the structure when the incident waves were non-breaking, but as soon as the next wave broke, the dye moved further seaward.

With closer inspection at individual rocks, it seemed that the orbital motion of the water particles was small compared to the diameter of an individual rock. The Keulegan-Carpenter number describes this phenomenon. In the situation explained, a small Keulegan-Carpenter number can be expected. The Keulegan-Carpenter number describes the relative importance of the drag forces over the inertia forces. Small KC-numbers indicate that inertia dominates, and larger KC-numbers indicate drag forces dominate. The flow did not initiate separation and did not develop vortices, as the wave height and orbital diameter were not unidirectional for long enough. It implies that the drag forces were minimal and that the inertia forces dominated. It created a flow pattern over individual rocks as shown on the left of Figure 4-12, instead of a flow pattern where the drag forces dominated as shown on the right. With large KC-numbers, the water particles travelled long distances compared to the size of the rock, which resulted in separation and vortex shedding similar to that described by Sumer & Fredsoe (2002).

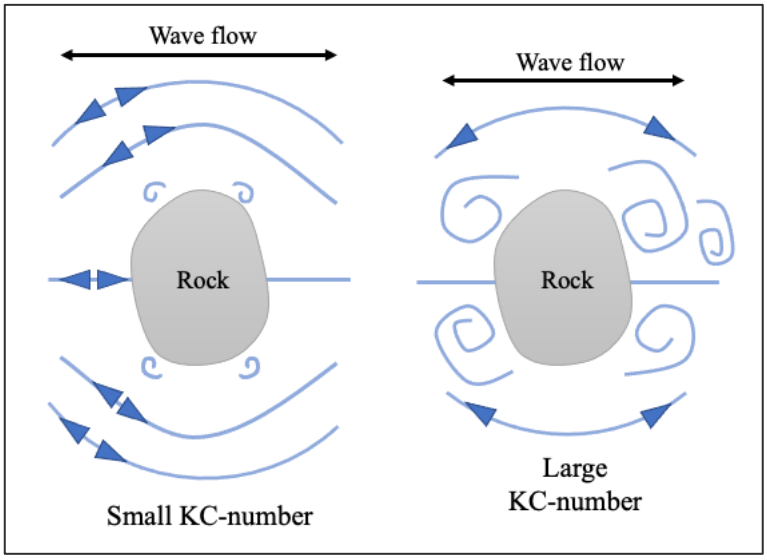

Figure 4-12: Flow around an individual rock for small and large KC-numbers

5 SCOUR EXPERIMENTAL RESULTS AND ANALYSIS

5.1 WAVE PERIOD VS SCOUR DEVELOPMENT

5.1.1 TEST SERIES A: FILTER RULE 1/10

Test Series A consists out of three sets of tests, as three different structures were tested with the median rock mass remaining constant. Test Series A is defined as the series where the underlying median rock mass should be a tenth of the median rock mass of the upper layer. The average screed scour depths (horizontal) for the three test sets are given in Figure 5-1.

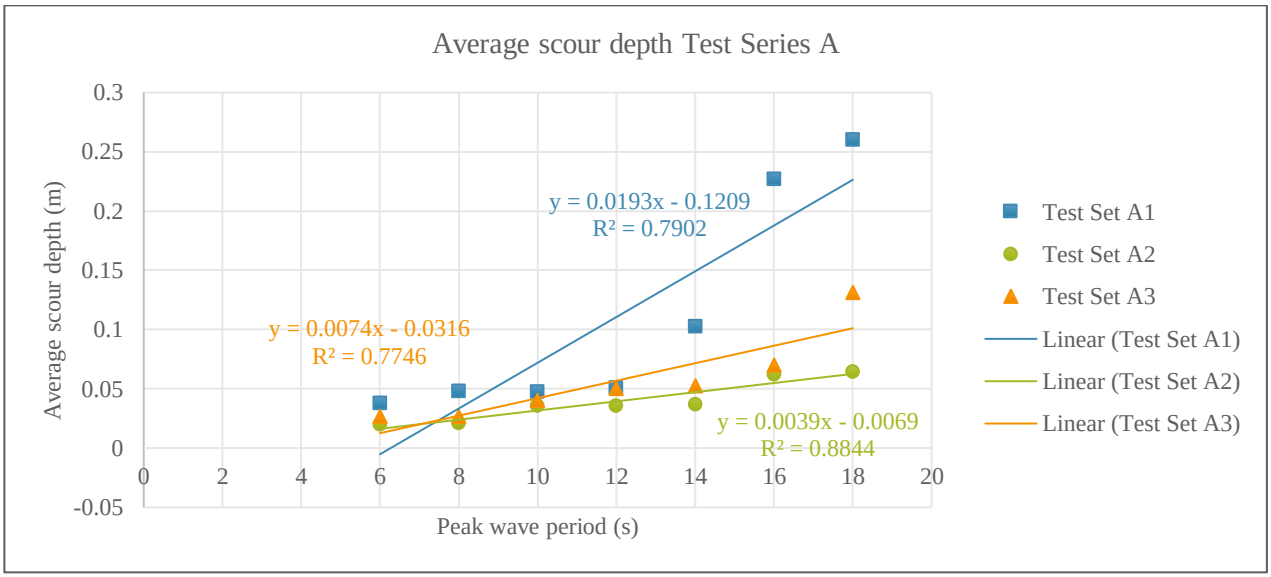

Figure 5-1: Average scour depths for Test Series A

The measured scoured areas and average scour depths for the prototype and model are given in Table 5-1. Each test set for Test Series A is discussed and analysed in the sub-sections to follow.

Table 5-1: Average scour depths and scour areas for Test Series A

	Scour depth		Scour area	
Test	Model (mm)	Prototype (m)	Model (mm^2)	Prototype (m^2)
A1 - 6S	37,8	0,8	36700	14,7
A1 - 8S	48,0	1,0	46522	18,6
A1 - 10S	47,6	1,0	46169	18,5
A1 -12S	50,8	1,0	49266	19,7
A1 - 14S	102,8	2,1	99713	39,9
A1 - 16S	227,0	4,5	220145	88,1
A1 - 18S	260,1	5,2	252313	100,9
A2 - 6S	20,3	0,4	19692	7,9
A2 - 8S	21,0	0,4	20389	8,2
A2 - 10S	35,6	0,7	34551	13,8
A2 - 12S	35,8	0,7	34678	13,9
A2 - 14S	36,7	0,7	35605	14,2
A2 - 16S	62,0	1,2	60142	24,1
A2 - 18S	64,7	1,3	62774	25,1
A3 - 6S	26,6	0,5	25819	10,3
A3 - 8S	26,7	0,5	25864	10,3
A3 - 10S	40,2	0,8	39036	15,6
A3 - 12S	50,6	1,0	49098	19,6
A3 - 14S	52,7	1,1	51098	20,4
A3 - 16S	70,0	1,4	67902	27,2
A3 - 18S	131,2	2,6	127280	50,9

5.1.1.1 Test Set A1

Structure A1 is indicated with a blue line in Figure 5-1. It is the structure that was recommended by Van Wageningen (2018) with regards to the berm width and screed layer thickness. The armour layer consisted of two layers of rock, and the filter layer also consisted of two layers of rock. Structure A1 was the smallest structure tested in Test Series A and the first set of tests for the two-dimensional model study.

The correlation coefficient for the seven wave periods in the test was 0.8889 ($R = \sqrt{0.7902}$), displaying the strength between the two variables (peak wave period and average scour depth) is strong. The results indicate that the scour for the first four wave periods (6s, 8s, 10s and 12s) remained moderately constant. The wave periods of 16s and 18s had a much larger scour area. The 18s wave period in this set, had the largest average scour depth in Test Series A. In the prototype, the scour depth was scaled up to 5.2m, which would be problematic. The screed layer had a designed depth (horizontal width) of 6.3m.

The interquartile range was calculated to determine if the scour areas of the two largest wave periods were outliers. The upper boundary for the outlier was calculated as 0.48m^2 scour. Even though these two values were much higher than the other measured scour areas, they were not considered outliers (calculations in Appendix M).

The top view of the screed layer after 2000 waves is given in Figure 5-2 for Test A1-18S. The remaining screed layer material is the light brown sand in the figure. The screed layer was practically washed out, exposing the core. The filter layer rocks (orange stones) can be seen on the core material where the vertical seawall was initially positioned. The relocating of the outer layer rocks is discussed in the Visual Inspection (Section 4.4).

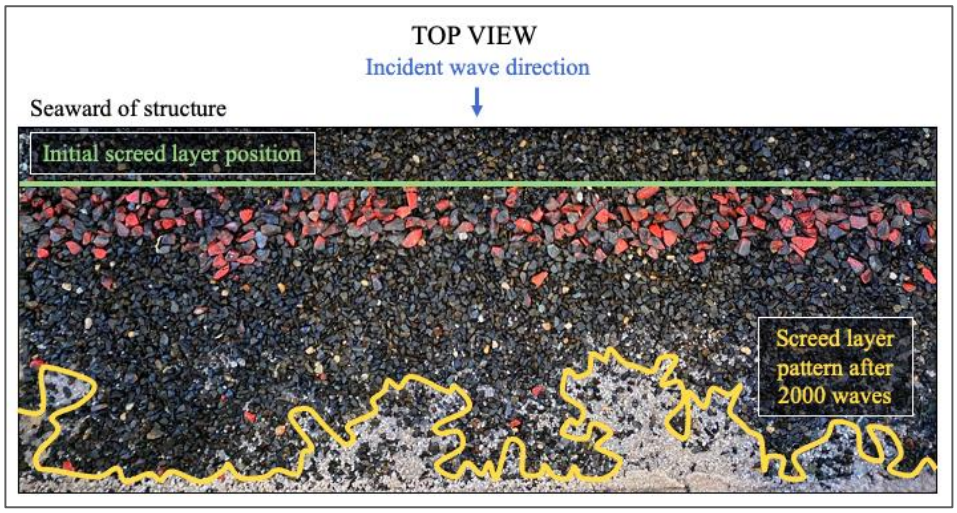

Figure 5-2: Scoured area for Test A1-18S

5.1.1.2 Test Set A2

Structure A2 is indicated with a green line in Figure 5-1. In Test Set A2, the armour layer had three layers of rock, and the filter layer also had three layers of rock. Structure A2 was the biggest structure tested in Test Series A. An increase in the scour area as the wave period increased was experienced. The scour for the largest two wave periods was again notably higher than the other wave periods, but not defined as outliers. Test A2-6S had the smallest scour depth of all the conducted experiments in Test Series A. On average, the scour depth is 0.4m in the prototype. Figure 5-3 display the scoured area after 2000 waves for Test A2-6S.

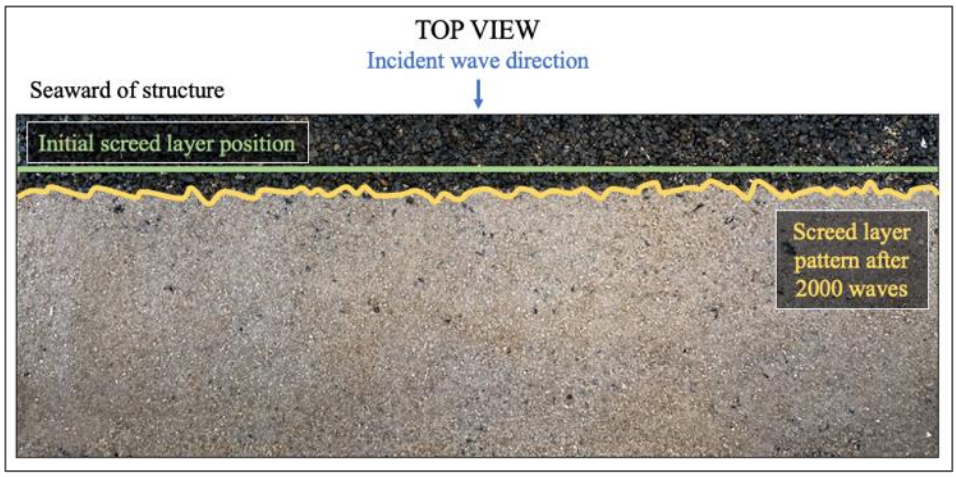

Figure 5-3: Scoured area for Test A2-6S

The increased scour area for a selected wave period was not that much higher than the scour area for the forgoing wave period in Test Set A2. The standard deviation for Test Set A1 and Test Set A2 was calculated to indicate the closeness of the values of the measured scour in Test Set A2. The sample range, correlation coefficient and gradient of the trendline are given in Table 5-2 to support this further. The calculations are provided in Appendix M.

Table 5-2: Standard deviation, sample range, correlation coefficient and trendline gradient for Test Set A1 and Test Set A2

	Test Set A1	Test Set A2	Explanation
Standard deviation (m^2)	0.09	0.02	The values in Test Set A2 is not as spread out as in Test Set A1. The values of Test Set A2 are closer to the mean than that of Test Set A1.
Sample range (m^2)	0.22	0.04	The range of the values for Test Set A1 is more extensive than that of Test Set A2, indicating Test Set A1 has a more considerable variability between wave periods.
Correlation coefficient	0.89	0.94	The correlation coefficient for Test Set A2 is more extensive, representing a stronger relationship between the two variables (scour vs wave period).
Gradient of trendline	0.02	0.003	The slope of the trendline of Test Set A1 is larger with a factor of five, indicating a steep incline from one wave period to the next.

5.1.1.3 Test Set A3

Structure A3 is indicated with an orange line in Figure 5-1. Structure A3 had the most rocks per layer in this series. The armour layer had two layers of rock, and the filter layer had four layers of rock. In practice, four layers of rock are generally the limit. The scour measured at the peak wave period of 16s was not significantly

higher than the other wave periods measured in this set. Whereas in Test Set A1 and Test Set A2, the 16s wave period had a higher measured value compared to the other wave periods.

A Box Plot with the first, second and third quartile is drawn of Test Set A3 in Figure 5-4. The whiskers extend to the smallest and largest data point within 1.5 interquartile from the first and third quartile, respectively. This box plot indicates that the distribution of the measured scour areas is asymmetric around the central value since the length of the whisker to the uppermost data point is exceptionally more prolonged than the length of the whisker to the bottom data point. The correlation coefficient for this test set was smaller than that of the two preceding tests sets due to the scour area of the 18s peak wave period being far higher.

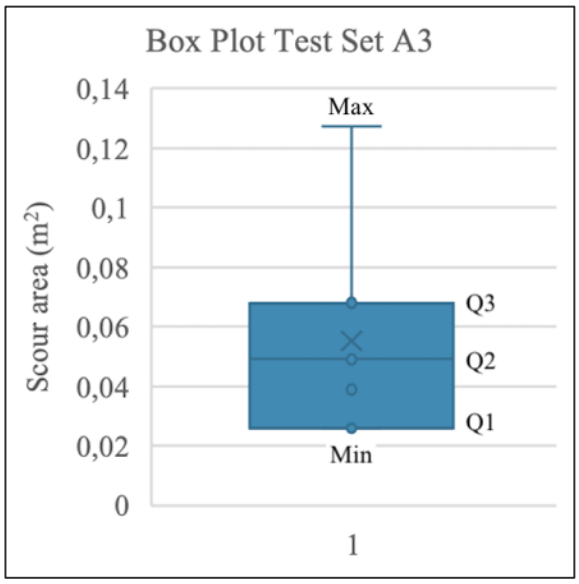

Figure 5-4: Box plot of Test Set A3

The Box Plots of the other data sets also had longer upper whiskers than lower whiskers but were not stretched as extensively as in Figure 5-4 (Appendix M). There may be an experimental flaw in Test A3-16S, or the construction process of the test was not exactly consistent with that of the other tests. This test was repeated as one of the verification tests in Section 5-4.

5.1.2 Test Series B: Filter Rule 1/15

Test Series B consisted of three sets of tests where three different structures were tested with the median rock mass remaining constant. Test Series B is defined as the series where the underlying median rock mass should be a fifteenth of the median rock mass of the upper lying layer. The average scour depth for the three test sets are given in Figure 5-5. The measured scoured areas and average scour depths for the prototype and model are given in Table 5-3. Each test set for Test Series B is discussed and analysed in the sub-sections to follow.

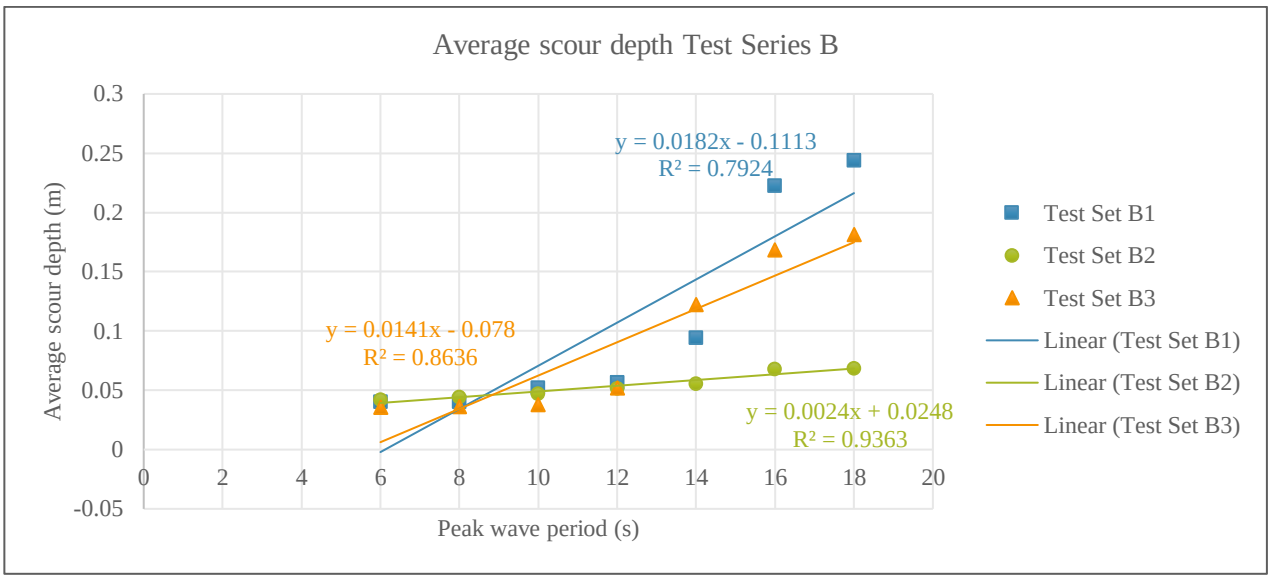

Figure 5-5: Average scour depths for Test Series B

Table 5-3: Average scour depths and scour areas for Test Series B

	Scour depth		Scour area	
Test	Model (mm)	Prototype (m)	Model (mm^2)	Prototype (m^2)
B1 - 6S	40,0	0,8	38844	15,5
B1 - 8S	40,0	0,8	38809	15,5
B1 - 10S	52,2	1,0	50625	20,3
B1 - 12S	56,6	1,1	54881	22,0
B1 - 14S	94,3	1,9	91517	36,6
B1 - 16S	222,8	4,5	216099	86,4
B1 - 18S	243,9	4,9	236539	94,6
B2 - 6S	42,1	0,8	40851	16,3
B2 - 8S	44,1	0,9	42748	17,1
B2 - 10S	47,0	0,9	45554	18,2
B2 - 12S	51,6	1,0	50068	20,0
B2 - 14S	55,8	1,1	54080	21,6
B2 - 16S	67,9	1,4	65856	26,3
B2 - 18S	68,5	1,4	66407	26,6
B3 - 6S	35,5	0,7	34457	13,8
B3 - 8S	36,3	0,7	35213	14,1
B3 - 10S	37,8	0,8	36698	14,7
B3 - 12S	51,8	1,0	50282	20,1
B3 - 14S	122,5	2,5	118845	47,5
B3 - 16S	168,3	3,4	163286	65,3
B3 -18S	181,5	3,6	176094	70,4

5.1.2.1 Test Set B1

Structure B1 is indicated with a blue line in Figure 5-5. It was the smallest structure in Test Series B. The armour layer had two layers of rock, and the filter layer also had two layers of rock. The design of the structure was very similar to that of Test Set A1, and the recommendations made by Van Wageningen (2018) were still applied in this structure. The difference was that Test Set B1 used a different filter rule, resulting in smaller rock sizes in the underlying layers.

The same was observed in Test Set B1 as in Test Set A1. The scour area increased with an increase in the wave period, and the scoured areas of the two largest wave periods were significantly higher. The 18s peak wave period had an average scour depth of 4.9m in prototype, which meant 78% of the screed layer was washed out through the rubble-mound structure by the wave action. A correlation coefficient of 0.8902 was obtained, which is very similar to that of Test Set A1, indicating a strong relationship between the two variables.

5.1.2.2 Test Set B2

Structure B2 is indicated with a green line in Figure 5-5. It was the largest structure tested in Test Series B. The armour layer and filter layer both had a thickness of three rocks. The design of Structure B2 was very similar to that of Structure A2, with only the median rock mass differing.

The same was observed as in Test Set A2 that the difference in scour between the wave periods was relatively small. A standard deviation was calculated with a value of 0.0105m^2, signifying the results are all relatively close to the mean value. The sample range was narrow, with a computed value of 0.0256m^2, indicating a small variability in measured scour values. The flat gradient (of 0.0023) and high correlation coefficient (0.9676) also show the scoured areas were all relatively close to each other.

5.1.2.3 Test Set B3

Structure B3 is indicated with an orange line in Figure 5-5. Structure B3 had three layers of rock in the armour layer and two layers of rock in the filter layer. Once again, an increase in the scour area was observed with an increase in the wave period. The data had a strong correlation coefficient.

5.1.3 Influence of Wave Period on Scour Conclusion

It was hypothesised that the shorter peak wave periods would cause more scour based on the study by Van Wageningen (2018) who explained that the wave energy of the shorter wave periods penetrated deeper into

the screed layer. The results above, however, display the contrary. Each set of the six groups indicated an increase in the scour area as the peak wave period increased. The screed scour areas of the first four wave periods (6s, 8s, 10s and 12s) were relatively close to each other. The 14s peak wave period had a slightly steeper gradient in the graphs constructed than the four smaller wave periods. The 16s and 18s peak wave periods showed significantly higher results than the rest.

The correlation coefficients were calculated for each set of tests (Appendix M), the six coefficients ranged between the values 0.89 and 0.97. Correlations above |0.8| are considered satisfactory. Thus, the linear relationship between the wave period and scour area indicates a strong positive relationship.

Based on the results, the six structures will experience extreme scour in the case of a storm where waves have a longer period. Structure A1, Structure B1 and Structure B3 will operate very poorly during a storm. Considering the total area of the screed layer in the model was 0.31185m^2, all three of these structures had scoured areas larger than half of the screed layer area for the peak wave periods 16s and 18s. Structure A1 had a scoured area of 0.26m^2 for the 18s wave period, which means 83% of the screed layer was washed out, which will directly lead to failure. The foundation soil bearing capacity and passive resistance will be reduced because of the scour at the front of the seawall. The wall will then overturn due to the backfill pressure, with wall weight and groundwater all acting against the seawall. Due to climate change, larger wave periods may occur more regularly and will become problematic in the future.

Past studies indicate that low steepness waves (low H_s/L_O ratio) cause more scour than steeper waves, assuming the depth remains constant. As the wavelength increase with the wave period, the wave steepness decreases. The growth in scour is explained by wave celerity which is directly influenced by the wave period ($c = \frac{gTd}{L}$). As the wave period increases, the speed of propagation of the wave will also increase. An increase in the wave celerity will lead to a rise in the rate of transmission of wave energy or wave power. The transmission coefficient describes the degree of wave transmission. A larger wave period leads to a larger transmission coefficient and consequently, long-wave periods lead to a greater transmission of wave energy through the permeable structure:

$$K_t = \frac{H_t}{H_i} = \sqrt{\frac{E_t}{E_i}}$$

Where E_t is the transmitted energy and E_i the incident energy.

When considering the linear wave theory, it is evident that a larger wave period leads to a larger orbital velocity at the toe of the seawall. The flow at the structure toe for larger wave periods will cause a more

complex and irregular flow with fluctuations in direction and velocity. This flow is described by the Reynolds number as turbulent (Equation 2-42).

As was noted in the visual inspection, the larger wave periods experienced overtopping, which is a hydraulic failure mode. When the waves overtop the seawall, there is a return flow which moves through the rubble structure, causing more wave energy to penetrate through the structure and consequently causing more scour (Figure 5-6). At the smaller wave periods, it is observed in the visual inspection that most of the wave energy is reflected and does not penetrate the berm as severely.

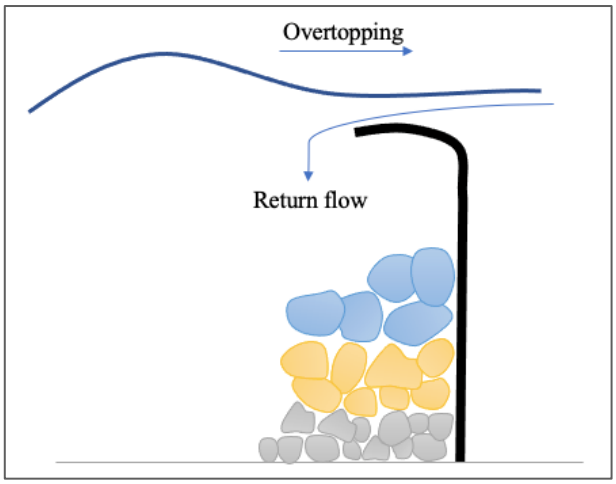

Figure 5-6: Return flow of wave overtopping causing scour

The visual inspection also revealed that with the larger wave periods, the berm would completely deform, causing structural failure. The hydraulic and structural failures, as identified in the visual inspection, are interactive with the scour failure; the deformation of the berm would speed up the scouring process. The deformation exposes the core of the structure. As the number of waves increases, the core gets more exposed, and the effect of hydraulic phenomenon (such as overtopping) has a much larger impact on the scouring of the screed layer.

5.2 Selecting the Optimum Layer Thickness

5.2.1 Test Series A

The scour area measured at each wave period for the three structures of Test Series A is shown in Figure 5-7. The screed scour areas for all three of the designs were very close to each other at the first four wave periods. Only the two larger wave periods displayed a big gap between the different scour areas of the distinctive structures. Structure A1 with the lowest crest had the most scour, whereas Structure A2 with the highest crest had the least scour.

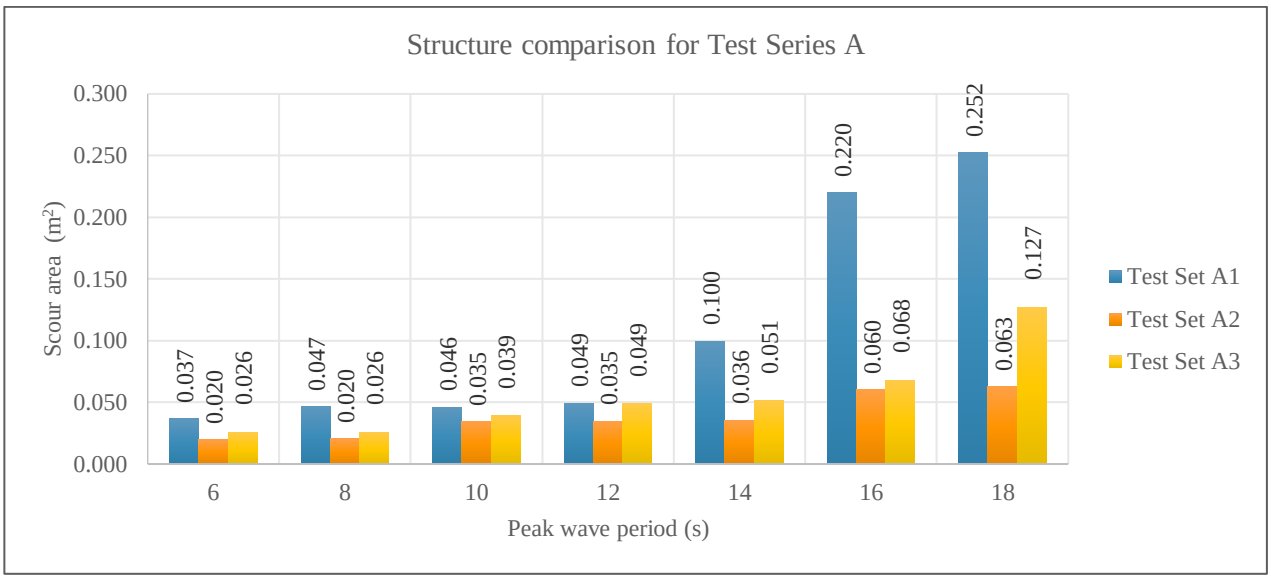

Figure 5-7: Scour area comparison for Test Series A

CIRIA (2007) states that it is more practical and effective to increase the thickness of the filter layer than to increase the thickness of the armour layer. This statement was tested by comparing Structure A1 and Structure A3. Structure A3 had four layers of rock in the filter layer (underlayer), where Structure A1 merely had two layers of rock in the filter layer (underlayer) while the armour layer thickness remained constant. This resulted in a 19% increase in the total crest height of Structure A3. It was determined from Figure 5-8 that the rise in crest height led to a 49% decrease in the average scour. Structure A1 had a 0.107m^2 scoured area on average and Structure A3 a 0.055m^2 scoured area on average. The average scour depths were 0.11m and 0.06m for Structure A1 and Structure A3, respectively. The results support the statement that a thicker filter layer (underlayer) can decrease the scour area significantly.

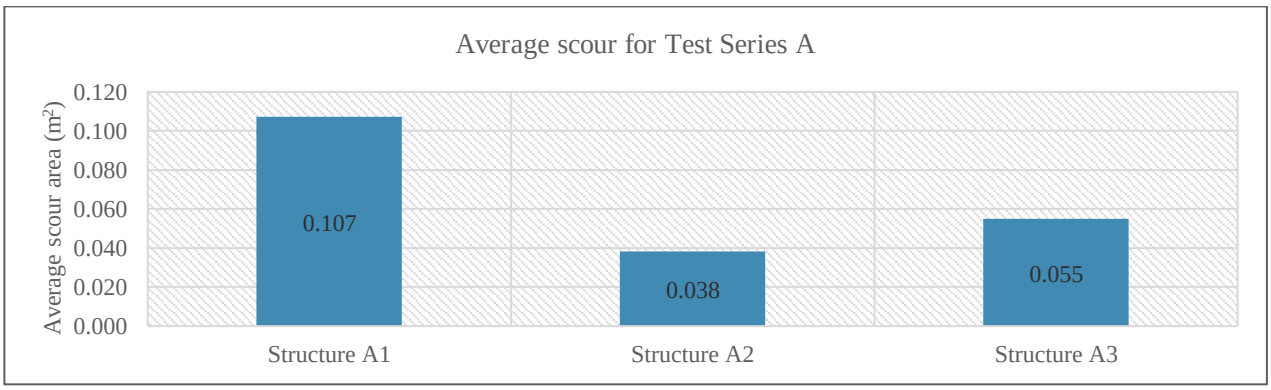

Figure 5-8: Average scour areas for Test Series A

There was a 31% difference in the average scour of Structure A2 compared to Structure A3. This was a large difference considering the model of Structure A2 was merely 13mm higher than that of Structure A3. In the prototype, this value scales to 260mm. Structure A2 had an armour layer thickness of 3 rocks instead of 2

rocks as in Structure A3. The armour layer protected the underlying layers and increased the internal stability of the structure. Consequently, Structure A2 responded the most satisfactory under wave attack with an average scoured area of 0.038m^2 and average scour depth of 0.04m.

5.2.2 Test Series B

The screed scour areas measured for each structure in Test Series B are given in Figure 5-9. Once again, the first four wave periods for the three structures showed similar results and the two larger wave periods showed a substantial difference.

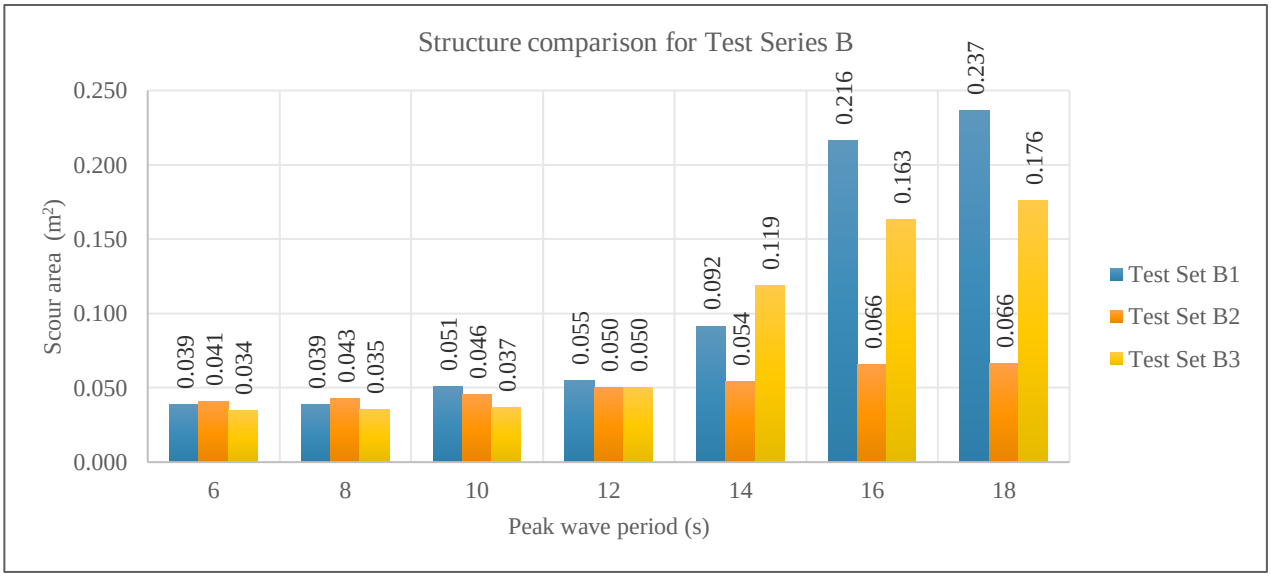

Figure 5-9: Scour area comparison for Test Series B

The 8% increase in the structure crest height of Structure B2 from Structure B3 caused a substantial reduction in scour. The small increase in size led to a 41% decrease in the average scour. Structure B2 had an average scoured area of 0.052m^2 and Structure B3 had an averaged scoured area of 0.088m^2 (as displayed in Figure 5-10). The average scour depths were 0.05m and 0.09m for Structure B2 and Structure B3, respectively. The difference between these two structures was that Structure B2 had a filter layer (underlayer) consisting of a 3-rock layer, whereas Structure B3 had a filter layer (underlayer) consisting of a 2-rock layer. This solidifies the statement that it is incredibly valuable to increase the thickness of the filter layer.

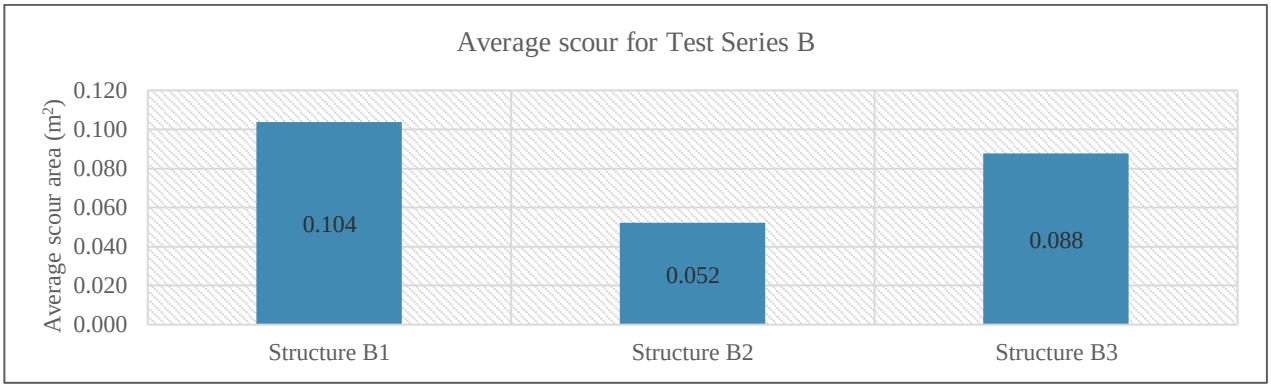

Figure 5-10: Average scour areas for Test Series B

There was a 21% crest height decrease from Structure B3 to Structure B1. Structure B3 had an armour layer with a thickness of three rocks, and Structure B1 had an armour layer with a thickness of two rocks. This resulted in Structure B1 experiencing on average 15% more scour than Structure B3. Structure B1 had an average scoured area and scour depth of 0.104m^2 and 0.11m, respectively.

5.2.3 Layer Thickness Recommendation

As hypothesized, the rubble structures with the highest crest provided the best protection. The two largest structures (Structure A2 and Structure B2) experienced merely 20% scour of the total screed layer area at the largest peak wave period of 18s. Whereas the two smallest rubble-mound structures, Structure B1 and Structure A1, at the same wave period of 18s experienced 75% and 80% scour respectively. By adding one layer of rock to both the filter layer and armour layer of Structure A1 and Structure B1, there was more than a 50% reduction in the average scour areas for Structure A2 and Structure B2 respectively.

The scour reduction was because there was more material in front of the screed layer as well as a larger permeable slope. The larger permeable slope caused less energy to be reflected. More energy was dissipated by the rubble-mound rocks, resulting in a steadier sea state in front of the structure. Another factor to consider is the deeper water depth. Due to the deeper water, the near-bottom velocity was not large enough to move a significant amount of sediment within the mobile bed area. Hence, scour, and deposition remained a minimum.

If the optimal layer thickness is solely based on scour development, a structure with the highest crest level will be chosen. However, the objective is to contribute to the optimal design of a rubble-mound structure. It remains vital to determine the magnitude of the protection offered and if it outweighs the extra cost of material and construction. A larger structure will increase the quantity of material needed as well as increase the construction cost.

Other than a high crest level being uneconomical, these structures (Structure A2 and B2) experienced more overtopping due to the water level having to remain constant at 0.05m above the berm in the model. This higher water level caused the seawall recurve to be filled with water at a faster rate, thus becoming ineffective. In practice, the seawall height would have to be increased to prevent overtopping to protect the infrastructure on land.

A higher rubble-mound crest level can be achieved either by increasing the thickness of the filter layer or that of the armour layer. Before designing a structure with a thicker armour layer, it should be critically examined. By increasing the armour layer thickness, the construction time of the project will increase due to armour stone having the requirement to be individually positioned. In contrast, the filter rock (in the underlayer) can be bulk placed by dumping using a wide range of equipment. Armour rock are also generally more expensive than smaller rocks used in the underlying layers.

The minimum layer thickness of any structure tested consisted out of 2 rocks per layer. Randomly placed stones should be packed in a double layer or thicker to ensure the core is protected everywhere along the length of the structure even if there is washing out of individual stones. A layer smaller than two rocks has a high probability of being destabilised by an absence of interlocking. The presence of larger voids between distinct rocks causes internal wave pressures, internal reflectivity, less wave energy dissipation and a loss of the filtering quality. The smaller the layer thickness, the easier it is for irregularities to occur, and the allowable tolerances for error become smaller.

Tolerances for the layer thickness are of critical importance. These tolerances remove the probability of negative deviations accumulating from the design profile, which could consequently lead to thin layers that are not up to standard in the prototype. The engineer needs to consider the possible deviations that may occur during construction from the design for the rubble-mound structure to remain effective. Thus, it is better to have more rocks per layer.

A mid-way should be established. It is recommended that the filter layer thickness ought to increase before that of the armour layer. The structures tested with a filter layer thicker than two rocks (such as Structure A2, A3 and B2) showed satisfying results. A larger underlayer creates an irregular surface which results in better interlocking and a more porous structure which improves wave dissipation and armour layer stability. Thus, it is recommended that the filter layer should have a thickness of three or four rocks, and the armour layer the minimum thickness requirement of a 2-rock layer.

5.3 The Ratio of Median Stone Mass between Armour and Under Layer vs Scour Development

5.3.1 Test set A1 vs Test Set B1

Structure A1 and Structure B1 were designed to have the same rubble-mound geometry (two layers of rock in the filter layer and two layers of rock in the armour layer). The difference between the two structures was that Structure A1 adheres to the rule $\frac{M_{50\ lower}}{M_{50\ upper}} = \frac{1}{10}$ and Structure B1 adheres to the rule $\frac{M_{50\ lower}}{M_{50\ upper}} = \frac{1}{15}$.

The scour results (given in m^2) in Figure 5-11 for the two structures were very similar. In four of the seven tests conducted per structure, Structure B1 performed better under the selected wave period. The average scour for Structure A1 was calculated as $0.107m^{2,}$ and the average scour for Structure B1 was calculated as $0.104m^2$. It is merely a 3% difference in the average scour area. The two structures reacted very similarly to the incident wave conditions, and a small difference between the scour areas was recorded.

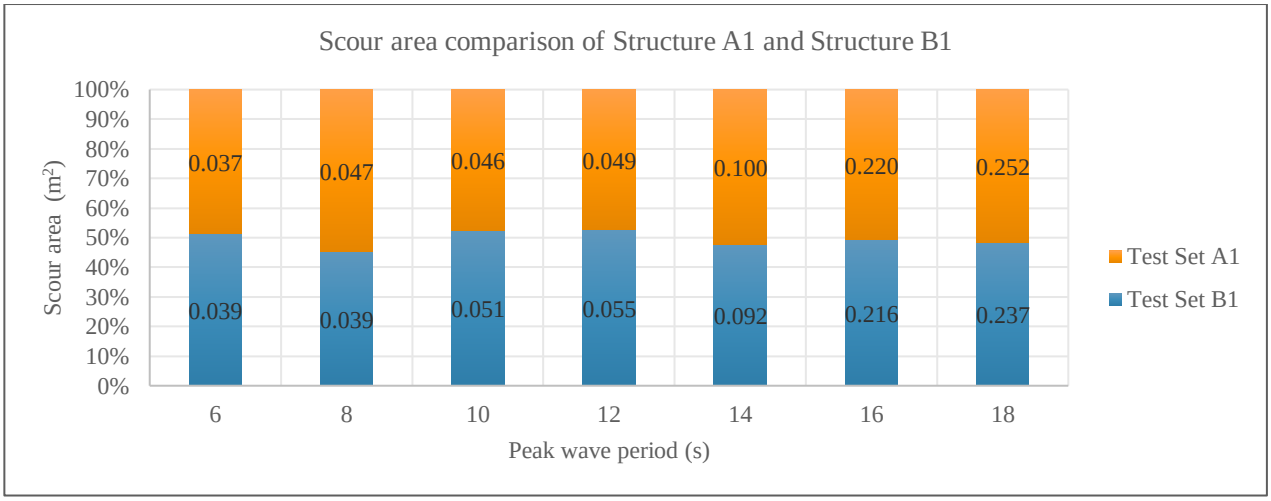

Figure 5-11: Average scour area comparison of Structure A1 and Structure B1

5.3.2 Test set A2 vs Test Set B2

Both the structures (Structure A2 and Structure B2) had three layers of rock in the armour layer, and three layers of rock in the filter layer (underlayer) while adhering to different median rock mass ratios.

Figure 5-12 indicates a more considerable difference between the measured scour areas between the two structures than the structure comparison in Figure 5-11. The data labels in Figure 5-12 are the scour areas given in m^2. Structure B2 had larger scoured areas than Structure A2 at all the tested wave periods. The average scours of Structure A2 and Structure B2 were calculated as $0.038m^2$ and $0.052m^{2,}$ respectively (there

is a 27% difference). The smaller wave periods show a big difference in scour between the two structures (Structure B2 had approximately double the scoured areas at peak wave periods 6s and 8s). In contrast, at the larger peak wave periods, the measured scour areas were very close to the same.

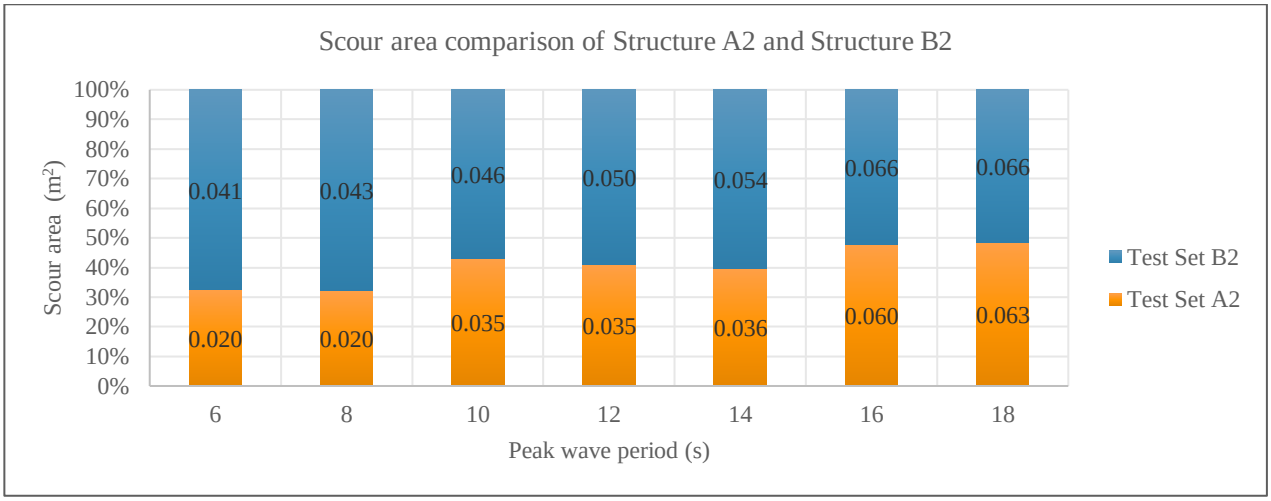

Figure 5-12: Average scour area comparison of Structure A2 and Structure B2

5.3.3 Test set A3 vs Test Set B3

Structure A3 and Structure B3 were not designed with the same number of rock layers in their respective layers, but their crest heights were very close to each other. Thus, the effect of the mass ratio could not be as definitely determined, since there were additional factors at work.

Based on Figure 5-13, Structure A3 reacted better under the wave attack with regards to the screed layer protection. The data labels in Figure 5-13 are the scour areas given in m^2. Six of the peak wave periods produced less scour in Structure A3 than in Structure B3. The performance of Structure A3 could be due to factors such as the mass ratio criterion applied, Structure A3 having a slightly higher crest level, thus providing more protection and lastly, the filter layer (underlayer) consisted of a four-rock layer.

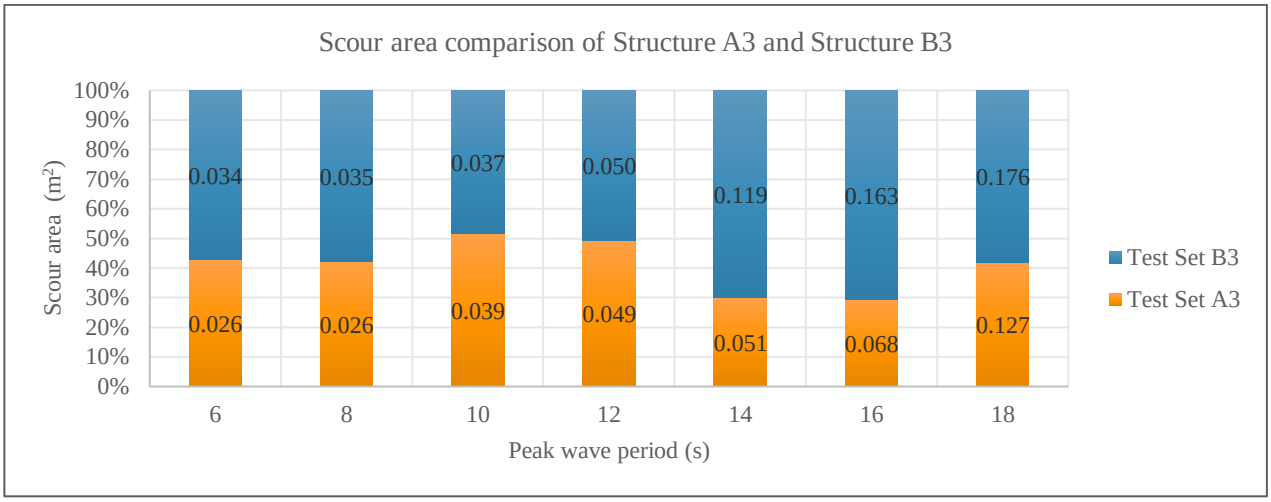

Figure 5-13: Average scour area comparison of Structure A3 and Structure B3

5.3.4 Influence of Stone Mass on Scour Conclusion

Evaluating the protection offered by the ratio between the stone masses is of critical importance. CIRIA (2007) states that this criterion is one of the most important rules the rubble-mound structure designer should apply. The filter layer should be designed to prevent the finer material from transporting through the rocks while simultaneously allowing water to be transported through the rocks.

From the results, it is concluded that a larger filter layer (applying the rule of $\frac{M_{50\ lower}}{M_{50\ upper}} = \frac{1}{10}$) produces more satisfying results. It is contradicting to the hypothesis. However, this statement is found to be especially true when there are more layers of rock in the respective layers of the rubble-mound structure. Having larger rocks in the filter layer (underlayer) gives you a more porous layer. An increase in permeability leads to increased stability due to more energy being dissipated by the larger rocks. Since the larger rocks dissipate more energy, less of the wave energy will travel towards the screed layer, resulting in less scour.

The first two structures discussed in Section 5.3.1. did however display a conflicting result. Even though the difference between the average scour area was minimal, it is still worth an analysis of why this was the case. It is believed that due to fewer rocks being in the layer, there was less interlocking in the structure. It caused the success of the structure to instead rely on a smaller porosity which in this specific case, led to higher stability. The increase in compaction disabled water from flowing through towards the screed layer.

It is thus concluded that the optimal mass ratio is case-specific. But based on the six structures tested in this thesis, it is more favourable to adhere to the mass ratio of $\frac{M_{50\ lower}}{M_{50\ upper}} = \frac{1}{10}$. When applying the filter rule leading to a larger median rock mass in the underlayer and a construction error occurs where smaller rock sizes are

used, the rocks will still fall within the of $\frac{M_{50\ lower}}{M_{50\ upper}} = \frac{1}{15}$ criterion. Thus, it is safer to use the $\frac{M_{50\ lower}}{M_{50\ upper}} = \frac{1}{10}$ filter rule in terms of rubble-mound construction.

5.4 Verification Tests

It was decided to verify three sets of groups: a possible experimental error, the tests with the largest scour areas and the tests showing the most satisfactory results. Thus, six additional experiments were conducted. Strict quality control was applied during the execution of all forty-eight experiments. The following points were addressed to ensure reliable results:

1. The seawall should be appropriately fixed in the flume with a strong adhesive to prevent any movement of the seawall
2. Depressions in the screed layer should be avoided since they create larger scour areas around the void
3. The correct incident wave conditions should be produced (this is achieved by practical experience with the wavemaker)

5.4.1 Evaluating Possible Experimental Errors

Test A3-16S was repeated due to the scour area being smaller than expected. In all the other test sets the scour areas of the 16s and 18s peak wave periods were much higher than the other wave periods. The scour measured in the repeated test was 0.135m^2. It was 13% higher than the scour area measured in the first A3-16S test conducted (Figure 5-1). The distribution of the results in the updated Box Plot was still asymmetric, and the scour of the 16S peak wave period was still not as close to the 18S wave period as the other conducted tests. The updated Box Plot and scatter plot of Test A3-16S can be seen in Appendix N.

The reason why the measured data was not as spread out as in previous tests may indicate that Structure A3 was less susceptible to storm wave conditions. The small scour area at a wave period of 16s showed that the structure was resilient to larger wave periods, and only in an extreme storm, would the scour start to increase. What makes this structure unique is that it was the structure with the thickest filter layer (4 rocks in the layer). Once again, supporting the statement that increasing the thickness of the filter layer is beneficial.

5.4.2 Most Extreme Scour Areas

The two tests that displayed the most scour are repeated to ensure the accuracy of their results. These two tests were A1-18S and B1-18S (the two smallest structures during the largest peak wave periods). Figure 5-14 compares the initial results with that of the repeated experiments.

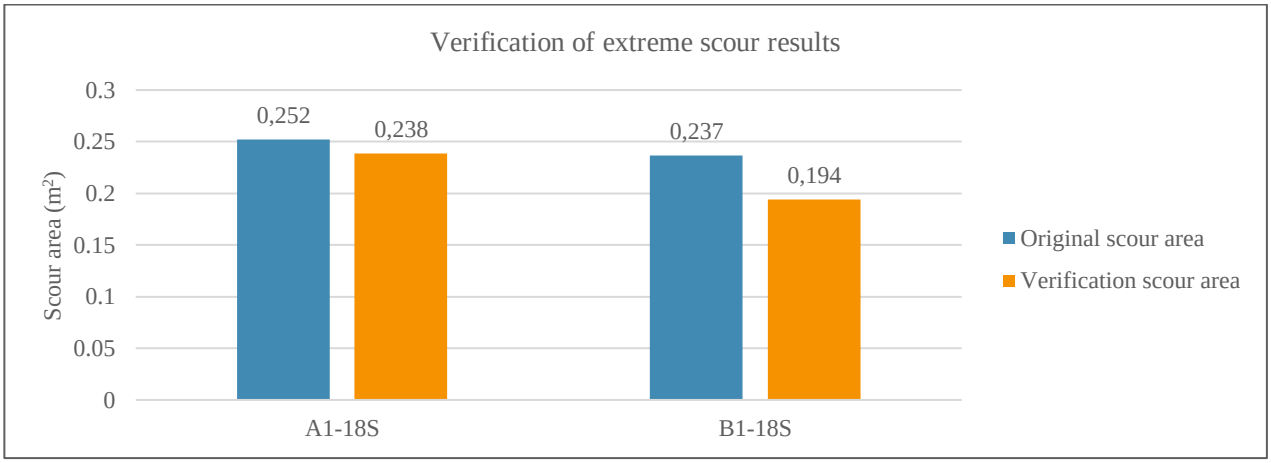

Figure 5-14: Verification of most extreme scour measurements

Test A1-18S showed a small variance of 6% in the measured scour. Test B1-18S showed a slightly larger variance of 18%. The change in the scour areas can be attributed to model construction variations. It was impossible to construct the model as precisely identical a second time. The difference in the measurements was nonetheless still acceptable.

5.4.3 Recommended Mass Ratio

One peak wave period for each structure of the three structures with the recommended mass ratio of $\frac{M_{50\ lower}}{M_{50\ upper}} = \frac{1}{10}$ was verified. It was decided to use the peak wave period of 10s since this is common to the South African coastline. The variance in all three of the repeated tests was relatively small. There was a 5%, 16% and 17% difference in Test A1-10s, Test A2-10S and Test A3-10S respectively. This difference, as mentioned above, was due to construction inconsistency and is nonetheless still satisfactory.

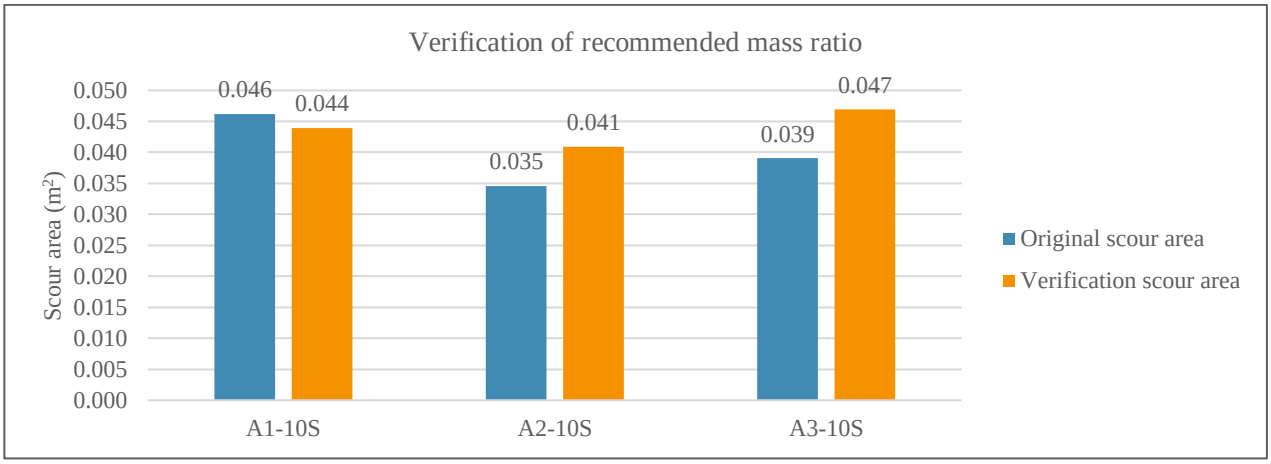

Figure 5-15: Verification of recommended mass ratio for a peak wave period of 10S

5.5 Scour Comparison with (Van Wageningen, 2018)

One of the objectives of Test Set A1 was to verify the results as presented by Van Wageningen (2018). This required all the design parameters to remain identical. The results of four tests conducted can directly be compared with the tests conducted in 2018. The four tests had a peak wave period of 8s, 10s, 12s and 14s. The scour measured in the two respective studies is illustrated in Figure 5-16. The wave flume at the CSIR is narrower than the wave flume at the Stellenbosch University Water Laboratory; the scour was scaled accordingly.

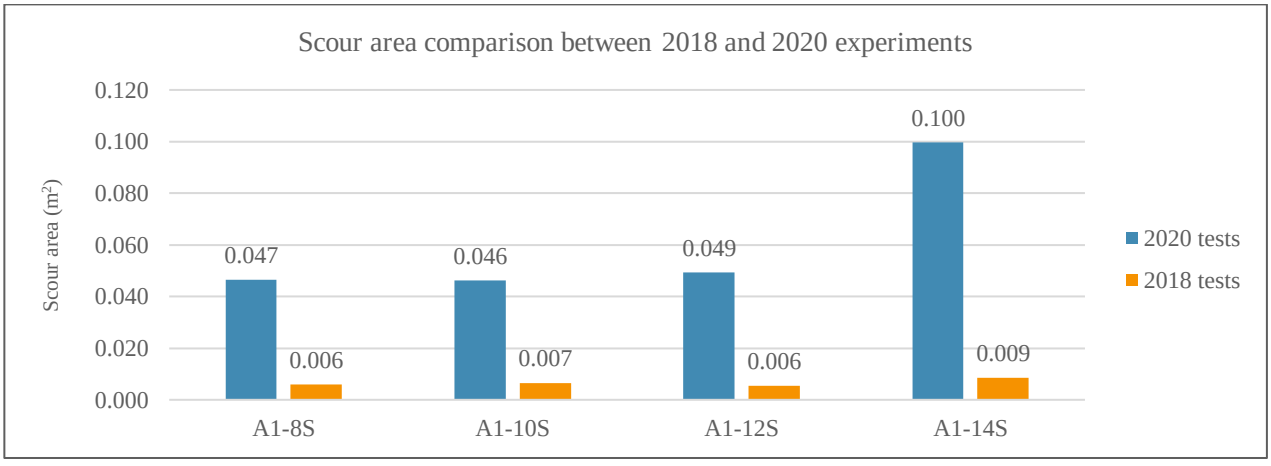

Figure 5-16: Scour area comparison with (Van Wageningen, 2018)

It is prominent that there is a big difference between the values measured in 2020 and that in 2018. The gap is too extensive when considering the entire model design and construction was intended to be as similar as possible. It is also fascinating that in the results obtained by Van Wageningen (2018) there is a decrease in scour as the wave period increases, which is in direct contrast to the results of the tests conducted in this study.

Certain factors identified in hindsight can cause differences in the results. The first factor is the method of data measurement. In 2018 a sonar machine was used. In 2020 photos were taken of the scour and imported into MATLAB to be processed. It is believed that the MATLAB method is more accurate. As explained in Section 3-6, it gives an accuracy of 99.8%. The medical sonar had an accuracy of 97.4%. For an actual measurement of 200mm, the medical sonar measured 205.1mm. When using the sonar at a shorter distance of 50mm, it measured 49.4mm; this is 98.8% accuracy, which is also very good. However, when scour distances with a range between 6mm and 93mm are measured (as in the 2018 tests), this kind of tolerance can be problematic.

An additional factor that can influence the results is that of the bathymetry. The bathymetry in the tests in 2018 and 2020 both designed a shallow water slope of 1:20 leading up to the seawall. However, due to the construction processes differing, the slope in 2018 ended up being 1:18.6, which means the slope of the 2018 tests was steeper. There is also a minimum requirement of the shallow water slope length for the design wave to develop. Since larger wave periods were tested in the 2020 model, the slope leading up to the seawall was longer. This difference in bathymetry will cause different surf similarity parameters resulting in different breaker types against the seawall.

The grading curves of the two structures were also different. Even though the rock grading was meant to remain the same, it proved to be a challenge since different rocks were used, which were obtained at different laboratories. It was noted that the grading curve in 2020 was steeper than the grading curve of the rocks used in 2018. The armour layer, filter layer and core rocks in 2020 had a narrow grading (see Appendix G). Whereas the rocks used in 2018 had a wide gradation. A wider gradation can decrease the porosity of bulk placed materials which inhibits the flow of water and energy entering the screed layer.

6 Flow Velocity and Energy Distribution in Layers

6.1 Accuracy of Measured Pressures

There was a high variability in the pressure heads measured. A general trend was identified, but the relationship among consecutive tests was relatively weak. It is believed that the small-scale model does not represent the prototype as accurately as the specific pressure transmitters require. Graphs indicating the maximum pressure head measured at the various points along the length of the vertical seawall are given in Appendix O. In these graphs, a clear and repeating pattern for the dynamic pressure head among the different test sets is absent. The measurements do not show the maximum dynamic pressure head occurring at the same pressure transmitter location during every test. The majority of tests (69%) indicated that the maximum dynamic pressure head was at the top of the armour layer. The remaining 31% of the maximum readings were scattered among the armour layer bottom, filter layer bottom and screed layer top.

The ratio of the top pressure measurement to the bottom pressure measurement of each layer is given in Appendix O for every conducted test. These ratios are used to indicate the accuracy of results. There is a weak trend amid consecutive wave periods or among the layers. Consider Test Set A2 in Figure 6-1; a weak connection exists among the pressure head measurement taken at the top (pressure transmitter 1) and bottom (pressure transmitter 5) of the armour layer for the different wave periods. The same can be applied to the pressure measurements taken at the top and bottom of the other two layers in Structure A2.

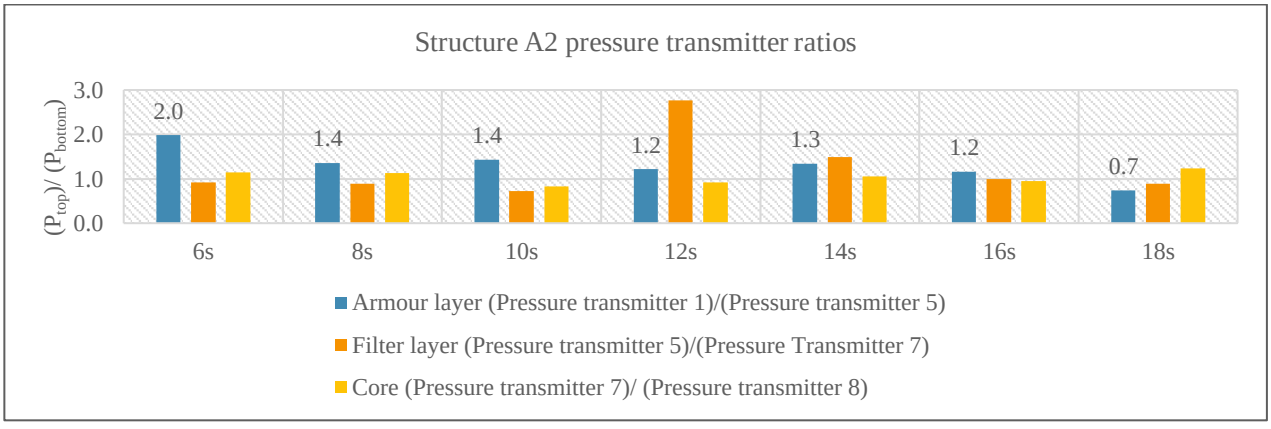

Figure 6-1: Ratio of pressure heads for layers in Structure A2

Furthermore, the ratio between layers does not remain the same or relatively close to that of the previous test. The coefficient of variation (COV) was calculated for each test set and given in Table 6-1. The standard deviation and average were used to obtain the coefficient of variation.

Table 6-1: Standard deviation, average and coefficient of variation for the ratio between pressure measurements

	Test A1	Test A2	Test A3	Test B1	Test B2	Test B3
Standard deviation						
(Armour top)/(Armour bottom)	0,13	0,34	0,15	0,24	0,49	0,10
(Filter top)/(Filter bottom)	0,37	0,66	0,29	0,48	0,31	0,57
(Core top)/(Core bottom)	0,01	0,13	0,13	0,35	0,19	0,45
Average						
(Armour top)/(Armour bottom)	0,89	1,32	1,31	1,78	1,23	1,10
(Filter top)/(Filter bottom)	1,44	1,24	1,45	0,82	0,96	2,00
(Core top)/(Core bottom)	1,05	1,03	1,27	0,98	0,88	0,91
Coefficient of variation						
(Armour top)/(Armour bottom)	14,58	25,99	11,83	13,31	39,69	9,19
(Filter top)/(Filter bottom)	25,96	53,36	20,13	58,12	32,63	28,59
(Core top)/(Core bottom)	0,93	12,78	10,03	35,30	21,21	48,88

Table 6-1 gives substantial values for the coefficient of variation. These large values indicate that the data points are dispersed widely around the mean, indicating a weak relationship among the data. The COV is marked according to good (green), acceptable (yellow), poor (orange) and unacceptable (red), as determined by general laboratory practice.

It is however noted that when considering the average pressure measurements of the structures over the range of wave periods, a stronger correlation is attained. The average pressure head ratios are plotted along with the pressure head ratios of the individual structures. The same values for the armour layer of Structure A2 in Figure 6-1 can be seen in Figure 6-2 where the line of Structure A2 is somewhat crooked. In contrast, the line indicating the average values is relatively straight.

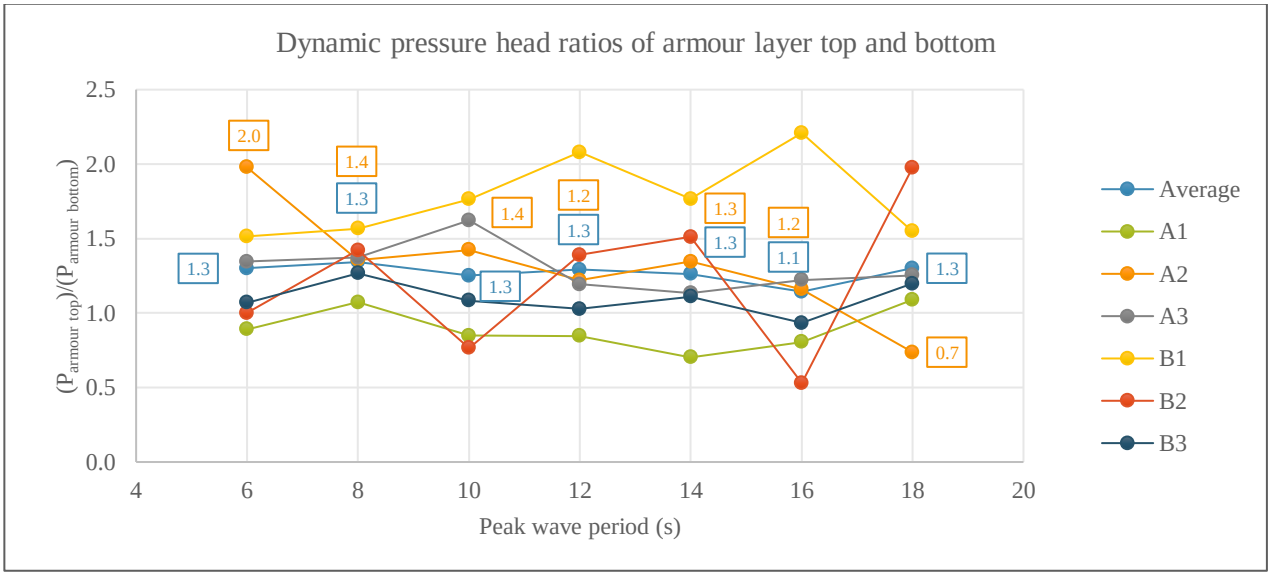

Figure 6-2: Dynamic pressure head ratio of armour layer top and bottom

The average of all the armour layer ratios has a COV of 4.6%, which is a decent result especially compared to the large coefficients of variations for the armour layers of the individual structures (Table 6-1). The filter layer and core have a COV of 16% and 11% respectively, which is still classified as acceptable. The plotted graphs of the average pressure head ratios of the filter layer and core are given in Appendix O.

It was decided to henceforward, where applicable, work with the average values since this indicates an overall trend. The results of the individual structures were poor, and it will be challenging to analyse and draw conclusions. It is more valuable to examine the average values and identify general trends.

The high variability measurements of the conducted tests can be contributed to the stochastic nature of wave impacts when breaking. When waves break, shock forces are created. The shock loads from breaking waves are caused by the breaking waves trapping pockets of air that are rapidly compressed (USACE, 2002). The shock loads in small-scale models are sensitive to the shape and kinematics of the breaking waves. The sensitivity of small-scale models requires the reproduction of natural waves in the laboratory to be very realistic and statistically correct, which can be challenging. As mentioned in the visual inspection, the waves break directly against the seawall and cause high impulsive loads. High impulsive loads tend to create extreme load values.

Scale effects can also be one of the factors that have a significant part in the low-quality measurements. The scale effects associated with the size and quantity of air bubbles as well as the shape and size of air pockets played a large role. Since most waves in the model are spilling or plunging (which are associated with high air entrainment), there is a considerable variation in air entrainment that is caused by the waves breaking or flow separation. The dissimilarity in the air entrainment will lead to the wrong viscous forces in the model and consequently affect the flow regime within the rubble-mound; this will influence the pressure measurements in the model.

Since this section is not the main objective of the study, no additional time is spent on the time-consuming process of obtaining the exact statistically correct wave conditions. A supplementary measuring technique is also not used to verify the results. Nonetheless, the measured values are still analysed as detailed in the methodology. Future studies on this topic should improve the measurement method and build on the research and procedures presented in this study.

6.2 FLOW VELOCITY USING THE FORCHHEIMER EQUATION

6.2.1 APPROACH TO THE FORCHHEIMER EQUATION

The Forchheimer equation contains three terms, each representing a flow type: laminar, turbulent and oscillatory. The laminar term will dominate in the equation when the flow velocity through the voids in the rockfill is small enough to be laminar, and the turbulent term will dominate when the flow is turbulent. The oscillatory term is used when the flow in the voids are strongly oscillating. An oscillating water particle is identified when the water element undergoes a closed-loop trajectory, thus completing one transverse of the orbit as each wave passes.

The third term for oscillating flow will, however, not be incorporated into the Forchheimer equation used in this study. The water particles move through the structure in an irregular pattern and do not merely oscillate to its original position as the wave passes over the rocks. It is established that the flow in the layers of the rubble-mound structure is not oscillating vigorously and that the turbulent term will dominate (see Section 4.5 where the dye is placed in the water).

6.2.2 CALCULATED VELOCITY RESULTS

The calculated variables used in the Forchheimer equation are given in Appendix P. The two Forchheimer coefficients (A_{For} and B_{For}) vary between the structures and their respective layers as the diameter of the rocks change. The second term in the Forchheimer equation dominates, indicating that the flow type is dominantly turbulent. Since the turbulent flow regime will govern, the hydraulic gradient (in the Forchheimer equation) is proportional to the velocity squared. Whereas in the laminar flow regime, the hydraulic gradient is proportional to the velocity.

There was a strong linear correlation between the wave period and the average flow velocity in the layers. As the wave period increased, the velocity in the layers also increased. The results are shown in Figure 6-3. The velocity in the core was the highest and the velocity in the armour layer the smallest.

A strong downward flow was generated when the waves broke against the structure. As the void area decreases when the water moves down through the different layers of the structure, the flow velocity increased. Even though the conservation laws of fluid flow cannot be applied to this model since the model is not a controlled volume; it gives insight into the increase in velocity in the core. When the flow discharge (q) remains roughly constant, the flow velocity will have to increase as the void area decreases as demonstrated by Equation 6-1.

$$u_v = \frac{q}{A_{void}} \qquad 6\text{-}1$$

The strong linear relationship in Figure 6-3 is only evident when considering the average velocities of the six structures in the layers between wave periods. When considering the velocities in each structure separately, such a strong relationship does not exist (see Appendix P).

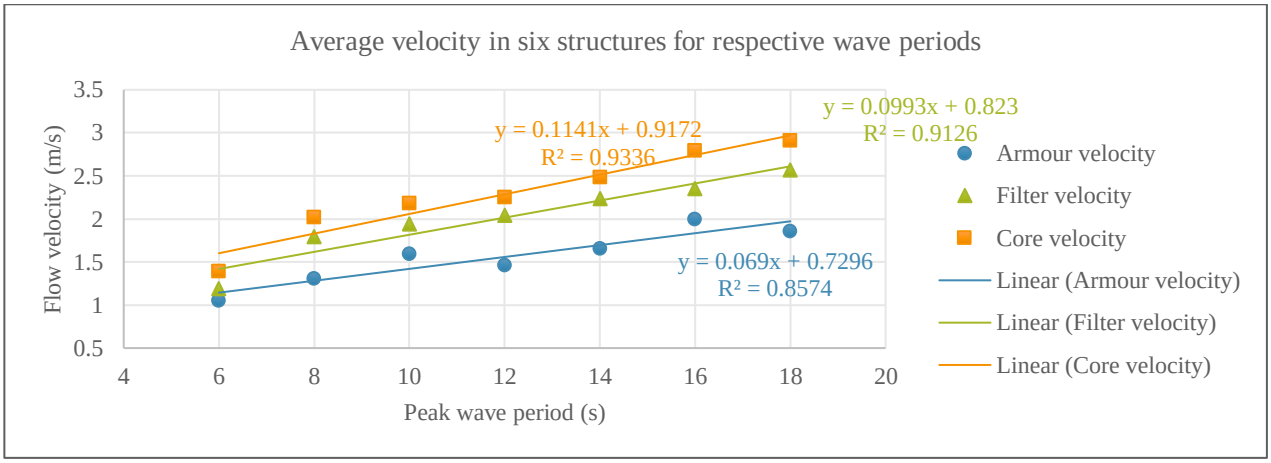

Figure 6-3: Average flow velocity in six structures for tested wave periods

There was a wide range of correlation coefficients for the individual structures, ranging from 0.2 for the armour layer of Structure B3 and 0.97 for the armour layer of Structure A3. The wide range of coefficients is attributed to the method of obtaining the velocity. Since no proper velocity measuring equipment is available, the velocity is calculated from basic principles. It is also the reason for the high measured velocities in the structure. The calculated velocities were higher than one would expect, this can be attributed to the dynamic pressure head measurements. However, the general trend is apparent and indicates a positive relationship.

6.3 Energy Distribution in Layers of the Rubble-Mound Structure

6.3.1 Energy Dissipation

6.3.1.1 External Energy Dissipation

The energy dissipation due to wave breaking was calculated for each prototype condition using the equation for wave breaking on a beach profile developed by (Battjes and Janssen, 1978). As a first approximation, this method was applied to wave breaking on a rubble-mound structure. Figure 6-4 illustrates the decrease in external energy dissipation as the wave period increased. The larger structures (Structure A2 and Structure B2) had slightly higher energy dissipation values due to higher water levels at the toe of the berm.

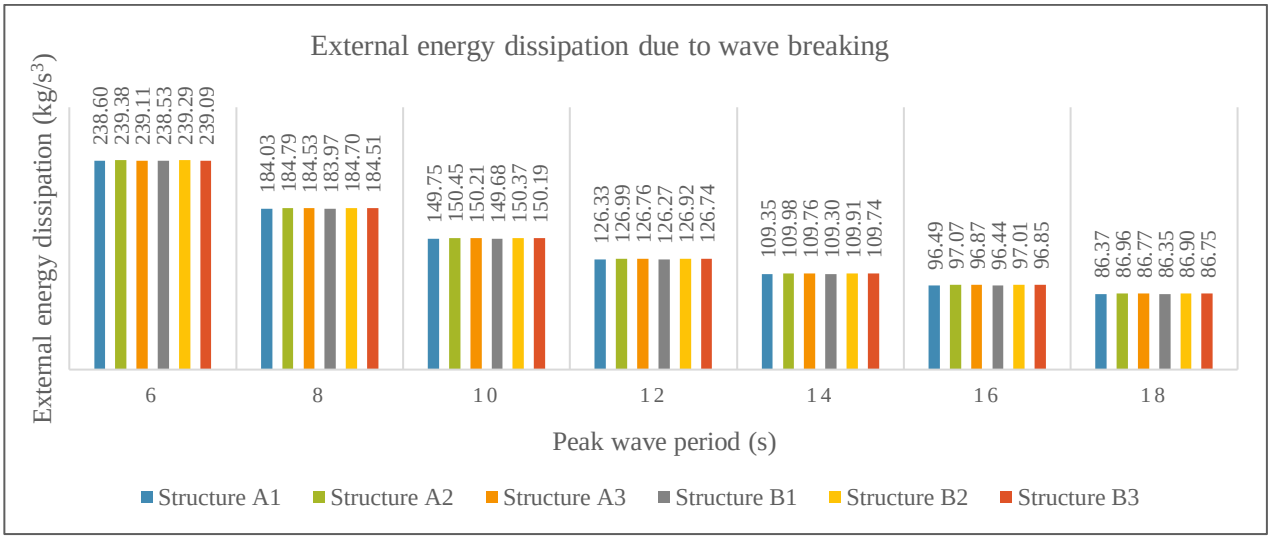

Figure 6-4: External energy dissipation in the prototype due to wave breaking

As the wave approaches shallower water, the ratio of broken waves will increase. It will increase so much that it compensates for a change in $H_m{}^2$ (see Equation 2-20), resulting in the energy dissipation to be mainly dependent on the ratio of broken waves. However, due to the ratio of broken waves remaining relatively constant in the model because of the small change in water level, this does not have such a large effect on the energy dissipation. Additionally, the maximum wave height used in the energy dissipation calculations similarly increases very little between consecutive tests (see calculated values in Appendix Q).

Hence, the primary variable affecting the energy dissipation is the wave period, and therefore a firm decline is seen in Figure 6-4. The wave period influences the breaker parameter, which in turns determine the shape of the breakers on the structure. The energy dissipation due to a spilling breaker will vary from the energy dissipation due to a plunging breaker. Plunging breakers (at the larger peak wave periods, see Appendix B) are associated with more energy than spilling breakers. This high quantity of energy travels to the core, causing immense scour. Whereas at the spilling breakers more wave power is dissipated by the wave breaking and a smaller amount of energy transfers to the core.

6.3.1.2 Internal Energy Dissipation

As Figure 6-5 illustrates, the outer layers dissipated the larger quantity of energy. 30% of the energy was more or less dissipated by the core. The diameter of the outer layer rocks was larger than the rocks in the core. Larger rocks allow increased porosity and an increase in the surface roughness and subsequently improve the extent of energy dissipation.

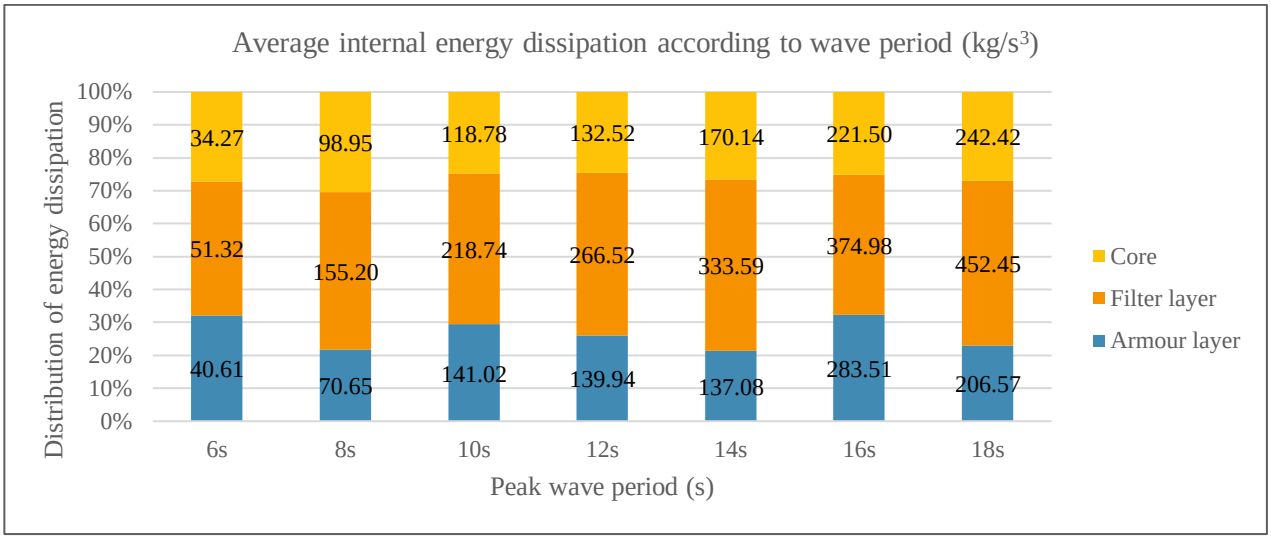

Figure 6-5: Average internal energy dissipation through layers of the rubble-mound structure according to the wave period

In Figure 6-6, it is again evident that the majority of the energy was dissipated by the filter layer when considering the six structures individually.

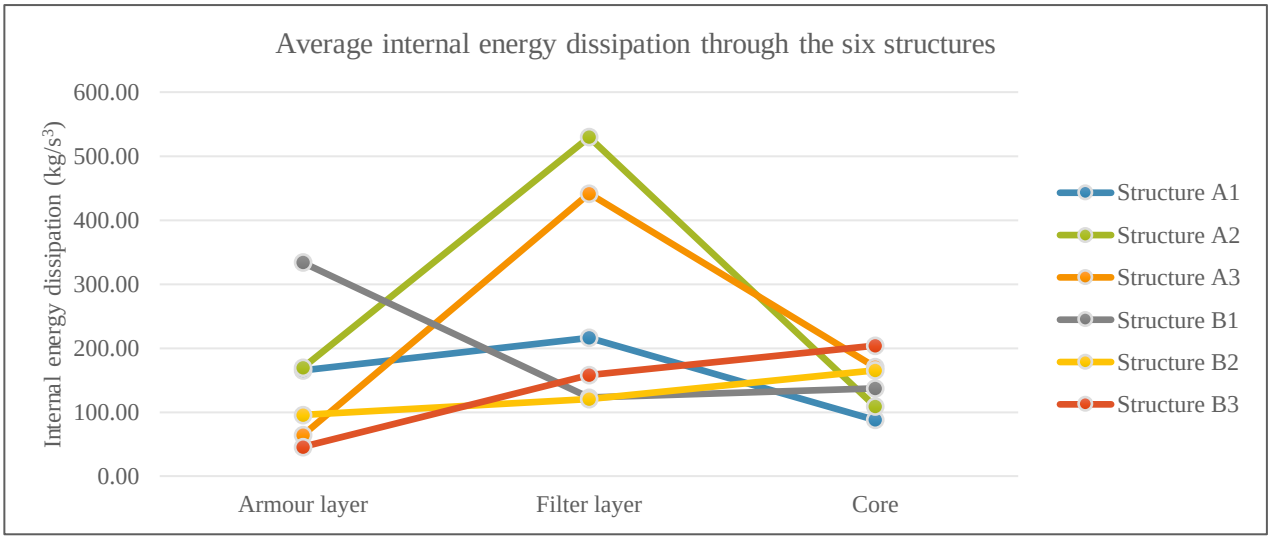

Figure 6-6: Average internal energy dissipation for the six structures

The general trend in the Figure 6-6 is expected – more energy is dissipated in an armour layer with three layers of rock than in an armour layer with two layers of rock (compare Structure A2 with Structure A3). Additionally, more energy is dissipated by the filter layer of a structure with a 2-rock armour layer than a structure with a 3-rock armour layer.

The structures adhering to the filter rule leading to larger diameter rocks in the underlayer (Test Series A) dissipated more energy in the respective layers than Test Series B (compare Structure A2 with Structure B2). A thicker filter layer (underlayer) improves the wave dissipation by producing a more permeable structure

and reduces the kinetic energy penetrating the core. Appendix R contains the values of the calculated internal energy dissipation for the individual tests.

6.3.1.3 Relationship between External and Internal Energy Dissipation

The high calculated velocities in Section 6.2.2. produced excessive energy components for the internal energy dissipation. It is believed that in reality, the wave energy dissipation due to wave breaking should be more or less in the same numerical range as the internal energy dissipation. Figure 6-7 indicates that external energy dissipation is negligibly small. It can, however, not be the case. The breaking wave will dissipate a significant amount of energy and all the energy will not solely be dissipated by the structure.

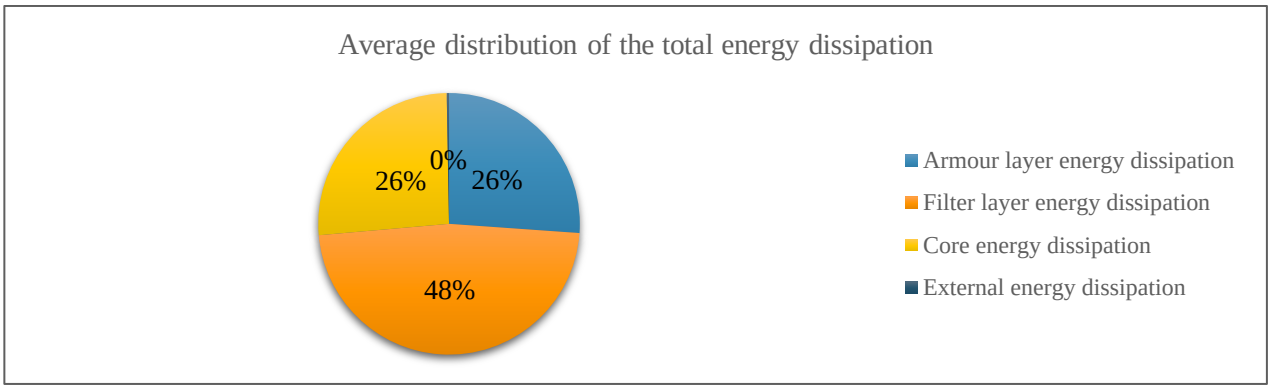

Figure 6-7: Internal and external energy dissipation

6.3.2 KINETIC ENERGY

From Figure 6-8, it is observed that the average calculated kinetic energy in each layer increases as the wave period increase. The armour and filter layer contain the most considerable quantity of the kinetic energy and a smaller fraction of the incident wave energy penetrates the core. On average, 34% of the total kinetic energy in the structure is situated in the core.

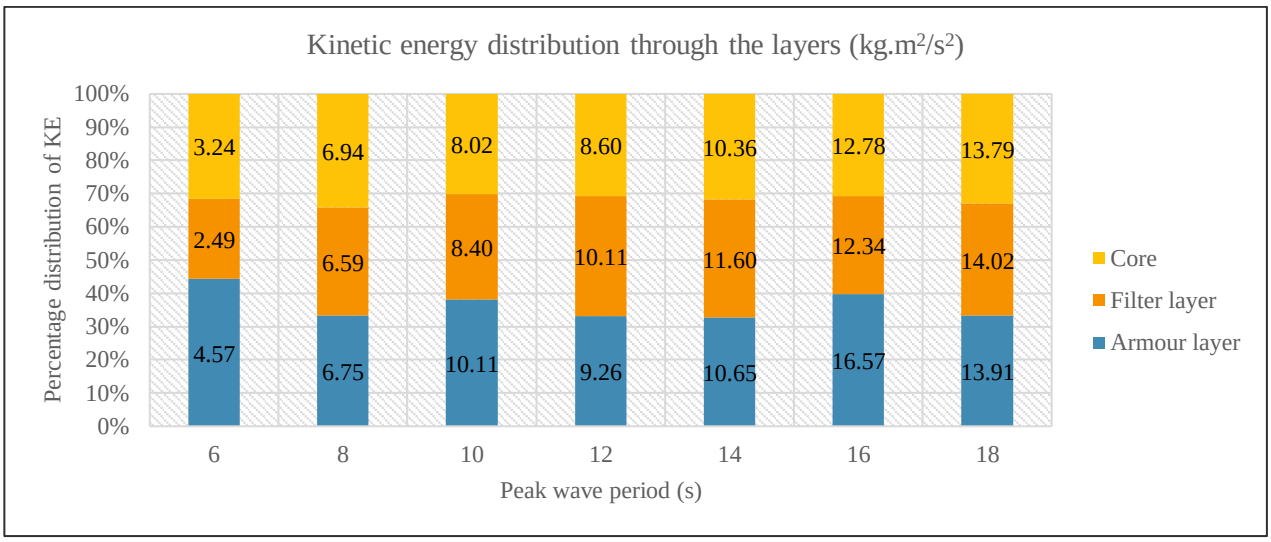

Figure 6-8: Distribution of kinetic energy through layers of rubble-mound structure

The kinetic energy in the individual structures does not indicate such a satisfying trend as that of the average kinetic energy of the six structures in Figure 6-8. The kinetic energy, as calculated for the six structures individually, is given in Appendix S. The designs with a lower crest height have the highest kinetic energy in the core at the majority of wave periods. This outcome is expected since less protection is provided for the core, allowing the energy to travel towards the core.

In the majority of tests, the highest energy regions are located at the outer layers. For the structures of Test Series A, it seems that the highest energy region is dominantly in the filter layer. Whereas for Test Series B, the filter layer is the region with the smallest kinetic energy. The permeability of the structures explains the low energy region. The structures of Test Series B have a filter layer with a smaller median rock diameter, making the structure less permeable and thus forcing the flow to be concentrated in the armour layer. The structures in Test Series A have a more permeable filter layer; the water is thus dissipated into the filter layer and consequently become less violent in the armour layer.

6.3.3 Kinetic Energy Prediction through Dimensional Analysis

Dimensional analysis was applied to predict the kinetic energy in each layer as well as the total kinetic energy of the structure. The experimental results were used to produce an equation to project the kinetic energy in a structure based on known parameters that will influence the energy distribution in the structure. The measured and calculated values are plotted on a scatter graph and a trend line was used to obtain an equation used for prediction. The dependent product is: $\Pi_1 = \frac{KE}{m_{50,core}} (\frac{T}{L})^2$, and the independent product is $\Pi_2 = \frac{t}{L}$ (as identified in Section 3.5.6). Two prediction equations are presented for each layer based on the two respective

filter rules tested in the two-dimensional model. The variable and the applicability range that the equations adhere to are given in the Table 6-2.

Table 6-2: Applicability range for kinetic energy prediction equations

Variable	Core range	Filter range	Armour range	Entire structure range
Filter 1/10				
Layer thickness	660mm	600mm-1200mm	1280mm-1940mm	2540-mm-3500mm
Wavelength	33m - 118m	33m - 118m	33m - 118m	33m - 118m
Peak wave period	6s-18s	6s-18s	6s-18s	6s-18s
Median rock mass	4,7kg	47kg	465kg	4,7kg
Filter 1/15				
Layer thickness	660mm	520mm-780mm	1280mm-1940mm	2460mm-3380mm
Wavelength	32,8m - 116m	32,8m - 116m	32,8m - 116m	32,8m - 116m
Peak wave period	6s-18s	6s-18s	6s-18s	6s-18s
Median rock mass	2,1kg	31kg	465kg	2,1kg

An exponential trend line best describes the relationship between dependent and independent products. The plotted values of the two dimensionless groups are given in Figure 6-9.

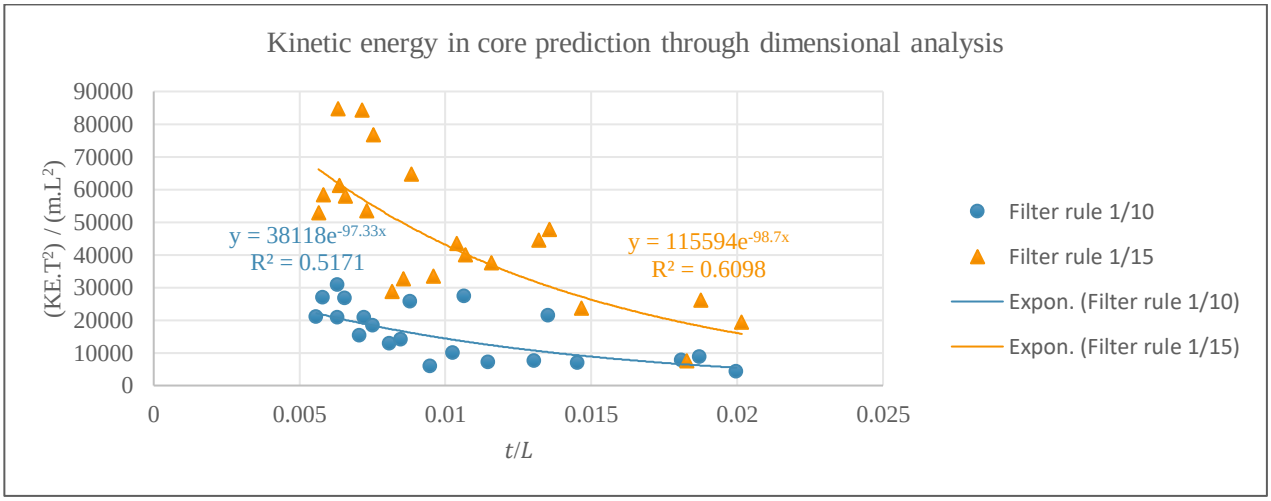

Figure 6-9: Core kinetic energy prediction through dimensional analysis

The equations and coefficients of determination resulting from dimensional analysis are given in Equation 6-2 and Equation 6-3 for predicting the kinetic energy in the core. The correlation coefficients (R) for both equations are above 0.7, which indicate a relatively strong relationship between the two dimensionless products.

Median mass filter rule 1/10:

$$\frac{KE_{core}}{m_{50,core}}\left(\frac{T}{L}\right)^2 = 38118e^{-97.33\left(\frac{t}{L}\right)} \quad 6\text{-}2$$

$$R^2 = 0.52$$

Median mass filter rule 1/15:

$$\frac{KE_{core}}{m_{50,core}}\left(\frac{T}{L}\right)^2 = 115594e^{-98.70\left(\frac{t}{L}\right)} \quad 6\text{-}3$$

$$R^2 = 0.61$$

The exponential trend line of the filter and armour layer is significantly weaker than that of the trend line for the core. Figure 6-10 and Figure 6-11 displays the plotted values for the filter and armour layer, respectively. The median mass of the core rocks is still used in the equations for the filter and armour layer. Since a filter rule is applied to the upper layers of the structure, the median rock mass of the filter and armour layer is merely a product of the core diameter. It will not change the relationship between dependent and independent products.

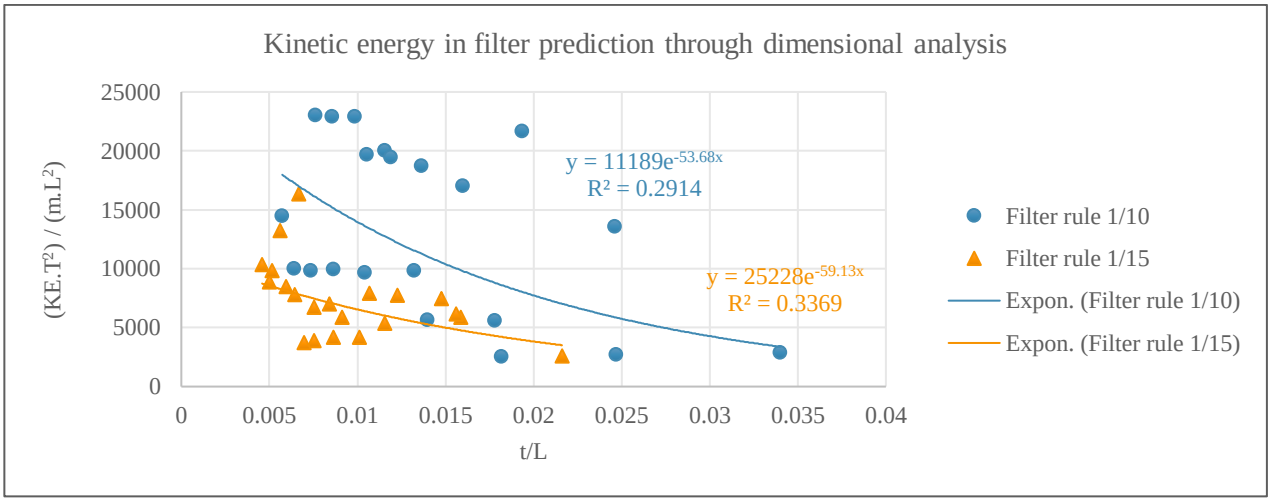

Figure 6-10: Filter kinetic energy prediction through dimensional analysis

The equations and coefficients of determination resulting from dimensional analysis to predict the kinetic energy in the filter layer are given in Equation 6-4 and Equation 6-5.

Median mass filter rule 1/10:

$$\frac{KE_{filter}}{m_{50,core}}\left(\frac{T}{L}\right)^2 = 11189e^{-53.68\left(\frac{t}{L}\right)} \quad 6\text{-}4$$

$$R^2 = 0.29$$

Median mass filter rule 1/15:

$$\frac{KE_{filter}}{m_{50,core}}\left(\frac{T}{L}\right)^2 = 25228e^{-59.13\left(\frac{t}{L}\right)} \qquad 6\text{-}5$$

$$R^2 = 0.37$$

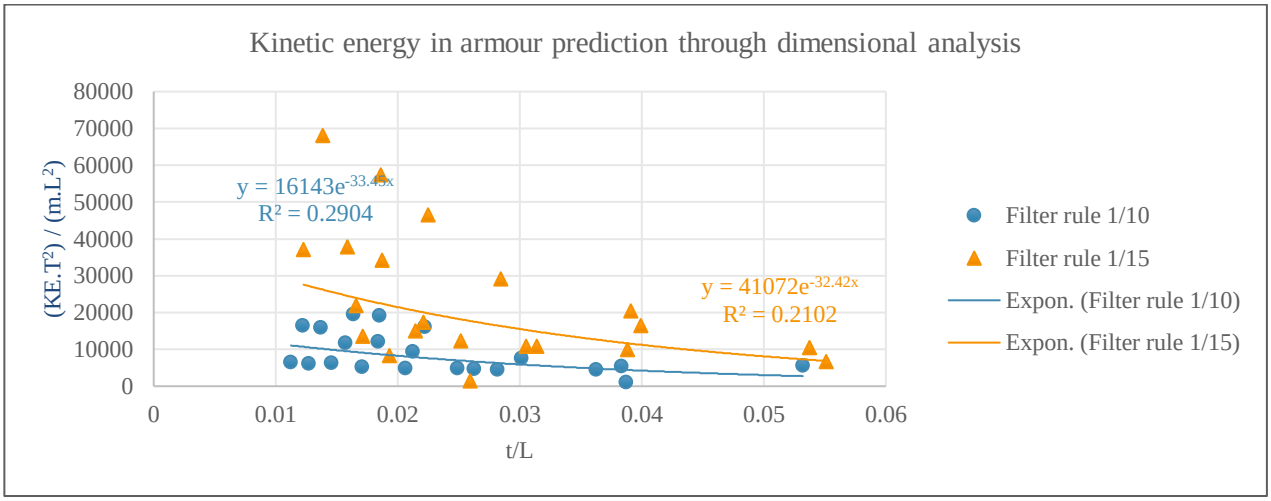

Figure 6-11: Armour kinetic energy prediction through dimensional analysis

The equations and coefficients of determination resulting from dimensional analysis to predict the kinetic energy in the armour layer are given in Equation 6-6 and Equation 6-7.

Median mass filter rule 1/10:

$$\frac{KE_{armour}}{m_{50,core}}\left(\frac{T}{L}\right)^2 = 16143e^{-33.45\left(\frac{t}{L}\right)} \qquad 6\text{-}6$$

$$R^2 = 0.29$$

Median mass filter rule 1/15:

$$\frac{KE_{armour}}{m_{50,core}}\left(\frac{T}{L}\right)^2 = 41072e^{-32.42\left(\frac{t}{L}\right)} \qquad 6\text{-}7$$

$$R^2 = 0.21$$

Lastly, the total kinetic energy in the whole structure is predicted. The graph with the plotted values is shown in Figure 6-12.

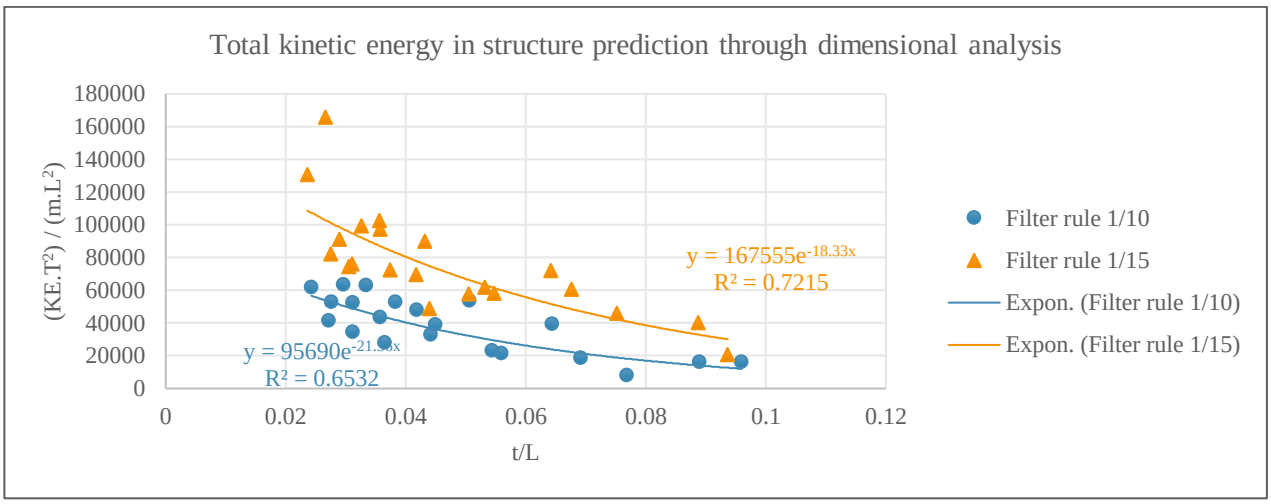

Figure 6-12: Total kinetic energy prediction through dimensional analysis

The equations and coefficients of determination resulting from dimensional analysis to predict the kinetic energy in the whole structure are given in Equation 6-8 and Equation 6-9.

Median mass filter rule 1/10:

$$\frac{KE_{total}}{m_{50,core}}\left(\frac{T}{L}\right)^2 = 95690e^{-21.56\left(\frac{t}{L}\right)} \qquad 6\text{-}8$$

$$R^2 = 0.65$$

Median mass filter rule 1/15:

$$\frac{KE_{total}}{m_{50,core}}\left(\frac{T}{L}\right)^2 = 167555e^{-18.33\left(\frac{t}{L}\right)} \qquad 6\text{-}9$$

$$R^2 = 0.72$$

Based on the correlation coefficients presented above, the kinetic energy in the core and the whole structure can be predicted using the equations generated through dimensional analysis. Interestingly, the flow velocity and kinetic energy in the core showed more satisfactory results compared to the other layers. A relationship with a high correlation coefficient is observed in the flow velocity and kinetic energy in the core for the individual structures (see Appendix P for the strong linear relationship in the core).

The coefficients of determination in Figure 6-10 and Figure 6-11, on the other hand, are extremely low. The equations generated for the filter and armour layer should not be used since it will give unreliable results. It is believed that the core and entire structure kinetic energy equations produce better results due to the pressure transmitters readings being more accurate when measuring under deeper water. Since the armour layer and filter layer were closer to the surface of the water, the variation in pressure head was not recorded as

accurately. Air bubbles possibly entered the pressure transmitters that were closer to the surface when the spilling and plunging waves broke against the structure during the duration of a test. Air bubbles will result in inaccurate readings.

6.3.4 Effect of Energy in Core on Scour Area

The placement of the structure abruptly breaks the approaching wave, and the energy is dissipated in a smaller region than when the wave would break on an unhindered profile. The sudden burst of energy is converted into turbulent flow through the rubble-mound structure to the core. This additional kinetic energy that is released in the core of the rubble-mound structure results in scouring underneath the seawall. Even though the element of longshore transport is not considered in the two-dimensional model, this will additionally increase the scour area. The additional turbulence supports the sediment motion and makes it more accessible to be transported by longshore currents.

It is observed that more energy was dissipated by spilling breakers (Figure 6-4). The plunging water jet of plunging breakers caused a strong downward directed flow. Consequently, less energy was dissipated by the breaking wave itself, and more energy entered the core. This flow was associated with higher velocities in the core as well as more energy in the core (see Figure 6-3 and Figure 6-8). Higher energy in the core caused more scouring of the screed layer, as expected. The effect of the kinetic energy in the core on the scouring of the screed layer is illustrated in Figure 6-13.

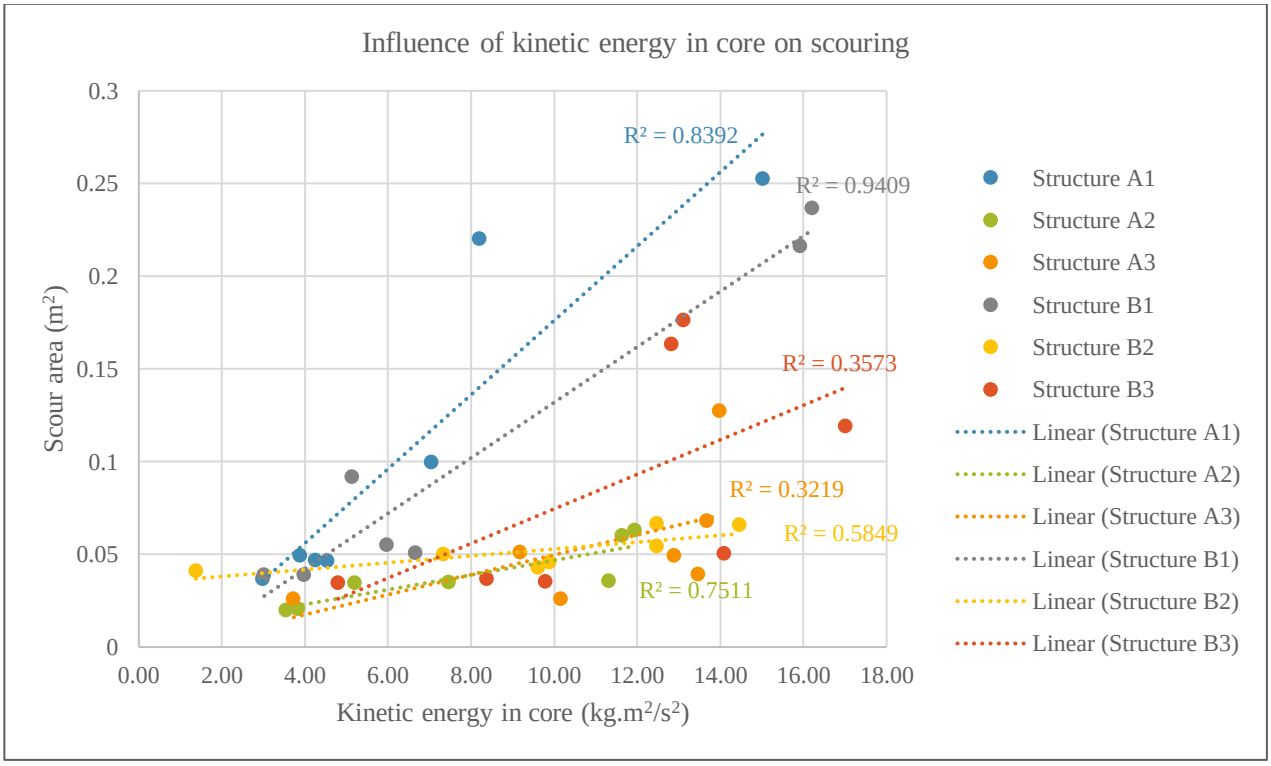

Figure 6-13: Influence of kinetic energy in the core on the scour area underneath seawall

The relationships in Figure 6-13 indicate that scouring of the screed layer can be minimised by limiting the kinetic energy penetrating the core. The design of rubble-mound structures should have the objective of dissipating the maximum possible energy at the outer layers to prevent energy from entering the core and subsequently the screed layer. As was determined in this study, the most effective designs in terms of energy dissipation include a higher rubble-mound crest and a larger median rock mass in the underlayers. These design criteria provide the best protection to the screed layer. Figure 6-13 indicates that the structure with the lowest kinetic energy on average is Structure A2. Structure A2 is the model with the highest crest as well as the largest median rock mass in the underlayers. Owing to its design, Structure A2 has the smallest scoured area of the screed layer.

Suppose during the construction process of a rubble-mound structure, the layer thickness or median rock mass is too narrow and small, and not according to design guidelines, the magnitude of the mistake is too large to ignore as established in this study. It is evident in Figure 6-13 that a smaller structure with a small median rock mass will cause high energy quantities penetrating the core, and consequently lead to disastrous scouring areas. It is advised that in such a scenario the designer and contractor must ensure the correct median rock mass is used and that the layer thickness is thick enough. Providing quality construction, even if it means restarting the building of the structure, will never outweigh the high cost of structural failure.

7 CONCLUSIONS AND RECOMMENDATIONS

7.1 GENERAL

The design of coastal defence systems has become an advancing science due to rapidly changing oceanic conditions as a result of climate change. The consequences of climate change on our coasts and landward infrastructures are a growing concern. The variability in design parameters that the structure might experience in its design life should be accommodated. In many coastal zones, the use of adaptation and soft engineering strategies is no longer an option. Hard engineering strategies are required to protect people and infrastructure from oceanic forces.

Hard engineering strategies are used as a last resort since they occasionally cause erosion on the seaward side as they attempt to protect the landward side. The construction of a structure, like a seawall, in a marine environment, will change the flow pattern in the local area. The change in flow pattern causes the generation of turbulent flow, increasing the wave orbital velocities. The increased velocity will increase the transport of the local sediment and consequently lead to scour. Scour is a major problem in the coastal environment due to it often leading to structural failure.

Hence, there is a need for updated design guidelines when it comes to coastal protection structures. This study aims to contribute to the design guidelines and present insight into the scouring process relating to the thin screed layer below a concrete seawall. The Literature Study had the objective to gain a better understanding of scour development in the marine environment, especially scour that develops next to and underneath a vertical seawall. Additional subjects were also researched in the Literature Study, including coastal parameters relevant to the study, the design of coastal defence structures, the motion of water through a porous structure and the energy dissipation caused by wave breaking.

Based on the findings of the Literature Study, areas were identified to contribute to the optimal design of a rubble-mound structure as protection of the screed layer underneath a vertical seawall. Two-dimensional laboratory tests were conducted to determine the most effective layer thickness of a rubble-mound structure, as well as the optimal median rock mass for the underlayer in the rubble-mound structure. The tests were conducted for typical South-African wave conditions with a wide range of peak wave periods. In total, forty-two tests were conducted where the screed scour area was measured after each test.

During the forty-two tests, the dynamic pressure heads were recorded at four elevations in the rubble-mound structure. The dynamic pressure head recordings were used to gain insight into the flow velocity and energy distribution through the layers of a rubble-mound structure.

7.2 Visual Inspection Conclusion

The visual inspection was conducted by recording and analysing the wave action in front of the vertical seawall. Even though the bathymetry was designed to generate spilling or plunging type breakers, the waves broke directly against the seawall. The direct wave breaking was due to the incident and reflected waves superimposing with each other.

It was observed that with the larger wave periods, the water level above the berm lowered significantly as the wave pulled back. In some cases, the berm was completely exposed. The larger wave periods created more time for the water to drawback, resulting in an immense build-up of water. The high overtopping rate in the large periods was a result of higher celerity and an increase in momentum carried by waves with a longer wavelength. In the most extreme cases (lowest crest height and longest wave period), the berm would completely deform after 2000 waves. The filter layer rocks transferred underneath the seawall and the top positioned rocks in the armour layer moved down the berm slope, extending the toe of the berm seawards.

Dye was placed in the rubble-mound structure to gain insight into the flow type between the rocks. With non-breaking waves, the dye would oscillate faintly. But when a wave broke against the structure, the dye was transported dominantly in a vertical direction and in an irregular pattern through the rubble-mound structure. Over a certain period, the dye would be diluted in the water and no longer visible.

7.3 Scour Development Conclusion

7.3.1 Wave Period vs Scour Development

All six the structures under investigation indicated an increase in the scour area as the wave periods became longer (Figure 5-1 and Figure 5-5). The correlation coefficient for each set of tests showed a strong positive relationship; the six structures had a coefficient of determination between 0.77 and 0.94. The two largest peak wave periods, 16s and 18s, showed significantly higher results than the other wave periods. The 16s and 18s wave periods tested in the models of Structure A1, Structure B1 and Structure B3 produced scoured areas larger than half the area of the initial screed layer after 2000 waves.

In Figure 5-2, the screed layer was 83% washed out for the Test A1-18S, resulting in an extremely exposed core. The poor performance of the structures under the large peak wave periods show that they will perform inadequately in a storm and will most definitely lead to structural failure. The wave celerity explains the increase in scour with the increase in the wave period. The speed of propagation of the wave will increase as the wave period increase leading to a rise in the rate of transmission of wave energy or wave power.

7.3.2 Layer Thickness vs Scour Development

The higher the crest level of a rubble-mound structure, the better is the protection to the screed layer. The larger structure will cause less energy to be reflected, creating a steady sea-state through dissipating the incident wave energy by the rocks in the structure. By adding one layer of rock to both the filter layer and armour layer of Structure A1 and Structure B1, there was a 50% reduction in the average scoured area for Structure A2 and Structure B2 respectively (Figure 5-8 and Figure 5-10).

The structures tested with a thicker filter layer performed quite satisfactorily. By increasing the number of rocks per layer in the filter layer, scour could be reduced significantly. Consider Structure B2 and Structure B3. The difference between these two structures was that Structure B2 had a filter layer consisting of three layers, whereas Structure B3 had a filter layer composed of two layers. The additional layer of rock led to a 41% decrease in the average scour.

Increasing the filter layer (underlayer) thickness had the advantage of a rough surface resulting in better interlocking and a more permeable structure that improved the wave dissipation and armour layer stability. Thus, when increasing the thickness of the berm, the filter layer thickness should be increased before the armour layer. A larger structure does have the disadvantage of potentially being uneconomical since more material is required and increased construction time.

7.3.3 Median Stone Mass vs Scour Development

It is determined that the optimal median stone mass is case-specific. For the smaller structures (Structure A1 and Structure B1) the ratio, $\frac{M_{50\ lower}}{M_{50\ upper}} = \frac{1}{15}$, offered better protection (Figure 5-11). In four of the seven tests conducted per structure, Structure B1 performed better than Structure A1 under the selected peak wave period. In contrast, Structure A2 and Structure A3, with a filter ratio, $\frac{M_{50\ lower}}{M_{50\ upper}} = \frac{1}{10}$, performed better than Structure B2 and Structure B3, respectively (Figure 5-12 and Figure 5-13).

For a peak wave period of 6s, Structure A2 had a scoured area of 0.02m^2, whereas Structure B2 had a scoured area of 0.04m^2. Even though the structures had the same layer thickness, Structure B2 experienced double the scouring than Structure A2 due to having a smaller median rock mass in the underlying layers. It is interesting that as the peak wave periods increased, the difference between the scoured areas among the two filter criteria decreased (Figure 5-12).

For the cases presented in this study, the ratio $\frac{M_{50\ lower}}{M_{50\ upper}} = \frac{1}{10}$ should be applied as it provided the best protection for the majority of tested scenarios. The better results in this ratio are due to an increase in

permeability that leads to increased stability. The larger rocks in the filter layer dissipate more energy, resulting in less energy penetrating the core and screed layer.

7.4 Recommended Design for Screed Layer and Rubble-Mound Structure as Toe Protection

This thesis met all the objectives stated in Chapter 1, and so contributed to the optimal design of a rubble-mound structure as toe protection for a vertical seawall. The research conducted by (Malan, 2016; Van Wageningen, 2018) preceded this study. The findings of the three studies are summarized in Table 7-1 to present rubble-mound structure design guidelines to reduce scouring of the screed layer. The recommendations are site-specific, based on pre-defined coastal conditions.

Table 7-1: Recommended design for screed layer and rubble-mound structure

Design criteria	Recommendation
Study by Malan (2016)	
Screed layer toe width	As small as possible (while still adhering to the filter rules)
Compaction of the foundation	No compaction (the seawall should sink into the screed layer)
Addition of sediment (sand, silt or clay)	Should be avoided
Study by Van Wageningen (2018)	
Rubble-mound structure width (in terms of scour protection, constructability, stability and economic factors)	Width = $4D_{n50}$
Screed layer thickness	100mm in prototype
Current study, 2020	
Rubble-mound structure layer thickness (in terms of scour protection, constructability and economic factors)	Armour layer: 2 layers of rock Filter layer: 3-4 layers of rock
Median rock mass in underlayers	Underlayer rocks should adhere to filter rule: $\frac{M_{50\ lower}}{M_{50\ upper}} = \frac{1}{10}$ (leading to larger rocks in underlayers)

7.5 Energy Distribution Conclusion

7.5.1 Accuracy of Measured Pressures

Stellenbosch University has a PIV system that was unavailable during the time of conducted tests, and the Water Laboratory has no other equipment to measure the velocity. Hence, the velocities used in the energy calculations were obtained from basic principles. The pressures were measured at different elevations in the rubble-mound structure and converted into velocities. This method is not preferred since the small-scale model does not represent the prototype adequately for this purpose.

It is believed that scale effects played a role in the measurements, especially the air entrainment associated with spilling or plunging type breaking waves. The shock loads caused by breaking waves are sensitive to the shape and kinematics of breaking waves, which is challenging to reproduce in the laboratory. And lastly, the water level is too shallow to measure the dynamic pressure head accurately. There is a possibility that air bubbles entered the pressure transmitters when the water level pulled back right before the wave breaks against the seawall and subsequently causing inaccurate readings.

7.5.2 Flow Velocity

The flow velocities within the mound structures were calculated with the Forchheimer equation. The turbulent coefficient in the Forchheimer equation dominated, indicating that the flow regime in the rubble-mound structure was dominantly turbulent. The velocity in the core is the highest, with the velocity in the armour layer being the lowest at all seven peak wave periods tested (Figure 6-3). The calculated flow velocities were higher than expected; this is believed to be due to the measuring technique. The highest average calculated velocity in the core was 2.9m/s at a peak wave period of 18s.

7.5.3 Energy Distribution in Layers of Rubble-Mound

7.5.3.1 Energy Dissipation

The external energy dissipation due to wave breaking showed a decline with an increase in wave periods. The calculated values at the various tested wave periods remained relatively constant for the different structures (Figure 6-4). The internal energy dissipation was the highest in the filter layer, with the core dissipating the least energy. The core dissipated less than 30% of the total energy in the structure for all seven peak wave periods (Figure 6-5). In the model, the measurements indicated that the energy dissipation due to wave breaking is negligible, where in the prototype a significant amount of energy will be dissipated by the breaking wave.

7.5.3.2 Kinetic Energy

The general trend displayed that an increase in the peak wave period produced an increase in the total kinetic energy in the structure. It was also observed that the structures with a lower crest height, allowed more energy to travel towards the core. On average, the highest energy regions were situated in the outer layers of the structure, and 34% of the energy was located in the core (Figure 6-8). A more permeable filter layer (underlayer) allowed the energy into the layer, and consequently, less energy was located in the armour layer. In contrast, a less permeable filter layer forced the flow to be concentrated in the armour layer.

The process of dimensional analysis was applied to determine the kinetic energy in the structure based on major identified parameters influencing the energy distribution through the structure. The equations produced for predicting the kinetic energy in the core and the kinetic energy in the entire structure generated a strong correlation (Figure 6-9 and Figure 6-12). In contrast, the equations for the filter and armour layer had weak correlation coefficients and are recommended not to be used to predict the kinetic energy (Figure 6-10 and Figure 6-11).

7.5.3.3 Influence of Energy in Core on Scour Development

As expected, the scoured screed area increased with an increase in kinetic energy in the core (Figure 6-13). The individual structures generated strong correlation coefficients between these two parameters. The relationship indicates the importance of the outer layers in terms of protecting the core to minimise scour. The outer layers should dissipate the larger quantity of energy, allowing limited energy into the core. Quality design and construction is vital to minimise energy penetrating the core. Providing quality construction, will not outweigh the high cost of structural failure.

7.6 Recommendations for Further Research

A wide range of peak wave periods was tested in the model. It is recommended that other incident wave conditions are tested in future research (this include wave height, water depth, slope, etc.). The scour trends according to varying wave periods gave contradictory results to those of Van Wageningen (2018). The possible reasons for the difference were identified in Section 5.5 as a slightly dissimilar bathymetry and different rock grading widths. These two factors can be investigated to determine if they will indeed produce different scouring patterns. The two studies also use other measuring techniques. It will be an insightful investigation to determine an accurate measuring technique since there is no proven technology or method used in practice to determine the scour.

The filter layer (underlayer) proved to be very effective in protecting the screed layer against scour. It is thus recommended that different filter layers (thickness, rock diameters, rock grading, rock shape, etc.) should be investigated to determine the optimal filter layer design.

Only one filter criterion is tested in this two-dimensional model. There are, however, many other criteria the rock gradings should obey (discussed in Section 2.2.4). The effect of these criteria on scour should be tested to determine the optimal rock sizes in the layers of the rubble-mound structure.

Only 2000 waves are conducted for each test in this study. The equilibrium stage is determined by Van Wageningen (2018); however, storm wave durations were not considered in this study. Due to scour not being a rapid process, the length of the storm duration will also have an impact on scour development. Future research should determine the equilibrium stage by considering storm wave durations.

The topic of energy distribution through the porous rubble-mound structure was briefly considered in this study. Future research should expand on this topic by firstly improving the measuring technique of the velocity in the rubble-mound structure. The method used to measure the pressure and to convert it into velocity requires very accurate modelling of the wave conditions. Future researchers should use other approaches to obtain flow velocity. Methods include particle image velocimetry (PIV) and laser doppler velocity (LDV) meters. One of the possible reasons for the weak relationship among the pressure measurements is the scale effects associated with air bubbles. The influence of this scale effect can be investigated by comparing the velocities with those obtained using the PIV and LDV methods.

In this study, only the average flow velocity during wave breaking was considered. Defining the orbital velocities in the structure to accurately determine the flow regime and to determine the fluctuation of the flow velocity as the waves approach the structure and break against the seawall will significantly contribute to the academic field. It will provide insight into the energy distribution over time and can determine the instant the structure is most vulnerable.

The energy dissipation due to wave breaking method by Battjes and Janssen (1978) was used as a first approximation to determine the energy dissipation on a rubble-mound structure. This method was, however, developed to be applied on a beach slope. The accuracy of using this method on different slopes (including a rubble-mound structure) should be researched in the future.

8 REFERENCES

Ayers, J. R. (1950) 'Seawalls and Breakwaters', in *Coastal Engineering Proceedings*. Washington, D.C., pp. 192–204.

Battjes, J. A. and Janssen, J.P.F.M. (1978) 'Energy loss and set-up due to breaking random waves', in *16th International Conference on Coastal Engineering*. Hamburg. doi: 10.9753/icce.v16.

Betzold, C. and Mohamed, I. (2017) 'Seawalls as a response to coastal erosion and flooding : a case study from Grande Comore , Comoros (West Indian Ocean)', *Regional Environmental Change*. 17(4), pp. 1077–1087. doi: 10.1007/s10113-016-1044-x.

CIRIA (2007) *The Rock Manual:The Use of Rock in Hydraulic Engineering*. 2nd edn. Edited by K. Asmerson et al. London: CIRIA.

Chadwick, A., Morfett, J. & Borthwick, M., (2013). *Hydraulics in Civil and Environmetal Engineering.* 5th Edition ed. New York: CRC Press.

Coastal Care, (2019). *A Retreat In The Face Of a Rising Sea, California.* [Online] Available at: http://coastalcare.org/2011/01/a-retreat-in-the-face-of-a-rising-sea/ [Accessed 6 June 2019].

CSIR, 2020. *Online Data.* [Online] Available at: http://wavenet.csir.co.za/OnlineData/RealtimeData.htm [Accessed 20 October 2020].

Fowler, J. E. (1992) *Scour Problems and Methods for Prediction of Maximum Scour at Vertical Seawalls*. USACE, Coastal Engineering Research Center, Vicksburg.

Gravesen, H. (2008) *Rubble Mound Breakwaters.* Lecture Notes. Technical University of Denmark.

Gregersen, E., 2020. *Britannica.* [Online] Available at: https://www.britannica.com/science/kinetic-energy [Accessed 28 November 2020].

Hoffmans, G. & Verheij, H., (1994). *Scour Manual.* Rotterdam: A.A. Balkema Publishers.

HR Wallingford (2010) *Flume Wave Generation System Technical Manual*. Wallingford, Oxfordshire.

Hudson, R. Y. *et al.* (1979) *Coastal Hydraulic Models*. Special Report No.5, USACE, Coastal Engineering

Research Center,Virginia.

Hughes, S.A. & Fowler, J.E., (1991). *Wave-induced scour prediction at vertical walls.* ASCE Proceedings Conference Coastal Sediments 91, pp.1886-1899.

Hughes, S. A., (1993). *Physical Models and Laboratory Techniques in Coastal Engineering.* New Jersey:World Scientific Publishing .

IADC: International Association of Dredging Companies, 2017. *Coastal Protection.* [Online] Available at: https://www.iadc-dredging.com/ul/cms/fck-uploaded/documents/PDF%20Facts%20About/facts-about-coastal-protection.pdf

[Accessed 6 June 2019].

Jensen, O. J. and Klinting, P. (1983) 'Evaluation of scale effects in hydraulic models by analysis of laminar and turbulent flows', *Coastal Engineering*, 7(1983), pp. 319–329.

Malan, C. T. (2016) *Scour of the screed layer underneath a vertical seawall with a rubble mound*. Master's Thesis. Stellenbosch: Stellenbosch University.

Mansard, E. P. D. and Funke, E. R. (1980) 'The measurement of incident and reflected spectra using a least squares method', in *17th International Conference on Coastal Engineering*, pp. 154–172.

McDougal, W. G., Kraus, N. C. and Ajiwibowo, H. (1996) 'The effects of seawalls on the beach: Part II, numerical modelling of SUPERTANK seawall tests', *Journal of Coastal Research*, 12(3), pp. 702–713.

Muttray, M., Oumeraci, H., Zimmermann, Z. and Partenscky, H.W., (1992) 'Wave Energy Dissipation on and in Rubble Mound Structures', *Coastal Engineering Proceedings, ICCE 1992*, pp. 1434–1447.

O'Donoghue, T. (2001) 'N-type sediment bed response understanding wave.pdf', *Journal of Waterway, Port, Coastal and Ocean Engineering*, pp. 245–248.

Oumeraci, H. and Partenscky, H. W. (1990) 'Wave-induced Pore Pressure in Rubble Mound Breakwaters', *Coastal Engineering Proceedings*, pp. 1334–1347.

Pico Technology (2009) *PicoLog 1000 Series User's Guide*.

Powell, K. (1987) *Toe Scour at Sea Walls Subject to Wave Action*. HR Wallingford, Wallingford, Oxfordshire.

Powell, K. A. and Lowe, J. P. (1994) 'The scouring of sediments at the toe of seawalls', in Viggosson, G. (ed.) *Proceedings of the Hornafjordur International Coastal Symposium*. Iceland, pp. 749–755.

Ryu, Y. *et al.* (2016) 'Wave Energy Dissipation by Permeable and Impermeable Submerged Breakwaters', 9(6), pp. 2635–2645. doi: 10.29252/jafm.09.06.25530.

Schoonees, J. S. (2001) *Longshore sediment transport: applied wave power approach, field data analysis and evaulation of formulae*. PhD Dissertation. Stellenbosch: Stellenbosch University.

Schoonees, T. (2014) *Impermeable recurve seawalls to reduce wave overtopping*. Master's Thesis. Stellenbosch: Stellenbosch University.

Sumer, B. M. & Fredsoe, J., (2002). *The Mechanics of Scour in the Marine Environment.* Singapore: World Scientific.

Sutherland, J. (2003) *Beach lowering in front of coastal structures, research scoping study*. London. doi: 10.13140/RG.2.1.2927.3365.

USACE: United States Army Corps of Engineers, (1984). *Shore Protection Manual.* 4th Edition ed. Vicksburg(Mississippi): s.n.

USACE: United States Army Corps of Engineers, (2002) *Coastal Engineering Manual*. Washington, D.C.: U.S. Army Corps of Engineers.

Van der Meer, J. W. (1992) *Conceptual Design of Rubble Mound Breakwaters*. Conference Short Course, 23rd ICCE 1992, Venice

Van der Meer, J. W. and Daemen, I. F. R. (1994) 'Stability and wave transmission at low crested rubble mound structures', *Journal of Waterway, Port, Coastal and Ocean Engineering*, 120(1), pp. 1–19.

Van der Meer, J.W, d'Angremond, K. and de Jong, R., (1996) *Wave transmission at low crested structures.* s.l., Coastal Engineering Proceedings.

Van der Meer, J. W. (1998) *Geometrical design of coastal structures. Ch 9 in Dikes and Revetments by Pilarczyk, IAHR.*

Van der Meer, J.W., Briganti, R., Wang, B. & Zanuttigh, B.,(2004) 'Wave transmission at low-crested structures, including oblique wave attack', in *Internaional Conference on Coastal Engineering*. Lisbon: ASCE.

Van Gent, M. R. A. (1992) 'Numerical model for wave action on and in coastal structures', Communications on hydraulic and geotechnical engineering, No. 1992-06. TU Delft, pp. 7–42.

Van Gent, M. R. A. (1995) 'Wave Interaction with Permeable Coastal Structures', *International journal of*

rock mechanics and mining sciences & geomechanics abstracts, 33(6), pp. 7–131. doi: 10.1061/(ASCE)0733-950X(1995)121.

Van Gent, M. R. A. and Wolters, G. (2015) 'Granular slopes with open filters under wave loading', *Coastal Engineering*. Elsevier B.V., 104, pp. 135–150. doi: 10.1016/j.coastaleng.2015.06.004.

Van Wageningen, E. (2018) *Design of Rubble-mound Foundations for Vertical Seawalls : Scour , Screed Layer and Berm Width*. Master's Thesis. Stellenbosch: Stellenbosch University.

Whitehouse, R. J. S. and Powell, K. (1998) 'The occurence and prediction of scour at coastal and estuarine structures', in *MAFF Conference of River and Coastal Engineers*. UK: Keele University. doi: 10.13140/RG.2.1.2927.3365.

Williams, A. T., Giardino, A. and Pranzini, E. (2016) 'Canons of Coastal Engineering in the United Kingdom: Seawalls/Groynes, a Century of Change', *Journal of Coastal Research*, 32(5), pp. 1196–1211.

APPENDICES

APPENDIX A: FROUDE AND REYNOLDS SIMILITUDES

Table A- 1: Froude and Reynolds similitude derivations

	Characteristic	Dimension	Froude	Reynolds
Geometric	Length	[L]	N_L	N_L
	Area	[L^2]	N_L^2	N_L^2
	Volume	[L^3]	N_L^3	N_L^3
Kinematic	Time	[T]	$N_L^{1/2} N_\rho^{1/2} N_y^{-1/2}$	$N_L^2 N_\rho N_\mu^{-1}$
	Velocity	[LT^{-1}]	$N_L^{1/2} N_\rho^{-1/2} N_y^{1/2}$	$N_L^{-1} N_\rho^{-1} N_\mu$
	Acceleration	[LT^{-2}]	$N_y N_\rho^{-1}$	$N_L^3 N_\rho^{-2} N_\mu^2$
	Discharge	[L^3T^{-1}]	$N_L^{5/2} N_\rho^{-1/2} N_y^{1/2}$	$N_L N_\rho^{-1} N_\mu$
	Kinematic viscosity	[L^2T^{-1}]	$N_L^{3/2} N_\rho^{-1/2} N_y^{1/2}$	$N_\rho^{-1} N_\mu$
Dynamic	Mass	[M]	$N_L^3 N_\rho$	$N_L^3 N_\rho$
	Force	[MLT^{-2}]	$N_L^3 N_y$	$N_\rho^{-1} N_\mu^2$
	Mass density	[ML^{-3}]	$N_L^{3/2} N_\rho^{-1/2} N_y^{1/2}$	N_ρ
	Specific weight	[$ML^{-2}T^{-2}$]	$N_L^{3/2} N_\rho^{-1/2} N_y^{1/2}$	$N_L^{-3} N_\rho^{-1} N_\gamma^{-2}$
	Dynamic viscosity	[$ML^{-1}T^{-1}$]	$N_L^{3/2} N_\rho^{1/2} N_y^{-1/2}$	N_μ
	Surface tension	[MT^{-2}]	$N_L^2 N_y$	$N_L^{-1} N_\rho^{-1} N_\mu^2$
	Volume elasticity	[$ML^{-1}T^{-2}$]	$N_L N_y$	$N_L^{-2} N_\rho^{-1} N_\mu^2$
	Pressure and stress	[$ML^{-1}T^{-2}$]	$N_L N_y$	$N_L^{-2} N_\rho^{-1} N_\mu^2$
	Momentum and impulse	[MLT^{-1}]	$N_L^{7/2} N_\rho^{1/2} N_y^{1/2}$	$N_L^2 N_\mu$
	Energy and work	[ML^2T^{-2}]	$N_L^4 N_y$	$N_L N_\rho^{-1} N_\mu^2$
	Power	[ML^2T^{-3}]	$N_L^{7/2} N_\rho^{-1/2} N_y^{3/2}$	$N_L^{-1} N_\rho^{-2} N_y^3$

APPENDIX B: WATER LEVEL, WAVELENGTH AND BREAKER TYPE

WATER LEVEL

The Table B-1 indicates the water depth at various points in the model and the prototype. The full bathymetry can be seen in Figure B-1.

Where

d_3 = Water depth above rubble-mound structure (m)

d_2 = Water depth at toe of rubble-mound structure (m)

d_1 = Water depth at the start of the 1:20 slope (m)

d_0 = Water depth at flat slope (m)

Table B- 1: Water levels in the prototype and the model

		Prototype				Model			
Test nu.	**Test Set**	**d_3 (m)**	**d_2 (m)**	**d_1 (m)**	**d_0 (m)**	**d_3 (m)**	**d_2 (m)**	**d_1 (m)**	**d_0 (m)**
1-7	A1	1	3,55	9,75	10,95	0,05	0,177	0,487	0,547
8-14	A2	1	4,49	10,69	11,89	0,05	0,224	0,534	0,594
15-21	A3	1	4,14	10,34	11,54	0,05	0,207	0,517	0,577
22-28	B1	1	3,47	9,67	10,87	0,05	0,174	0,484	0,544
29-35	B2	1	4,38	10,58	11,78	0,05	0,219	0,529	0,589
36-42	B3	1	4,11	10,31	11,51	0,05	0,206	0,516	0,576

WAVELENGTH

The wavelength is calculated using the Equation B-1. The calculation thereof is an iterative process.

$$L = \frac{gT^2}{2\pi} tanh\left(\frac{2\pi d}{L}\right) \qquad B\text{-}1$$

Table B-2 and Table B-3 is the values obtained for the shallow water wavelengths and the deepwater wavelengths through the iterative process. L_{10} in each case is used as the wavelength for the two-dimensional model. The difference between L_9 and L_{10} is negligible.

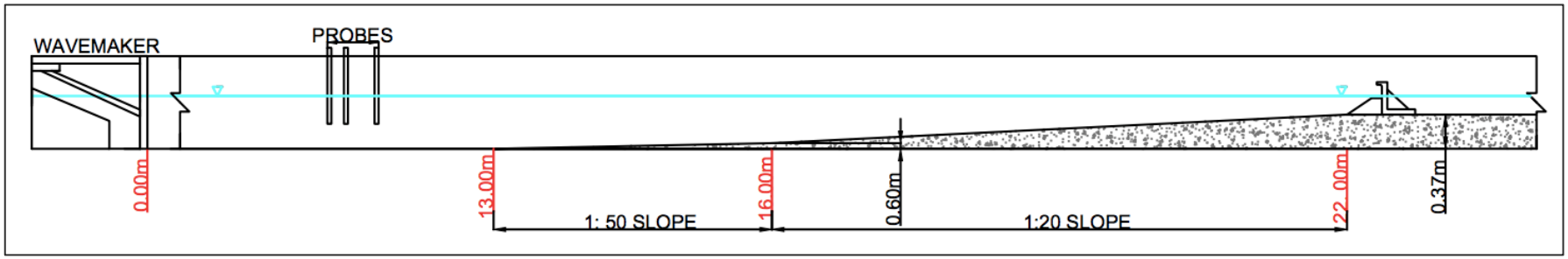

Figure B- 1: Bathymetry drawn on scale for the model

Table B- 2: Shallow water wavelength iterative process

Test Code	Shallow water wavelength (m)																				
A1 – 6S	L0	56	L1	21	L2	39	L3	29	L4	34	L5	32	L6	33	L7	33	L8	33	L9	33	L10	33
A1 – 8S	L0	100	L1	22	L2	61	L3	35	L4	48	L5	43	L6	46	L7	45	L8	45	L9	45	L10	45
A1 – 10S	L0	156	L1	22	L2	89	L3	38	L4	64	L5	52	L6	58	L7	57	L8	58	L9	58	L10	58
A1 -12S	L0	225	L1	22	L2	124	L3	40	L4	82	L5	60	L6	71	L7	69	L8	70	L9	70	L10	70
A1 – 14S	L0	306	L1	22	L2	164	L3	41	L4	103	L5	65	L6	84	L7	79	L8	82	L9	81	L10	82
A1 – 16S	L0	400	L1	22	L2	211	L3	42	L4	127	L5	70	L6	98	L7	89	L8	94	L9	93	L10	93
A1 – 18S	L0	506	L1	24	L2	265	L3	45	L4	155	L5	77	L6	116	L7	103	L8	109	L9	109	L10	109
A2 – 6S	L0	56	L1	26	L2	41	L3	33	L4	37	L5	36	L6	37	L7	36	L8	36	L9	36	L10	36
A2 – 8S	L0	100	L1	27	L2	64	L3	42	L4	53	L5	49	L6	51	L7	50	L8	51	L9	51	L10	51
A2 – 10S	L0	156	L1	28	L2	92	L3	46	L4	69	L5	60	L6	65	L7	64	L8	64	L9	64	L10	64
A2 – 12S	L0	225	L1	28	L2	126	L3	49	L4	88	L5	70	L6	79	L7	77	L8	78	L9	78	L10	78
A2 – 14S	L0	306	L1	28	L2	167	L3	51	L4	109	L5	77	L6	93	L7	90	L8	92	L9	91	L10	91
A2 – 16S	L0	400	L1	28	L2	214	L3	52	L4	133	L5	83	L6	108	L7	102	L8	105	L9	105	L10	105
A2 – 18S	L0	506	L1	28	L2	267	L3	53	L4	160	L5	88	L6	124	L7	113	L8	119	L9	118	L10	118
A3 – 6S	L0	56	L1	24	L2	40	L3	32	L4	36	L5	35	L6	35	L7	35	L8	35	L9	35	L10	35
A3 – 8S	L0	100	L1	25	L2	63	L3	39	L4	51	L5	47	L6	49	L7	49	L8	49	L9	49	L10	49
A3 – 10S	L0	156	L1	26	L2	91	L3	44	L4	67	L5	58	L6	62	L7	62	L8	62	L9	62	L10	62
A3 – 12S	L0	225	L1	26	L2	125	L3	46	L4	86	L5	66	L6	76	L7	74	L8	75	L9	75	L10	75
A3 – 14S	L0	306	L1	26	L2	166	L3	48	L4	107	L5	73	L6	90	L7	86	L8	88	L9	88	L10	88
A3 – 16S	L0	400	L1	26	L2	213	L3	49	L4	131	L5	79	L6	105	L7	97	L8	101	L9	101	L10	101
A3 – 18S	L0	506	L1	26	L2	266	L3	49	L4	158	L5	83	L6	120	L7	108	L8	114	L9	114	L10	114
B1 – 6S	L0	56	L1	21	L2	38	L3	29	L4	34	L5	32	L6	33	L7	33	L8	33	L9	33	L10	33
B1 – 8S	L0	100	L1	21	L2	61	L3	34	L4	48	L5	43	L6	45	L7	45	L8	45	L9	45	L10	45
B1 – 10S	L0	156	L1	22	L2	89	L3	38	L4	63	L5	52	L6	58	L7	57	L8	57	L9	57	L10	57
B1 – 12S	L0	225	L1	22	L2	123	L3	39	L4	81	L5	59	L6	70	L7	68	L8	69	L9	69	L10	69

Table B-2: Shallow water wavelength iterative process continued

B1 - 14S	L0	306	L1	22	L2	164	L3	40	L4	102	L5	64	L6	83	L7	78	L8	81	L9	81	L10	81
B1 - 16S	L0	400	L1	22	L2	211	L3	41	L4	126	L5	68	L6	97	L7	88	L8	93	L9	92	L10	93
B1 - 18S	L0	506	L1	22	L2	264	L3	42	L4	153	L5	72	L6	112	L7	97	L8	105	L9	104	L10	104
B2 - 6S	L0	56	L1	25	L2	41	L3	33	L4	37	L5	36	L6	36	L7	36	L8	36	L9	36	L10	36
B2 - 8S	L0	100	L1	27	L2	63	L3	41	L4	52	L5	48	L6	50	L7	50	L8	50	L9	50	L10	50
B2 - 10S	L0	156	L1	27	L2	92	L3	45	L4	69	L5	59	L6	64	L7	63	L8	64	L9	64	L10	64
B2 - 12S	L0	225	L1	27	L2	126	L3	48	L4	87	L5	69	L6	78	L7	76	L8	77	L9	77	L10	77
B2 - 14S	L0	306	L1	27	L2	167	L3	50	L4	108	L5	76	L6	92	L7	89	L8	90	L9	90	L10	90
B2 - 16S	L0	400	L1	27	L2	214	L3	51	L4	132	L5	82	L6	107	L7	100	L8	104	L9	103	L10	104
B2 - 18S	L0	506	L1	27	L2	267	L3	52	L4	159	L5	86	L6	123	L7	111	L8	117	L9	117	L10	117
B3 - 6S	L0	56	L1	24	L2	40	L3	32	L4	36	L5	35	L6	35	L7	35	L8	35	L9	35	L10	35
B3 - 8S	L0	100	L1	25	L2	63	L3	39	L4	51	L5	47	L6	49	L7	48	L8	49	L9	49	L10	49
B3 - 10S	L0	156	L1	26	L2	91	L3	43	L4	67	L5	57	L6	62	L7	61	L8	62	L9	62	L10	62
B3 - 12S	L0	225	L1	26	L2	125	L3	46	L4	86	L5	66	L6	76	L7	74	L8	75	L9	75	L10	75
B3 - 14S	L0	306	L1	26	L2	166	L3	47	L4	107	L5	73	L6	90	L7	86	L8	88	L9	88	L10	88
B3 - 16S	L0	400	L1	26	L2	213	L3	48	L4	131	L5	78	L6	104	L7	97	L8	101	L9	100	L10	101
B3 -18S	L0	506	L1	26	L2	266	L3	49	L4	157	L5	82	L6	120	L7	107	L8	114	L9	113	L10	113

Table B- 3: Deep-water wavelength iterative process

Test Code	**Deepwater wavelength (m)**																					
A1 - 6S	L0	56	L1	47	L2	52	L3	49	L4	50	L5	49	L6	50	L7	50	L8	50	L9	50	L10	50
A1 - 8S	L0	100	L1	60	L2	80	L3	70	L4	75	L5	73	L6	74	L7	73	L8	73	L9	73	L10	73
A1 - 10S	L0	156	L1	65	L2	110	L3	86	L4	98	L5	94	L6	96	L7	96	L8	96	L9	96	L10	96
A1 -12S	L0	225	L1	67	L2	146	L3	99	L4	122	L5	115	L6	118	L7	118	L8	118	L9	118	L10	118
A1 - 14S	L0	306	L1	68	L2	187	L3	108	L4	147	L5	133	L6	140	L7	139	L8	140	L9	140	L10	140
A1 - 16S	L0	400	L1	68	L2	234	L3	114	L4	174	L5	150	L6	162	L7	160	L8	161	L9	161	L10	161
A1 - 18S	L0	506	L1	68	L2	287	L3	119	L4	203	L5	165	L6	184	L7	181	L8	182	L9	182	L10	182
A2 - 6S	L0	56	L1	49	L2	53	L3	50	L4	51	L5	50	L6	51	L7	51	L8	51	L9	51	L10	51
A2 - 8S	L0	100	L1	63	L2	82	L3	72	L4	77	L5	75	L6	76	L7	75	L8	76	L9	76	L10	76
A2 - 10S	L0	156	L1	69	L2	113	L3	91	L4	102	L5	98	L6	100	L7	99	L8	99	L9	99	L10	99
A2 - 12S	L0	225	L1	72	L2	148	L3	104	L4	126	L5	119	L6	123	L7	122	L8	122	L9	122	L10	122
A2 - 14S	L0	306	L1	73	L2	190	L3	115	L4	152	L5	139	L6	146	L7	144	L8	145	L9	145	L10	145
A2 - 16S	L0	400	L1	74	L2	237	L3	122	L4	179	L5	157	L6	168	L7	167	L8	167	L9	167	L10	167
A2 - 18S	L0	506	L1	74	L2	290	L3	127	L4	209	L5	174	L6	191	L7	188	L8	190	L9	190	L10	190
A3 - 6S	L0	56	L1	48	L2	52	L3	50	L4	51	L5	50	L6	50	L7	50	L8	50	L9	50	L10	50
A3 - 8S	L0	100	L1	62	L2	81	L3	71	L4	76	L5	74	L6	75	L7	75	L8	75	L9	75	L10	75
A3 - 10S	L0	156	L1	68	L2	112	L3	89	L4	100	L5	96	L6	98	L7	98	L8	98	L9	98	L10	98
A3 - 12S	L0	225	L1	70	L2	147	L3	102	L4	125	L5	118	L6	121	L7	120	L8	121	L9	121	L10	121

Table B-3: Deep-water wavelength iterative process continued

A3 - 14S	L0	306	L1	71	L2	189	L3	112	L4	150	L5	137	L6	144	L7	143	L8	143	L9	143	L10	143
A3 - 16S	L0	400	L1	72	L2	236	L3	119	L4	177	L5	155	L6	166	L7	164	L8	165	L9	165	L10	165
A3 - 18S	L0	506	L1	72	L2	289	L3	124	L4	207	L5	171	L6	189	L7	185	L8	187	L9	187	L10	187
B1 - 6S	L0	56	L1	47	L2	52	L3	49	L4	50	L5	49	L6	50	L7	49	L8	50	L9	49	L10	50
B1 - 8S	L0	100	L1	59	L2	80	L3	69	L4	75	L5	72	L6	73	L7	73	L8	73	L9	73	L10	73
B1 - 10S	L0	156	L1	64	L2	110	L3	86	L4	98	L5	94	L6	96	L7	95	L8	96	L9	96	L10	96
B1 - 12S	L0	225	L1	66	L2	146	L3	98	L4	122	L5	114	L6	118	L7	117	L8	118	L9	118	L10	118
B1 - 14S	L0	306	L1	67	L2	187	L3	107	L4	147	L5	133	L6	140	L7	139	L8	139	L9	139	L10	139
B1 - 16S	L0	400	L1	68	L2	234	L3	114	L4	174	L5	150	L6	162	L7	160	L8	161	L9	160	L10	161
B1 - 18S	L0	506	L1	68	L2	287	L3	118	L4	203	L5	164	L6	183	L7	180	L8	182	L9	182	L10	182
B2 - 6S	L0	56	L1	49	L2	52	L3	50	L4	51	L5	50	L6	51	L7	50	L8	51	L9	50	L10	51
B2 - 8S	L0	100	L1	63	L2	81	L3	72	L4	77	L5	75	L6	76	L7	75	L8	75	L9	75	L10	75
B2 - 10S	L0	156	L1	69	L2	113	L3	90	L4	101	L5	97	L6	99	L7	99	L8	99	L9	99	L10	99
B2 - 12S	L0	225	L1	71	L2	148	L3	104	L4	126	L5	119	L6	122	L7	122	L8	122	L9	122	L10	122
B2 - 14S	L0	306	L1	73	L2	189	L3	114	L4	152	L5	139	L6	145	L7	144	L8	144	L9	144	L10	144
B2 - 16S	L0	400	L1	73	L2	236	L3	121	L4	179	L5	157	L6	168	L7	166	L8	167	L9	167	L10	167
B2 - 18S	L0	506	L1	73	L2	290	L3	126	L4	208	L5	173	L6	190	L7	187	L8	189	L9	189	L10	189
B3 - 6S	L0	56	L1	48	L2	52	L3	50	L4	51	L5	50	L6	50	L7	50	L8	50	L9	50	L10	50
B3 - 8S	L0	100	L1	62	L2	81	L3	71	L4	76	L5	74	L6	75	L7	75	L8	75	L9	75	L10	75
B3 - 10S	L0	156	L1	68	L2	112	L3	89	L4	100	L5	96	L6	98	L7	98	L8	98	L9	98	L10	98
B3 - 12S	L0	225	L1	70	L2	147	L3	102	L4	125	L5	117	L6	121	L7	120	L8	121	L9	121	L10	121
B3 - 14S	L0	306	L1	71	L2	189	L3	112	L4	150	L5	137	L6	144	L7	142	L8	143	L9	143	L10	143
B3 - 16S	L0	400	L1	72	L2	236	L3	119	L4	177	L5	155	L6	166	L7	164	L8	165	L9	165	L10	165
B3 -18S	L0	506	L1	72	L2	289	L3	124	L4	206	L5	170	L6	188	L7	185	L8	187	L9	187	L10	187

BREAKER TYPE

Table B- 4: Wave breaker type for each test

Test Code	Wave periods	Breaking wave height	Water depth	Wave length	Slope	Iribarren no.	Breaker Type (Equation 2-1)
A1 - 6S	6	1,3	3,5	33	0,05	0,252	Spilling breaker
A1 - 8S	8	1,3	3,5	45	0,05	0,296	Spilling breaker
A1 - 10S	10	1,3	3,5	58	0,05	0,333	Spilling breaker
A1 -12S	12	1,3	3,5	70	0,05	0,366	Spilling breaker
A1 - 14S	14	1,3	3,5	82	0,05	0,396	Spilling breaker
A1 - 16S	16	1,3	3,5	93	0,05	0,424	Plunging breaker
A1 - 18S	18	1,3	3,8	109	0,05	0,458	Plunging breaker
A2 - 6S	6	1,3	4,5	36	0,05	0,265	Spilling breaker
A2 - 8S	8	1,3	4,5	51	0,05	0,312	Spilling breaker
A2 - 10S	10	1,3	4,5	64	0,05	0,352	Spilling breaker
A2 - 12S	12	1,3	4,5	78	0,05	0,387	Spilling breaker
A2 - 14S	14	1,3	4,5	91	0,05	0,419	Plunging breaker
A2 - 16S	16	1,3	4,5	105	0,05	0,449	Plunging breaker
A2 - 18S	18	1,3	4,5	118	0,05	0,477	Plunging breaker
A3 - 6S	6	1,3	4,1	35	0,05	0,261	Spilling breaker
A3 - 8S	8	1,3	4,1	49	0,05	0,306	Spilling breaker
A3 - 10S	10	1,3	4,1	62	0,05	0,345	Spilling breaker
A3 - 12S	12	1,3	4,1	75	0,05	0,380	Spilling breaker
A3 - 14S	14	1,3	4,1	88	0,05	0,411	Plunging breaker
A3 - 16S	16	1,3	4,1	101	0,05	0,441	Plunging breaker
A3 - 18S	18	1,3	4,1	114	0,05	0,468	Plunging breaker
B1 - 6S	6	1,3	3,5	33	0,05	0,251	Spilling breaker
B1 - 8S	8	1,3	3,5	45	0,05	0,294	Spilling breaker
B1 - 10S	10	1,3	3,5	57	0,05	0,331	Spilling breaker
B1 - 12S	12	1,3	3,5	69	0,05	0,364	Spilling breaker
B1 - 14S	14	1,3	3,5	81	0,05	0,394	Spilling breaker
B1 - 16S	16	1,3	3,5	93	0,05	0,422	Plunging breaker
B1 - 18S	18	1,3	3,5	104	0,05	0,448	Plunging breaker
B2 - 6S	6	1,3	4,4	36	0,05	0,263	Spilling breaker
B2 - 8S	8	1,3	4,4	50	0,05	0,310	Spilling breaker
B2 - 10S	10	1,3	4,4	64	0,05	0,350	Spilling breaker
B2 - 12S	12	1,3	4,4	77	0,05	0,385	Spilling breaker
B2 - 14S	14	1,3	4,4	90	0,05	0,417	Plunging breaker
B2 - 16S	16	1,3	4,4	104	0,05	0,446	Plunging breaker
B2 - 18S	18	1,3	4,4	117	0,05	0,474	Plunging breaker
B3 - 6S	6	1,3	4,1	35	0,05	0,260	Spilling breaker
B3 - 8S	8	1,3	4,1	49	0,05	0,306	Spilling breaker
B3 - 10S	10	1,3	4,1	62	0,05	0,345	Spilling breaker
B3 - 12S	12	1,3	4,1	75	0,05	0,379	Spilling breaker
B3 - 14S	14	1,3	4,1	88	0,05	0,411	Plunging breaker
B3 - 16S	16	1,3	4,1	101	0,05	0,440	Plunging breaker
B3 -18S	18	1,3	4,1	113	0,05	0,467	Plunging breaker

APPENDIX C: PROBE SPACINGS

Table C- 1: Probe spacings for each test according to 3-point model

Test number	Peak wave period	$X_{12\_shallow}$	$X_{13\_shallow}$	$X_{23\_shallow}$	X_{12_deep}	X_{13_deep}	X_{23_deep}
1	6	170	425	255	248	620	372
2	8	234	586	352	366	916	549
3	10	297	744	446	479	1198	719
4	12	360	900	540	589	1472	883
5	14	422	1055	633	697	1742	1045
6	16	484	1209	725	804	2009	1205
7	18	545	1363	818	910	2274	1365
8	6	185	461	277	252	631	379
9	8	256	641	384	376	940	564
10	10	326	815	489	494	1235	741
11	12	395	988	593	608	1520	912
12	14	464	1160	696	720	1801	1081
13	16	532	1330	798	831	2079	1247
14	18	600	1500	900	942	2354	1412
15	6	180	449	269	251	627	376
16	8	249	621	373	373	932	559
17	10	316	790	474	489	1221	733
18	12	383	957	574	601	1503	902
19	14	449	1122	673	712	1780	1068
20	16	515	1287	772	821	2054	1232
21	18	581	1452	871	930	2325	1395
22	6	169	422	253	247	619	371
23	8	233	581	349	365	914	548
24	10	295	738	443	478	1195	717
25	12	357	892	535	587	1468	881
26	14	418	1046	627	695	1737	1042
27	16	479	1199	719	801	2003	1202
28	18	541	1351	811	907	2268	1361
29	6	183	457	274	252	630	378
30	8	254	634	381	375	937	562
31	10	323	807	484	492	1230	738
32	12	391	978	587	606	1515	909
33	14	459	1147	688	718	1794	1076
34	16	526	1316	790	828	2070	1242
35	18	594	1484	891	938	2345	1407
36	6	179	448	269	251	627	376
37	8	248	620	372	372	931	558
38	10	315	788	473	488	1220	732
39	12	382	954	572	601	1502	901
40	14	448	1119	671	711	1778	1067
41	16	513	1283	770	821	2051	1231
42	18	579	1447	868	929	2323	1394

APPENDIX D: MODEL SET-UP ROUTINE

The following steps are followed for the execution of each test:

1. Partial construction of the berm (the bottom 20mm of the core and the screed layer is packed).
2. The seawall is placed in the flume using the gantry crane.
3. Seal the wall with *SOUDAL Fix All* and leave overnight to dry.
4. Construct the remaining part of the rubble-mound structure (the top 13mm of the core, filter layer and armour layer).
5. Fill flume with water until the desired water level using a pump (this will also adequately mix the water to prevent any change in temperature, surface tension, etc.).
6. Reposition probes, according to 3-point model.
7. Calibrate probes.
8. Insert desired wave conditions into wavemaker and HRDAQ.
9. Turn on the Motor Drive Cabinet.
10. Set the Absorption Gain to 1000, adjust the Water Level accordingly.
11. When the water surface is still, run the wavemaker and adjust the absorption gain according to specific water and wave conditions.
12. Use HRDAQ to collect data, start probe sampling 60 seconds after waves are being generated, allowing the wave to develop entirely.
13. While the test is running, take pressure measurements using pressure transmitters located in the vertical seawall.
14. After completion of the test, analyse data from probes.
15. Drain flume until adequate dry working space in front of the structure.
16. Deconstruct berm partially (remove armour layer, filter layer, and top part of core) and remove *Fix All* from the sides of the seawall.
17. Slowly lift seawall with gantry crane without disturbing screed layer.
18. Record scouring outcome by taking photos with a camera.
19. Remove all the remaining rocks from the core and screed layer from the flume for a clean working space.
20. Restart process from Step 1.

APPENDIX E: DIAMETER OF SCREED LAYER MATERIAL

The average K-value of Le Méhauté and Keulegan is used to determine the diameter of the material in the screed layer. The parameters used in these two methods can be seen in Table E-1.

Table E- 1: Parameters used in the calculation of the screed layer material diameter

Parameter	Prototype value	Model value
P (porosity)	0,38	0,38
ΔL (average width of core material)	0,1	0,005
D (quarry stone diameter)	0,019	0,00095
H_i (incident wave height)	1,3	0,065
ν (kinematic viscosity of water)	1E-06	1E-06
g (standard gravity)	9,81	9,81

- *Le Méhauté*

The y-axis value is 20 (the model scale), and the x-axis value is calculated as 0,707. Reading this from the Figure E-1, the K-value using Le Méhauté is 3,2.

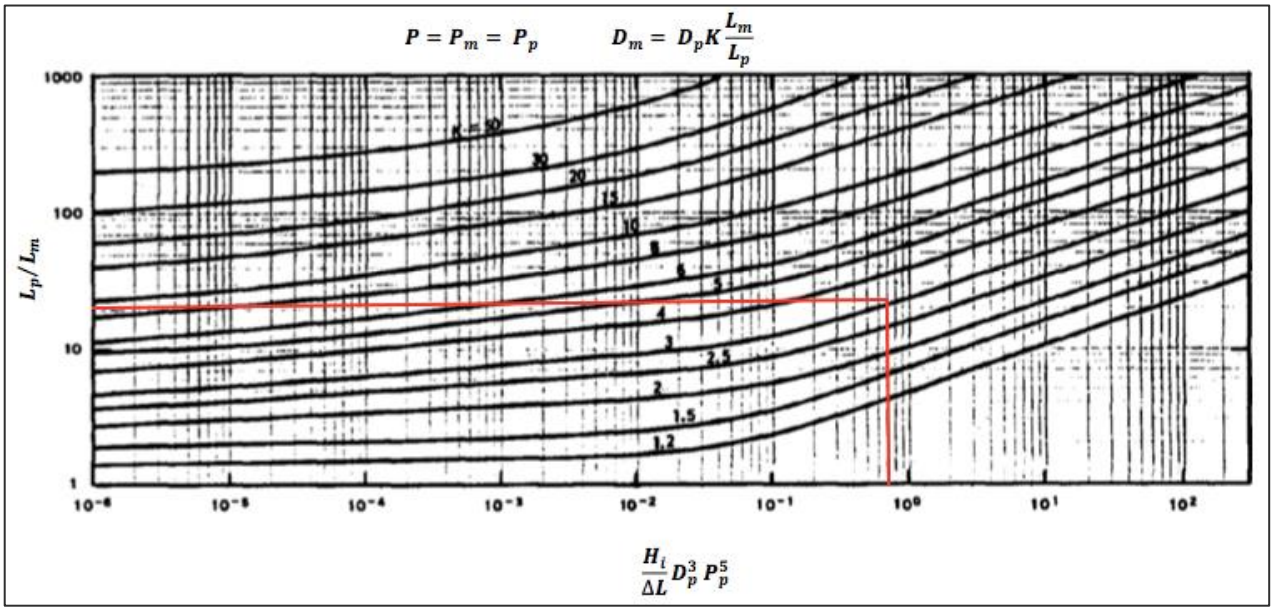

Figure E- 1: Obtaining the K-value using the Le Méhauté graph

- *Keulegan*

The two equations for γ_m are solved, a D_m is chosen to satisfy both these equations. The average D_m-value that would satisfy the tests is taken as 0,0019m. The K-value is calculated:

$$K = model\ scale\ \frac{D_m}{D} = 20\ \frac{1{,}9}{19} = 2$$

- *Average K-value*

The average of the two methods is K = 2,6, which gives a final D_m of 2,5m. Filter sand with a grading between 0,9 and 3,5mm is used for the screed layer.

APPENDIX F: RUBBLE-MOUND STRUCTURE MATERIAL

Figure F- 1: Armour layer rocks D50 = 28mm

Figure F- 2: Screed layer material (grading 0.9 - 3.4mm)

Figure F- 3: Filter layer rocks D50 = 13mm

Figure F- 4: Filter layer rocks D50 = 11mm

Figure F- 5: Core rocks D50 = 6mm

Figure F- 6: Core rocks D50 = 5mm

APPENDIX G: GRADING CURVES AND FILTER RULES

GRADING CURVES

The grading range for the rocks in the various layers is given in the Table G-1.

Table G- 1: Grading range for each layer

Layer	Median Mass (kg)	EUL	NUL	NLL	ELL	Grading Range
Armour Layer (D50 =28mm)	465	970	505	340	175	175-970kg
Filter Layer (D50 =13mm)	47	97	51	34	18	18-97kg
Filter Layer (D50 11mm)	31	65	34	23	12	12-65kg
Core (D50 = 6mm)	4,7	9,7	5,1	3,4	1,8	1,8-9,7kg
Core (D50 = 5mm)	2,1	4,3	2,3	1,5	0,8	0,8-4,3kg

Where

ELL = Extreme Lower Limit (mass where no more than 2% passing is permitted)

NLL = Nominal Lower Limit (mass where no more than 10% passing is permitted)

NUL = Nominal Upper Limit (mass where no less than 70% passing is permitted)

EUL = Extreme Upper Limit (mass where no less than 97% passing is permitted)

The limits above are used to compute the theoretical grading curve. The theoretical grading curve is computed using the Rosin-Rammler method:

$$y = 1 - \exp\left\{\ln\left(\frac{1}{2}\right)\left(\frac{M_y}{M_{50}}\right)^{n_{RRM}}\right\} = 1 - \exp\left\{-0.693\left(\frac{M_y}{M_{50}}\right)^{n_{RRM}}\right\} \quad \textit{G-1}$$

Where

y = Fraction passing value

M_y = Mass corresponding to passing value y

n_{RRM} = Uniformity index (steepness of grading curve)

RRM = Rosin-Rammler Mass

The inverse of the Rosin-Rammler equation is given in Equation G-2:

$$M_y = M_{50}\left\{\frac{ln(1-y)}{ln\left(\frac{1}{2}\right)}\right\}^{\frac{1}{n_{RRM}}} = M_{50}\left\{\frac{-ln(1-y)}{0.693}\right\}^{\frac{1}{n_{RRM}}} \quad \textit{G-2}$$

The Ros-Ram equation can also be used to describe particle size by replacing the mass (M) with the diameter (D). n_{RRM} will then be replaced with n_{RRD}, where $n_{RRD} = 3\ n_{RRM}$.

$$M_{50} = NLL\left(\frac{ln\ (1-y_{NLL})}{-0.693}\right)^{-1/n_{RRM}} \quad G\text{-}3$$

$$M_{50} = NUL\left(\frac{ln\ (1-y_{NIL})}{-0.693}\right)^{-1/n_{RRM}} \quad G\text{-}4$$

$$n_{RRM} = \frac{log\ (\frac{ln\ (1-y_{NUL})}{ln(1-y_{NLL})})}{log\ (\frac{NUL}{NLL})} \quad G\text{-}5$$

The computed grading curves for the different rock sizes can be seen in Figure G-1 to Figure G-5. The Theoretical curve is calculated using the Ros-Ram equation. Theoretical Curve 2 is computed using the values in Table G-1. The dark blue curve is calculated by taking a sample of 300 rocks from each layer.

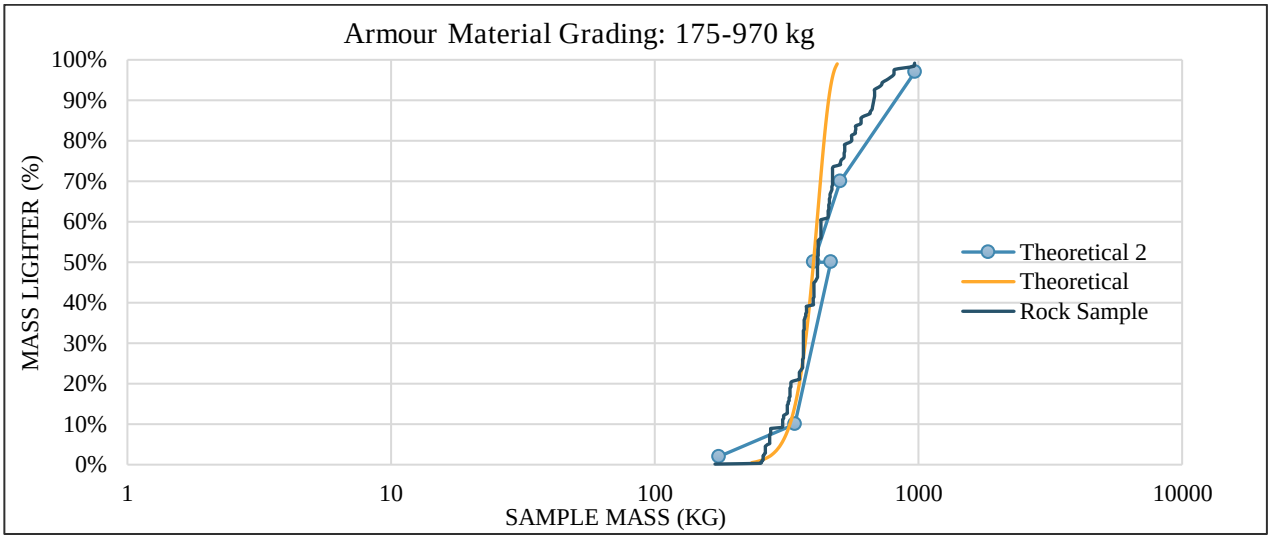

Figure G- 1: Grading curve of the 28mm armour layer

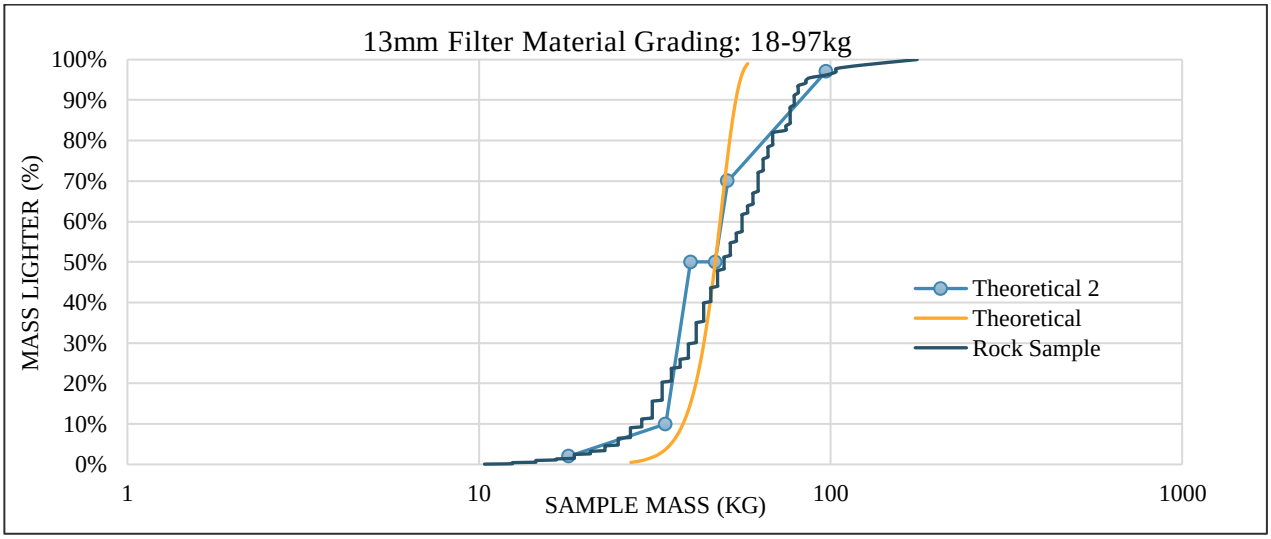

Figure G- 2: Grading curve of the 13mm filter layer

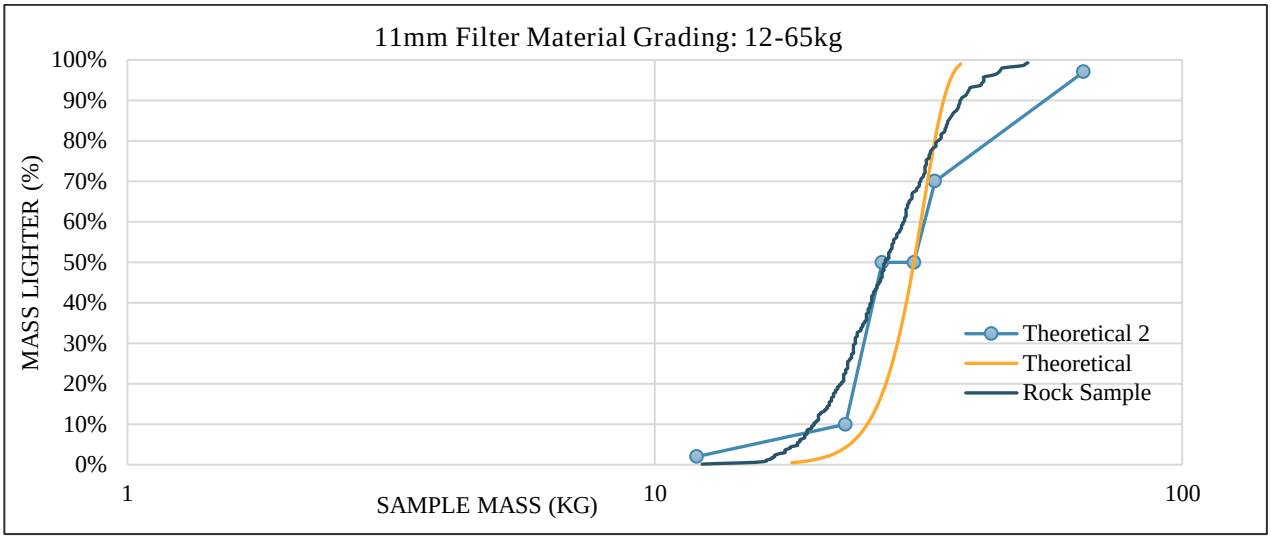

Figure G- 3: Grading curve of the 11mm filter layer

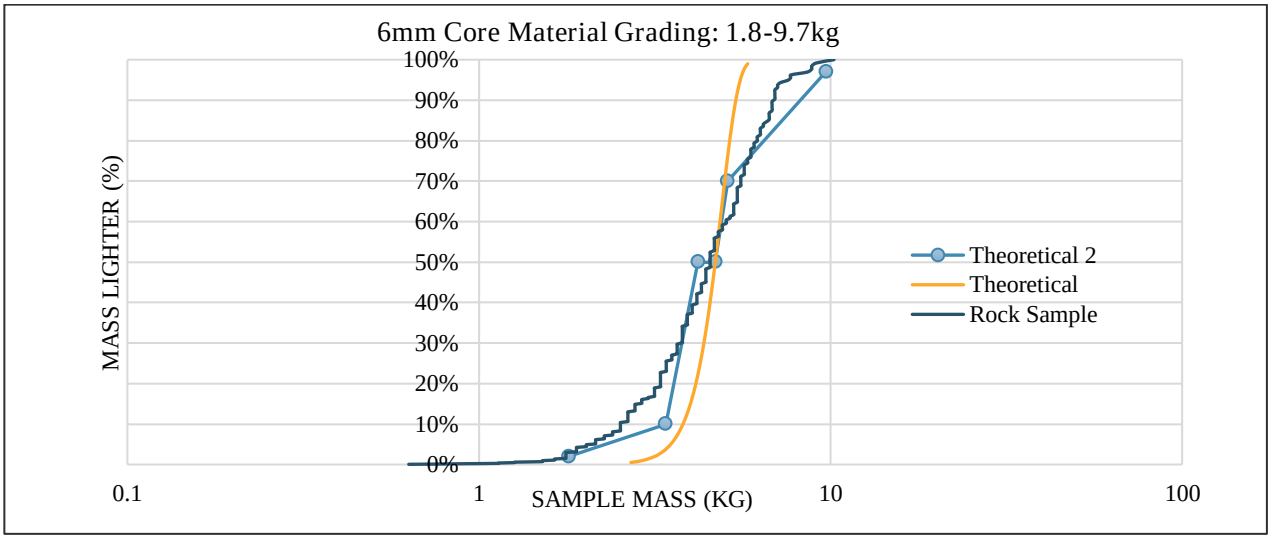

Figure G- 4: Grading curve of the 6mm core

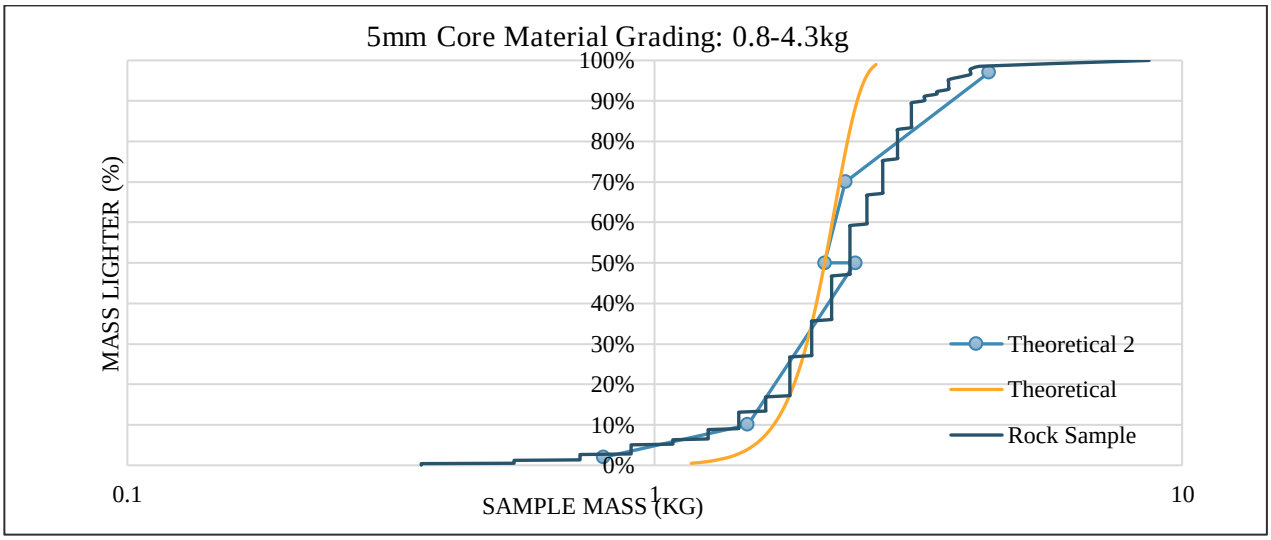

Figure G- 5: Grading curve of the 5mm core

All six of the rocks used in the model has a narrow grading. The M_{85}/M_{15}-ratio can be seen in Table G-2.

Table G- 2: Narrow grading ratio of rocks

Armour Material		
M85 (kg)	600	Between 1.7 and 2.7 (narrow grading)
M15 (kg)	310	
M85/M15	1,9	
Filter Material (13mm)		
M85 (kg)	73	Between 1.7 and 2.7 (narrow grading)
M15 (kg)	32	
M85/M15	2,3	
Core Material (6mm)		
M85 (kg)	6,3	Between 1.7 and 2.7 (narrow grading)
M15 (kg)	2,5	
M85/M15	2,5	
Filter Material (11mm)		
M85 (kg)	36	Between 1.7 and 2.7 (narrow grading)
M15 (kg)	21	
M85/M15	1,7	
Core Material (5mm)		
M85 (kg)	3,1	Between 1.7 and 2.7 (narrow grading)
M15 (kg)	1,4	
M85/M15	2,2	

FILTER RULE CRITERIA

Table G- 3: Filter rule criteria for Structure A1, Structure A2 and Structure A3

Filter Criteria Structure A1, Structure A2, Structure A3			
Criterion 1			
D15_armour/D85_filter	3,6	< 4 to 5	OK
D15_filter/D85_core	1,4	< 4 to 5	OK
Criterion 2			
D15_filter/D15_core	1,9	> 4 to 5	NOT OK
Criterion 3			
D60_filter/D10_core	2,9	<10	OK

Table G- 4: Filter rule criteria for Structure B1, Structure B2 and Structure B3

Filter Criteria Structure B1, Structure B2, Structure B3			
Criterion 1			
D15_armour/D85_filter	1,6	< 4 to5	OK
D15_filter/D85_core	2,1	< 4 to5	OK
Criterion 2			
D15_filter/D15_core	2,4	> 4 to 5	NOT OK
Criterion 3			
D60_filter/D10_core	3,0	<10	OK

APPENDIX H: RUBBLE-MOUND STRUCTURE CONSTRUCTION

The construction of the rubble-mound structure is discussed in this Appendix.

- *Screed Layer*

20mm of the core is packed first. The screed layer is placed on the first 20mm of the core (Figure H-1).

Figure H- 1: Screed layer placed on a core thickness of 20mm

- *Core*

After the wall is placed on the screed layer, the remaining part of the core is packed.

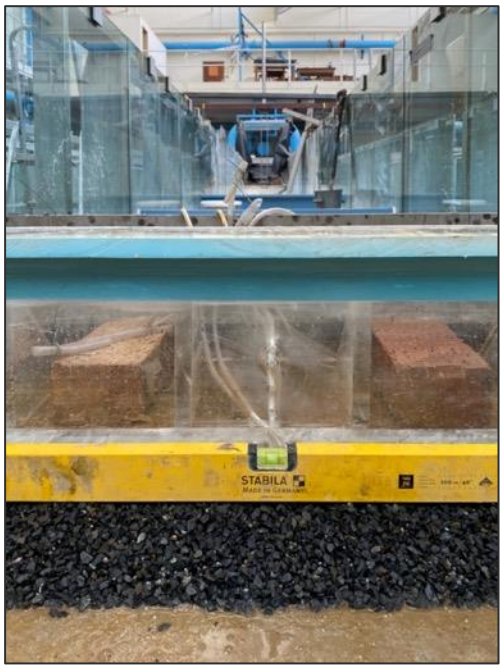

Figure H- 2: Remaining part of core packed in front of the seawall

- *Filter Layer*

The filter layer is packed after the core.

Figure H- 3: Filter layer packed over the core

- *Armour Layer*

The armour layer is packed last.

Figure H- 4: Armour layer packed over the filter layer

APPENDIX I: HANDHELD 3D SCANNING TABLET ACCURACY

The DPI-10 Handheld 3D Scanning Tablet (which uses Dot3D Pro Software) is tested to see if it is sufficient for measuring scour in this two-dimensional model. Three scans are taken from a scenario where "scour" developed. The results from the scans can be seen in Table I-1. The scanned images are imported into AutoCAD to take the measurements every 5cm along the width of the vertical seawall. The AutoCAD imported image for Scan 3 (as given in Table I-1) can be seen in Figure I-1.

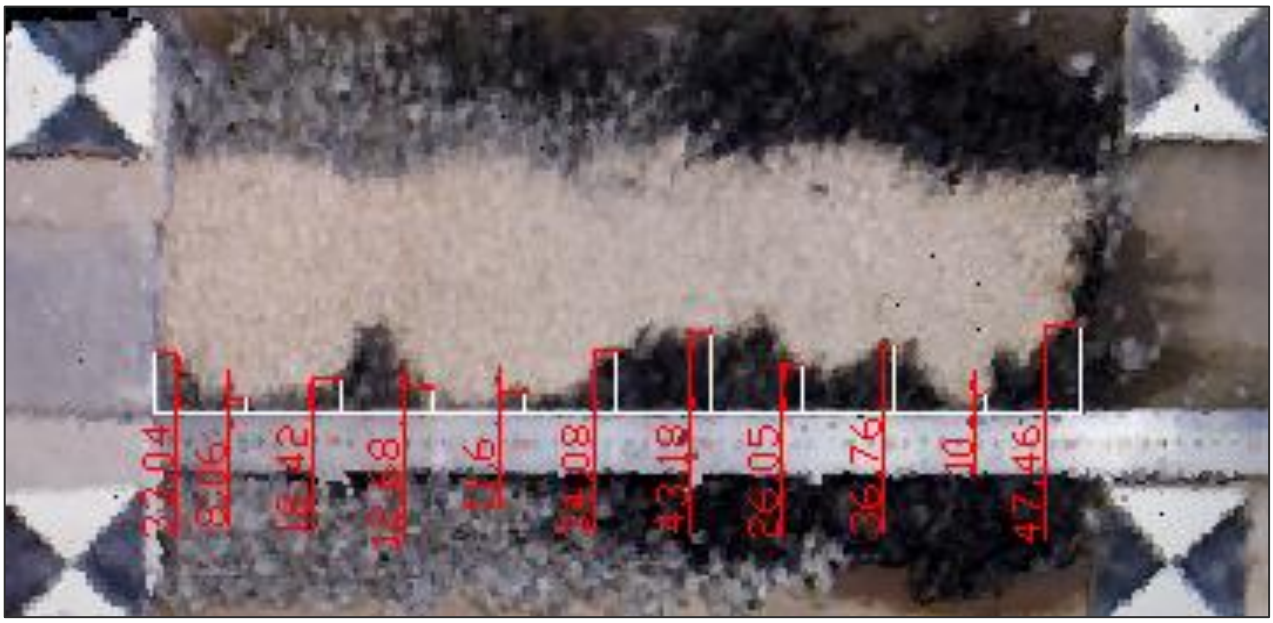

Figure I- 1: Imported scour image from the Handheld 3D scanning tablet

Since less "scouring" occurred between 16cm-22cm on the ruler in the Figure I-1, the depths at every centimetre are taken. The tablet must also be accurate for smaller measurements since this can be expected in the model tests to be conducted.

Table I- 1: Measurements of the Handheld 3D scanning tablet

Distance along x-axis (mm)	True Measurement (mm)	Measurement Scan 1 (mm)	Error Scan 1 (%)	Accuracy Scan 1 (%)	Measurement Scan 2 (mm)	Error Scan 2 (%)	Accuracy Scan 2 (%)	Measurement Scan 3 (mm)	Error Scan 3 (%)	Accuracy Scan 3 (%)
Points every 5cm										
0	28	34,6	24	76	33,9	21	79	33	18	82
5	9	9,5	6	94	4,9	46	54	8	11	89
10	16	18,2	14	86	24	50	50	18,4	15	85
15	11	5,3	52	48	6	45	55	12,7	15	85
20	14	11,4	19	81	8,2	41	59	11,6	17	83
25	33	35,7	8	92	34,8	5	95	34	3	97
30	42	41,5	1	99	42,3	1	99	43,2	3	97
35	27	24,8	8	92	24,1	11	89	26,1	3	97
40	35	36,8	5	95	31,6	10	90	36,8	5	95
45	6	10	67	33	11,9	98	2	10	67	33
50	51	45,3	11	89	47,2	7	93	47,5	7	93
Points every centimetre (between 16cm and 22cm on the ruler)										
16	11	8	27	73	6,5	41	59	7,4	33	67
17	6	4	33	67	6,5	8	92	4,5	25	75
18	7	6	14	86	8,9	27	73	7,3	4	96
19	7	13	86	14	13,9	99	1	11,4	63	37
20	14	11,4	19	81	8,2	41	59	11,6	17	83
21	11	10,7	3	97	10,3	6	94	11,3	3	97
22	11	10	9	91	13	18	82	12	9	91

APPENDIX J: MATLAB IMAGE PROCESSING ACCURACY

The image of the 0.3cm x 0.3cm black square imported into the program is shown in Figure J-1. The known dimensions are used to calibrate.

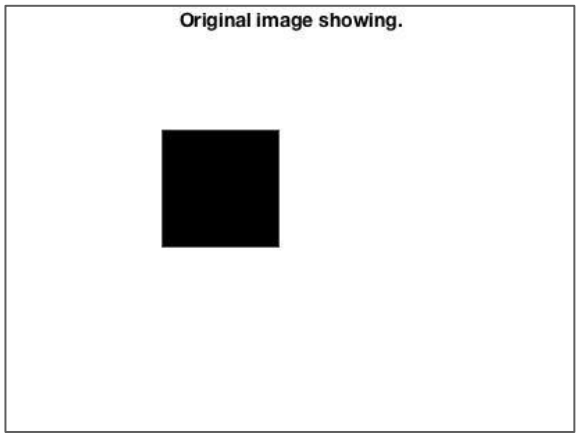

Figure J- 1: Original black square image imported into MATLAB

The binary image obtained through thresholding is given in Figure J-2.

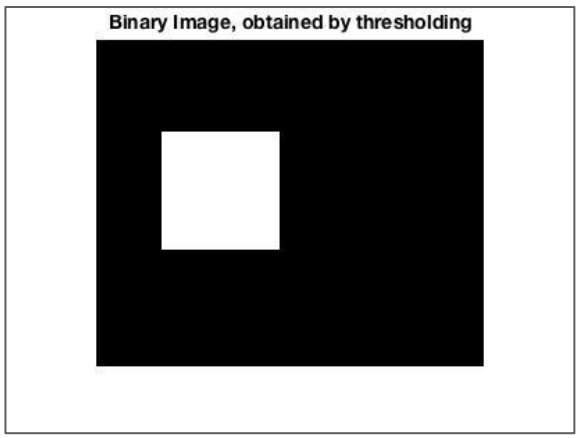

Figure J- 2: Binary image of the black square

The green outline in Figure J-3 illustrates how MATLAB identifies the area to be calculated.

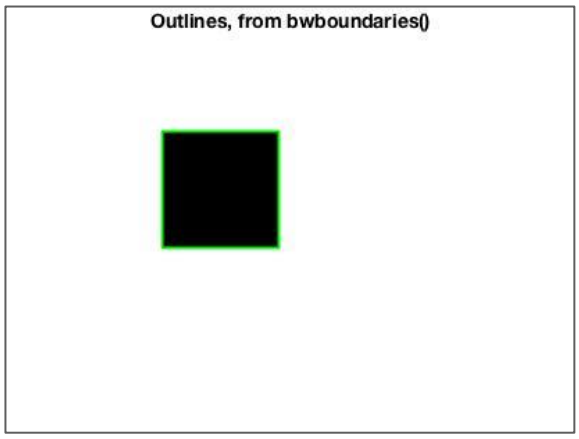

Figure J- 3: The black square area identified and to be calculated by MATLAB

The screenshot of the calculated area of the black square is given in Figure J-4.

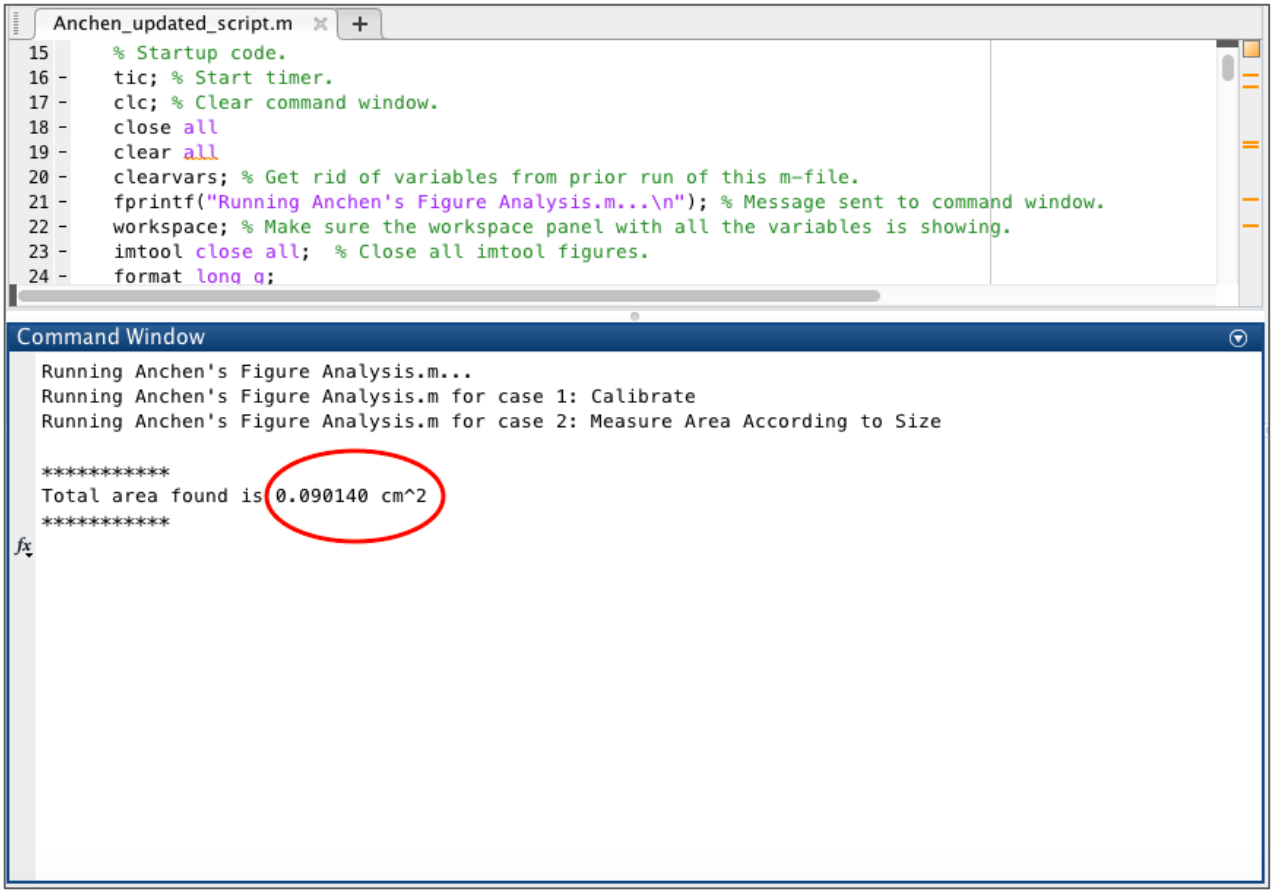

Figure J- 4: Results of the area of the imported black square

APPENDIX K: EXAMPLE OF PROBE OUTPUT FOR TEST A2-12S

The probe recordings of Test A2-12S is used to display the outcome of the recordings. Figure K-1 is an example of the voltage output of the probes for the deep-water set-up. Where Channel 1, Channel 2 and Channel 3 each represent a probe. Table K-1 shows the results generated by the probes.

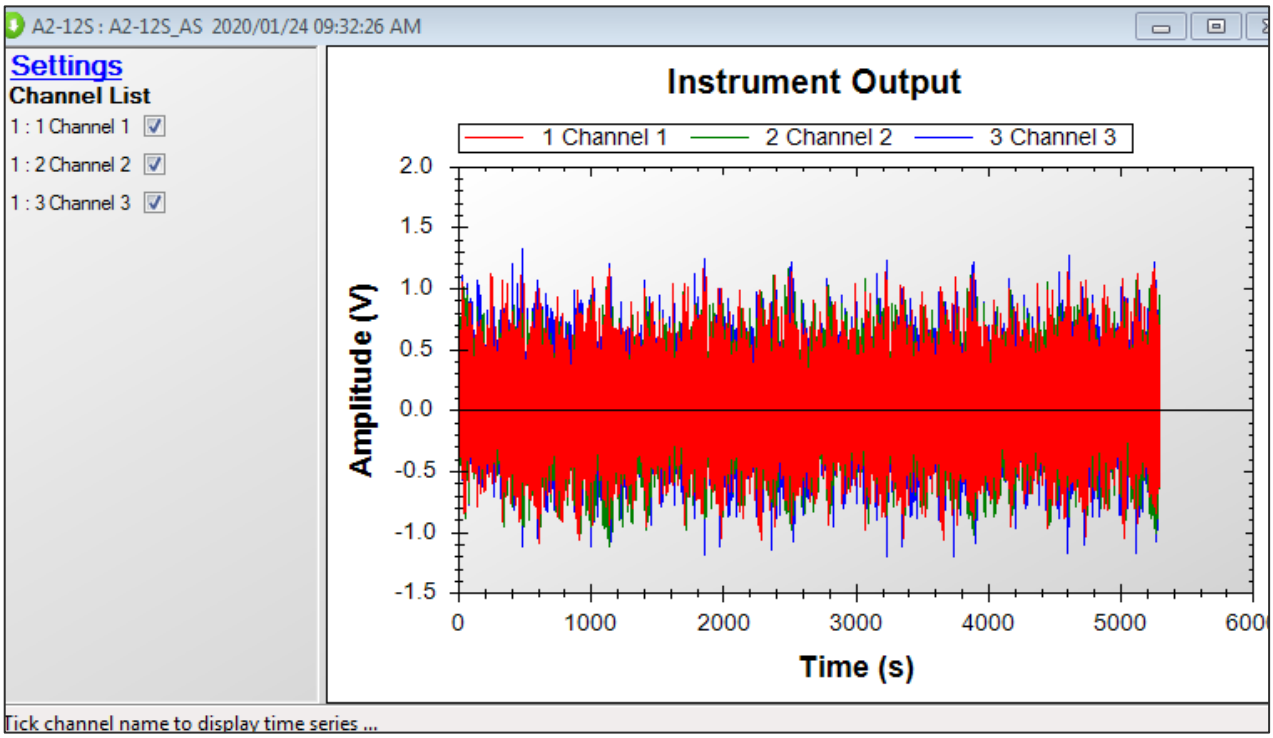

Figure K- 1: Probe output for Test A2-12S

Table K- 1: Measurements of the deep-water probes

Channel	N-1	N0	N2	N4	Hm0	Tm0,2	Tm-1,0	Tp
A2-12S_AS_200124093226 Ch: 1 Channel 1 (m)	3.005	0.102	0.001	0.001	1.28	8.54	29.57	12.53
A2-12S_AS_200124093226 Ch: 2 Channel 2 (m)	17.007	0.111	0.001	0.001	1.33	8.71	153.10	12.41
A2-12S_AS_200124093226 Ch: 3 Channel 3 (m)	3.857	0.108	0.001	0.001	1.31	8.64	35.83	12.41

APPENDIX L: SCOUR IMAGES

TEST SET A1 SCOUR IMAGES

Figure L- 1: Scour image Test A1-6S

Figure L- 2: Scour image Test A1-8S

Figure L- 3: Scour image Test A1-10S

Figure L- 4: Scour image Test A1-12S

Figure L- 5: Scour image Test A1-14S

Figure L- 6: Scour image Test A1-16S

Figure L- 7: Scour image Test A1-18S

TEST SET A2 SCOUR IMAGES

Figure L- 8: Scour image Test A2-6S

Figure L- 9: Scour image Test A2-8S

Figure L- 10: Scour image Test A2-10S

Figure L- 11: Scour image Test A2-12S

Figure L- 12: Scour image Test A2-14S

Figure L- 13: Scour image Test A2-16S

Figure L- 14: Scour image Test A2-18S

Test Set A3 Scour Images

Figure L- 15: Scour image Test A3-6S

Figure L- 16: Scour image Test A3-8S

Figure L- 17: Scour image Test A3-10S

Figure L- 18: Scour image Test A3-12S

Figure L- 19: Scour image Test A3-14S

Figure L- 20: Scour image Test A3-16S

Figure L- 21: Scour image Test A3-18S

Test Set B1 Scour Images

Figure L- 22: Scour image Test B1-6S

Figure L- 23: Scour image Test B1-8S

Figure L- 24: Scour image Test B1-10S

Figure L- 25: Scour image Test B1-12S

Figure L- 26: Scour image Test B1-14S

Figure L- 27: Scour image Test B1-16S

Figure L- 28: Scour image Test B1-18S

Test Set B2 Scour Images

Figure L- 29: Scour image Test B2-6S

Figure L- 30: Scour image Test B2-8S

Figure L- 31: Scour image Test B2-10S

Figure L- 32: Scour image Test B2-12S

Figure L- 33: Scour image Test B2-14S

Figure L- 34: Scour image Test B2-16S

Figure L- 35: Scour image Test B2-18S

Test Set B3 Scour Images

Figure L- 36: Scour image Test B3-6S

Figure L- 37: Scour image Test B3-8S

Figure L- 38: Scour image Test B3-10S

Figure L- 39: Scour image Test B3-12S

Figure L- 40: Scour image Test B3-14S

Figure L- 41: Scour image Test B3-16S

Figure L- 42: Scour image Test B3-18S

APPENDIX M: STATISTICAL CALCULATIONS

INTERQUARTILE CALCULATIONS

The first quartile (q_1), second quartile (q_2) and third quartile (q_3) is calculated for each set of tests to determine if there are any outliers. The values are displayed in Table M-1.

Table M- 1: Interquartile calculations to determine outliers (m^2)

Test Set	Test Set A1	Test Set A2	Test Set A3	Test Set B1	Test Set B2	Test Set B3
First quartile (q_1)	0,05	0,02	0,03	0,04	0,04	0,04
Second quartile (q_2)	0,05	0,03	0,05	0,05	0,05	0,05
Third quartile (q_3)	0,22	0,06	0,07	0,22	0,07	0,16
Interquartile range (IQR)	0,17	0,04	0,04	0,18	0,02	0,13
Lower outlier = q_1 -1.5IQR	-0,21	-0,04	-0,04	-0,23	0,01	-0,16
Upper outlier = q_3+1.5IQR	0,48	0,12	0,13	0,48	0,10	0,36
q_2- q_1	0,00	0,01	0,02	0,02	0,01	0,02
q_3- q_2	0,17	0,03	0,02	0,16	0,02	0,11

The Box Plots for each Test Set is given in Figure M-1 to Figure M-5.

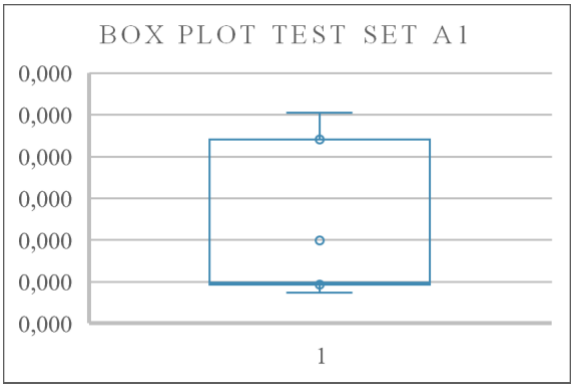

Figure M- 1: Box plot Test Set A1

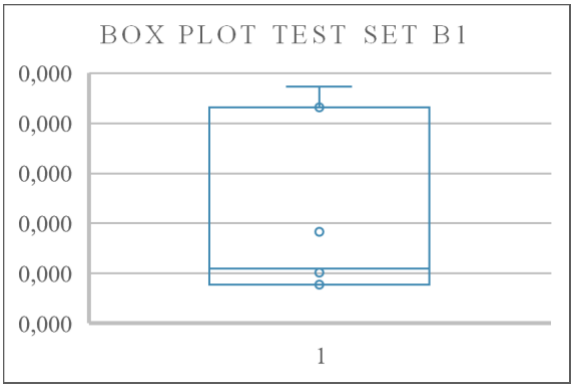

Figure M- 3: Box plot Test Set B1

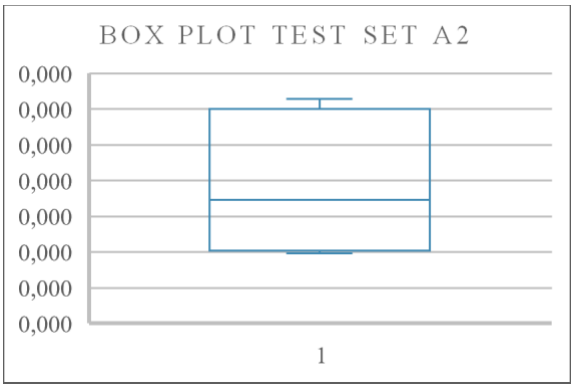

Figure M- 2: Box plot Test Set A2

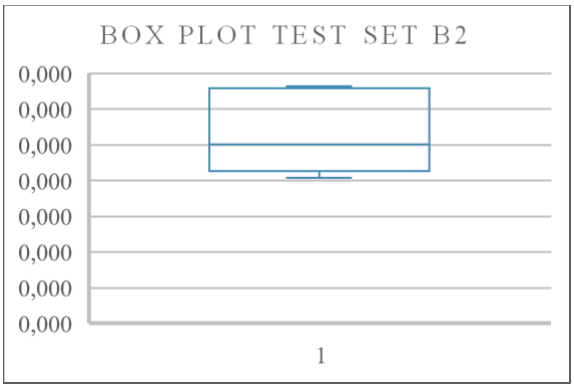

Figure M- 4: Box plot Test Set B2

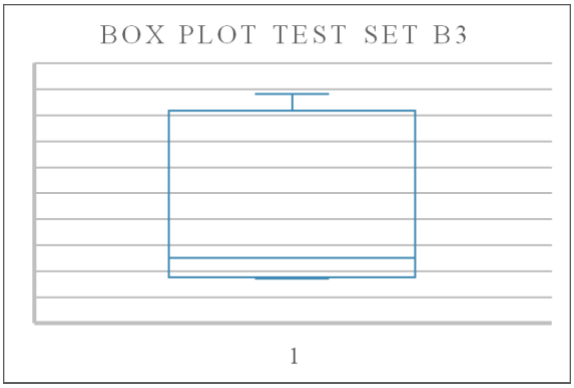

Figure M- 5: Box plot Test Set B3

STANDARD DEVIATION, SAMPLE RANGE AND CORRELATION COEFFICIENT CALCULATIONS

The standard deviation (σ^2), sample range (r) and correlation coefficient are calculated using Equation M-1, Equation M-2 and Equation M-3 respectively.

$$\sigma^2 = \frac{\sum_{i=1}^{N}(x_i - \mu)^2}{N} \qquad M\text{-}1$$

$$r = max\ (x_i) - min(x_i) \qquad M\text{-}2$$

$$r_{xy} = \frac{\sum_{i=1}^{n} y_i\,(x_i - \bar{x})}{[\sum_{i=1}^{n}(y_i - \bar{y})^2\ \sum_{i=1}^{n}(x_i - \bar{x})^2]^{\frac{1}{2}}} \qquad M\text{-}3$$

The variables and results are given in Table M-2. The scour measurements are denoted as an "x" in the table.

Table M- 2: Standard deviation, sample range and correlation coefficient of test sets

	Test A1	Test A2	Test A3	Test B1	Test B2	Test B3
N	7	7	7	7	7	7
x1	0,04	0,02	0,03	0,04	0,04	0,03
x2	0,05	0,02	0,03	0,04	0,04	0,04
x3	0,05	0,03	0,04	0,05	0,05	0,04
x4	0,05	0,03	0,05	0,05	0,05	0,12
x5	0,10	0,04	0,05	0,09	0,05	0,12
x6	0,22	0,06	0,07	0,22	0,07	0,16
x7	0,25	0,06	0,13	0,26	0,07	0,18
σ^2	0,09	0,02	0,04	0,09	0,01	0,06
r	0,22	0,04	0,10	0,22	0,03	0,14
r_{xy}	0,89	0,94	0,88	0,89	0,97	0,95

APPENDIX N: VERIFICATION TEST RESULT

A new graph is produced for Test Set A3, indicating the repeated Test A3-16S (Figure N-1). Under the chart, the updated Box Plot is given in Figure N-2.

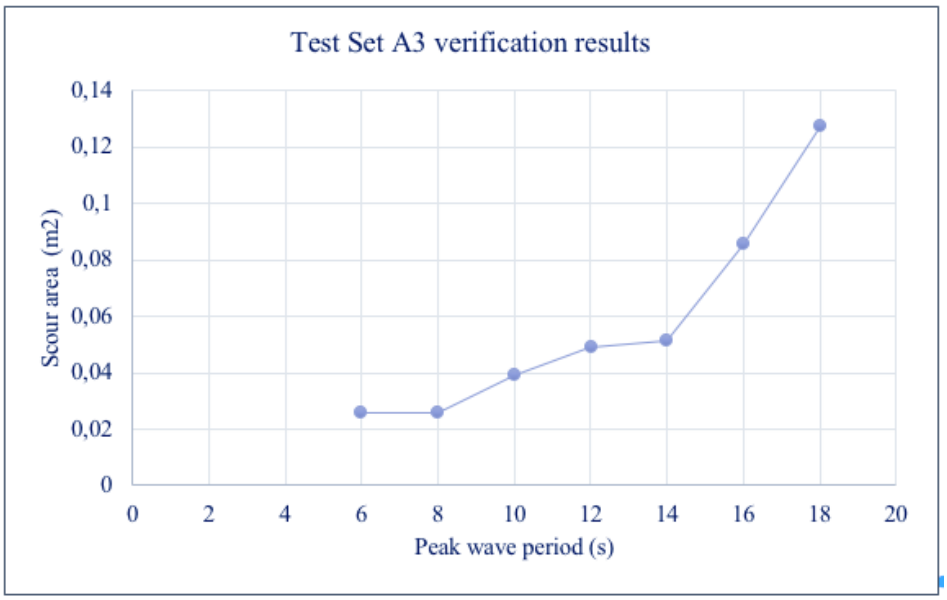

Figure N- 1: Test Set A3 scour results with repeated Test A3-16S

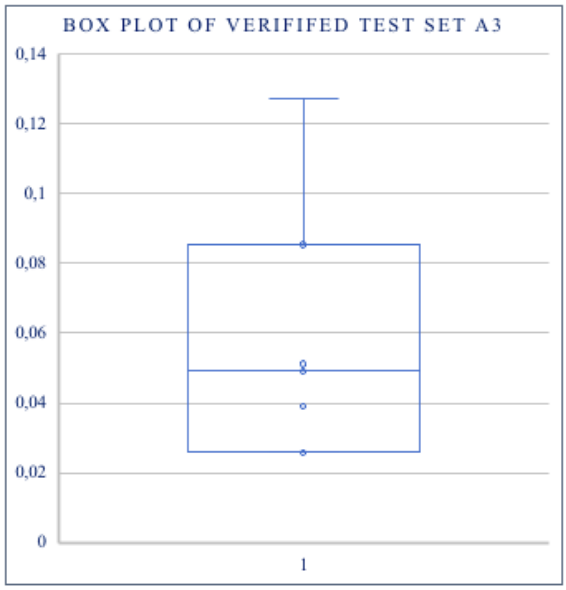

Figure N- 2: Box plot including repeated Test A3-16S

APPENDIX O: DYNAMIC PRESSURE HEAD MEASUREMENTS

Figure O-1 to Figure O-6 indicate the measured dynamic pressure heads in the six structures at the seven tested peak wave periods. The y-axis gives the position where the pressure transmitter is located, with the starting point being the pressure transmitter located right above the screed layer (pressure transmitter 8).

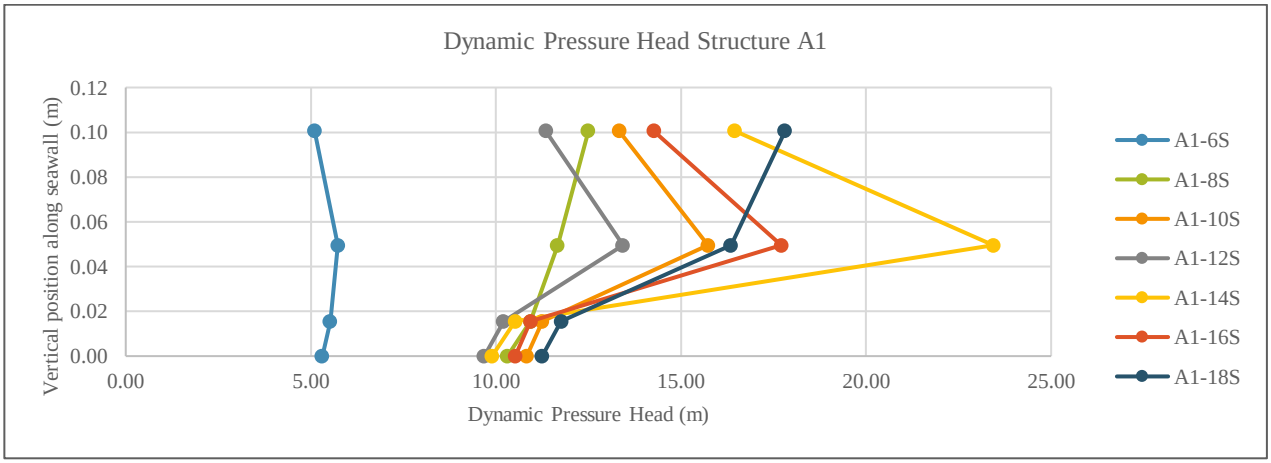

Figure O- 1:Dynamic pressure head Test Set A1

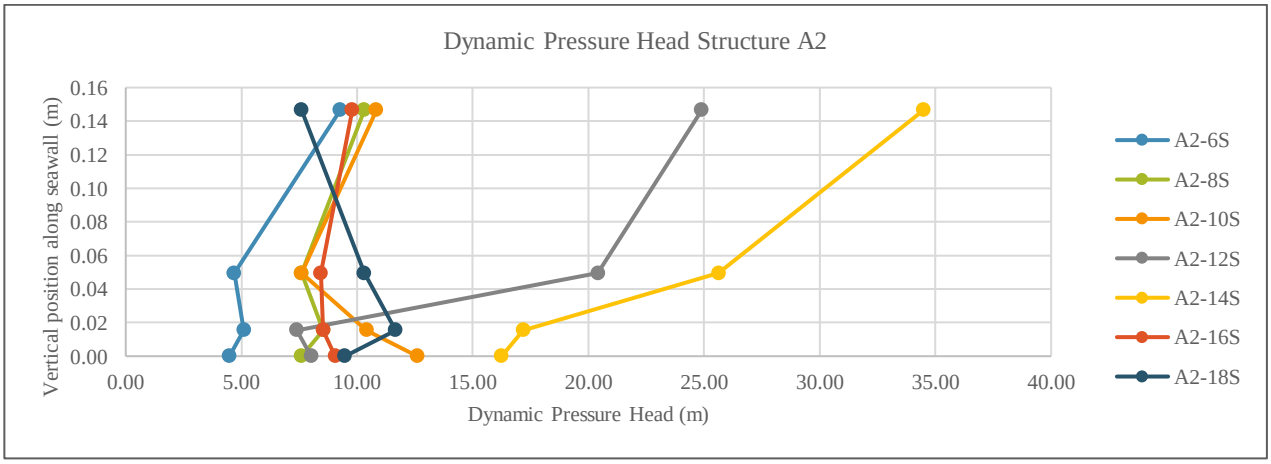

Figure O- 2: Dynamic pressure head Test Set A2

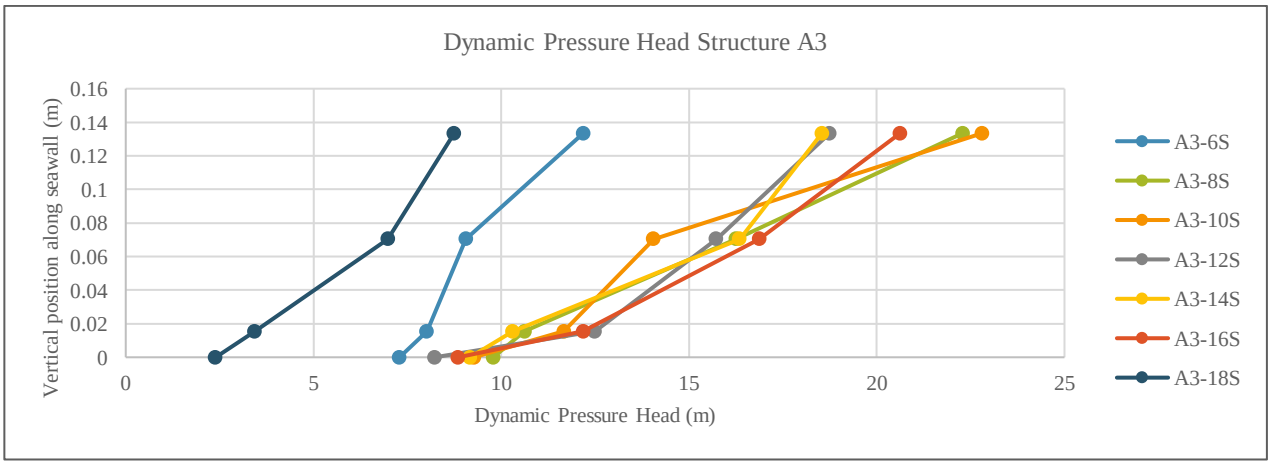

Figure O- 3: Dynamic pressure head Test Set A3

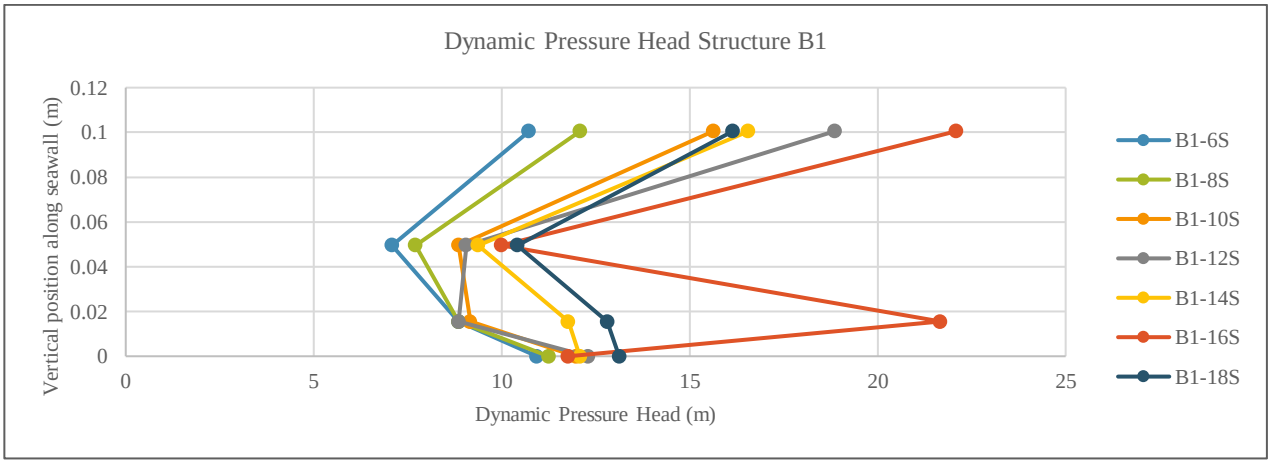

Figure O- 4: Dynamic pressure head Test Set B1

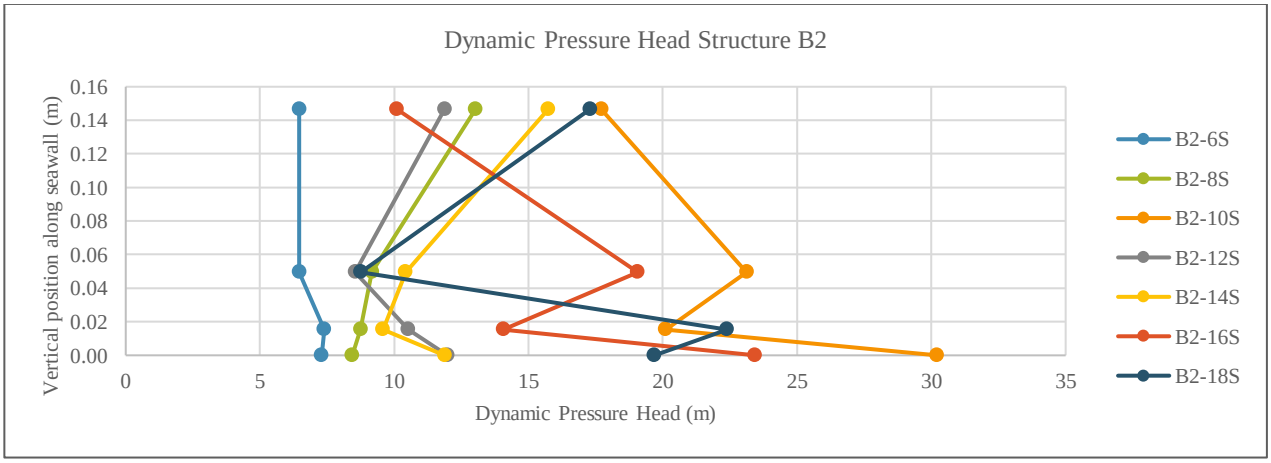

Figure O- 5: Dynamic pressure head Test Set B2

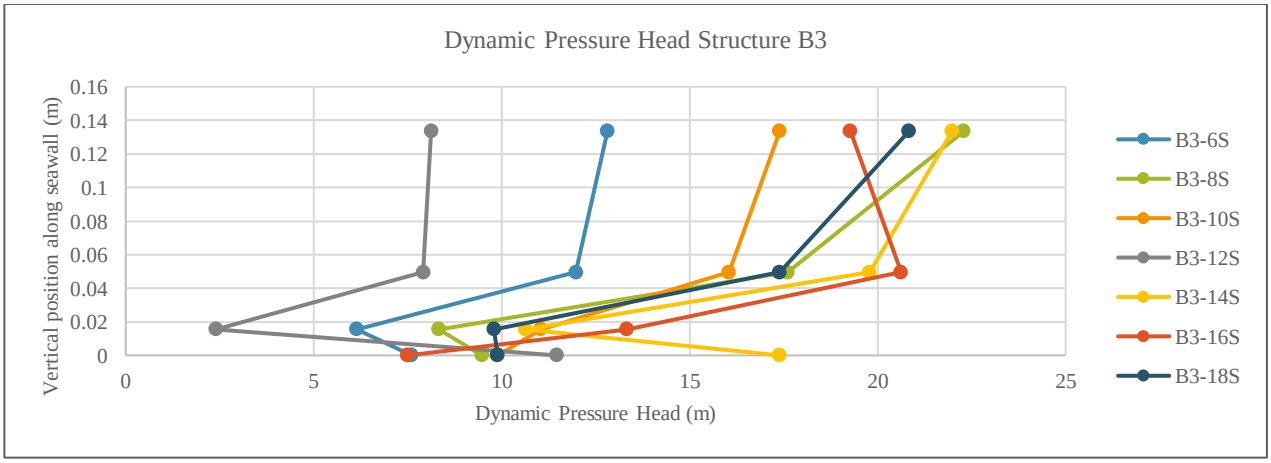

Figure O- 6: Dynamic pressure head Test Set B3

Table O-1 gives the ratio of the top pressure head measurement to the bottom pressure head measurement. These values are used to calculate the coefficient of variation in Chapter 6.

Table O- 1: Ratio of pressure head at the top to the pressure head at the bottom

	The ratio of maximum pressure head at top to that of bottom					
6s	**Test A1**	**Test A2**	**Test A3**	**Test B1**	**Test B2**	**Test B3**
Armour top/ Armour bottom	0,9	2,0	1,3	1,5	1,0	1,1
Armour bottom/ Filter bottom	1,0	0,9	1,1	0,8	0,9	1,9
Filter bottom/ Screed top	1,0	1,1	1,1	0,8	1,0	0,8
8s						
Armour top/ Armour bottom	1,1	1,4	1,4	1,6	1,4	1,3
Armour bottom/ Filter bottom	1,1	0,9	1,5	0,9	1,0	2,1
Filter bottom/ Screed top	1,1	1,1	1,1	0,8	1,0	0,9
10s						
Armour top/ Armour bottom	0,8	1,4	1,6	1,8	0,8	1,1
Armour bottom/ Filter bottom	1,4	0,7	1,2	1,0	1,2	1,5
Filter bottom/ Screed top	1,0	0,8	1,3	0,8	0,7	1,1
12s						
Armour top/ Armour bottom	0,8	1,2	1,2	2,1	1,4	1,0
Armour bottom/ Filter bottom	1,3	2,8	1,3	1,0	0,8	3,3
Filter bottom/ Screed top	1,1	0,9	1,5	0,7	0,9	0,2
14s						
Armour top/ Armour bottom	0,7	1,3	1,1	1,8	1,5	1,1
Armour bottom/ Filter bottom	2,2	1,5	1,6	0,8	1,1	1,9
Filter bottom/ Screed top	1,1	1,1	1,1	1,0	0,8	0,6
16s						
Armour top/ Armour bottom	0,8	1,2	1,2	2,2	0,5	0,9
Armour bottom/ Filter bottom	1,6	1,0	1,4	0,5	1,4	1,5
Filter bottom/ Screed top	1,0	0,9	1,4	1,8	0,6	1,8
18s						
Armour top/ Armour bottom	1,1	0,7	1,3	1,6	2,0	1,2
Armour bottom/ Filter bottom	1,4	0,9	2,0	0,8	0,4	1,8
Filter bottom/ Screed top	1,0	1,2	1,4	1,0	1,1	1,0

The ratios in Table O-1 are plotted for each test set in Figures O-7 to O-11.

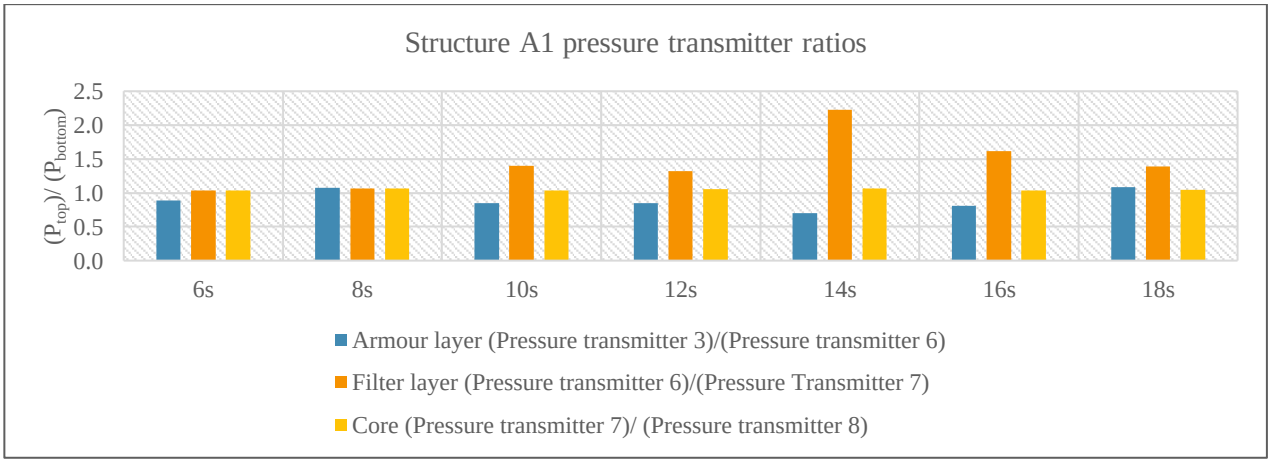

Figure O- 7:Ratio of pressure heads for layers in Structure A1

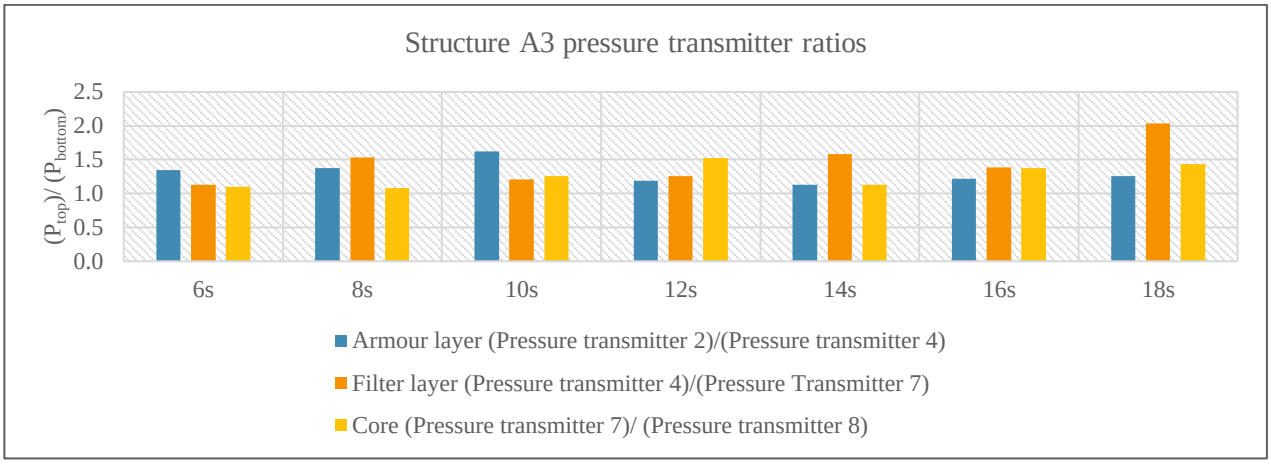

Figure O- 8: Ratio of pressure heads for layers in Structure A3

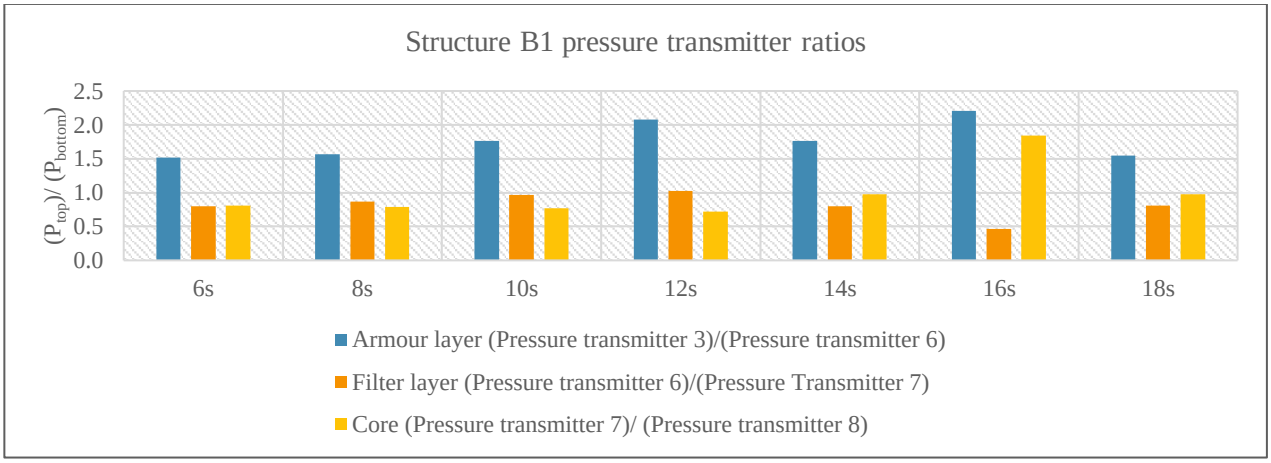

Figure O- 9: Ratio of pressure heads for layers in Structure B1

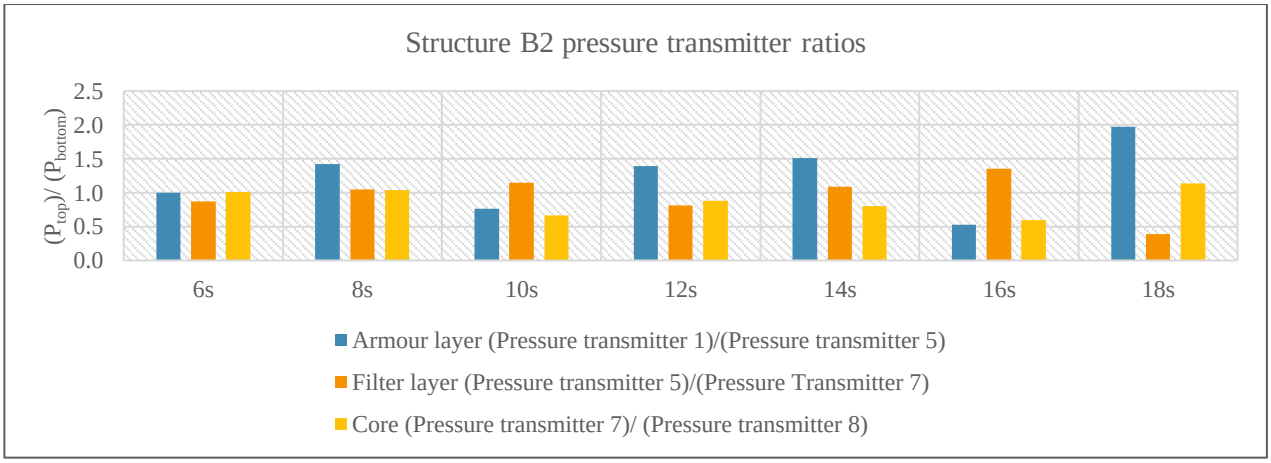

Figure O- 10: Ratio of pressure heads for layers in Structure B2

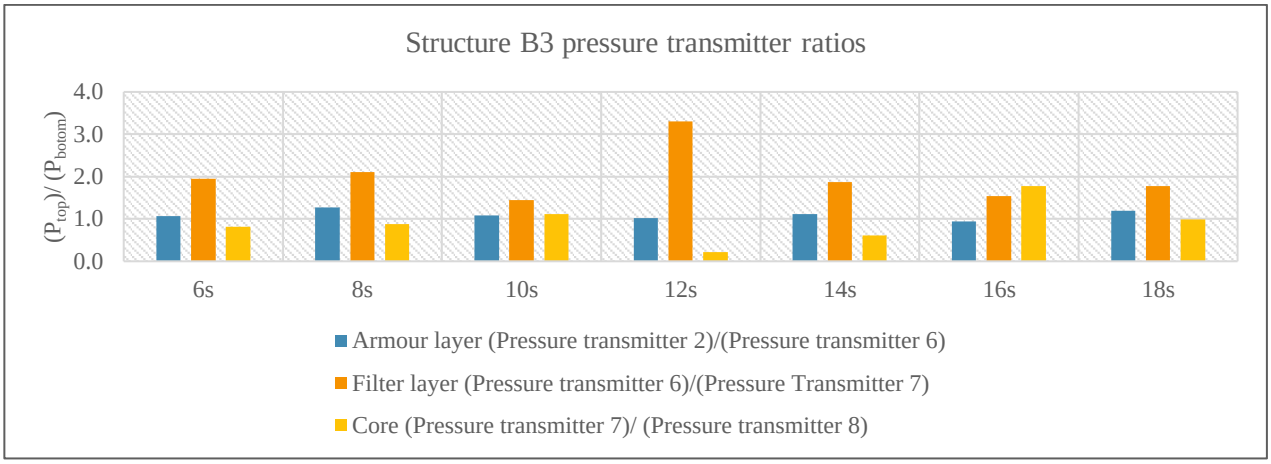

Figure O- 11: Ratio of pressure heads for layers in Structure B3

The dynamic pressure head ratios for the armour layer and filter layers for each structure is given in Figure O-12 and Figure O-13. The average dynamic pressure head at the wave periods is included in the graph.

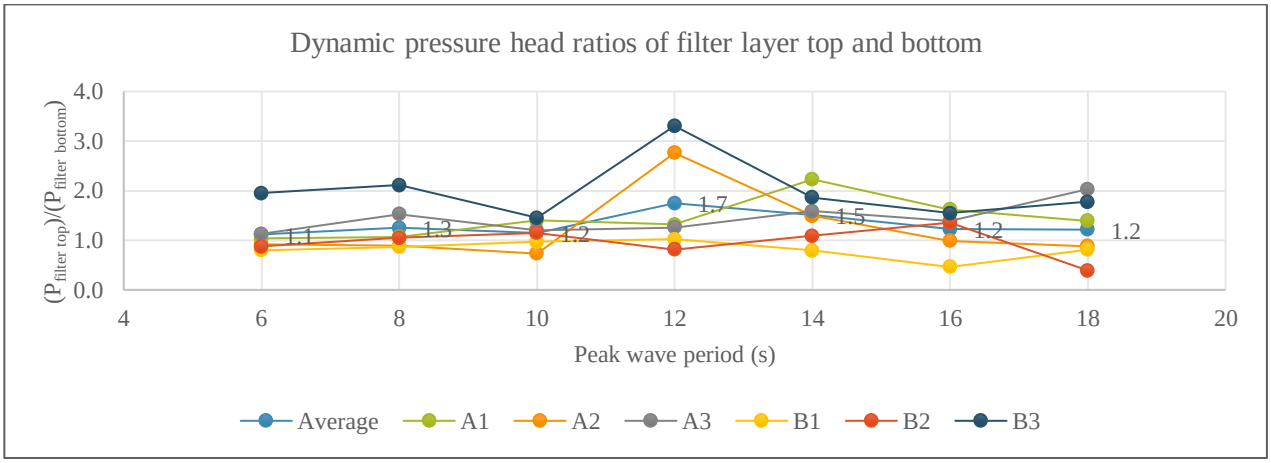

Figure O- 12: Dynamic pressure head ratio of filter layer top and bottom

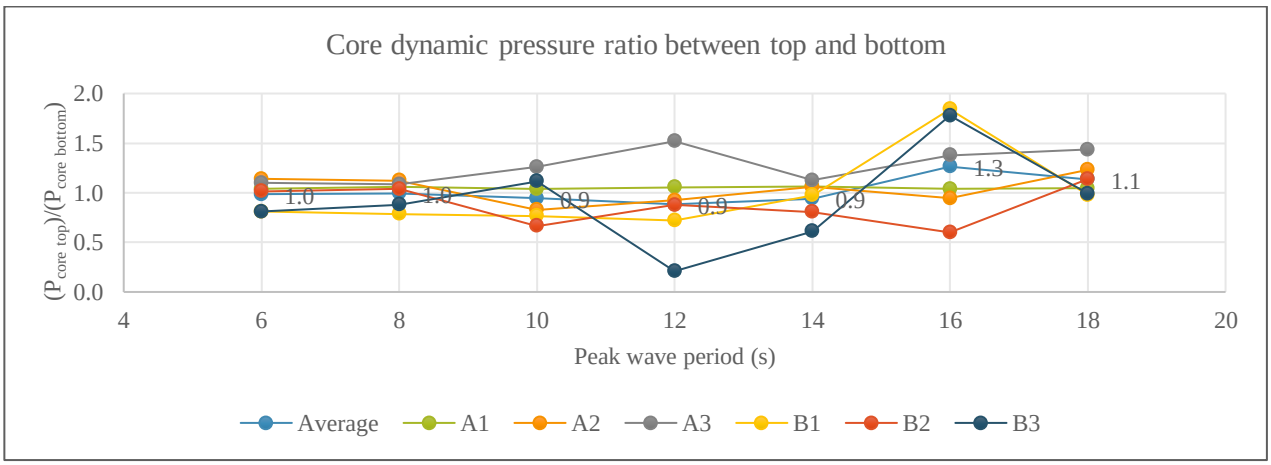

Figure O- 13: Dynamic pressure head ratio of core top and bottom

APPENDIX P: FLOW VELOCITY CALCULATIONS

VOLUMETRIC POROSITY VARIABLES

Table P- 1: Variables used to calculate the volumetric porosity

Armour 28mm		Filter 13mm		Filter 11mm		Core 6mm		Core 5mm	
n_{RRM}	6,16	n_{RRM}	6,01	n_{RRM}	6,23	n_{RRM}	6,01	n_{RRM}	5,70
n_{RRD}	18,47	n_{RRD}	18,02	n_{RRD}	18,70	n_{RRD}	18,02	n_{RRD}	17,10
y_{NUL}	0,70	y_{NUL}	0,70	y_{NUL}	0,70	y_{NUL}	0,70	y_{NUL}	0,70
y_{NLL}	0,10	y_{NLL}	0,10	y_{NLL}	0,10	y_{NLL}	0,10	y_{NLL}	0,10
NUL	0,06	**NUL**	0,01	**NUL**	0,00	**NUL**	0,00	**NUL**	0,00
NLL	0,04	**NLL**	0,00	**NLL**	0,00	**NLL**	0,00	**NLL**	0,00
e	0,89	**e**	0,89	**e**	0,89	**e**	0,89	**e**	0,89
n_v	0,47	n_v	0,47	n_v	0,47	n_v	0,47	n_v	0,47

FORCHHEIMER COEFFICIENTS

The laminar coefficient ($\propto_{FOR}$), is calculated to have values greater than 1500. Irregular and angular grains typically have values larger than 1500. Irregular and angular grains usually have a turbulent coefficient ($\boldsymbol{\beta_{FOR}}$) of up to 3.6 or more.

Table P- 2: Forchheimer laminar and turbulent coefficients

$\propto_{FOR}$ Coefficient				β_{FOR} Coefficient			A_{FOR} Coefficient			B_{FOR} Coefficient		
Test	**armour**	**filter**	**core**	**armour**	**filter**	**core**	**armour**	**filter**	**core**	**armour**	**filter**	**core**
A1 - 6S	2491,4	1854,5	1719,1	1,8	2,2	2,6	1,0	3,1	14,3	36,7	44,0	23,7
A1 - 8S	2491,4	1854,5	1719,1	1,8	2,2	2,6	1,0	3,1	14,3	36,7	44,0	23,7
A1 - 10S	2491,4	1854,5	1719,1	1,8	2,2	2,6	1,0	3,1	14,3	36,7	44,0	23,7
A1 -12S	2491,4	1854,5	1719,1	1,8	2,2	2,6	1,0	3,1	14,3	36,7	44,0	23,7
A1 - 14S	2491,4	1854,5	1719,1	1,8	2,2	2,6	1,0	3,1	14,3	36,7	44,0	23,7
A1 - 16S	2491,4	1854,5	1719,1	1,8	2,2	2,6	1,0	3,1	14,3	36,7	44,0	23,7
A1 - 18S	2491,4	1854,5	1719,1	1,8	2,2	2,6	1,0	3,1	14,3	36,7	44,0	23,7
A2 - 6S	2491,4	1854,5	1719,1	1,8	2,2	2,6	1,0	3,1	14,3	36,7	44,0	23,7
A2 - 8S	2491,4	1854,5	1719,1	1,8	2,2	2,6	1,0	3,1	14,3	36,7	44,0	23,7
A2 - 10S	2491,4	1854,5	1719,1	1,8	2,2	2,6	1,0	3,1	14,3	36,7	44,0	23,7
A2 - 12S	2491,4	1854,5	1719,1	1,8	2,2	2,6	1,0	3,1	14,3	36,7	44,0	23,7
A2 - 14S	2491,4	1854,5	1719,1	1,8	2,2	2,6	1,0	3,1	14,3	36,7	44,0	23,7
A2 - 16S	2491,4	1854,5	1719,1	1,8	2,2	2,6	1,0	3,1	14,3	36,7	44,0	23,7
A2 - 18S	2491,4	1854,5	1719,1	1,8	2,2	2,6	1,0	3,1	14,3	36,7	44,0	23,7
A3 - 6S	2491,4	1854,5	1719,1	1,8	2,2	2,6	1,0	3,1	14,3	36,7	44,0	23,7
A3 - 8S	2491,4	1854,5	1719,1	1,8	2,2	2,6	1,0	3,1	14,3	36,7	44,0	23,7
A3 - 10S	2491,4	1854,5	1719,1	1,8	2,2	2,6	1,0	3,1	14,3	36,7	44,0	23,7
A3 - 12S	2491,4	1854,5	1719,1	1,8	2,2	2,6	1,0	3,1	14,3	36,7	44,0	23,7
A3 - 14S	2491,4	1854,5	1719,1	1,8	2,2	2,6	1,0	3,1	14,3	36,7	44,0	23,7
A3 - 16S	2491,4	1854,5	1719,1	1,8	2,2	2,6	1,0	3,1	14,3	36,7	44,0	23,7
A3 - 18S	2491,4	1854,5	1719,1	1,8	2,2	2,6	1,0	3,1	14,3	36,7	44,0	23,7
B1 - 6S	2491,4	1817,1	1707,8	1,8	2,3	2,7	1,0	3,0	22,2	36,7	111,8	24,6
B1 - 8S	2491,4	1817,1	1707,8	1,8	2,3	2,7	1,0	3,0	22,2	36,7	111,8	24,6
B1 - 10S	2491,4	1817,1	1707,8	1,8	2,3	2,7	1,0	3,0	22,2	36,7	111,8	24,6
B1 - 12S	2491,4	1817,1	1707,8	1,8	2,3	2,7	1,0	3,0	22,2	36,7	111,8	24,6
B1 - 14S	2491,4	1817,1	1707,8	1,8	2,3	2,7	1,0	3,0	22,2	36,7	111,8	24,6

Table P-2: Forchheimer laminar and turbulent coefficients continues

B1 - 16S	2491,4	1817,1	1707,8	1,8	2,3	2,7	1,0	3,0	22,2	36,7	111,8	24,6
B1 - 18S	2491,4	1817,1	1707,8	1,8	2,3	2,7	1,0	3,0	22,2	36,7	111,8	24,6
B2 - 6S	2491,4	1817,1	1707,8	1,8	2,3	2,7	1,0	3,0	22,2	36,7	111,8	24,6
B2 - 8S	2491,4	1817,1	1707,8	1,8	2,3	2,7	1,0	3,0	22,2	36,7	111,8	24,6
B2 - 10S	2491,4	1817,1	1707,8	1,8	2,3	2,7	1,0	3,0	22,2	36,7	111,8	24,6
B2 - 12S	2491,4	1817,1	1707,8	1,8	2,3	2,7	1,0	3,0	22,2	36,7	111,8	24,6
B2 - 14S	2491,4	1817,1	1707,8	1,8	2,3	2,7	1,0	3,0	22,2	36,7	111,8	24,6
B2 - 16S	2491,4	1817,1	1707,8	1,8	2,3	2,7	1,0	3,0	22,2	36,7	111,8	24,6
B2 - 18S	2491,4	1817,1	1707,8	1,8	2,3	2,7	1,0	3,0	22,2	36,7	111,8	24,6
B3 - 6S	2491,4	1817,1	1707,8	1,8	2,3	2,7	1,0	3,0	22,2	36,7	111,8	24,6
B3 - 8S	2491,4	1817,1	1707,8	1,8	2,3	2,7	1,0	3,0	22,2	36,7	111,8	24,6
B3 - 10S	2491,4	1817,1	1707,8	1,8	2,3	2,7	1,0	3,0	22,2	36,7	111,8	24,6
B3 - 12S	2491,4	1817,1	1707,8	1,8	2,3	2,7	1,0	3,0	22,2	36,7	111,8	24,6
B3 - 14S	2491,4	1817,1	1707,8	1,8	2,3	2,7	1,0	3,0	22,2	36,7	111,8	24,6
B3 - 16S	2491,4	1817,1	1707,8	1,8	2,3	2,7	1,0	3,0	22,2	36,7	111,8	24,6
B3 -18S	2491,4	1817,1	1707,8	1,8	2,3	2,7	1,0	3,0	22,2	36,7	111,8	24,6

HYDRAULIC GRADIENT CALCULATIONS

Table P- 3: Calculated hydraulic gradients

Test	Armour layer	Filter layer	Core
A1 - 6S	12,3	70,5	62,6
A1 - 8S	51,1	281,9	84,7
A1 - 10S	181,8	284,9	89,7
A1 -12S	138,9	297,2	78,4
A1 - 14S	136,8	297,2	132,1
A1 - 16S	185,9	303,3	151,0
A1 - 18S	190,9	432,0	261,5
A2 - 6S	47,3	61,3	72,6
A2 - 8S	49,4	134,8	77,6
A2 - 10S	70,9	140,9	101,0
A2 - 12S	47,3	496,3	138,9
A2 - 14S	91,3	572,9	202,0
A2 - 16S	185,9	577,9	207,0
A2 - 18S	190,9	582,9	212,0
A3 - 6S	54,4	66,3	75,8
A3 - 8S	59,4	244,3	183,1
A3 - 10S	64,4	388,3	236,7
A3 - 12S	69,4	295,5	227,3
A3 - 14S	86,0	327,7	167,3
A3 - 16S	84,3	342,8	239,9
A3 - 18S	89,3	347,8	244,9
B1 - 6S	94,0	202,2	75,8
B1 - 8S	140,9	196,1	94,7
B1 - 10S	230,8	220,6	145,2
B1 - 12S	288,0	257,4	132,6
B1 - 14S	192,0	300,2	116,8
B1 - 16S	347,2	508,6	309,3
B1 - 18S	190,0	343,1	314,3
B2 - 6S	38,7	73,5	41,0
B2 - 8S	39,7	186,9	198,9
B2 - 10S	44,7	242,0	203,9
B2 - 12S	51,5	134,8	157,8
B2 - 14S	63,4	134,8	249,4
B2 - 16S	145,0	128,2	284,1
B2 - 18S	93,4	527,0	249,4
B3 - 6S	23,6	297,2	110,5
B3 - 8S	62,0	337,0	202,0
B3 - 10S	42,2	309,4	176,8
B3 - 12S	6,2	168,5	277,8
B3 - 14S	69,4	383,0	328,3
B3 - 16S	33,5	447,3	255,7
B3 -18S	54,6	471,8	260,7

CALCULATED VELOCITIES

The calculated flow velocities of the different structures through the armour layer, filter layer and core are given in Figure P-1, Figure P-2 and Figure P-3 respectively.

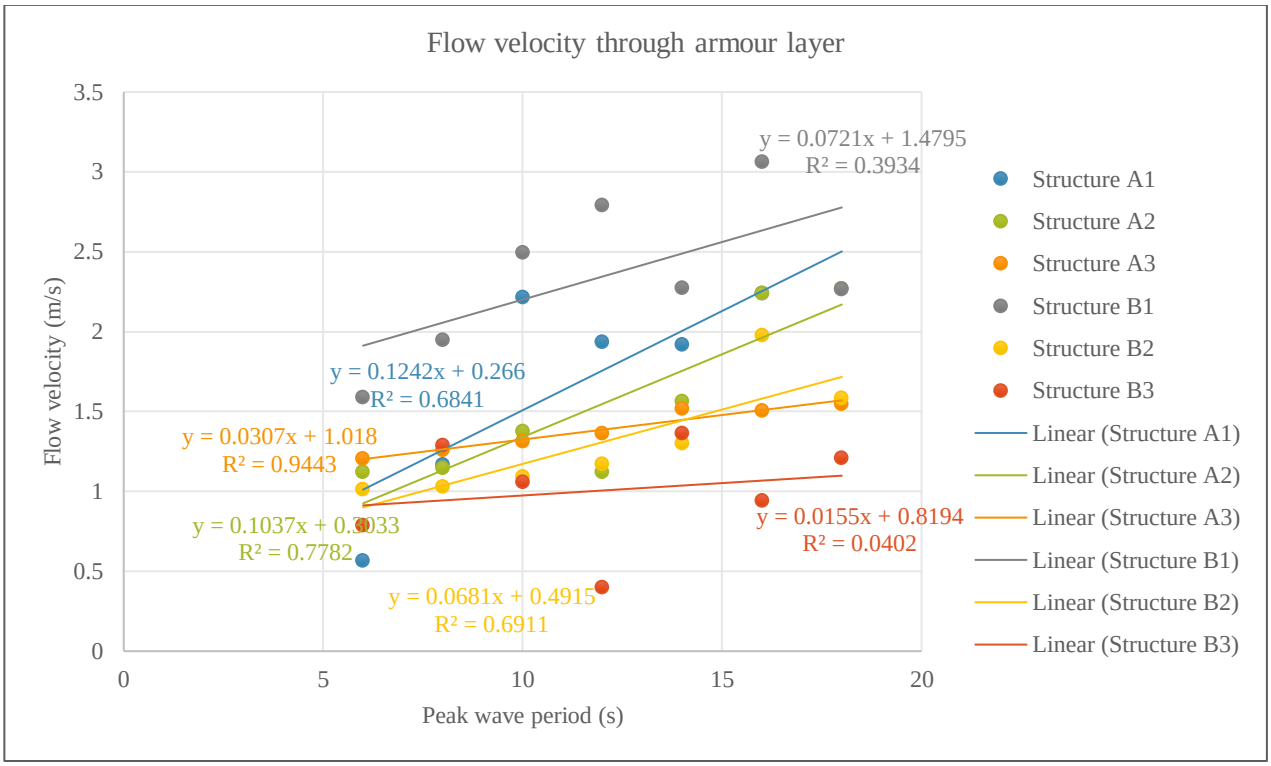

Figure P- 1: Flow velocity through armour layer

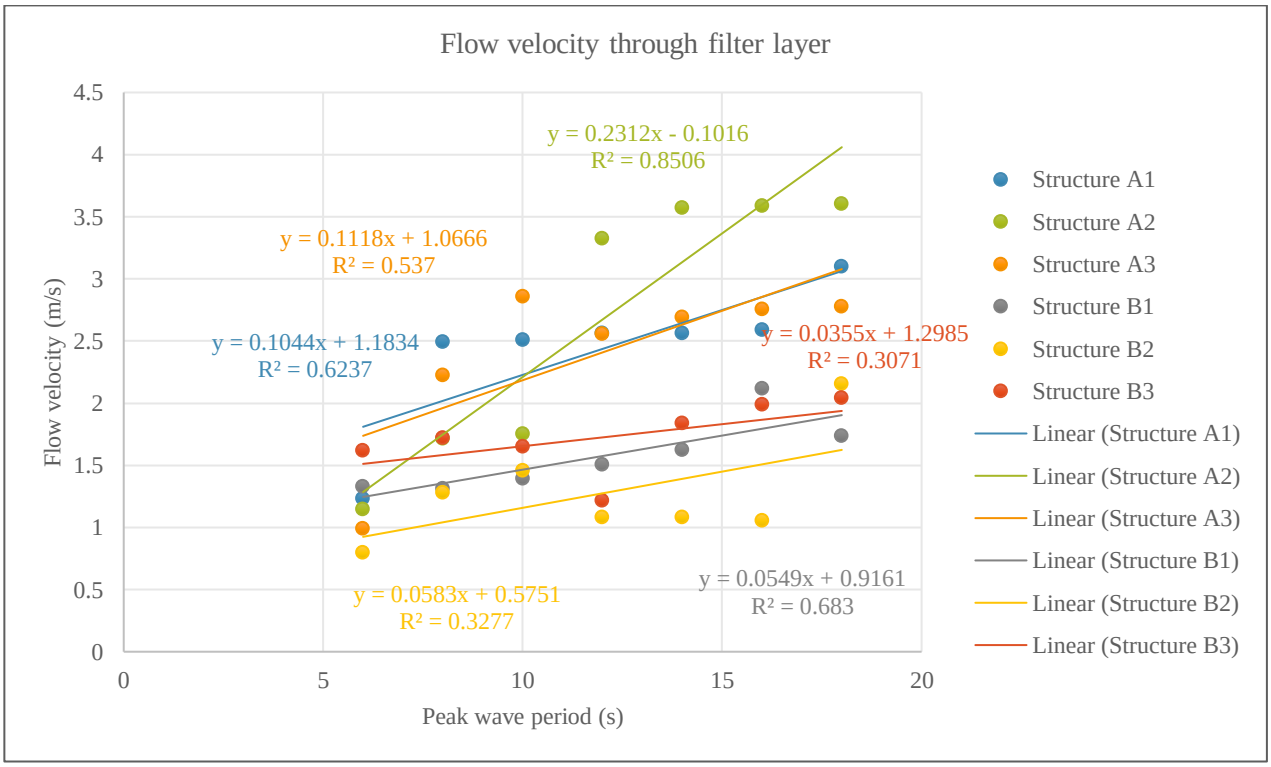

Figure P- 2: Flow velocity through filter layer

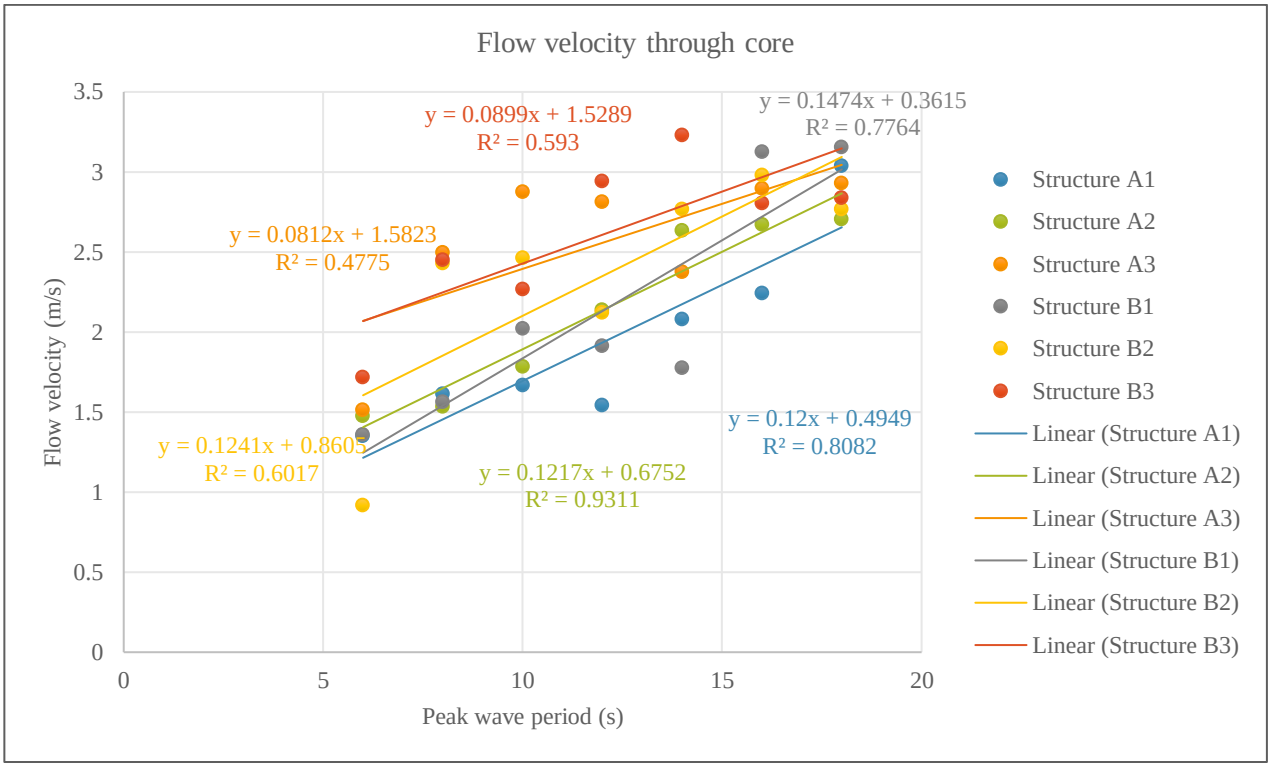

Figure P- 3: Flow velocity through core

APPENDIX Q: EXTERNAL ENERGY DISSIPATION DUE TO WAVE BREAKING

The transmitted wave height is calculated first using the equation by (van der Meer & Daemen, 1994). It is found that $\frac{B}{H_i} < 10$ thus, the transmission coefficient is calculated using Equation 2-5. The parameters used for the calculation of the transmitted wave height is given in Table Q-1.

Table Q- 1: Parameters used to calculate the transmitted wave height

Test nu.	T_p (proto)	Breaker parameter	K_t	H_t (m)
1	6	0,25	0,37	0,48
2	8	0,30	0,38	0,50
3	10	0,33	0,39	0,51
4	12	0,37	0,40	0,52
5	14	0,40	0,40	0,53
6	16	0,42	0,41	0,53
7	18	0,45	0,42	0,54
8	6	0,26	0,37	0,49
9	8	0,31	0,39	0,50
10	10	0,35	0,39	0,51
11	12	0,39	0,40	0,52
12	14	0,42	0,41	0,53
13	16	0,45	0,42	0,54
14	18	0,48	0,42	0,55
15	6	0,26	0,37	0,49
16	8	0,31	0,38	0,50
17	10	0,35	0,39	0,51
18	12	0,38	0,40	0,52
19	14	0,41	0,41	0,53
20	16	0,44	0,41	0,54
21	18	0,47	0,42	0,55
22	6	0,25	0,37	0,48
23	8	0,29	0,38	0,50
24	10	0,33	0,39	0,51
25	12	0,36	0,40	0,52
26	14	0,39	0,40	0,53
27	16	0,42	0,41	0,53
28	18	0,45	0,42	0,54
29	6	0,26	0,37	0,49
30	8	0,31	0,39	0,50
31	10	0,35	0,39	0,51
32	12	0,38	0,40	0,52
33	14	0,42	0,41	0,53
34	16	0,45	0,42	0,54
35	18	0,47	0,42	0,55
36	6	0,26	0,37	0,49
37	8	0,31	0,38	0,50
38	10	0,34	0,39	0,51
39	12	0,38	0,40	0,52
40	14	0,41	0,41	0,53
41	16	0,44	0,41	0,54
42	18	0,47	0,42	0,55

The equation by (Battjes & Janssen, 1978) is used to calculate the energy dissipation due to wave breaking. In the equation, the calibration coefficient is taken as one. The maximum wave height is calculated using the equation:

$$H_m = 0.88\frac{\mathrm{L}}{2\pi}\tanh\left(\frac{2\pi\mathrm{h}}{\mathrm{L}}.\frac{\gamma_b}{0.88}\right)$$

The Raleigh distribution is used to determine the ratio for broken waves. The significant wave height (H_s) is taken as the transmitted wave height as calculated using Equation 2-5. The transmitted wave height is used to calculate $\mathrm{H_{rms}} = \frac{\mathrm{H_s}}{\sqrt{2}}$. The variables used to obtain the energy dissipation is given in Table Q-2.

$$1 - \mathrm{Q} + \left(\frac{\mathrm{H_{rms}}}{\mathrm{H_m}}\right)^2 \ln\mathrm{Q} = 0$$

Table Q- 2: Parameters used to calculate the external energy dissipation

Test nu.	$H_s = H_t$ (m)	L	h	H_m	H_{rms}	Q	D_b
1	0,48	18,44	1	0,68	0,34	1,25	238,60
2	0,50	24,79	1	0,69	0,35	1,26	184,03
3	0,51	31,11	1	0,69	0,36	1,27	149,75
4	0,52	37,42	1	0,70	0,37	1,28	126,33
5	0,53	43,72	1	0,70	0,37	1,29	109,35
6	0,53	50,03	1	0,70	0,38	1,29	96,49
7	0,54	56,36	1	0,70	0,38	1,30	86,37
8	0,49	18,44	1	0,68	0,34	1,25	239,38
9	0,50	24,79	1	0,69	0,35	1,26	184,79
10	0,51	31,11	1	0,69	0,36	1,27	150,45
11	0,52	37,42	1	0,70	0,37	1,28	126,99
12	0,53	43,72	1	0,70	0,38	1,29	109,98
13	0,54	50,03	1	0,70	0,38	1,30	97,07
14	0,55	56,36	1	0,70	0,39	1,31	86,96
15	0,49	18,44	1	0,68	0,34	1,25	239,11
16	0,50	24,79	1	0,69	0,35	1,26	184,53
17	0,51	31,11	1	0,69	0,36	1,27	150,21
18	0,52	37,42	1	0,70	0,37	1,28	126,76
19	0,53	43,72	1	0,70	0,38	1,29	109,76
20	0,54	50,03	1	0,70	0,38	1,30	96,87
21	0,55	56,36	1	0,70	0,39	1,31	86,77
22	0,48	18,44	1	0,68	0,34	1,25	238,53
23	0,50	24,79	1	0,69	0,35	1,26	183,97
24	0,51	31,11	1	0,69	0,36	1,27	149,68
25	0,52	37,42	1	0,70	0,37	1,28	126,27
26	0,53	43,72	1	0,70	0,37	1,28	109,30
27	0,53	50,03	1	0,70	0,38	1,29	96,44
28	0,54	56,36	1	0,70	0,38	1,30	86,35
29	0,49	18,44	1	0,68	0,34	1,25	239,29
30	0,50	24,79	1	0,69	0,35	1,26	184,70
31	0,51	31,11	1	0,69	0,36	1,27	150,37
32	0,52	37,42	1	0,70	0,37	1,28	126,92
33	0,53	43,72	1	0,70	0,38	1,29	109,91
34	0,54	50,03	1	0,70	0,38	1,30	97,01
35	0,55	56,36	1	0,70	0,39	1,31	86,90
36	0,49	18,44	1	0,68	0,34	1,25	239,09
37	0,50	24,79	1	0,69	0,35	1,26	184,51
38	0,51	31,11	1	0,69	0,36	1,27	150,19
39	0,52	37,42	1	0,70	0,37	1,28	126,74
40	0,53	43,72	1	0,70	0,38	1,29	109,74
41	0,54	50,03	1	0,70	0,38	1,30	96,85
42	0,55	56,36	1	0,70	0,39	1,31	86,75

APPENDIX R: INTERNAL ENERGY DISSIPATION RESULTS

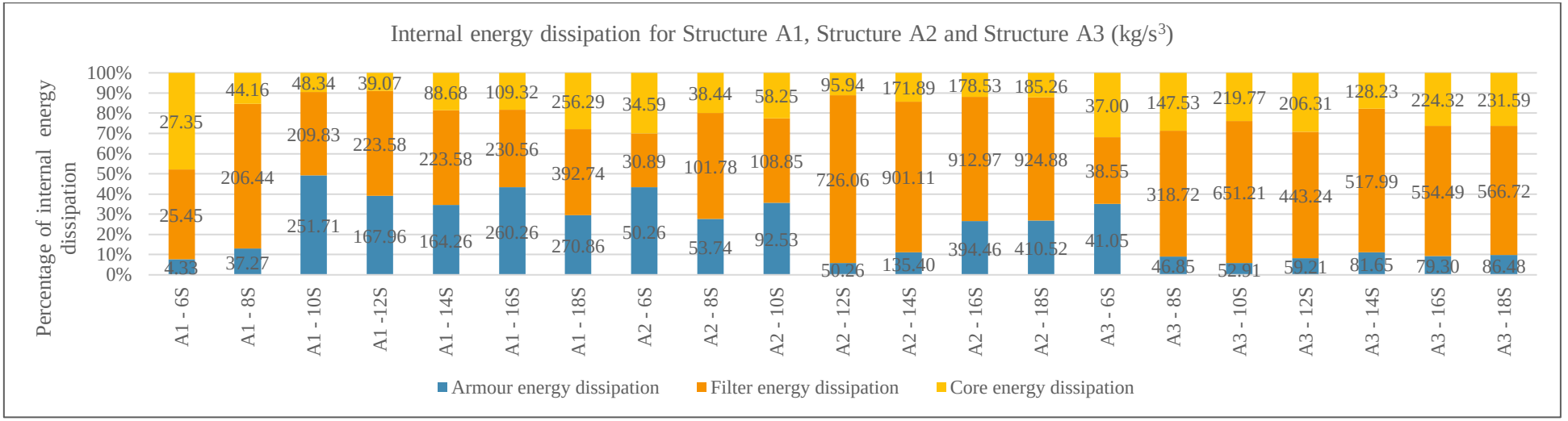

Figure R- 1: Internal energy dissipation for Structure A1, Structure A2 and Structure A3

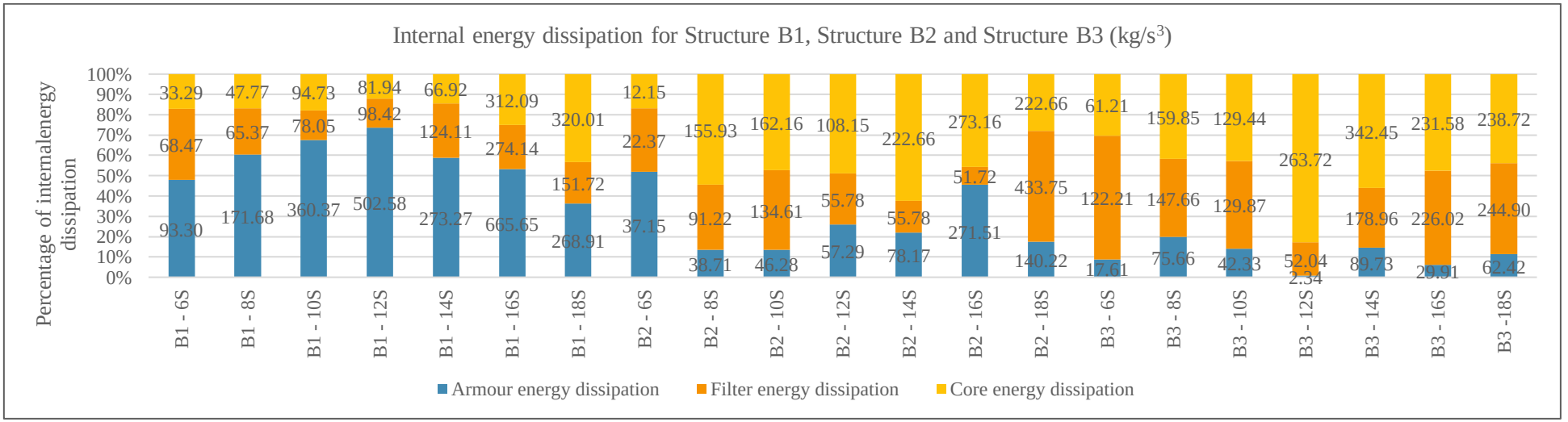

Figure R- 2: Internal energy dissipation for Structure B1, Structure B2 and Structure B3

APPENDIX S: KINETIC ENERGY CALCULATED RESULTS

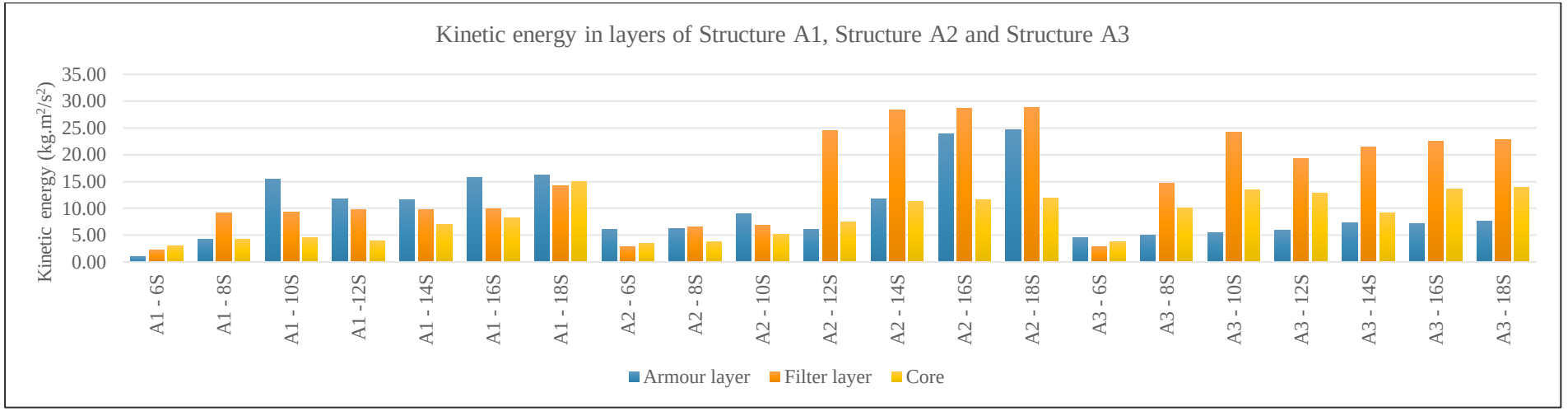

Figure S- 1: Kinetic energy in layers of Structure A1, Structure A2 and Structure A3

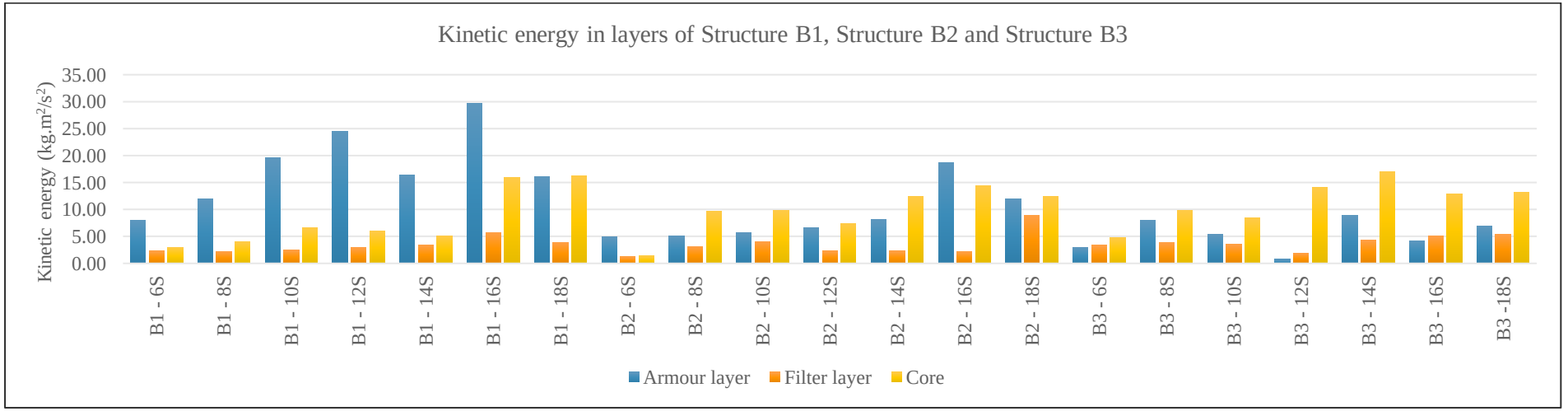

Figure S- 2: Kinetic energy in layers of Structure B1, Structure B2 and Structure B3

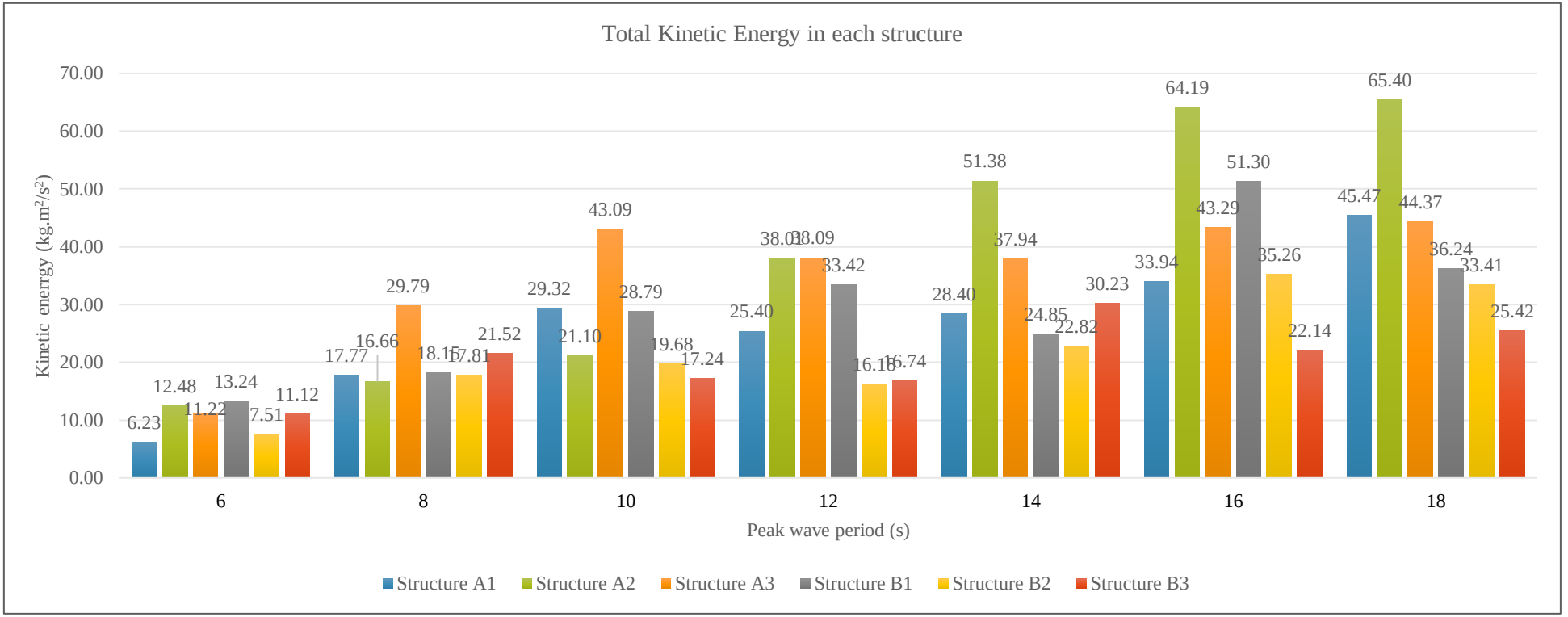

Figure S- 3: Total kinetic energy in each structure during the seven tested wave periods